UNIVERSITY OF SOUTHAMPTON

FACULTY OF ENGINEERING AND THE ENVIRONMENT

Performance Quantification of Tidal Turbines Subjected to Dynamic Loading

by

Pascal Galloway

Thesis for the degree of Doctor of Philosophy

March 2013

Abstract

The behaviour of Tidal Stream Turbines (TST) in the dynamic flow field caused by waves and rotor misalignment to the incoming flow (yaw) is currently poorly understood. The dynamic loading applied to the turbine could drive the structural design of the power capture and support subsystems, device size and its proximity to the water surface and sea bed. In addition, the strongly bi-directional nature of the flow encountered at many tidal energy sites may lead to devices omitting yaw drives; accepting the additional dynamic loading associated with rotor misalignment and reduced power production in return for a reduction in capital cost. For such a design strategy it is imperative to quantify potential unsteady rotor loads so that the TST device design accommodates the inflow conditions and avoids an unacceptable increase in maintenance action or, more seriously, suffers sudden structural failure.

The experiments presented as part of this work were conducted using a 1:20th scale 3-bladed horizontal axis TST at a large towing tank facility. The turbine had the capability to measure rotor thrust and torque, blade root strain, azimuthal position and speed. The maximum out-of-plane bending moment was found to be as much as 9.5 times the in-plane bending moment, within the range of experiments conducted. A maximum loading range of 175% of the median out-of-plane bending moment and 100% of the median in-plane bending moment was observed for a turbine test case with zero yaw, scaled wave height of 2m and intrinsic wave period of 12.8s.

A Blade Element-Momentum (BEM) numerical model has been developed and modified to account for wave motion and yawed flow effects. This model includes a new dynamic inflow correction which is shown to be in close agreement with the measured experimental loads. The gravitational component was significant to the experimental in-plane blade bending moment and was included in the BEM model. Steady yaw loading on an individual blade was found to be negligible in comparison to wave loading (for the range of experiments conducted), but becomes important for the turbine rotor as a whole, reducing power capture and rotor thrust.

Contents

List of Figures

List of Tables

Nomenclature

Abbreviations

ADCP	Acoustic Doppler Current Profiler
AWAC	Acoustic Wave And Current
BEM	Blade Element Momentum
CAD	Computer Aided Design
CFD	Computational Fluid Dynamics
CfD	Contract for Difference
CNC	Computer Numerically Controlled
DAQ	Data Acquisition
DEL	Damage Equivalent Load
EMR	Electricity Market Reform
FEA	Finite Element Analysis
NREL	National Renewable Energy Laboratory
PerAWaT	Performance Assessment of Wave and Tidal array systems
RANS	Reynolds Averaged Navier Stokes
ROC	Renewable Obligation Certificate
TSR	Tip-Speed Ratio
TST	Tidal Stream Turbine

WSB	Wheatstone Bridge

Latin Symbols

A	Turbine rotor area (m^2) Cross-sectional area of object (m^2)
a	Stretching parameter ($-$) Axial inflow factor ($-$)
a'	Tangential inflow factor ($-$)
$\dot{a}$	Axial inflow factor time derivative ($-$)
a_{skew}	Skewed axial inflow factor ($-$)
A_{TD}	Empirical time delay coefficient for dynamic stall ($-$)
B	Number of blades on the turbine ($-$)
c	Chord length (m)
C_A	Coefficient of added mass ($-$)
c_a	Apparent wave celerity ($m.s^{-1}$)
C_D	Coefficient of drag ($-$)
C_{DMAX}	Maximum coefficient of drag ($-$)
$C_{D_{mor}}$	Coefficient of drag ($-$)
c_i	Intrinsic wave celerity ($m.s^{-1}$)
C_L	Coefficient of lift ($-$)
$C_{L_{3D}}$	Three dimensional coefficient of lift ($-$)
$C_{L,d}$	Coefficient of lift corrected for dynamic stall effects ($-$)
C_M	Coefficient of inertia ($-$)
C_{MX}	Coefficient of in-plane blade root bending moment ($-$)
C_{MY}	Coefficient of out-of-plane blade root bending moment ($-$)

C_P	Coefficient of power $(-)$
C_{PX}	Sectional power coefficient as a function of blade azimuth $(-)$
C_T	Coefficient of thrust $(-)$
$C_{T,d}$	Contribution to the total thrust coefficient of the dynamic acceleration $(-)$
C_{TX}	Sectional thrust coefficient as a function of blade azimuth $(-)$
C_X	Sectional blade element force coefficient normal to the rotor plane $(-)$
C_{XX}	Sectional blade element force coefficient normal to the rotor plane as a function of blade azimuth $(-)$
C_Y	Sectional blade element force coefficient parallel to the rotor plane $(-)$
C_{YX}	Sectional blade element force coefficient parallel to the rotor plane as a function of blade azimuth $(-)$
d	Water depth (m)
d_s	Stretching depth (m)
F	Total inline force on the object (N)
F_s	Stretching factor $(-)$
g	Acceleration due to gravity $(m.s^{-2})$
H	Wave height (m)
K	Prandtl correction factor for tip and root losses $(-)$
k	Wave number (m^{-1})
L	Wave length (m)
L_{years}	Life-time of a part subject to fatigue $(years)$
M_{IP}	In-plane bending moment $(-)$
M_{OP}	Out-of-plane bending moment $(-)$
N_i	Number of load cycles to failure $(-)$

n_i	Number of load cycles $(-)$
P	Power density per unit width of wavefront $(W.m^{-1})$
	Once per revolution $(-)$
Q	Rotor/shaft torque $(N.m)$
q	Power density in a water current $(W.m^{-2})$
$\bar{q}$	Average power density in a water current $(W.m^{-2})$
R	Blade radius (m)
r	Blade radial distance (m)
R_1	Radius of the outer element section (m)
R_2	Radius of the inner element section (m)
T	Thrust on the rotor (N)
t	Time (s)
T_a	Apparent wave period (s)
T_{drel}	Relative dynamic thrust force (N)
T_i	Intrinsic wave period (s)
t_I	Time instant at a blade element position (s)
t_X	Time change caused by yawed inflow (s)
U	Current velocity $(m.s^{-1})$
u	Fluid velocity $(m.s^{-1})$
U_0	Fluid velocity upstream of the rotor $(m.s^{-1})$
U_1	Fluid velocity at the rotor $(m.s^{-1})$
U_2	Fluid velocity downstream of the rotor $(m.s^{-1})$
u_a	Apparent horizontal wave particle velocity $(m.s^{-1})$

u_b	Velocity of the body in the line of flow ($m.s^{-1}$)
U_c	Freestream current velocity unaffected by blockage ($m.s^{-1}$)
u_i	Intrinsic horizontal wave particle velocity ($m.s^{-1}$)
U_{max}	Maximum current velocity ($m.s^{-1}$)
u_{Range}	Velocity range attributed to waves ($m.s^{-1}$)
u_{rRange}	Velocity range attributed to blade rotation and waves ($m.s^{-1}$)
V	Object volume (m^3)
W	Resultant velocity at a blade element ($m.s^{-1}$)
w_a	Apparent vertical wave particle velocity ($m.s^{-1}$)
w_i	Intrinsic vertical wave particle velocity ($m.s^{-1}$)
x	Dimensionless blade radius ($-$)
x_a	Apparent distance (m)
x_i	Intrinsic distance (m)
Y	Year sample time ratio ($-$)
z	Particle reference depth (m)
z_H	Turbine hub depth from water surface (m)
z_I	Blade element reference depth position (m)
z_s	Stretched vertical 'depth' (m)
z_X	Change in vertical distance as a result of blade rotation (m)

Greek Symbols

α	Angle of attack ($radians$)
α_0	Angle of attack when coefficient of lift is zero ($radians$)
α_d	Angle of attack corrected for dynamic stall ($radians$)

$\dot{\alpha}$	Rate of change of angle of attack ($rad.s^{-1}$)
α_S	Angle of attack when at static stall ($radians$)
β	Direction of the current with respect to the wave propagation direction (m) Blade pitch angle ($radians$)
χ	Wake skew angle ($radians$)
η	Water surface elevation ($-$)
γ	Rotor yaw angle ($radians$)
λ	Tip-Speed-Ratio ($-$)
Ω	Angular velocity ($rad.s^{-1}$)
ω_a	Apparent wave frequency (Hz)
ω_i	Intrinsic wave frequency (Hz)
ϕ	Relative angle of the resultant velocity at a blade element position ($radians$)
ψ	Azimuthal blade position ($radians$)
ρ	Water density ($kg.m^{-3}$)
σ	Local blade solidity ($-$)
τ	Period of natural tide (s)
θ	Wave phase at a fixed location in space ($radians$)

Form of Declaration

I, Pascal Galloway, declare that the thesis entitled *Performance Quantification of Tidal Turbines Subjected to Dynamic Loading,* and the work presented in the thesis are both my own, and have been generated by me as the result of my own original research.

I confirm that:

- This work was done wholly while in candidature for a research degree at this University.
- Where any part of this thesis has previously been submitted for a degree or any other qualification at this university or any other institution, this has been clearly stated.
- Where I have consulted the published work of others, this is always clearly attributed.
- Where I have quoted from the work of others, the source is always given. With the exception of such quotations, this thesis is entirely my own work.
- I have acknowledged all main sources of help.
- Where the thesis is based on work done by myself jointly with others, I have made clear exactly what was done by others and what I have contributed myself.
- Part of this work will be published as Galloway, P.W. et al. (2014)
- Part of this work has been published as Myers, L.E. et al. (2011)
- Part of this work has been published as Galloway, P.W. et al. (2011)
- Part of this work has been published as Galloway, P.W. et al. (2010)

Signed:..

Date:..

Acknowledgments

I would like to thank the following people who played important roles in the completion of my doctorate:

My supervisor, Luke Myers, for the support, expert knowledge and trust in my expensive designs as well as the use of a pre-existing model turbine. My other supervisor, AbuBakr Bahaj, for the opportunity to undertake the research in the first place and my internal examiner John Chaplin, whose influence was crucial. Everyone within the Sustainable Energy Research Group, who listened to me and gave me useful suggestions with regards to programming, data analysis techniques and experimental technology. Tassos Papafragkou, whose insights were invaluable and for always being willing to assist with any problem. My great friends and colleagues Despoina Teli, Matt Harrison, Nick Bakker, Martyn Hann, Brad Keogh, Davide Magagna, Mark Leybourne, Jack Giles and Tom Blackmore with whom I shared time in the office; for the continuous and mutual help both at an academic and a personal level.

Thistle Design (MMC) Ltd. for being willing to design a new encoder to suit my needs. The National Renewable Energy Centre for their assistance with FAST and additional BEM concerns. The physics workshop at the University of Southampton for machining the aluminium turbine blade required for load measurements at quite short notice.

My parents Colette and Ian and my sister Céline for their support (both emotional and financial!) and belief in my ability to complete this doctorate. My girlfriend Athena, flatmate Peter Sparkes and close friends Mark Nicholson and Ian Cooke who helped me stay relatively sane during the whole experience.

Chapter 1

Introduction and Overview

1.1 Tidal Current Energy

Energy from ‘free-stream’ tidal currents could provide electrical power for a significant number of countries worldwide. Free-stream refers to fast tidal flows around headlands or islands and differs from a tidal barrage in the way that energy is extracted. A tidal barrage requires the blocking of a river to create a pressure head for power extraction by converting potential energy to mechanical then electrical energy. Free-stream devices extract power from the kinetic energy of tidal flows and as a result are significantly less environmentally damaging by not having a barrage that would typically result in the flooding of low lying land in the vicinity. These free-stream devices closely resemble underwater wind turbines with a horizontal axis rotor aligned perpendicular to the flow direction, however other forms of free-stream device are also under development. The United Kingdom, United States, Canada and South Korea amongst others have been at the forefront of the evolution of freestream tidal energy technology. In many parts of the world freestream tidal energy presents a lucrative resource; estimates for the UK are that the technically extractable resource is 18TWh/year (Black and Veatch, 2005) which equates to approximately 5% of the total demand. In North America 1.6TWh/year has been estimated from 7 specific locations (Bedard et al., 2006). South Korea has a number of locations on the south coast where it has been projected that several hundred MW of installed capacity could be deployed in order to reduce the country’s reliance upon energy imports (Jo et al., 2010), implying a resource of at least 1.7TWh/year.

Historically there has been incidental data regarding flow velocities at sites with strong tidal flows often only stating spring peak and neap velocities for shipping and navigational purposes. With the advent of Tidal Stream Turbine (TST) technology, high quality data sets with increased temporal and spatial resolution are slowly being acquired at locations where technology is either installed or planned for deployment. Existing equipment (primarily Acoustic Doppler Current Profilers or ADCPs) used to measure tidal currents employ vertically divergent acoustic beams in order to measure flow speed and direction through the water column, often with the added capability to measure water surface elevation to determine wave characteristics. Whilst binned data through the water column is advantageous, device geometry and principles of operation mean that standard deviation of acquired data over very short time intervals is significant, requiring time-averaging. In addition the measurement volumes (especially far from the instrument) are large. This means that short timescale effects cannot be accurately quantified (due to data averaging) and eddies and turbulence are poorly quantified although efforts have been made to correlate divergent and convergent acoustic instruments to provide better estimates of higher-order flow effects such as turbulence intensity (Thomson et al., 2010).

The effect that short-duration and length-scale flow features will have on TSTs is unclear, which will undoubtedly lead to prototype devices being over-engineered and installed at sheltered locations where such effects are minimised (Myers and Bahaj, 2008). The state of the industry to date has predominantly seen deployment at relatively sheltered sites (minimal waves). MCT (Marine Current Turbines, 2012) have installed their TST in a loch in Ireland, Hammerfest Strom (Andritz Hydro Hammerfest, 2012) in a fjord in Norway, Open Hydro (OpenHydro Group, 2012) at the EMEC (European Marine Energy Centre, 2012) test facility in Scotland and Scottish Power Renewables (Scottishpower Renewables, 2012) have recently received consent for an array off the isle of Islay in a sound protected from the Atlantic. The use of such sheltered sites is logical in the early stages of the technology where reliability and operability are key issues. However, the largest resource often lies at locations exposed to waves or with strong turbulent flow features due to varying bathymetry or eddies shed from land masses. Bearing in mind that TSTs of a given rated power can experience five times the thrust of a wind turbine of the same rated power (combination of the increased fluid density and reduced flow speed), the need to quantitatively assess the dynamic blade loading under such unsteady flow conditions is essential if the technology is to move into the most energetic waters.

The UK is already a world leader in the development of marine energy and this emerging sector could provide major economic opportunities. Unfortunately the cost of generating marine energy is currently high relative to more conventional forms of power generation. This is due to its relative infancy as a technology and the high cost of key components from the wind turbine industry such as gearbox and generator combinations which range from 16% to 27% of the total device cost (Polinder et al., 2006). Another expensive aspect is the cost attributed to installing the devices in turbulent, fast flowing waters. This is a difficult process and at present there are only a limited number of vessels that can be used to deploy the large and heavy marine devices, consequently tidal developers are competing with oil and gas companies and offshore wind developers for access to these vessels (Mackay, 2009). The Carbon Trust's 'Marine Energy Accelerator' has demonstrated the potential for significant cost reductions in the technology through the use of innovative installation and recovery techniques (Carbon Trust, 2011). Separately, the Energy Technologies Institute's 'Marine Energy Programme' is focused on addressing key technological challenges faced by the industry by supporting sea-trials of near-commercial marine energy devices. The outcomes from these trials will be used to influence their 'Performance Assessment of Wave and Tidal array systems' (PerAWaT) project to develop key support tools for the acceleration of the industry (ETI, 2010). A potential barrier to the success of marine renewables such as Tidal Stream Turbines (TST) is the current state of the electricity networks. A study has shown that £8.8 billion of investment in the UK electricity network will be required to bring Scotland's renewable energy potential to the rest of the nation (ENSG, 2012). Much of the work needed will be to bring renewable energy generated in the north of Scotland where the majority of the resources are, down to markets in southern Scotland and England.

The government support for marine renewables is currently being increased. In 2011, DECC announced that it had designated £20 million for funding marine energy development. Even more importantly, the UK government proposed to increase support of the Renewable Obligation Certificates (ROCs) to offer 5 ROCs per MWh of electricity generated by wave and tidal devices from 2013 – 2017 (DECC, 2011). This is intended to encourage significant growth in the marine energy industry and encourage investors to finance the deployment of device arrays. The current support through the ROCs scheme will close in 2017 and will be replaced by a Feed-in Tariff with Contracts for Difference (CfD) under the new Electricity Market Reform (EMR) . At the time of writing, the price per unit of electricity supplied (called the strike price) has not been set future, leaving funding levels unknown (DECC, 2011). Twidell et al. (2006) predicted that the cost (in p/kWh) of marine renewables would halve within ten years based on 'learning curves'. This is supported by Carbon Trust (2011) who suggest a cost of 15p/kWh by 2020 and 10p/kWh by

2040 (based on their ‘medium learning rates’). This reduced cost will help the technology move from supplying power to the local distribution network, to the national transmission network, possibly sharing sub-sea grids with offshore wind power.

Reliability and low operational costs are the most critical factors in achieving low average cost per kWh for systems which are capital intensive. The same can be said for the success of a tidal power device. As with other capital intensive energy technologies, the economic cost per kWh generated can be reduced if other advantages can be costed as benefit to the project. This includes carbon abatement, ROCs and low interest rates on borrowed finance. With such economic complexity, smaller schemes may perhaps be more economical, at least in the current fiscal climate. The UK’s Crown Estate, which owns and manages the seabed around the UK’s coast, has already leased 1000MW of sites to tidal energy projects in the Pentland Firth and Orkney waters, Scotland (The Crown Estate, 2010). Powerful semi-diurnal tides flow between the Atlantic Ocean and the North Sea, hence the area has been dubbed by the media as the ‘Saudi Arabia’ of tidal power.

1.2 Project Overview

TST technology is currently at the prototype stage where unique devices are being deployed at isolated testing sites. There is little detailed knowledge of the flow field properties at highly energetic tidal energy sites. Generally peak flow speeds are measured but the effect of wave and bed generated turbulence is neglected. The effect this will have on TSTs is unclear, which may lead to prototype devices being installed at sheltered sites where these effects are minimized (Myers and Bahaj, 2008). If this becomes a trend with developers it may result in reduced energy capture as blade diameters are constrained and potentially higher energy flows are not utilised. This work intends to quantify the effect of dynamic loading on TST rotors and the individual blades through a series of laboratory experiments and numerical modelling.

The fluid dynamics of TSTs is similar to that of wind turbines. There are however important differences in the nature of the flow. Saltwater is approximately 800 times denser than air, which when combined with slower flow speeds, results in TSTs experiencing four times greater thrust over the rotor than that of a similarly rated wind turbine. Flow around the TSTs is constrained by boundaries above and below, and for some sites, to the sides. There is approximately 70% percent more power available in the upper half of a tidal stream than the lower half, based on a 1/7th power law approximation as used by many authors (Gooch et al., 2009; McCann, 2007; Black and Veatch, 2005; Burton et al., 2001). Attempting to operate near the surface region however, will impose greater steady forces on the structure of the device before the dynamic effects of wave-current interaction are even considered. The strongly bi-directional nature of the flow encountered at many tidal energy sites may lead to devices omitting yaw drives; accepting the additional dynamic loading associated with rotor misalignment and reduced power production in return for a reduction in capital cost. These factors could result in structural problems associated with the blades and rotor and may lead to structural failures.

1.2.1 Research Needs

There is a need for better understanding of the effects of waves and misaligned flows on TST rotors and blades. This will increase reliability through the informed design of more optimised TST blades and rotor structures. Increased reliability and enhanced TST design may also lead to devices being installed in more energetic sites permitting greater power capture.

1.2.2 Research Aims

This project aims to quantify the effect of waves and misaligned flows on TST rotors and the individual blades through a series of scale laboratory experiments and numerical modelling.

1.2.3 Research Objectives

- Modify an existing scale model horizontal axis tidal turbine to measure rotor torque and thrust at high frequency in a towing tank facility
- Examine the effect of thrust and torque on the rotor in combined wave-current flow for varying wave-current conditions and rotor proximity to the surface region
- Repeat the experiments to include the quantification of individual blade loading. Strain gauge the blade root for Out-of-plane and In-plane bending. Synchronise the data with blade azimuthal position and acceleration
- Investigate loading effects when operating the turbine in yawed flow conditions in combination with waves
- Compare measurement data to existing theory and where necessary expand this theory to account for the measured effects

1.2.4 Research Limitations

- Wave spectra or sheared currents have not been tested on the scale model TST. It is not possible to simulate a real sea state in a towing tank due to the limited towing time available
- Sheared currents are possible using a flume, however there are few facilities available with a large enough cross-section to accommodate the model and also combine waves and as a result are cost prohibitive
- No experimental data has been corrected for blockage (unless explicitly stated) since there is arguably no adequate theory available, particularly for the case of an individual blade

1.2.5 Research Contributions

- [In Review] Galloway, P.W., Myers, L.E. and Bahaj, A.S. (2012) “Quantifying wave and yaw effects on a scale tidal stream turbine”, *Renewable Energy*
- Myers, L.E., Galloway, P.W. and Bahaj, A.S. (2011) “Operational issues surrounding the use of towing tanks for performance quantification of marine current energy converters”, *European Wave and Tidal Energy Conference, Southampton, UK*
- Galloway, P.W., Myers, L.E. and Bahaj, A.S. (2011) “Experimental and numerical results of rotor power and thrust of a tidal turbine operating at yaw and in waves”, *World Renewable Energy Congress, Linköping, Sweden*
- Galloway, P.W., Myers, L.E. and Bahaj, A.S. (2010) “Studies of a scale tidal turbine in close proximity to waves”, *3rd International Conference on Ocean Energy, Bilbao, Spain*

These publications have been included in Appendix J

Chapter 2

Literature Review

2.1 The Tides and Waves

2.1.1 Tides

The seas are liquids held on the surface of the rotating Earth by gravity. The gravitational attraction between the Earth, Moon and Sun upsets these forces and motions, resulting in tides. The level of water in the oceans rises and falls based on predictable patterns, with a semi-diurnal tide having a period of approximately 12.42 hours (Kamphuis, 2010). The change in height between consecutive high and low tides is the range, which varies enormously between sites from anything between almost 0m to over 12m (Dyer, 1986). The range, flow and periodic behaviour of tides at most coastal regions are well documented for navigation and oceanographic purposes (Kamphuis, 2010). This reliability is what makes tidal power such a useful form of renewable energy. In practice tidal stream generation is likely to be attractive in areas where the speed of the fluid is increased. It is the change in water level which leads to currents, with water flowing from a region of high water to a region of low water since water is unable to resist shear. Couple this with shallow shelf seas and bathymetric features and you get strong tides with high kinetic energy. This occurs in straits between islands and mainland or between relatively large islands (Black and Veatch, 2005), where the movement of the water produces tidal currents that can reach speeds greater than 2m/s (BERR, 2008). Other tidal forcing can occur from temperature/salinity gradients.

The theory of tidal stream power is very similar to wind power (for most devices), but with the advantage of being able to predict fluid velocities more precisely, hence power generation. Water has a density of approximately 800 times that of air; therefore the turbines can be smaller and still produce the same power. Unfortunately there are several drawbacks to tidal current power:

- The disparity of lunar periods (e.g. semi-diurnal is 12.42 hours) with the human solar period (24 hours)
- The changing tidal range and flow over a two week period, producing changing power production (Batten et al., 2007)
- The harsh marine environment makes the installation of devices extremely difficult
- The large capital cost of the installations (several million pounds (GBP) per MW)
- The requirement for a high flow speed (in the order of $1.5ms^{-1}$ or greater)
- The location of sites with adequate flow speed are generally distant from the areas requiring the power (leading to grid connection and transmission problems)

The power density (Wm^{-2}) in the water current is defined as (Gooch et al., 2009): $q = \frac{\rho U^3}{2}$, where q is the power density, ρ is the water density and U is the current speed. Only some of this power can be converted into useful power and, as with wind power, this is limited to a maximum of approximately 59% for an un-augmented horizontal axis rotor. This is known as the Betz limit (Betz, 1920) which describes the maximum kinetic energy that can be extracted from the flow. With device inefficiencies (blade tip losses, power train inefficiency etc.) a practical maximum of around 40-45% is to be expected. Tidal current velocities vary with time approximately as $U = U_{max} sin\left(2\pi t/\tau\right)$, where τ is the period of the natural tide (12.42 hours), t is the time and U_{max} is the maximum current velocity (Twidell et al., 2006). This assumes that a tidal cycle is composed of a single sinusoid, which in general is not a true representation, but is considered sufficient for a simplistic analysis. The expression is integrated over one quarter of the tidal cycle, an acceptable assumption for a semi-diurnal, single sinusoidal tide. Generation of electrical power per unit cross-section, assuming a 40% efficiency of tidal current power to electricity, may therefore average as:

$$\bar{q} \approx \frac{0.4}{2} \rho U_{max}^3 \frac{\int_{t=0}^{t=\tau/4} sin^3\left(\frac{2\pi t}{\tau}\right) dt}{\int_{t=0}^{t=\tau/4} dt} = 0.2 \rho U_{max}^3 \left(\frac{\tau}{3\pi}\right)\left(\frac{4}{\tau}\right) = \frac{4}{15\pi} \rho U_{max}^3 \tag{2.1}$$

For a device which can generate in both ebb (outgoing) and flood (incoming) tidal currents, with a maximum current of $3.5ms^{-1}$, $\bar{q} \approx 3.73kWm^{-2}$. If the intercepted area of a device is

$400m^2$, two SeaGen rotors for example (Marine Current Turbines, 2012), then the estimated average power generation will be 1.5MW (SeaGen is rated at 1.2MW i.e. this is the maximum achievable power from this device). This assumes that the turbine can produce power at all flow velocities with an efficiency of 40%. This is of course not the case. The TST will have design cut-in velocity, under which it will not produce any power and a cut-out velocity above which it will stop to prevent damage to the device. A capacity factor is sometimes used to quantify how much power is extracted from the resource over time. This is defined as the ratio of actual power output over a period of time and its theoretical maximum power output if operating at full nameplate capacity over the same time period.

2.1.2 Waves

Ocean gravity waves of a much shorter period than tides are formed through friction between the water surface and the wind (Dunn, 1986). These waves can be considered a concentrated form of solar energy since winds are generated by the differential heating of the earth. A normal sea will be composed of an irregular pattern of waves of varying period, direction and amplitude. From a more general point of view, it is well established that the surface of water waves show a definite progression, however the water particles themselves show no net progression. In addition, the motion of any water particle is circular in the case of deep water and becomes elliptical in shallower waters. In deep water, the amplitude of the waves decays exponentially with depth, but this is not the case with shallow or intermediate water depths where the wave motion can still be significant deeper into the water column. Research has shown that wave motion in the upper part of the water column induces large variations in velocity at a particular spatial location i.e. at the TST (Milne et al., 2010; Norris and Droniou, 2007; McCann, 2007; Swan et al., 2001). These large variations in velocity are what will lead to blade fatigue because of relative variations in blade loading. This is supported by Garrad Hassan Ltd. (2008) who describe the total unsteadiness in the flow experienced by a TST rotor and support structure as being the sum of wave effects and the background turbulence.

Linear wave theory (also known as Airy wave theory or small-amplitude wave theory) is a well-established method for describing gravity waves (Kamphuis, 2010; Sorensen, 2006; Dean and Dalrymple, 1991; Dyer, 1986). There are several required assumptions for this theory to be applicable, but most important (in this case) is that the wave height is small compared to the wavelength and water depth. The wave height is essentially independent of the wavelength, wave velocity or wave period (Sorensen, 2006). It depends only on the history of the wind regimes above the surface. If the wave height becomes too large compared to the wavelength or depth, then non-linearities will deform the wave profile meaning that alternative wave theories will be required to more accurately describe the wave parameters e.g. Stoke's 5th order wave theory (Fenton, 1985). The wave height is limited to a steepness ratio $H/L = 1/7$, after which the wave will break (H is the wave height and L the wavelength). Linear wave theory describes horizontal and vertical particle velocities using the following equations:

$$u_i = \frac{\pi H}{T_i}\left[\frac{\cosh k(d+z)}{\sinh kd}\right]\cos(kx_i - \omega_i t) \tag{2.2}$$

$$w_i = \frac{\pi H}{T_i}\left[\frac{\sinh k(d+z)}{\sinh kd}\right]\sin(kx_i - \omega_i t) \tag{2.3}$$

u_i is the horizontal wave particle velocity, w_i is the vertical wave particle velocity, T_i is the intrinsic wave period (see Section 2.2.1), $k = 2\pi/L$ is the wave number, d is the water depth, z is the particle reference depth, ω_i is the intrinsic wave frequency and x_i is the intrinsic distance in the direction of wave propagation.

In reality, sea waves are not continuous single frequency sine waves. They form an irregular, complex surface, thus the power (P) is usually described per unit width of wavefront, Wm^{-1} (Sorensen, 2006). This can be written in the form of:

$$P = \frac{\rho g H^2 L}{16 T_i}\left(1 + \frac{2kd}{\sinh 2kd}\right) \tag{2.4}$$

g is the acceleration due to gravity. It is not possible to predict with any precision the forces on the turbine using this equation ($Force = Power/Velocity$) since it is unclear how the wave power is imparted to the complex rotating TST blades/rotor. The nature of this research requires detailed understanding of the interaction processes involved and thus the incorporation of the wave velocity components (equation 2.2 and equation 2.3) directly into modified wind turbine theory (see Section 4).

2.1.3 Wave-Tidal Current Interaction

One of the enduring topics of interest in the field of coastal and offshore engineering is that of wave-current interactions and their impact on structures. The co-existence of waves and currents is a common occurrence in most marine environments (Swan and James, 2001). Waves are strained and refracted by currents, causing exchanges of mass, momentum and energy to occur between the waves and mean flow (Smith, 2006). The main energy in the coastal region can be attributed to tides, storm surges and wind waves. The resulting interaction occurs because the tides and surges change the mean water depth and current field experienced by the waves (Wolf and Prandle, 1999). The usual approach to the interaction problem has been to ignore the interaction between waves and currents and simply add the two together (see Section 2.2.1) so as to calculate the forces on the structure. There are problems with this approach, namely that it is unclear whether this process will under-estimate or over-estimate the loading on the structure (Srokosz, 1987).

Zheng et al. (2008) showed that for combined wave-current experiments, the mean velocity profiles generally vary from those suggested by linear superposition of wave and current velocities. As the wave steepness increases, nonlinear wave profiles have more skewed non-symmetric forms and the height of wave crests increase and the trough height decreases. For deep water the selection of wave velocity profile is important, however in shallow water the choice of theory may be critical as it can make a significant difference to the observed velocities (Eastwood et al., 1987). TSTs are likely to be based in intermediate to deep water; therefore the selection of wave velocity profile should be appropriate. In a non-breaking flow field, if the height of an approaching wave and the magnitude of an opposing current are sufficiently large, the wave height of the combined wave-current interaction could become huge (Zaman, 2008). Rogue waves could cause serious damage to the TST arrays they propagate over and the same could be said for storm surges. In addition to these concerns there may also be the influence of salinity/temperature gradients which could affect the velocity profile in the location of a TST. This effect may be intensified should a TST be situated near river estuaries because of fresh-salt water mixing.

Much offshore design is modelled using a regular two-dimensional wave motion, superimposed on a one-dimensional current flow aligned along the direction of wave propagation, with a prescribed vertical profile (Eastwood et al., 1987). Traditionally the wave velocity profile is calculated using suitably chosen nonlinear wave theory, neglecting the presence of a current. The current profile is calculated separately and extrapolated up to the wave crest. The wave and current flows are then superimposed by the addition of velocity vector fields. Although this approach neglects the interaction effects, there is currently no 'industry standard' method for the inclusion of wave-current interaction, therefore this method must suffice at present as an approximation to predicted flow velocities. Wolf and Prandle (1999) state that linear wave theory should be sufficiently accurate in depths of water greater than 12.5m with significant wave heights of less than 5m. This is directly applicable to the TSTs described in Section 1.1.

2.2 Doppler Shift

Wave periods appear different depending on the reference frame of the observer and the relative velocity of wave propagation. This is because of an effect called Doppler shift. A simple example of Doppler shift is for an observer travelling in the direction of the waves, the appearance of wave crests will be slower than if the observer was travelling against the waves. When waves are superimposed on a uniform current, the reference frame for the waves travels at the velocity of the underlying current (ISO, 2005). Several situations arise where the wave period can be described in different ways. Two wave periods are applicable to TSTs; these are the intrinsic wave period, T_i and the apparent wave period, T_a. The intrinsic wave period is a measure of the wave period whilst travelling with the current in the current's direction. The apparent wave period is what will be observed at the fixed TST. In the case of no current (e.g. slack tide), the apparent period would equal the intrinsic period.

When currents propagate against the waves, the waves are compressed and when currents propagate in the same direction, then the waves are elongated (Wolf and Prandle, 1999). The degree to which this Doppler shift modifies the surface waves depends on the current speed relative to the wave propagation speed. This naturally means that slow propagating waves (waves of a short period) are most affected by currents. It is important to note that currents flowing in a direction perpendicular to the wave direction will have no effect on the waves. It is therefore not just the magnitude of the currents but how much the currents project into the wave direction (cosine of the angle between the reference direction) (Wolf and Prandle, 1999).

To be more precise, a Doppler shift is observed when surface waves and current velocities interact. The effect is to change the apparent period of the waves, which could be described as one-dimensional wave-current interaction. The relationship between the intrinsic and apparent wave components can be described using the wave celerity (phase speed), where the apparent wave celerity $c_a = c_i + U$ is equivalent to $c_a = L/T_a$ and the intrinsic wave celerity is $c_i = L/T_i$. $U = U_c \cos(\beta)$ where U_c is the free-stream current velocity unaffected by blockage and β is the direction of the current with respect to the direction of wave propagation. The velocity seen by the TST can therefore be expressed as:

$$\frac{L}{T_a} = \frac{L}{T_i} + U \tag{2.5}$$

By multiplying equation 2.5 by the wave number (k) the equation can also be expressed in terms of the apparent and intrinsic frequencies:

$$\omega_a = \omega_i + kU \tag{2.6}$$

where ω is the wave frequency, $\omega = 2\pi/T$. If the current velocity, U, is positive (waves and current in same direction, $-90° < \beta < +90°$) then the apparent frequency of the waves is increased above that of the intrinsic frequency. If U is negative the opposite is true (waves and current in opposing direction, $\beta > +90°$ or $\beta < -90°$) and the apparent frequency is lower than the intrinsic. It must be emphasised that the equations given in this section are only valid for first and second order waves on a steady uniform current (ISO, 2005).

The experiments presented in Chapter 6 present the case of waves and a current travelling in the same direction. The carriage-mounted turbine travels towards the waves, however, when the turbine is viewed from a stationary frame of reference, the resulting current must be in the opposite direction to that of the carriage motion.

In the case of sufficiently high opposing currents ($c_i + U \leq 0$), the waves will be unable to propagate against the current. In these opposing current cases, the wave steepness becomes larger as the current speed increases. This is due to a shorter wavelength and increased wave height from wave action conservation (Wolf and Prandle, 1999) and can result in standing waves if $c_i + U = 0$ and $\beta = 0$. There is of course a limiting wave steepness described previously as approximating $H/L = 1/7$. This effect is significantly more complex than a Doppler shift and cannot be modelled in a towing tank (Chapter 6) since there is no actual current present to modify the waves.

2.2.1 Linear Superposition

Linear superposition is a relatively straightforward approach to the wave-current interaction problem and can yield adequate results for a TST (see Section 7). The method is to calculate the wave velocities using linear wave theory (suitably modified for Doppler shift) and combine this with the current velocity (ISO, 2005; Hedges et al., 1985). The formulae may be readily modified to allow for a steady uniform current flowing at an angle to the direction of wave propagation as described in Section 2.2. This however includes the added complication of refraction as the waves interact with the current (Hedges et al., 1985), as well as the difficulty of applying this to a laboratory situation.

The wavelength is related to the intrinsic wave period by the dispersion equation (suitable for first and second order waves):

$$T_i^2 = \frac{2\pi L}{g\tanh\left(\frac{2\pi d}{L}\right)} = \frac{4\pi^2}{kg\tanh(kd)} \tag{2.7}$$

(ISO, 2005; Hedges et al., 1985). From Equation 2.5 it can be shown that:

$$T_a = \frac{2\pi T_i}{2\pi + T_i kU} \tag{2.8}$$

In order to model this Doppler shift for a combined wave and current case, the relationship between apparent and intrinsic reference frames can be expressed as:

$$x_a = x_i - Ut \tag{2.9}$$

where t is the time and x is the relative distance in the direction of wave propagation ($x_a = x_i$ at $t = 0$). Combining Equations 2.9 and 2.6 gives the wave phase:

$$\theta = kx_i - \omega_i t = kx_a - (\omega_i + kU)t = kx_a - \omega_a t \tag{2.10}$$

For a fixed location in space (such as at the TST rotor), the wave phase can be expressed as:

$$\theta = -\frac{2\pi}{T_a}t \tag{2.11}$$

This simplifies because the apparent distance is zero at the TST location. Equations 2.2 and 2.3 can then be applied to the case of a fixed TST to describe the apparent horizontal and vertical velocities at the device by including Equation 2.11:

$$u_a = \frac{\pi H}{T_i}\left[\frac{\cosh k(d+z)}{\sinh(kd)}\right]\cos(\theta) + U \tag{2.12}$$

$$w_a = \frac{\pi H}{T_i}\left[\frac{\sinh k(d+z)}{\sinh(kd)}\right]\sin(\theta) \tag{2.13}$$

u_a is the apparent horizontal wave particle velocity relative to the TST, w_a is the equivalent vertical wave particle velocity. Note that U must be added to equation 2.12 for absolute velocity (Swan and James, 2001; Hedges et al., 1985). Equation 2.12 was used to show 'one-dimensional' wave-current interaction (Doppler shift) of monochromatic waves on an opposing uniform current in Figure 2.1. The top chart in Figure 2.1 contains two dashed lines to describe possible extents for a TST rotor (approximately accounting for wave and bottom surface effects). It is clear why a developer would be reluctant to install a TST near the surface due to the significant velocity perturbations. The increased loading caused by this changing velocity will not be uniform with depth, causing further irregular loading to the blades. This chart does not include the effects of turbulence and bottom friction effects. Norris and Droniou (2007) provide a more detailed description of bottom/turbulence effects, which are outside the scope of this research.

2.2.2 Limitations of Linear Superposition

Use of linear wave theory superimposed on a uniform current does not give a strictly accurate representation of wave-current interaction effects (Zheng et al., 2008). It is well understood that in steep waves there are high non-linearities; hence linear wave theory may under-estimate the dynamic loading behaviour on the rotor blades in steep waves. This effect is corroborated to some extent by the experimental work of Barltrop et al. (2006), meaning that linear wave theory is generally more appropriate for modelling long waves. It has been shown that linear superposition of waves and currents can under-predict the fluid velocity by up to 30% and over-predict them by up to 10% (Srokosz, 1987). Horizontal velocities measured in the laboratory and in the field show continual differences from the simple theory (Smith, 2006; Swan and James, 2001), indicating a need for further work and understanding. A drawback of linear wave theory is that it only defines wave particle kinematics up to the mean water level ($z = 0$), so does not consider the kinematics into the wave crest. There are methods available for extending the wave kinematics such as delta stretching and Wheeler stretching (Hahn, 1994). Delta stretching is a simple empirical correction which can be applied directly to Equations 2.12 and 2.13. z_s is used to describe the stretched vertical coordinate, which replaces z when z is above the stretching depth, d_s (ISO, 2005). $z_s = F_s(d_s + z) - d_s$, where F_s is a stretching factor (less than 1) defined by: $F_s = \frac{d_s + a\eta}{d_s + \eta}$. The stretching depth, d_s, is typically set to half the significant wave height. a is the stretching parameter ($0 < a < 1$), typically set to 0.3. η is the water surface elevation at the location of interest i.e. TST position, given by $\eta = \frac{H}{2}\cos(\theta)$. A similar method to Delta

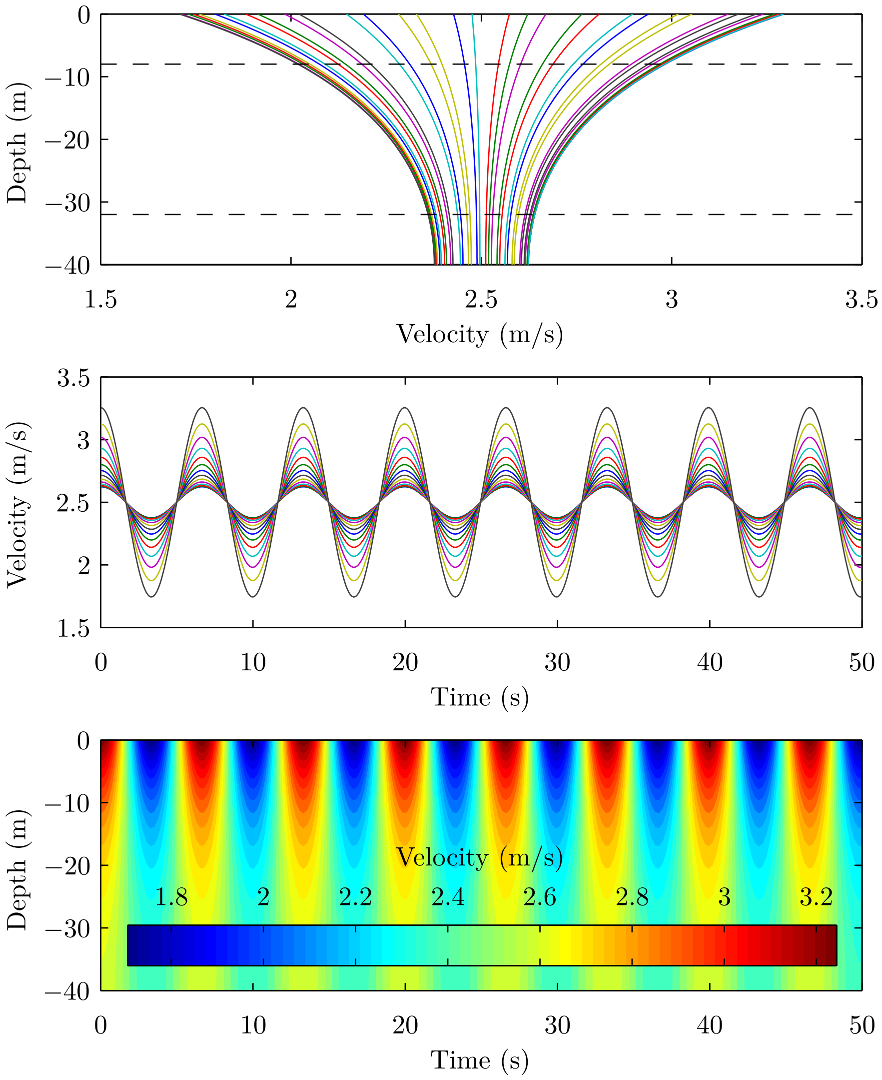

Figure 2.1: Opposing wave-current interaction showing apparent velocity relative to the TST. Top plot shows the horizontal velocity profiles (each line is a time instant), centre plot shows time varying velocity (each line is a depth position) and bottom contour plot combines the previous plots. $H = 2m$, $T_i = 8s$, $U = 2.5m/s$ and $d = 40m$

stretching can be used for linear current stretching, however if the waves are sufficiently small then stretching will have a negligible effect for both wave and current velocity profiles so can be neglected (Hahn, 1994).

Sorensen (2006) provides a generic template for selection of an applicable wave theory. The experiments carried out here could be modelled using Stokes' 5th order wave theory rather than linear wave theory because the waves are not strictly small in amplitude. The risk is that the increased complexity of the problem obscures the interpretation of the results. It is for this reason that laboratory tow tank testing was modelled numerically using linear wave theory due to its simplicity in combination with a uniform current profile. The selection of either a depth-averaged (uniform) current or linear current to model the true current is subjective along with the method used to fit the linear profile to the true profile (Srokosz, 1987). This is because the effect being modelled is not linear. It has been shown that mean current velocity profiles agree well with a logarithmic law and that waves are approximated closely by Stokes' second-order theory (Zheng et al., 2008). Some authors have chosen to use a 1/7th power law approximation to model a tidal current (Gooch et al., 2009; McCann, 2007; Black and Veatch, 2005; Burton et al., 2001). Due to the complexities of wave-current interaction, it has become common design practice to assume the current is uniform with depth and linearly sum the individual motions due to waves and currents, accepting the inherent errors (Swan and James, 2001). In many practical situations the current profile can be assumed to be uniform with depth, such as with the majority of tidal flows (Swan and James, 2001).

2.3 Defining a wave induced velocity ratio and blade rotation ratio

Wave induced velocities and the resulting loads are dependent on wave period, wave height and water depth. The induced velocity range can be calculated from the magnitude of the wave induced velocity oscillation from Equations 2.2 and 2.3 excluding the wave phase term (it is neglected because the problem is time and relative distance independent). The wave induced variation is normalised by the current speed resulting in ratios of $2|u|/U$ and $2|w|/U$, where u is the longitudinal velocity component and w is the vertical velocity component. Wave induced variation is also dependent on water depth therefore the cases of intermediate water ($\frac{L}{20} < d < \frac{L}{2}$) and deep water ($d > \frac{L}{2}$) are shown in Figure 2.2.

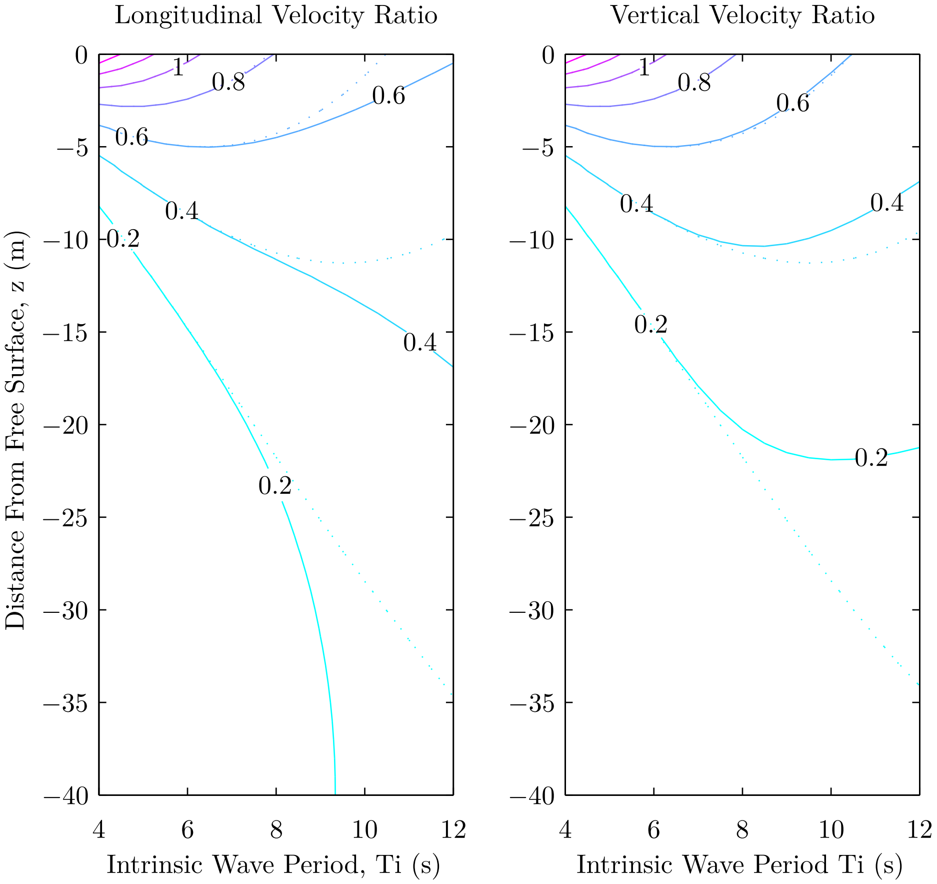

Figure 2.2: Normalised wave induced velocity range for longitudinal component $2|u|/U$ (left) and vertical component $2|w|/U$ (right). The solid line represents intermediate water depth (40m); the dotted line represents deep water (120m). $H = 2m$ and $U = 2m/s$ (Adapted from Milne et al., 2010).

The deep water case is evident because the ratios for both the longitudinal and vertical velocities are the same, meaning that the wave particle orbit is circular rather than elliptical as in the intermediate case. Disregarding the region in close proximity to the free surface, the depth to which the wave velocities penetrate the water column will generally increase with an increase in wave period. For intermediate water depth, longitudinal wave velocities can affect the entire water column. This is a concern because it is the longitudinal component which will normally cause the greatest fluctuations in aerofoil angle of attack and will therefore result in the highest bending moments in the out-of-plane direction (see Section 6). Defining blade load response requires the inclusion of the velocity seen by a rotating blade. This will mean that a per-revolution contribution to the induced velocity seen by the blade must be defined. In the context of a 3-bladed TST there will be important $1P$ and $3P$ loading components, where $1P$ is the loading that occurs once per revolution and $3P$ is the loading three times per revolution. The $3P$ component is generally defined by the first flapping mode of the blades and is likely to be more applicable to wind turbine technology with their longer, more flexible blades (van Wingerden et al., 2008). Tidal turbines should have much stiffer blades due to their relatively short length and requirement to resist greater thrust, hence the driving frequency for design is expected to be the $1P$ component. Milne et al. (2010) describe the effect as equivalent to a rotational sampling effect found in the context of turbulence. The importance of the P variation compared to the T_a variation can be represented by the ratio of the range of the $1P$ velocity fluctuation to the $1T_a$ variation :

$$\frac{u_{rRange}}{u_{Range}} = \frac{\cosh[k(d + z_H + r)] - \cosh[k(d + z_H - r)]}{2\cosh[k(d + z_H)]} \tag{2.14}$$

z_H represents hub-depth and r is blade radial distance. This ratio is illustrated by comparing hub-depth against intrinsic wave period in Figure 2.3. In this case, the blade element position $r = 0.8R$ is for a position 80% of the way along the blade, towards the tip. This was chosen because the maximum out-of-plane loading usually occurs at around this region of the blade (Galloway et al., 2011). The amplitude of the P fluctuation decreases as T_i increases. The blade is likely to suffer most damage at lower values of T_i where the ratio tends to 1 (within a realistic range of large wave periods). These integer ratios will likely lead to load cycles with a greater range of amplitude, which will impact on the blade strength/fatigue requirements. Whilst the turbine will experience a greater number of loading cycles at lower values of T_i,

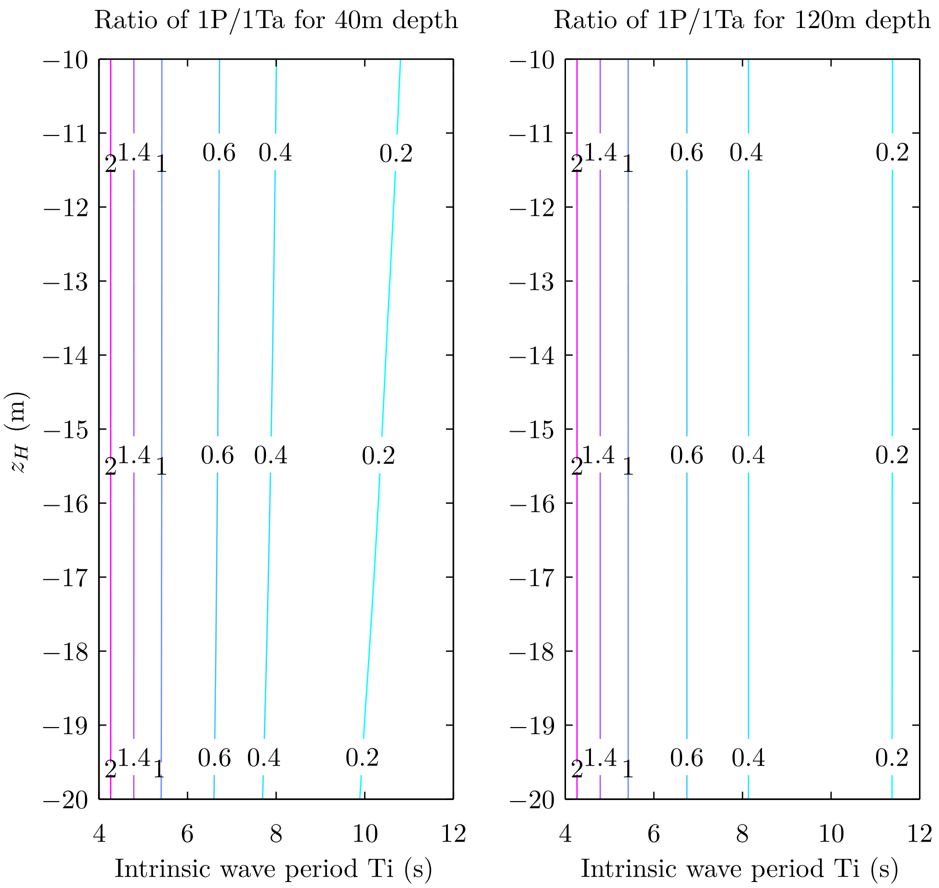

Figure 2.3: Ratio of longitudinal rotational wave induced velocity range (u_{rRange}) to the longitudinal velocity fluctuation range observed at the hub (u_{Range}) as a function of intrinsic period for 40m depth (left) and 120m depth (right). $r = 0.8R$, $R = 8m$ and $H = 2m$ (Adapted from Milne et al., 2010).

the load amplitude is likely to be greatest at the highest values of T_i, which is an important consideration for ultimate strength design of a blade.

2.4 Scaling and Blockage Effects

Waves are incorporated into most of the experiments therefore Froude scaling was adopted to define the various parameters (length, time, velocity etc.) in the experimental design. The model turbine (see Figure 2.4) is a scale representation of a 16m diameter TST. The maximum current speed at full-scale is $4ms^{-1}$, which is fast for a TST location, however it is significantly more realistic than the full-scale current speed of $8.55ms^{-1}$ used in the model turbine experiments conducted by Barltrop et al. (2006). The other dimensionless number that could have been used to scale experiments is the Reynolds number (Mach number is also important for an aerofoil, however the fluid flow is incompressible and at very low velocity so this has been neglected). A low Reynolds number can degrade the dynamical properties of an aerofoil and can be a source of irregularity between the experimental data and simulation data since turbulence directly affects the boundary-layer thickness around the aerofoil (Abbott and von Doenhoff, 1949). There is nothing that can be done to increase this value since the velocity and depth are constrained by the Froude scaling. This may be a factor of some significance since calculations show that the blade Reynolds number (based on mean chord length) is only 21000 for the experiments.

Fraenkel (2005) believes there is little use in testing models since the performance of axial flow rotors is well understood and relatively predictable. Whilst this may be true for wind turbines, it does not translate directly to TSTs because the fluids behave differently. Wind for example does not have a characteristic property that resembles wave-current interaction; therefore this must be taken into account when designing prototype TSTs, whether through laboratory testing or computer modelling. The model TST has a 1:20 scale rotor (0.8m diameter model-scale). Lengths are scaled by multiplying by the scale factor (1/20), while time and velocity are multiplied by the square root of the scale factor (see Appendix A).

An important aspect for scaling all TST experiments is blockage. Blockage is a term used to describe how the incident flow is constrained by the surrounding boundaries relative to the TST rotor area. In the case of the TST experiment in Chapter 5, the flow is constrained by the floor and walls of the test facility. Using a realistic blockage is important because a heavily blocked flow (small channel area compared to rotor area) will improve the performance of the

Figure 2.4: Underwater photograph of a 1:20 scale tidal turbine model

turbine due to more fluid passing through the rotor plane, resulting in unrealistically high energy extraction (higher C_P than expected as well as a higher C_T resulting in greater thrust loading). This is unlikely to occur at a real site since the side wall boundaries will probably be sufficiently far apart to avoid any change in the streamtube shape (see Figure 2.5), unlike in a towing tank facility where the side walls are only a few metres apart. This results in a compromise between using the largest possible rotor diameter to minimise scaling error (such as maximising the Reynolds number), whilst keeping the diameter sufficiently small so as to reduce the effect of blockage. There is no current theory available to determine the maximum blockage allowed, before additional correction to the data is required. In these experiments the blockage is 7.2% based on TST rotor area to channel area. Some blockage corrections have been suggested in the literature, but none of them have proven to be sufficiently robust, resulting in quite different results (see Appendix B). Other authors have carried out model turbine experiments without correcting for blockage blockage effects of 6%, 4% and 6.3% respectively (Ordonez-Sanchez et al., 2010; Maganga et al., 2009; Myers and Bahaj, 2009), although none of them give any explanation as to why this blockage is sufficiently small so as to be neglected? Turner and Owen (2009) present some numerical work which suggests that blockages as low as 1% have a small, but noticeable effect on C_P when above the optimum TSR and ratios above 7.8% are beginning to have quite a significant influence. The question remains as to what the limiting blockage is

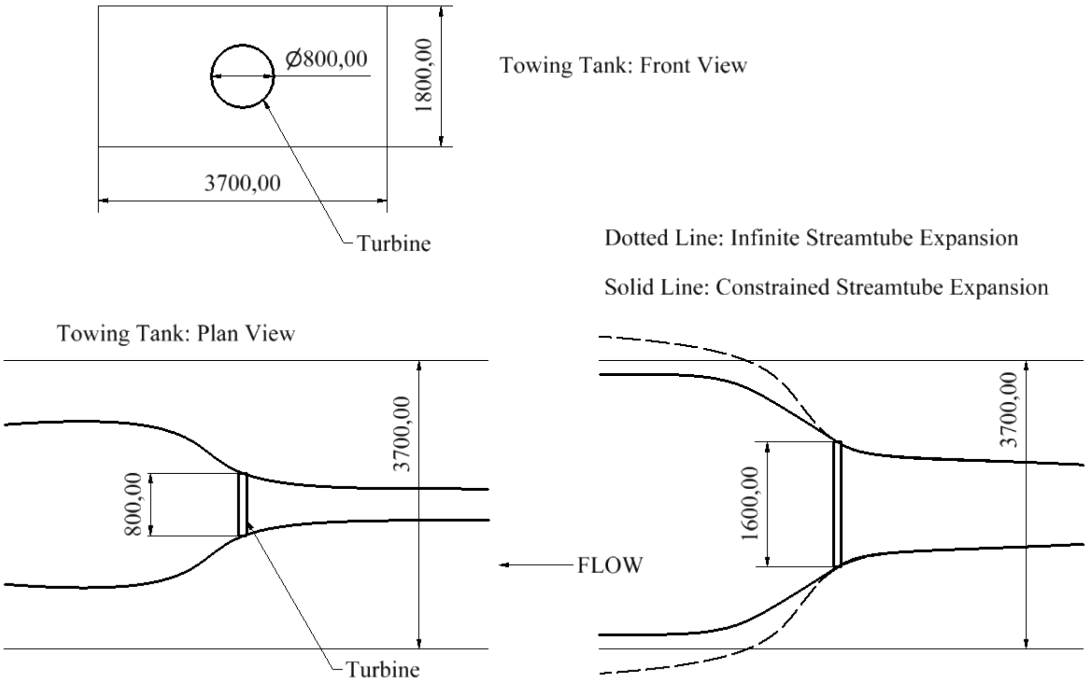

Figure 2.5: Streamtube Description of Blockage Effects

before corrections must be made to the data to account for its effect?

2.5 Dynamic Loading on Horizontal Axis Turbines

2.5.1 Dynamic Stall: Changing Angle of Attack

Changing flow conditions complicate the applicability of BEM theory for wind turbines. Applying BEM theory at high angles of attack is problematic because of aerodynamic stall. Viterna and Corrigan (1981) developed some modifications to the classical theory described in Section 3.1, which assume the aerofoil behaves like a flat plate at these high angles of attack:

$$C_L = A_1 \sin 2\alpha + A_2 \frac{\cos^2 \alpha}{\sin \alpha} \tag{2.15}$$

$$C_D = B_1 \sin^2 \alpha + B_2 \cos \alpha \tag{2.16}$$

Where $A_1 = \frac{C_{DMAX}}{2}$, $A_2 = (C_{LS} - C_{DMAX} \sin \alpha_S \cos \alpha_S) \frac{\sin \alpha_S}{\cos^2 \alpha_S}$, $B_1 = C_{DMAX}$ and $B_2 = C_{DS} - \frac{C_{DMAX} \sin^2 \alpha_S}{\cos \alpha_S}$. C_{DMAX} is the maximum drag coefficient (around 90°) and α_S is the static stall angle of attack. The Viterna-Corrigan correction was shown to be an effective method of predicting steady-state performance of a small-scale TST model when operating at high blade inflow angles (Myers, 2005). Unfortunately these simple corrections are only applicable to steady state flow conditions, not dynamic conditions.

Another area of importance is that of stall delay. This is a phenomenon which occurs as a result of the blade rotation. Lift coefficients are found to significantly exceed that of static aerofoil tests as a result of adverse pressure gradients slowing the fluid as it approaches the trailing edge of the blade (Burton et al., 2001). This effect is most noticeable near the blade root. Snel et al. (1994) derived a correction which adjusts for the three-dimensional effects of this problem using two-dimensional static aerofoil data and has been shown to be quite effective:

$$C_{L_{3D}} = C_L + 3\left(\frac{c}{r}\right)^2 \left[2\pi(\alpha - \alpha_0) - C_L\right] \tag{2.17}$$

$C_{L_{3\mathrm{D}}}$ is the 3-Dimensional coefficient of lift and α_0 is the angle of attack when the coefficient of lift is zero. Aerodynamic stall can be coupled to stall delay using the Viterna and Corrigan (1981) correction within the Snel et al. (1994) correction. Moriarty and Hansen (2005) suggest that it is prudent to extrapolate the lift and drag data over the range of ±180° to prevent any errors being returned when running the BEM theory. Suitable methods are suggested for mirroring and modifying the data over this range. These effects have been included in a BEM model described in Chapter 4.

An effect which has not yet been discussed is that of dynamic stall. Dynamic stall events occur as a result of unsteady or oscillatory time histories which lead to a variation in velocity over the turbine rotor. Modifications to the lift and drag coefficients are needed to account for flow separation around the aerofoil, however, this is not a straight forward process since it is dependent on previous changes in the angle of attack. Wave and yaw misalignment may lead to dynamic stall conditions, therefore its inclusion in BEM theory is important. There are many models used to account for dynamic stall, the most common being the Leishman-Beddoes model originally used in the helicopter industry (Leishman and Beddoes, 1986). The model has twelve empirical parameters which require experimentation in order to calibrate. This is impractical as blade/aerofoil sections are likely to require significant oscillatory blade testing to determine these values. A more straight-forward approach was to use the Boeing-Vertol model developed by Tarzanin (1971), which only has one tuning parameter, thus avoiding the need for further costly experimental work.

$$C_{L,d} = C_L(0) + \frac{C_L(\alpha_d) - C_L(0)}{\alpha_d}\alpha \tag{2.18}$$

$$\alpha_d = \alpha - A_{TD}\sqrt{\frac{c|\dot{\alpha}|}{2U}}\frac{\dot{\alpha}}{|\dot{\alpha}|}$$

$C_{L,d}$ is the coefficient of lift corrected for dynamic stall , α_d is the angle of attack corrected for dynamic stall and A_{TD} is an empirical time delay coefficient (tuning parameter; 0.87 has been quoted previously for a Vertol 23010-1.58 profile (Larsen et al., 2007)). The BEM model presented in Chapter 4 includes modification of the coefficient of lift for dynamic stall events. The effects were applied after a complete time series run in order to obtain values for the rate of change of angle of attack, $\dot{\alpha}$, at a blade element position.

2.5.2 Dynamic Inflow: Steady and Unsteady Velocity

Dynamic inflow refers to the reaction of the greater flow field to turbulence and changes in rotor operation (such as variation in rotor speed or blade pitch angle). Steady state BEM theory shows us that increased flow speed results in an instantaneous increase in power. This also infers that there was an instantaneous increase in the axial induction factor and changes in the flow field upstream and downstream of the turbine. For rapid changes in the flow and rotor operation, the greater flow field cannot respond quickly enough to instantly establish steady state conditions (Manwell et al., 2009; Burton et al., 2001).

When considering the wave and current forces on a fixed object in water, one must consider both the drag forces and inertial forces. The common method for describing the total force on a slender structure (wavelength greater than 5 diameters) is to use Morison's equation, which sums the two force types:

$$F = F_D + F_I = \frac{1}{2}\rho C_{D_{mor}} A u|u| + \rho C_M V \dot{u} \tag{2.19}$$

F is the total force on the structure, A is the cross-sectional area of the object, V is the volume of the object, u is the fluid velocity accounting for wave and current effects, $C_{D_{mor}}$ is the coefficient of drag of the object (not the same as C_D for an aerofoil) and C_M is the coefficient of inertia which is related to the coefficient of added mass, C_A by: $C_M = 1 + C_A$. The object and the fluid cannot occupy the same space simultaneously as they accelerate, therefore added mass can be thought of as some of the fluid moving with the object and increasing its effective mass (Sorensen, 2006). Equation 2.19 is normally used for calculating the forces on a fixed structure e.g. a TST pile tower. The problem becomes more complicated when the object is also in motion such as for rotating turbine blades. The motion results in a different flow field in the vicinity of the turbine, which in turn results in an additional pressure gradient in the outer flow region due to the accelerated fluid (Sumer and Fredsoe, 2006). This is described using the Froude-Krylov force, the last term expressed in a different form of Morison's equation:

$$F = \frac{1}{2}\rho C_{D_{mor}} A(u-u_b)|u-u_b| + \rho C_A V\left(\dot{u}-\dot{u_b}\right) + \rho V\dot{u} \tag{2.20}$$

u_b is the velocity of the body in the axial flow direction, which is important for dynamic nacelle yaw control only, so if the TST is subjected to quasi-steady yaw, this parameter can be neglected. Gravitational effects are accounted for within the inertia coefficient, however buoyancy forces from the blades and rotor may cause additional loading to the TST support structure. There will also be gyroscopic forces acting on the rotor, which need only be considered if using a nacelle yaw drive (Manwell et al., 2009).

Theoretically it may be possible to use Morison's equation to predict the loading on a turbine rotor/blade when coupled with BEM theory. This is speculative and is not considered practical since it would require an extensive range of experiments to obtain values for $C_{D_{mor}}$ and C_M (Chaplin, 1984), which may not prove to be representative. A more convenient equation used to determine thrust loading on a TST rotor is given by Whelan et al. (2009b) based on the work of Pitt and Peters (1981):

$$C_T = 4a(1-a) + \frac{16}{3\pi U}\left(\frac{R_2^3 - R_1^3}{R_2^2 - R_1^2}\right)\dot{a} \tag{2.21}$$

$\dot{a}$ is the time derivative of the axial inflow factor, R_1 is the radius of the outer section and R_2 is the radius of the inner section. Whelan gives no detail on the derivation of this equation or what 'section' refers to but presumably it determines the width of each blade element. Whelan shows that the axial added mass of a turbine in uniform current with waves is small; hence it may be possible to neglect inertial effects for thrust loading and use only the drag force component.

The thrust force on a TST can be expressed as shown in Equation 2.22. This equation gives the total force acting on a plane area normal to the fluid flow, multiplied by a coefficient (shown in brackets) to account for losses in the system.

$$T_{drel} = \frac{1}{2}\rho U_0^2 \pi R^2 \left[C_{T,d}\right] \tag{2.22}$$

Steady state BEM uses C_T, however this does not take into account any dynamic effects. The coefficient $C_{T,d}$ can be used to describe the "contribution to the total thrust coefficient of the dynamic acceleration" as stated by Burton et al. (2001). It is not clear exactly how this is calculated, but a logical interpretation could be that by zeroing the time-series thrust coefficient (subtracting the average of its magnitude), this will provide a relative contribution to the dynamic acceleration (see Section 4.3 for the proposed method). T_{drel} is termed the relative dynamic thrust force. This is then added to the mean thrust force from steady state BEM theory to give the total dynamic thrust force on a TST.

$$T_d = \bar{T} + T_{drel} \tag{2.23}$$

None of these theories take account of the effect that dynamic inflow will have on the power output of a TST. Theodorsen (1954) uses propeller theory to determine a power coefficient which includes a type of inertia coefficient. The theory may be applicable to TSTs, however this is currently unclear. If inertia and drag effects are successfully applied to the thrust and power coefficients, it should be possible to extract the elemental blade force coefficients C_X and C_Y by back calculating the BEM theory (see Section 3.1). More recently, a study into added mass properties on ship propellers by Macpherson et al. (2007) has demonstrated empirical relationships which could be applied to BEM theory for both thrust and torque. This would require experimental validation however, since it has never been applied to TSTs and may not scale correctly.

It is evident that modelling dynamic inflow is possible, however, as a concept dynamic inflow is still relatively unexplained and unadapted to the problem of a TST. The result is the requirement for dynamical inflow models capable of predicting the effects on a blade and rotor for a TST device. A new dynamic inflow model has been created for this purpose (see Section 4.3).

2.5.3 Wind Turbine Load Measurement

Wind turbine developers often incorporate strain monitoring of their turbines in order to understand the stochastic loading to which they are subjected. This facilitates the optimisation of future blade profiles for improved fatigue life and material reduction. The basic installation of strain gauges on a wind turbine consists of load measurements on the blade, rotor and tower (Pedersen et al., 2008). The load measurements are achieved by arranging strain gauges in a Wheatstone Bridge (WSB). The low WSB voltage signal is then amplified using a telemetry system to prevent increased signal error caused by noise interference over a relatively long length of cable.

Using strain gauges for load measurement is very effective, but they can also be used for determining fatigue i.e. indicating when the blade may fail. This can be observed from the gauges when they begin to exhibit non-linear behaviour. In order to extend the present research from load testing to the area of fatigue analysis, the model TST blades would have to be made from a fibre reinforced plastic or a similar product suitable for a full-scale TST. In addition the material properties of the blade would have to scale representatively. This is not practical, therefore any fatigue analysis will have to rely on numerical modelling validated against data from the experimental blade root loads. Freebury and Musial (2000) describe a simple model for predicting equivalent damage loading on a wind turbine based on load-cycle curves (rather than stress-cycle curves as would normally be used in fatigue analysis). This method does not require any knowledge of blade geometry or material, but does require historical load-cycle data. An attempt at a full-scale TST blade fatigue study has been carried out for a specific tidal site in Chapter 8.

Shimizu et al. (1987) measured the bending moment in the root of a rotating blade using strain gauges and these experimental results were compared with the theoretical values estimated by annular momentum theory (now known as BEM theory). This experiment was conducted by welding strain gauges to the blade root mounting shaft of a 6m diameter, 2-bladed, 10kW wind turbine. The outcome was that both the theoretical and experimental values agreed well. The mean values of in-plane bending moment in the blade root were about three times larger than those of the out-of-plane bending moment. The in-plane moment was also heavily affected by the self-weight of the blade compared to the fluid force; therefore this should be monitored closely in the TST experiments to see how much of an effect the gravity moment has, as well as inertia effects (see Section 2.5.2). Another interesting outcome of the work conducted by Shimizu et al. (1987) was that the maximum bending moments in the blade root were about two times larger than those of the mean values averaged over a minute. A similar effect may be notable with the model TST experiments, hence the need to strain gauge a blade and not just rely on rotor thrust and torque measurements to estimate blade bending moments.

A more recent series of wind turbine field experiments were undertaken by Bechly and Clausen (1999) where the aeroelastic response of a wind turbine blade was measured with surface mounted strain gauges. The trigger for strain gauge data collection came from two separate sources to provide either azimuthal domain triggering or time domain triggering. The former resulted in consecutive data samples every 45 degrees from turbine azimuth. This method is likely to be more useful for the analysis of TST strain gauge data since the position of the blade relative to the bending moment is an important factor for reasons of gravity, wave loading, yaw etc. Unfortunately the specific contributions to the fluctuations in strain measurements due to the combination of gravity effects and periodic flapping motion (out-of-plane) were not determined by Bechly and Clausen (1999), although it was postulated that there is coupling between the two.

2.6 Dynamic Loading on Tidal Stream Turbines

At present, few dynamic studies have been carried out relative to TSTs. Any commercial experience gained through testing full-scale prototypes is usually considered too valuable to be made public (see Section 1.1 for a description of some of the important developers currently involved).

Bahaj et al. (2005) carried out extensive high quality experiments on a model scale TST in a towing tank and cavitation tunnel for steady flow conditions. Batten et al. (2006) extended the research in an effort to model performance under yawed flow conditions. Whilst the experiments provided good results they were only verified against momentum theory with modification of the coefficients of thrust and power. No attempt was made at the incorporation of yawed flow in BEM theory to provide time series analysis of the loading effects. Orme et al. (2007) uses a BEM code to simulate yawed flow effects on a TST, however the outcomes are limited due to the research project's commercially sensitive nature. Orme also states the need for yawed TST data to validate the BEM code. Maganga et al. (2009) experimented using a scaled commercial turbine rotor in yawed flows and discovered similar effects to those of Batten et al. (2006) regarding the coefficients of thrust and power. Yaw has the effect of reducing the coefficients of power and thrust and has a significant effect at angles greater than ten degrees. The frequency spectra presented were normalised to avoid publishing commercial data and no description was made of time-domain loading.

Waves, like yaw, will result in a changing angle of attack of the aerofoil leading to undesired blade loading. In the design of one particular floating full-scale TST, the safety factor was as high as 10 to account for wave effects on blade thrust loading (Francis and Hamilton, 2007). In the laboratory, Barltrop et al. (2006) combined Blade Element-Momentum (BEM) theory for wind turbines with linear wave theory. This was verified with tow tank experiments to predict torque and thrust and to assess the influence of waves on the dynamic properties of bending moments at the roots of rotor blades. He showed that the bending moments at the roots of TST blades were found to fluctuate significantly; up to 50% of the mean value for out-of-plane bending moment and 100% of mean value for in-plane bending moment. It is well understood that in steep waves there are non-linearities; hence linear wave theory may no longer be appropriate for modelling the dynamic loading behaviour on the rotor blades. Barltrop et al. (2006) found that steep waves impose less bending moments in both directions about the roots of TST blades. It should also be noted that the in-plane bending moment is significantly affected by the gravity bending moment component, by as much as 50% in these model tests, although this is likely to be reduced at full-scale (achieving a neutrally buoyant blade would be desirable if not impractical). Clarke et al. (2005) also focused on BEM theory in combination with scale model TST experiments, however these were aimed predominantly at understanding a contra-rotating TST, having the advantage of zero net torque on the support structure. Ordonez-Sanchez et al. (2010) continued this research by analysing system dynamic response for a floating contra-rotating TST model in a towing tank. Research focus was on blade configuration, looking at dynamic response to achieve a stable contra-rotating system. The only reference to wave loading is for the moorings. No yawed flow is considered since a floating device is expected to be able to yaw passively. Whelan et al. (2009b) uses some interesting theoretical approaches to describing wave loading and inertia effects on TSTs in combination with some basic model experiments. Unfortunately there is insufficient detail to permit application of the results to further work. These authors use Morison's equation (see Section 2.5.2) to predict loading successfully but only provide a single graph to verify the findings. Whelan et al. (2009b) states that added mass has little effect on the loading of TSTs, however, Young et al. (2010) claims that the added mass directly affects the harmonics of the TST blades, which have been shown to be significantly different from those of wind turbine blades. This is particularly important in terms of the structural design of the blades for fatigue loading since it is postulated that TST blades will have higher harmonic frequencies due the likely requirement for increased stiffness.

In the field, research carried out at the European Marine Energy Centre (EMEC) showed that in a water depth of 45m, wave effects penetrated as far down as 15m whilst turbulence from the bottom boundary layer penetrated up by as much as 17m. This resulted in approximately a third of the water column remaining relatively tranquil (Norris and Droniou, 2007), which is rather limiting for TST developers. It is more advantageous to exploit the area near the surface (in waters no deeper than 50m to avoid increasingly energetic waves) since the currents are more energetic near the surface. This will mean understanding more about the impact of waves and cavitation on tidal turbines. Batten et al. (2007) describes how reduced depth of immersion can increase risk of cavitation on blades. Cavitation is the formation and immediate implosion of small pockets of air caused by relatively low pressures. Cavitation results in damage to the blade surface, which will degrade the hydrodynamic properties of the blades and therefore reduce the power capture (blade tip-speed should also be limited to 7m/s to prevent cavitation (Bahaj and Myers, 2001)), although this is slightly dependent on the blade design. The effect of wave loading caused by reduced rotor immersion has been described by Milne et al. (2010) where the wave and current effects are considered along with TST immersion depth (see Section 2.3).

Several numerical models have been developed to simulate TSTs but not many have been experimentally verified. McCann (2007) and McCann et al. (2008) give details of the significance of fatigue loading using Tidal Bladed, a commercial TST development tool (Bossanyi, 2007). It was found that fatigue varies as a function of mean flow turbulence and is also sensitive to wave action. Milne et al. (2010) describes important characteristics of the dynamic environment in which a TST will exist. Useful equations are provided as well as logical ratio descriptors to help quantify the complex loading problem. The author makes the most comprehensive use of the tidal development tool, Tidal Bladed, but currently there is no experimental evidence to validate any of the findings. Milne et al. (2011) expands his previous research by undertaking TST experiments with a similar set-up to Barltrop et al. (2005). Unfortunately very little experimental data is presented. In addition, the waves are generated using a carriage mounted actuator to simulate a wave in phase with the rotor. This affects the realism of the results since the ‘wave velocity profile’ is uniform instead of decaying exponentially with depth. These authors use Morison’s equation in a similar way to that of Whelan et al. (2009b) albeit with an equation that is more applicable to a TST with terms altered to represent a blade rather than a cylinder. Work has also been carried out to look at dynamic stall characteristics based on Theodorsen's theory for a foil subjected to oscillatory flows. Masters et al. (2007) uses BEM theory, with the difference being that the numerical modelling is carried out using matrix algebra to model the flow field in three dimensions. Some detail is given on how the wave component is applied to the numerical model and it is a similar method to that used in Chapter 4. Buckland et al. (2010) extends this research with the addition of a three-dimensional tip loss correction by Shen et al. (2005). The author has verified their numerical code with that of Tidal Bladed and the results are very closely matched. This is a good result assuming that Tidal Bladed has been effectively validated?

A significant cost reduction in the deployment of TSTs could be attributed to better understanding the service conditions and behaviour of fibre-reinforced composite TST blades (Carbon Trust, 2011). It has been demonstrated that TST blades are likely to cost approximately the same as an equivalent wind turbine of the same rated power (Wadia et al., 2011). This is due to a combination of reduced rotor size, but increased solidity and the use of carbon fibre for added strength. Assuming that all costs are equal, it can be said that blades on a typical 3-bladed TST are likely to represent approximately 12% of the total TST cost and 5% of the total installed cost, assuming a monopile foundation (Fingersh et al., 2006). Whilst this may not seem like a significant proportion of the total cost, should a blade need replacing there will be device downtime and further maintenance costs involved. It has been shown that using adaptive composite TST blades with bend-twist coupling can reduce loading and improve power capture (Nicholls-Lee et al., 2008; Nicholls-Lee and Turnock, 2007). This is likely to be important as second generation turbines are installed, hence the need to quantify dynamic loading to design for predicted blade frequency harmonics, loading range and ultimate loads.

2.6.1 Key Outcomes from the Literature

- Current research shows that there are only two published experimental studies of a model TST with the inclusion of waves (Barltrop et al. (2006); Milne et al. (2011)). Both studies were carried out at the same test facility, therefore both include errors inherent in the facility's architecture. Neither study has yet published any significant amount of experimental data which could be used by the research community for validation of numerical models.

- There is a need for detailed TST data, synchronising time, wave height, blade load, rotor loads and blade azimuthal position. This should theoretically provide all the basic parameters required for detailed numerical validation. Further detail will be required on dynamic frequency response of composite TST blades for hydro-elastic calculations, however this is beyond the scope of this research

- Different immersion depths should be studied in order to assess whether the effect of immersion is simply related to wave particle excursions, or whether blockage and cavitation play a role.
- Yaw misalignment should be studied as this greatly complicates the flow dynamics on a TST blade (see Section 4.1)
- There is a clear need for other robust design tools which can comprehensively predict complex blade loads caused by dynamic flows. Currently there is only the commercial program, Tidal Bladed, which appears to include all the different dynamic effects associated with the harsh marine environment. The creation of a validated open source design tool would be extremely useful for academic purposes, facilitating the inclusion of any unusual design modules. This could then be used to improve existing research and development.
- A detailed study should permit for future fatigue and extreme loading investigations with a view to the creation of design standards with suitable factors of safety

Chapter 3

Basic Wind/Tidal Turbine Theory

3.1 Blade Element-Momentum Theory

Blade Element-Momentum (BEM) theory is one of the most commonly used methods for calculating induced velocities on wind turbine blades (Manwell et al., 2009; Moriarty and Hansen, 2005; Burton et al., 2001). The theory is actually a combination of two separate theories, momentum theory and blade element theory. Blade element theory assumes that a blade can be split into small elements that act independently of other elements allowing each element to be treated as a two-dimensional aerofoil. The local flow conditions at each element position are determined and used to calculate the sectional forces, which are then summed along the length of each blade to calculate the total force on the turbine rotor. The other part of BEM, momentum theory, describes the rate of change of momentum caused by a pressure difference across the rotor. It is possible to calculate the induced velocities in both the axial and tangential directions. These induced velocities affect the inflow to the rotor plane, which in turn affect the forces calculated by blade element theory. An iterative process is used to achieve a converged solution to the induced velocities by combining both theories. The rate of change of momentum or thrust across the turbine rotor can be described as:

$$T = \rho A U_1 (U_0 - U_2) \tag{3.1}$$

where T is the thrust on the rotor, ρ is the density of the fluid, A is the turbine area, U is the fluid velocity with subscripts 0 , 1 and 2 denoting velocities upstream, at the rotor and downstream respectively (see Figure 3.1). Velocities for U_1 and U_2 are unknown, but by applying Bernoulli's

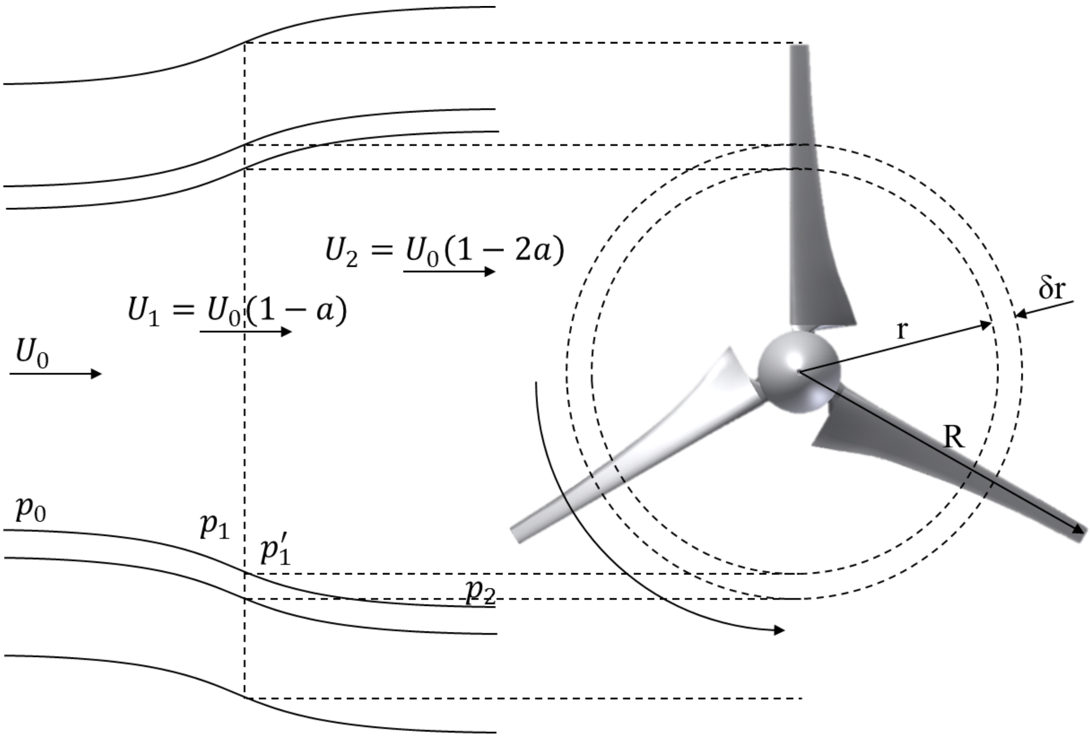

Figure 3.1: Momentum change across the TST disc. U denotes velocity, p is pressure and the subscripts denote location (0 is upstream, 1 is at the rotor and 2 is downstream). δr is an annulus projected by a blade element at position r along a blade of length R

equation for the conservation of energy, one can obtain $U_1 = \frac{1}{2}(U_0 + U_2)$ and $U_2 = U_0(1-2a)$ where a is the axial inflow factor. Similarly, the tangential inflow factor a' leads to an angular fluid velocity at the disc of $a'\Omega$ (see Figure 3.2) and $2a'\Omega$ downstream in the wake region (Ω is the angular velocity).

From momentum changes, the thrust forces per unit radius are defined by: Thrust = Mass flow rate × Change in axial velocity + Pressure increase due to wake rotation. The rotor thrust gradient is then:

$$\frac{dT}{dr} = 4\rho\pi r[U_0^2 a(1-a)K + (a'\Omega rK)^2] \tag{3.2}$$

$$K = \frac{2}{\pi}\cos\left[e^{-((N/2)(1-\mu)/\mu)\sqrt{1+(\lambda\mu)^2/(1-a)^2}}\right]$$

K is the Prandtl correction factor for blade tip losses (Burton et al., 2001), which can also be multiplied by the blade hub/root losses, but the tip-losses are normally much more significant. r is the radial distance of the annulus in question. The torque change is defined by: Torque = Mass flow rate × Change in tangential velocity × Radius. The rotor torque gradient is then:

$$\frac{dQ}{dr} = 4\pi r^3\rho U_0\Omega a'(1-a)K \tag{3.3}$$

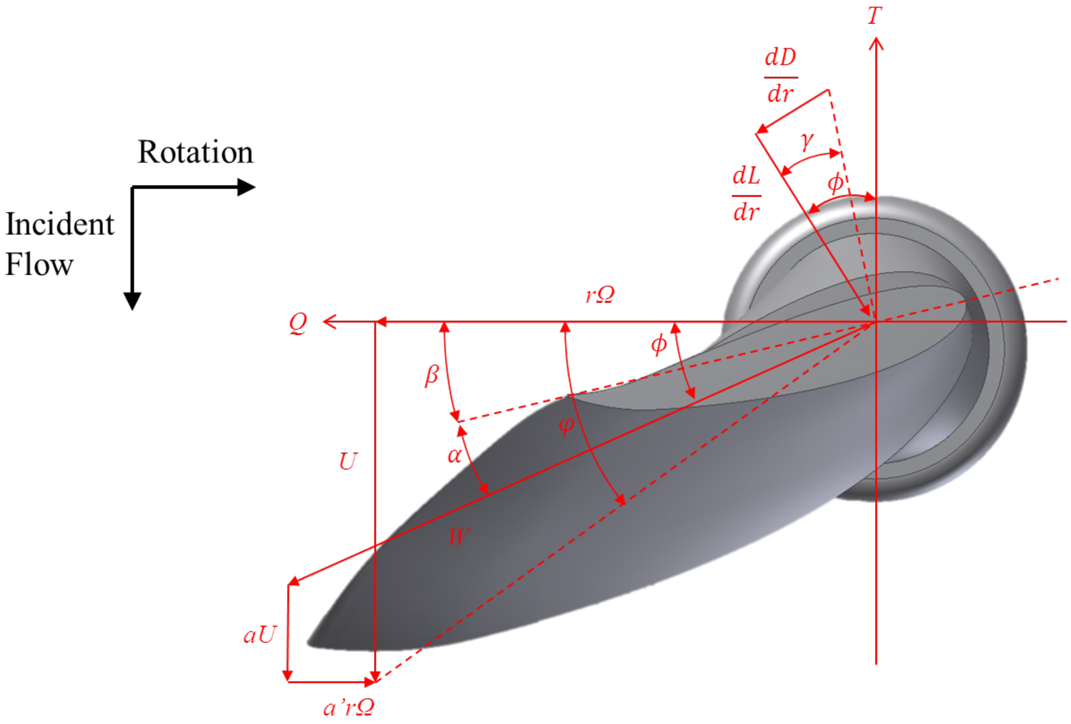

Figure 3.2: Forces and velocities on a blade element section. Symbols used are defined within Section 3.1.

Power can be obtained knowing that: Power output = Force × Velocity. The blade element part is best explained using Figure 3.2. The resultant velocity, W at the blade element is: $W = \sqrt{U_0^2(1-a)^2 + \Omega^2 r^2 (1+a')^2}$, which also equates to:

$$W = \frac{U_0\,(1-a)}{\sin\phi} \tag{3.4}$$

$$W = \frac{r\Omega\,(1+a')}{\cos\phi} \tag{3.5}$$

ϕ is the relative angle of the resultant velocity. The lift force on a span-wise length dr of the blade, normal to the direction of W, is:

$$\frac{dL}{dr} = \frac{1}{2} C_L \rho W^2 B c \tag{3.6}$$

C_L is the coefficient of lift, $\frac{1}{2}\rho W^2$ is the dynamic pressure, B is the number of blades and c is the chord length. The drag force parallel to W is:

$$\frac{dD}{dr} = \frac{1}{2} C_D \rho W B c \tag{3.7}$$

C_D is the coefficient of drag. Rotor thrust gradient can then be defined as (see Figure 3.2): $\frac{dT}{dr} = \frac{dL}{dr}\cos\phi + \frac{dD}{dr}\sin\phi$, which when combined with Equations 3.6 and 3.7 results in:

$$\frac{dT}{dr} = \frac{1}{2}\rho c W^2 B C_X \tag{3.8}$$

where C_X is the sectional blade element force normal to the rotor plane:

$$C_X = C_L\cos\phi + C_D\sin\phi \tag{3.9}$$

By applying Equations 3.8 and 3.2, the blade element and momentum parts are combined and simplified:

$$\frac{W^2}{U_0^2}\sigma C_X = 4\pi[a(1-a)K + (a'\lambda x K)^2]x \tag{3.10}$$

$x = \frac{r}{R}$ is the dimensionless blade radius, R is the length of a blade, $\lambda = \frac{\Omega r}{U_0}$ (this is the Tip-Speed-Ratio or TSR) and the local solidity is $\sigma = \frac{cB}{2R}$. Similarly the rotor torque gradient: $\frac{dQ}{dr} = r[\frac{dL}{dr}\sin\phi - \frac{dD}{dr}\cos\phi]$, which when combined with Equations 3.6 and 3.7 results in:

$$\frac{dQ}{dr} = \frac{1}{2}\rho c W^2 B C_Y \tag{3.11}$$

where $C_{YX} = C_L\sin\phi - C_D\cos\phi$, which is the sectional blade element force parallel to the rotor plane. Equating 3.11 and 3.3 and simplifying:

$$\frac{W^2}{U_0^2}\sigma C_Y = 4\pi\lambda x^2 a'(1-a)K \tag{3.12}$$

Using Equations 3.10, 3.12 and 3.4 or 3.5, equations can be derived for both the axial and tangential inflow factors:

$$\frac{a}{(1-a)} = \frac{\sigma}{4\pi K x\sin^2\phi}\left[C_X - \frac{\sigma C_Y^2}{4\pi x\sin^2\phi}\right] \tag{3.13}$$

$$\frac{a'}{(1+a')} = \frac{\sigma C_Y}{4\pi K x\sin\phi\cos\phi} \tag{3.14}$$

Equations 3.13 and 3.14 are solved iteratively to find a and a' by the convergence of the angle of attack, $\alpha = \phi - \beta$, where β is the blade pitch angle (see Figure 3.2 and Figure 4.4). The lift and drag coefficients are obtained here from a 2-dimensional panel code by Drela and Youngren

(2001) and are based on scaled blade Reynolds numbers (see Section 2.4).

It is useful to define non-dimensionalised coefficients for power and thrust (coefficients for individual blade element forces are given by C_X and C_Y). This provides a good basis for comparing numerical and experimental data, as well as blade types. The coefficient of power is described by C_P= Power extracted / Power available. Power extracted = $Q\Omega$ and Power available = Energy / Time = $\left(\frac{1}{2}mv^2\right)/t = \frac{1}{2}\rho A U_0^3$. The coefficients described in terms of x for each element position can be obtained from Equations 3.11 and 3.8 respectively and then simplified:

$$\frac{dC_{PX}}{dx} = \frac{2\lambda(1-a)^2\sigma x C_{YX}}{\pi \sin^2\phi} \tag{3.15}$$

$$\frac{dC_{TX}}{dx} = \frac{2(1-a)^2\sigma C_{XX}}{\pi \sin^2\phi} \tag{3.16}$$

where C_{PX}, C_{TX}, C_{XX} and C_{YX} are functions of the dimensionless blade radius x. The coefficients are then integrated along the blade (x) to obtain C_P, C_T, C_X and C_Y. Maximum C_P occurs when $a = 0.333$, so $C_P = 59.3$ (Betz limit for an actuator disc). In reality, the maximum C_P cannot be reached because it is not possible to achieve perfect efficiency due to aerodynamic phenomena such as blade drag- and tip-losses. Most large turbine rotors have a C_P around 50% at their optimum TSR (excluding drive train and generator losses).

3.2 Blade Element-Momentum Limitations

Blade element-momentum theory has several limitations because of its relative simplicity. One of the limitations comes from blade element theory, which assumes there is no span-wise flow along the blade (Moriarty and Hansen, 2005; Burton et al., 2001). This is not the case for heavily loaded rotors with large pressure gradients across the span and rotors subjected to a dynamic inflow, therefore making the theory less accurate. Another assumption is that the fluid around the aerofoil remains in equilibrium and the passing flow accelerates instantly. In practice this is not the case with the aerofoil requiring time to adjust to the changing wake resulting from a dynamic inflow (Burton et al., 2001). A further limitation is that BEM theory breaks down when the blades are subjected to large deflections outside the rotor plane. Because the theory assumes momentum is conserved in a plane parallel to the rotor, any deflection will incur aerodynamic errors (Moriarty and Hansen, 2005). The inclusion of waves and yaw will only serve to amplify the error in BEM theory; the question is by how much and is it acceptable?

Classical momentum theory breaks down for values of thrust coefficient when the axial inflow factor exceeds 0.5. For completeness, one needs to be able to model situations when this occurs, albeit infrequently. Various empirical curves have been developed to account for this discrepancy, a recent one being that by Buhl (2005). Another method which has been applied with slight modifications is that of Burton et al. (2001), which applies a straight line fit rather than a polynomial. Arguably this provides a better representation of the experimental data (see Buhl, 2005).

The original BEM theory does not provide for the influence of vortices shed from the tip and root of the blades into the wake and how this changes the induced velocities. Most modern BEM theory accounts for this using Prandtl's theory (see Section 3.1) (Manwell et al., 2009; Moriarty and Hansen, 2005; Burton et al., 2001).

Chapter 4

Blade Element-Momentum Modifications

4.1 Inclusion of Misaligned Flow (Yaw)

In order to incorporate the effects of yaw of a tidal stream (current) into BEM theory, the geometry of the problem needs to be understood. Figure 4.1 includes additional variables to describe this change in geometry. ψ is the azimuthal position and γ is the yaw angle of the upstream flow. χ is the skew angle of the wake, which is always slightly greater than the yaw angle due to flow accelerations around the turbine (Burton et al., 2001). ψ and x (blade element positions) are the two parameters which define the data resolution in the BEM code. A sensitivity analysis can be conducted which will determine the minimum number of required positions for each parameter. 19 blade element positions and 24 azimuth positions were found to be sufficient for the blade types used and dynamic flow conditions applied (Section 7.1).

The skew angle χ, can be solved iteratively using Equation 4.1 (Burton et al., 2001).

$$\tan\chi = \frac{U_0\left(\sin\gamma - \arctan\frac{\chi}{2}\right)}{U_0\left(\cos\gamma - a\right)} \tag{4.1}$$

It can however be closely approximated with Equation 4.2 (Burton et al., 2001) which is sufficiently accurate and saves computational time in a BEM code.

$$\chi = (0.6a + 1)\gamma \tag{4.2}$$

A correction to the axial inflow factor (Equation 4.3), based on the skewed wake, is based on a

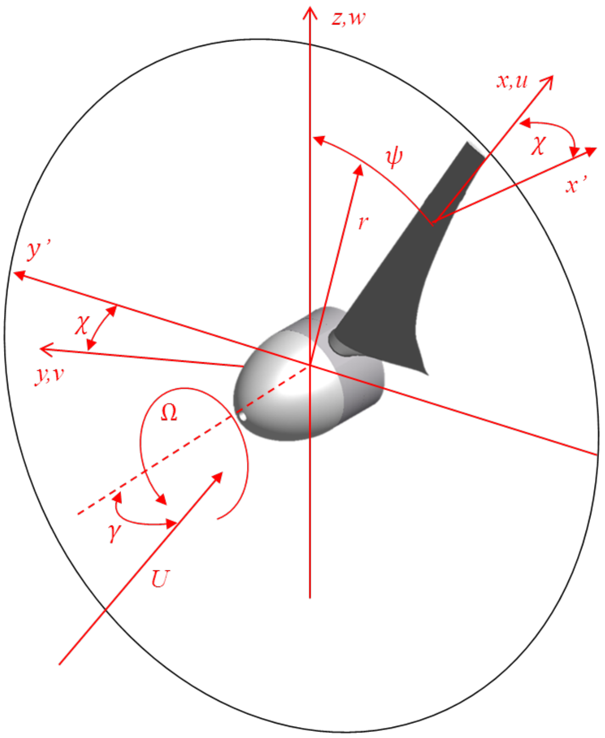

Figure 4.1: Velocities on a yawed rotor. γ denotes yaw angle, χ is skew angle and ψ is rotational angle of a blade (azimuthal position). y' is the rotor plane in the horizontal direction before yaw, the new plane is denoted by y (same principle for x' and x).

method developed by Pitt and Peters (1981), and used in the "AeroDyn" BEM model (Moriarty and Hansen, 2005). a is replaced by a_{skew} during each iteration:

$$a_{skew} = a\left[1 + \frac{15\pi x}{32}\tan\left(\frac{\chi}{2}\right)\cos(\psi)\right] \tag{4.3}$$

In order to complete the modifications to BEM theory for yawed flow, the effect of yaw must be included in the coefficients C_P, C_T, C_X and C_Y. From momentum theory for a turbine rotor in steady yaw:

$$C_P = 4a(\cos\gamma - a)^2 \tag{4.4}$$

Similarly a thrust coefficient can be defined:

$$C_T = 4a(\cos\gamma - a) \tag{4.5}$$

It can be said that C_P is a function of $cos^2(\gamma)$, likewise for C_Y since they are coplanar. Applying this assumption to BEM theory yields:

$$\frac{dC_{PX}}{dx} = \frac{2\lambda(1-a)^2\sigma x C_{YX}\cos^2\gamma}{\pi sin^2\phi}$$

C_T and C_X are then functions of $cos\gamma$:

$$\frac{dC_{TX}}{dx} = \frac{2(1-a)^2\sigma C_{XX}\cos\gamma}{\pi\sin^2\phi}$$

C_{XX} is the sectional blade element force coefficient normal to the rotor plane as a function of blade azimuth and C_{YX} is the sectional blade element force coefficient parallel to the rotor plane as a function of blade azimuth. C_{PX} is the sectional power coefficient as a function of blade azimuth and C_{TX} is the sectional thrust coefficient as a function of blade azimuth. The coefficients are integrated, first over the azimuthal range (this can be many cumulative blade revolutions), then along the blade length to obtain C_P, C_T, C_X and C_Y, for example:

$$C_P = \int_{x_0}^{x_n}\int_{\psi_0}^{\psi_n} C_{PX}d\psi\left(\frac{1}{\psi_n}\right)dx \tag{4.6}$$

The same must then be done for each blade, ensuring that the value for ψ is correctly phase shifted to ensure the correct relative position of each blade. The coefficients C_P and C_T must be averaged over the number of blades, B, to give obtain the correct behaviour of all the blades i.e. the entire TST rotor (neglecting the additional thrust force on the hub, although this is likely to be negligible in comparison).

Momentum theory is not normally considered adequate for a yawed rotor (Burton et al., 2001), but because a correction has already been made for skew, it is proposed that this may be sufficient to justify the application of these functions to each blade element position.

4.2 Inclusion of Waves (and Yaw)

The azimuthal positions of the TST blades is important not only for yaw but also for waves because the velocity across the rotor plane can no longer be considered uniform, as shown in Figure 4.2, which presents the velocity ratios predicted for the towing tank used in the experiments (Section 5.1). In order to model the velocity at each blade element position, the problem becomes dependent on both time and space (azimuth and yaw). To determine the wave

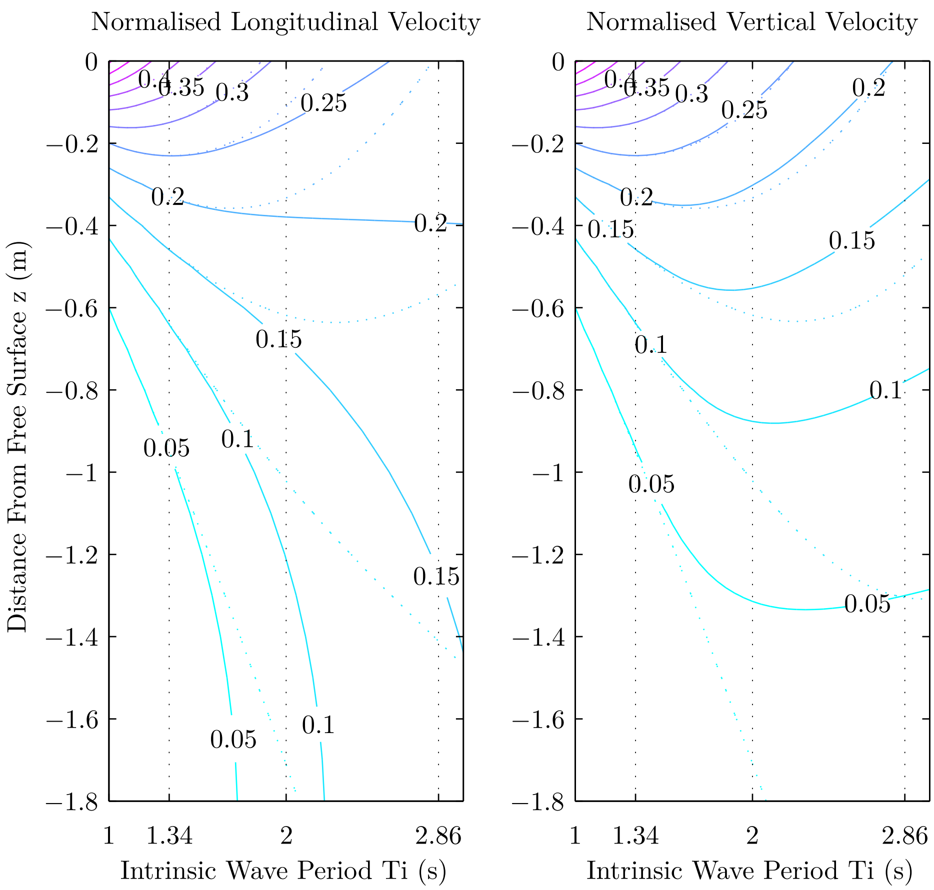

Figure 4.2: Normalised wave induced velocity range for longitudinal component $2|u|/U$ (left) and vertical component $2|w|/U$ (right) for the towing tank used in the experiments (Section 5.1). The solid line represents intermediate water depth (1.88m, experimental depth); the dotted line represents deep water (5m). The vertical grid lines denote values of experimental intrinsic wave period. $H = 0.08m$ and $U = 0.9m/s$.

velocity at each blade element position using Equations 2.2 and 2.3, there are two unknowns which are t (time) and z (reference depth). Equations have been derived within this section for the purpose of finding these two terms and then applying the new results to existing BEM theory.

Time can be described simply by $t = \psi/\Omega$. This works only if ψ is cumulative in the BEM code e.g. 2 full revolutions equate to 4π. The time at a blade element position, t_I, can be described with Equation 4.7

$$t_I = \frac{\psi R}{\lambda U_0} + t_X \tag{4.7}$$

where t_X is the time change caused by the yawed flow and is equivalent to $t_X = \frac{r\sin(\psi)\sin(\gamma)}{U_0}$.

The change in reference depth, z, through the water column at each blade element position is relative to the fixed hub depth, z_H and is described by z_I :

$$z_I = z_H + z_X \tag{4.8}$$

where z_X is the change in vertical distance with blade rotation $z_X = r\cos(\psi)$. Figure 4.3 describes how the relative velocities vary as a result of waves and yaw for a single turbine blade based on Equations 2.12 (neglecting the last term, current velocity) and 2.13. t and z are replaced with t_I and z_I to give Equations 4.9 and 4.10.

$$u_r = \frac{\pi H}{T_i}\left[\frac{\cosh k\left(d + z_H + r\cos\psi\right)}{\sinh kd}\right]\cos\left[\frac{2\pi}{T_a U_0}\left(\frac{\psi R}{\lambda} + r\sin\psi\sin\gamma\right)\right] \tag{4.9}$$

$$w_r = \frac{\pi H}{T_i}\left[\frac{\sinh k\left(d + z_H + r\cos\psi\right)}{\sinh kd}\right]\cos\left[\frac{2\pi}{T_a U_0}\left(\frac{\psi R}{\lambda} + r\sin\psi\sin\gamma\right)\right] \tag{4.10}$$

The largest fluctuations in velocity will be observed at the outer element position i.e. at the tip of the blade as shown in Figure 4.3. The hub velocity shows no change relative to blade rotation because there is no spatial displacement. The dotted line therefore represents the apparent wave period.

Now that it is possible to establish the relative velocities at a blade element position this can be applied to BEM theory. From the velocity vector diagram (Figure 3.2) the relative blade inflow angle can be described as:

$$\tan\phi = \frac{U_0(1-a)}{r\Omega(1+a')} = \frac{(1-a)}{\lambda(1+a')} \tag{4.11}$$

With the inclusion of waves and yawed flow effects, the relative blade inflow angle becomes:

$$\tan\phi = \frac{(1-a) + u_r(1-a)}{\lambda(1+a') + w_r} \tag{4.12}$$

4.3 A New Dynamic Inflow Model

Steady state BEM theory suggests that increased flow speeds result in an instantaneous increase in power. This cannot happen due to what can be termed an inertial response of the system. This is important for TSTs because there will be constantly varying inflow velocities caused by waves, yaw and turbulence which will lead to an inertial response. This can be modelled using

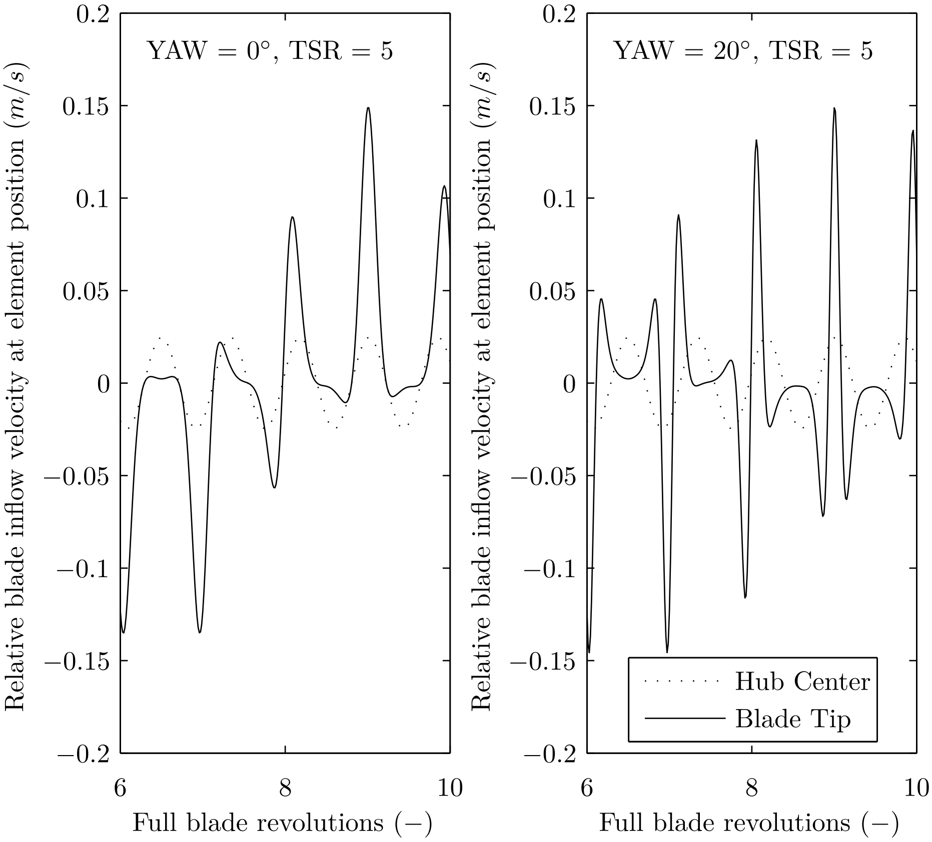

Figure 4.3: 1st order wave-current interaction velocities as seen at individual blade elements over two revolutions. The left figure is for 0° yaw, the right figure is for 20° yaw. The dotted line represents hub velocity; the solid line represents tip-velocity. $H = 0.08m$, $T_i = 1.34s$, $U = 0.9m/s$ and $d = 1.88m$

dynamic inflow theory as described in Section 2.5.2. Correcting for dynamic inflow has been shown to improve thrust loading on a TST (see Section 6, where Equation 2.22 is applied), but it is not readily applicable to the inertial loading of a single blade since the accelerations are based on the rotor disc as a whole. Dynamic inflow of an individual blade is not covered in the literature, therefore a new model for the dynamic out-of-plane bending moment of a blade has been created (Equation 4.13), based on Equation 2.22 and Equation 3.8.

$$M_{OP,d} = \bar{M}_{OP} + M_{OP,rel} \tag{4.13}$$

M_{OP} is the out-of-plane bending moment from BEM theory given by Equation 4.14, where W is the relative inflow velocity at a blade element.

$$M_{OP} = \frac{1}{2}\rho W^2 c R^2 C_X \tag{4.14}$$

$M_{OP,rel}$ is the relative out-of-plane blade bending moment given by Equation 4.15

$$M_{OP,rel} = \frac{1}{2}\rho R^3 U^2 \pi C_{X,d} \tag{4.15}$$

The contribution to the total axial blade force coefficient of the dynamic acceleration can be approximated as:

$$C_{X,d} = \int_{x_0}^{x_n} \left(C_{XX_{(\psi,x)}} - \bar{C}_{XX_{(x)}} \right) dx$$

where $C_{XX_{(\psi,x)}}$ is the axial force coefficient at an azimuthal and elemental position. The dimensionless coefficient of force will be proportional to the dimensionless coefficient of dynamic acceleration assuming Newton's second law is valid; $F = ma$. This new model appears to provide a good fit to the experimental data even for experimental data with higher non-linearities (see Chapter 7).

Dynamic inflow will also have an effect on the rotor torque and in-plane blade bending moments, although this effect is comparatively small and could be neglected for added simplicity if required (see Figure 7.7). Calculation of these loads requires substitution of the relevant coefficients. The dynamic in-plane bending moment has been reproduced below for completeness:

$$M_{IP,d} = \bar{M}_{IP} + M_{IP,rel}$$

$$M_{IP} = \frac{1}{2}\rho W^2 c R^2 C_Y$$

In order to calculate $M_{IP,rel}$, the relative in-plane blade bending moment, C_{XX} should be substituted with C_{YX}.

$$M_{IP,rel} = \frac{1}{2}\rho R^3 U^2 \pi C_{Y,d}$$

$$C_{Y,d} = \int\limits_{x_0}^{x_n} \left(C_{YX_{(\psi,x)}} - \bar{C}_{YX_{(x)}} \right) dx$$

4.4 Implementing a Modified Blade Element-Momentum code

The main reason for choosing to use BEM theory to model dynamic loads is the fast execution time. This is measured in seconds rather than hours/days as one would expect from a full RANS-CFD simulation (RANS; Reynolds Averaged Navier Stokes , CFD; Computational Fluid Dynamics). There are other methods for modelling dynamic fluid-turbine interaction, which may be more appropriate than RANS-CFD. McCombes et al. (2009) solve the vorticity transport solution to the Navier-Stokes equations. The authors consider this more applicable since vorticity is treated directly and not as a by-product of the velocity field as in RANS-CFD. Another method is the acceleration potential model based on a potential flow solution to Laplace's equation. Peters et al. (1987) uses this method with a time lag in the induced velocities to model the dynamic effects of a turbine. These methods are technically more advanced than BEM theory, however the time required to run these models is several orders of magnitude greater than BEM theory. The main disadvantage with using BEM theory is that the simplicity of the original theory (Section 3.1) requires many additional empirical corrections to model the different dynamic effects such as dynamic inflow, dynamic stall and yaw (Section 2.5 and Chapter 4). These effects are inherent in the other methods, providing the boundary conditions, meshing and other parameters are set correctly.

4.4.1 Modified Blade Element-Momentum Flow Chart

The modified BEM code was written using Matlab® and then optimised for speed using Matlab's built in profiler to locate lines which performed badly and improve them if possible. To understand the processes involved with the modified BEM numerical model and the order in which the processes occur, a flow chart has been produced (Figure 4.4). The iterations are dependent only on dimensionless blade radius (x) and azimuthal position (ψ) to converge on a value for the angle of attack (α) at a single time instant. The full numerical model has been reproduced in Appendix D

4.4.2 Model Inputs

The modified BEM code requires only a few input parameters for full functionality as shown in Table 4.1. The 2-dimensional array for static angle of attack against the coefficients of lift and drag can be obtained using either a 2-dimensional panel code (Drela and Youngren, 2001) or by experimentation. If experimentation is chosen, it may be more logical to determine dynamic values for the lift and drag coefficients in order to reduce the required number of BEM modifications and possibly improve predictions. An example of the actual input parameters has been reproduced in Appendix E. There are over 400 outputs resulting from the model since the calculations must be repeated for each blade separately. The outputs are therefore too numerous to list, but the important outputs are evident from the comparative results in Chapter 7.

4.5 NREL FAST Blade Element-Momentum code

In order to verify both the experimental results and the modified BEM code it was considered necessary to use a different industry certified code for comparison. The options were limited, but two suitable choices were found to be NREL's FAST (Jonkman, 2012) and GL Garrad Hassan's Tidal Bladed (GL Garrad Hassan, 2012). Both of these codes are based on BEM theory but are heavily modified to account for dynamic effects. FAST was chosen over Tidal Bladed because it is open source, thereby enabling full access to the source code for implementing modifications and understanding the processes.

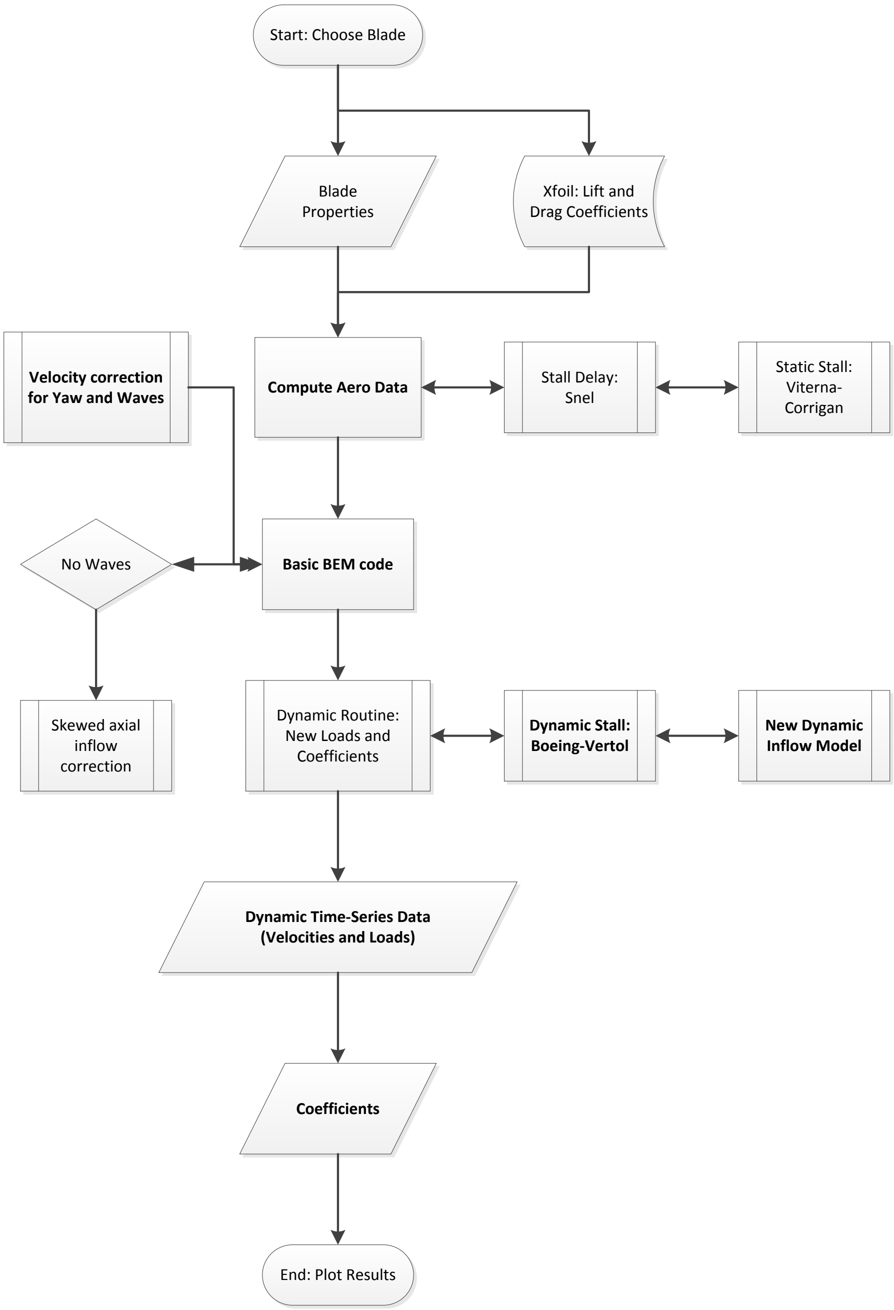

Figure 4.4: Flow chart showing processes of the modified BEM numerical model

Parameter	Description	Format	Units	Other
γ	Yaw Angle	Singular	°	
Ti	Intrinsic Wave Period	Singular	s	
H	Wave Height	Singular	m	
z_H	Hub Depth	Singular	m	$> R$
d	Water Depth	Singular	m	
U	Mean Current Velocity	Singular	m/s	
R	Blade Radius	Singular	m	
B	No. of Blades	Integer	-	
SET_PITCH	Fixed Pitch Setting	Singular	°	
PSIi	No. Azimuthal Nodes	Integer	-	
no_rev	No. Blade Revolutions	Integer	-	
r/R	Dimensionless Blade Radius	1D Array	-	each element: $r/R = x$
c/R	Dimensionless Chord Length	1D Array	-	each element position
TWIST	Blade Twist Angle	1D Array	°	each element position
THICK	Thickness to Chord Ratio	1D Array	%	each element position
$\alpha - C_L - C_D$	Angle of Attack vs. Lift/Drag	2D Array	°, -, -	*Re* & THICK dependent

Table 4.1: Inputs to the modified BEM code

4.5.1 Creation of FAST Input Files (Including Waves)

FAST is a complex numerical code including aeroelastic modules to describe blade and structure behaviour. These features were disabled when running the code as a comparison because the blade is extremely stiff (solid aluminium) and the structure itself is oversize therefore deflections are assumed to be negligible.

FAST is compiled in Fortran® and runs from an executable file using the command prompt. The executable calls upon a huge amount of input data in the form of various text files as shown in Table 4.2. Most of the files are relatively simple to edit for the required turbine properties. A Matlab script was created to generate the AeroData files in the correct format for FAST. The data used was the same lift-drag data obtained from Xfoil and post processed with the BEM code described previously in Section 4.4. FAST is a code designed for wind turbines and as such there was no input for waves. Full-field velocity input files can be used, so another Matlab script was written to produce velocity inputs including waves. This was a complex process involving conversion of the 4-dimensional array to the correct binary format. The script is reproduced in Appendix F. FAST offers good control over the output files where the user can specify only the required outputs and apply a data reduction factor should it be required. The importance of the integration time-step is emphasised since this can cause numerical instability if incorrectly specified. 0.004s was applied in all test cases, as specified by Jonkman (2012).

Input File	File Extension
Main FAST Input File	.fst
AeroDyn Input Parameters (BEM module)	.ipt
Blade Input Properties	.dat
Tower Input Properties	.dat
AeroData (folder containing lift-drag data for AeroDyn)	.dat
Wind (folder containing velocity input files)	.wnd & .sum

Table 4.2: Input Files for FAST

4.5.2 Recompiling FAST with Dynamic Inflow enabled

Intel® Visual Fortran Compiler 2008 was used to recompile the code (Pre-2003 versions will not work). The distributed executable included an empirical correction to disable dynamic inflow below 8m/s. Whilst this may be applicable to full-scale wind turbines, it is not applicable to TSTs that operate at much lower average flow speeds (0.9m/s in the scaled experiments presented in Chapter 6). This was corrected and the code recompiled with adjustment of the default optimisation settings (using /Qsave, /Qzero and maximum optimisation). Results from the numerical and experimental comparison are shown in Chapter 7.

Chapter 5

Experimental Design and Construction

Laboratory experiments are useful for prototyping and theoretical research when there is insufficient field data available. Little information exists for specific tidal energy sites as there has never been the need for dense spatial and temporal site measurements (Thomson et al., 2010). In addition, there is no experimental data available from full-scale devices to validate any theory since the technology is still too commercially sensitive. Wave-current interactions are difficult subjects to study in the laboratory because it is not easy to generate a uniform steady current field with waves (Swan et al., 2001). Whilst this is true for experiments in flumes, the use of a towing tank means that the current profile will be perfectly uniform. It is advantageous to have controllable conditions in the laboratory since it facilitates the interpretation of the results. It should be noted that experiments in a towing tank will contain no turbulence nor sheared velocity profile to distort the wave frequency as would occur in the field. The purpose of these experiments is to generate high quality loading data for a model turbine in the presence of waves and misaligned flow conditions.

5.1 Experimental Overview

The experiments presented in this report were carried out at Solent University's wave-towing tank, which is jointly run with the University of Southampton. The towing tank is 60m long, 3.7m wide and 1.8m deep. The towing carriage has a maximum forward speed of 4.5m/s and a fixed reverse speed of 0.46m/s. The wave generator is of the hinged-flap type. There is

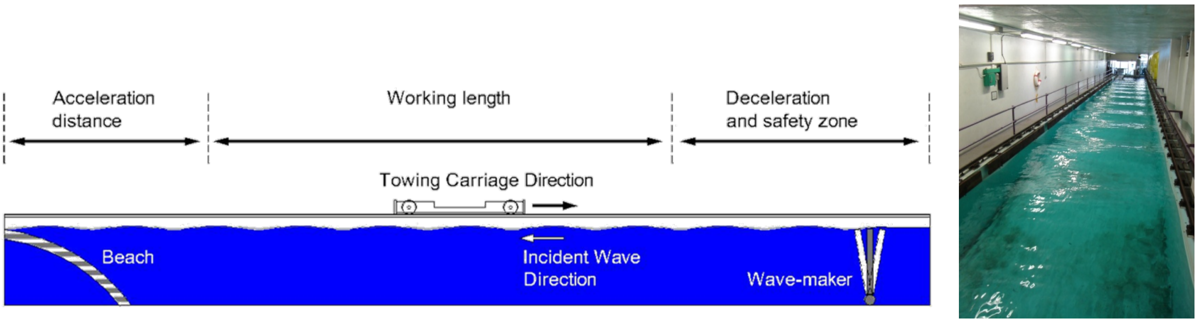

(a) CAD drawing showing experimental tank set-up

(b) Experimental facility with waves

Figure 5.1: Experimental Facility: Solent University's wave-towing tank, which is jointly run with the University of Southampton

a beach at the far end for wave energy dissipation (Figure 5.1). Experiments used a scale 1:20 horizontal axis tidal turbine model, provided by Dr. Luke Myers. The original turbine was used for characterisation of downstream flow from a TST. As part of this work it has been extensively modified for the measurement and recording of blade-rotor loading (Section 5.2). The specification and parameters varied during the experiments are detailed in Table 5.1. Chapter 6 describes some of the results from these experiments.

The turbine wiring loom was attached to a DAQ box, a power supply and two large rheostats which were used to apply load to the turbine generator (DC motor) and subsequently adjust the TSR of the turbine. Approximately 50 towed runs could be achieved per day. A range of TSRs, yaw angles, waves and immersion depths were tested as detailed in the experimental log in Appendix I. The blades used in these experiments were NACA 48XX with varying thickness and twist. The blade pitch angle was fixed at 0 degrees. Turbine monitoring consisted of strain gauge signals from the wireless telemetry system for rotor thrust and torque, in-plane and out-of-plane blade root bending moments and encoder position data. The data was passed through a data acquisition box to a LabVIEW program which applied calibrations to the data, allowing real-time viewing of the data and saved each run as a synchronised data file for post-processing of the raw data.

5.2 Horizontal Axis Turbine Model

The three bladed, horizontal axis turbine was modified as part of this work to measure thrust and torque with a new rotor hub dynamometer (see Section 5.3). The material used for the main shaft was changed from aluminium to stainless steel for increased durability and the lower hub was re-designed to suit the new dynamometer system along with adequate cable holes for strain gauging a blade (see Section 5.3.2). Blade position was measured using a specially commissioned hollow shaft encoder, which consequently provided speed and acceleration data when combined with time measurements. The shaft was connected by a spring-bellow shaft coupler to the gearbox and generator/motor in the rear of the nacelle. Access to all the internal mechanisms was achieved through specially designed hatches on the nacelle. A wireless telemetry system provided amplified voltage signals from the various strain gauge bridges mounted on the dynamometer and blade. Data was then transmitted via a sealed umbilical cable to a LabVIEW program that synchronised the data and provided a live-feed of the loads. Figure 5.2 provides a CAD drawing with a sectional view of the turbine nacelle.

The turbine nacelle was mounted to two different length tower sections to change the immersion depth and consequently the proximity to the water surface and wave effects. The experimental set-up can be seen in Figure 5.3 along with the yaw angles and the maximum wave height used for the test program. The turbine blockage was 7.2% (more detail on blockage is given in Section 2.4 and Appendix B). Figure 5.4 and Figure 5.5 show a number of images of the turbine installation. For this work a winch tower was built for the facility depicted since the turbine was simply too heavy to be positioned manually. See Appendix C for further photos of the turbine and experiment. The towing carriage was fixed at a constant speed of 0.9m/s (equivalent to a full-scale current speed of 4m/s). This resulted in a usable run-time of approximately 20s (after removing the time taken to accelerate at the start and finish of a run - see Figure 6.1).

5.3 Load Measurement

The high current velocities experienced by a TST will result in substantial loads, before dynamic conditions are even considered. A TST blade set would probably be modelled based on the typical tidal velocity variation and turbulence (for fatigue loading) and the maximum current velocity (for ultimate loading). These could be statistical interpretations, real site data or a combination of both. Modelling the dynamic loading on turbine blades during the combination of wave-current-yaw loads is not well understood. The model TST measured thrust and torque via a novel thrust-torque dynamometer (Section 5.3.1) and out-of-plane and in-plane blade bending moments at the root of a modified blade (Section 5.3.2). Strain gauges were used to

Turbine Specification				
Parameter	Name	Units	Description	Other
R	Blade Radius	m	0.4	
B	No. of Blades	-	3	Aluminium, Hard anodised
	Blade Geometry		See Figure 7.1	e.g. chord to thickness ratio
	Nacelle, Tower, Shaft			Stainless steel
	Shaft Bearings		Angular contact bearing Self aligning bearing	Sealed Sealed
	Shaft Seal		Double Lip	Viton Rubber
	Shaft Encoder		Custom 1200 CPR	Thistle Design (MMC) Ltd.
	Dynamometer		Custom Thrust and Torque	Aluminium Bronze
	Slip-rings		Custom 2-channel	Brass on Nylon, Carbon Brushes
	Wireless Telemetry		Amplifies strain gauge signals Transmits them to a computer	Includes inductive pick-up
	Shaft coupler		Spring-bellow system	
	Generator-Motor		24V DC 3000 RPM	
	Gearbox		Step-up ratio 1:10	
	Hatches		Gasket sealed	
	Cable glands		IP69	
	Hub		2-part, split	Aluminium

Experimental Variables				
Parameter	Name	Units	Description	Measurement Technique
TSR	Tip-Speed-Ratio	-	Range of TSRs (~8) between 4 and 7.5	Control - Rheostat Speed - Shaft Encoder and Clock
γ	Yaw Angle	°	0.0, 7.5, 15.0, 22.5	
ψ	Azimuth Angle	°	Sensitivity - 0.3°	Angle - Shaft Encoder
T_i	Intrinsic Wave Period	s	1.33, 2.00, 2.86	Wave Maker & Wave Probe
H	Wave Height	m	0.08, 0.10, 0.15	Wave Maker & Wave Probe
z_H	Hub Depth	m	0.90, 0.67	
d	Water Depth	m	1.88	
U	Mean Current Velocity	m/s	0.9	Carriage Speed Controller
SET_PITCH	Fixed Pitch Setting	°	0°	Adjustable

Table 5.1: Model Turbine Specification and Experimental Parameters

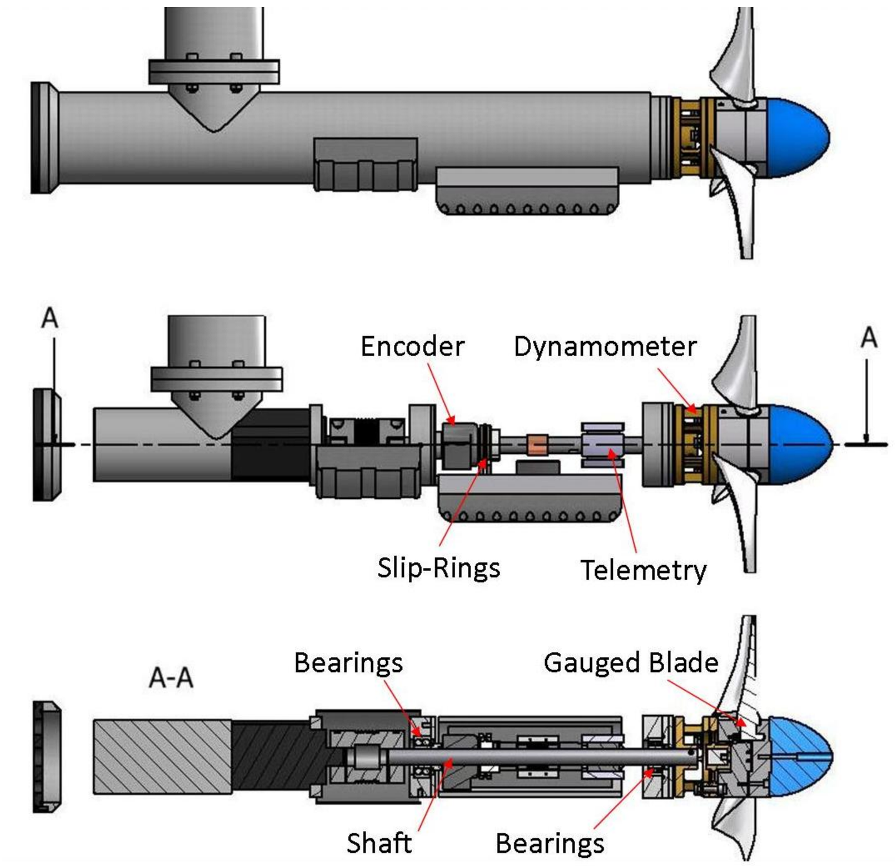

Figure 5.2: Sectional view of model nacelle showing modified components

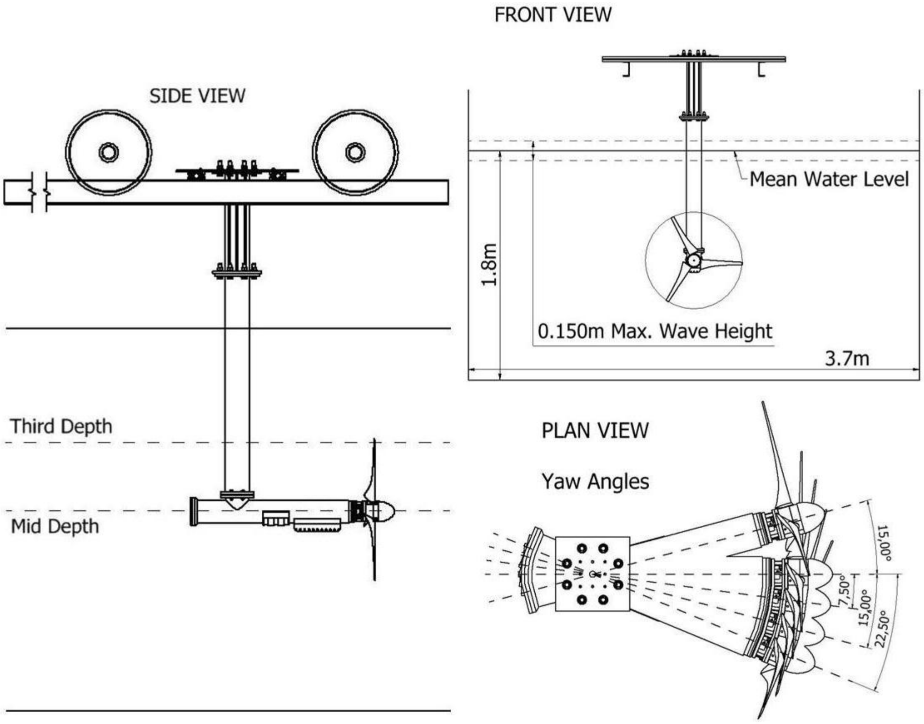

Figure 5.3: Elevations of model TST experimental dimensions

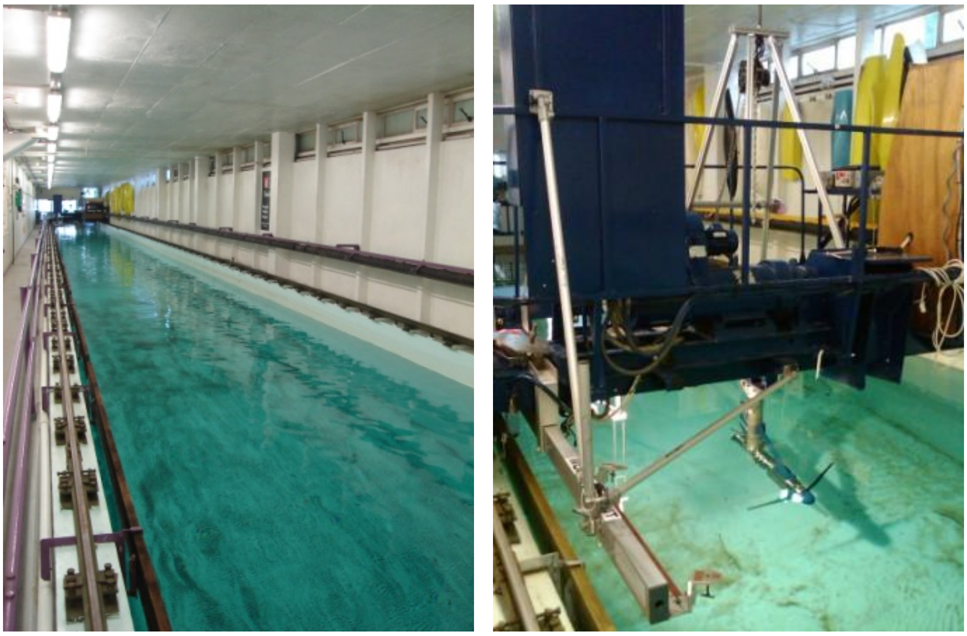

(a) Towing tank used during testing with model turbine

(b) Installed model turbine with winch rig above

Figure 5.4: Model tidal stream turbine installation

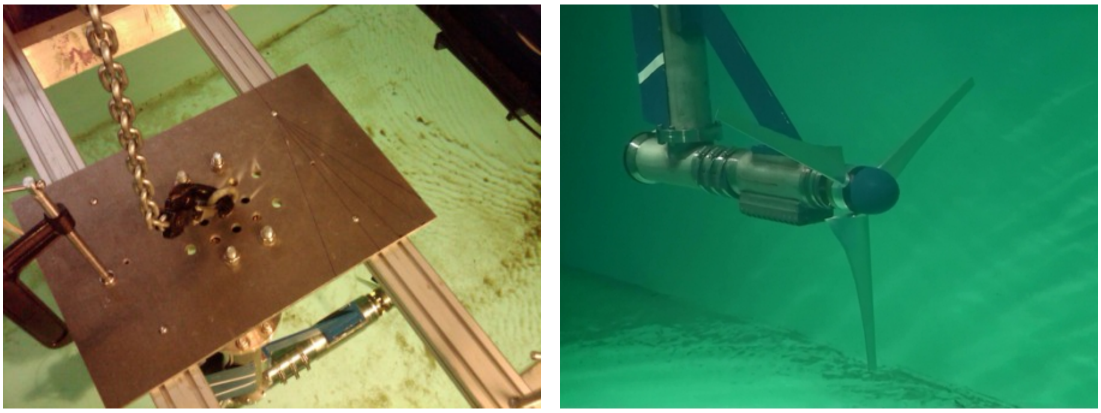

(a) Turbine winch chain attached to tower top plate

(b) Underwater photograph of turbine model

Figure 5.5: Model tidal stream turbine installation detail

measure these loads in the form of Wheatstone bridge. A constant voltage was applied to the bridge and when the part was subjected to deflection from imposed loads, it resulted in a change in strain proportional to the imposed load. The strain was also proportional to the voltage since the strain affects the gauge resistance linearly. Measuring the actual loads imposed on a part required calibration of the WSB to obtain the relationship between voltage and applied load (Section 5.3.3). The potential factors affecting strain gauge measurement are numerous and include the mounting procedure, temperature effects, fatigue and exceeding permissible limits (Papadopoulos et al., 2000). All strain gauging was carried out by a commercial company experienced in applying gauges. The gauges were fully waterproofed as all the parts were submerged in water. An important consideration applicable to tank testing a model turbine is the scaling and blockage. These are defined in Section 2.4.

5.3.1 Design of a New Thrust-Torque Dynamometer

Loading on the model turbine rotor was measured using a specially designed thrust-torque dynamometer. The dynamometer was a two-component system based on the extensive work carried out by Molland and Turnock (2002) for research on ship propellers. The measurement of thrust and torque was achieved using strain gauged flexures bending in contraflexure. The dynamometer was attached directly to the end of the turbine shaft, downstream of the rotor but upstream of all bearings and seals (providing actual loads with no losses). The design of the torque part used an increased number of flexures in order to increase the stiffness of the part in directions other than torsion as shown in Figure 5.6. The design also incorporated the facility to strain gauge the turbine blades in order to observe the direct effect of wave-current interaction on blade loading.

Assumed worst case parameters

- $C_T = 1.0$ maximum
- $C_P = 0.45$ maximum
- $U = 1.5ms^{-1}$ maximum (scaled to tank conditions)
- RPM = 80 minimum revolutions per minute (maximum rpm of model is approximately 200RPM but a slower rotation produces more torque)

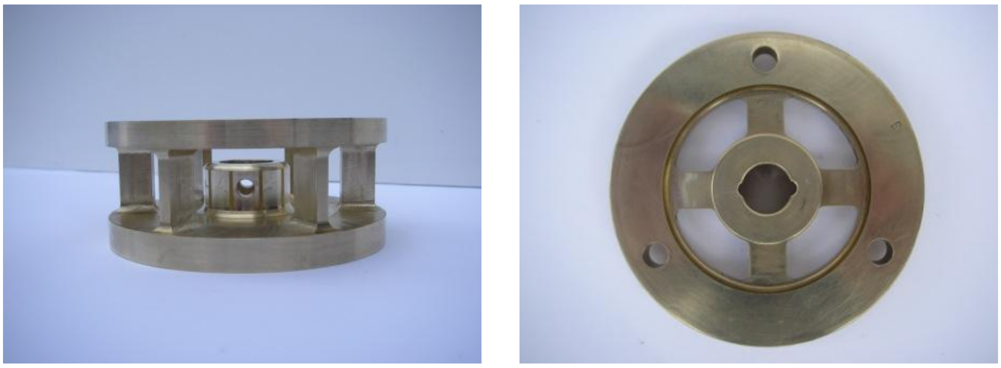
(a) Torque Part (un-gauged) (b) Thrust Part (un-gauged)

Figure 5.6: 2-Part Model Turbine Dynamometer

Calculation Summary

Maximum power: $P = \frac{1}{2} C_P \rho A U^3 = 382W$

Minimum rotational speed: $\Omega = \left(\frac{80}{60}\right) 2\pi = 8.38 rad/s$

Maximum torque: $Q = \frac{P}{\Omega} = 46Nm$

Maximum thrust: $T = \frac{1}{2} C_T \rho A U^2 = 565N$

The thrust and torque parts were CNC machined separately from a solid piece of Aluminium Bronze CA104 and bolted together using fitted shoulder bolts (Figure 5.7). Aluminium Bronze was used for its high yield stress (YS = $350 Nmm^{-2}$, E = $115 kNmm^{-2}$) and corrosion resistance. The maximum allowable strain at the flexure ends was assumed to be $1000 \mu\varepsilon$, based on the broad review by Molland (1976). The resulting stress was considered to provide a satisfactory safety margin with respect to hysteresis and load fluctuations. The TST nacelle was too compact to house the dynamometer internally as per Molland and Turnock (2002), thus it was mounted directly downstream of the rotor with a bearing at only one end, hence the increased potential for vibration. The dynamometer was mounted to the shaft using spring pins to alleviate vibration where possible. Alignment of the shaft and dynamometer was controlled using a self-aligning front bearing. The maximum diameter of the dynamometer was constrained by the TST nacelle diameter at 100mm. For calculations see Appendix G.

A torque cage concept with four flexures working in contraflexure was adopted by Molland and Turnock (2002), however there were some concerns that the dynamometer may be subject to increased lateral deformation as a result of mounting it at the end of the shaft rather than between two shafts. The solution adopted for this work was to use a similar cage concept, but with six flexures instead of four (see Figure 5.6). The assumed design stress levels led to an

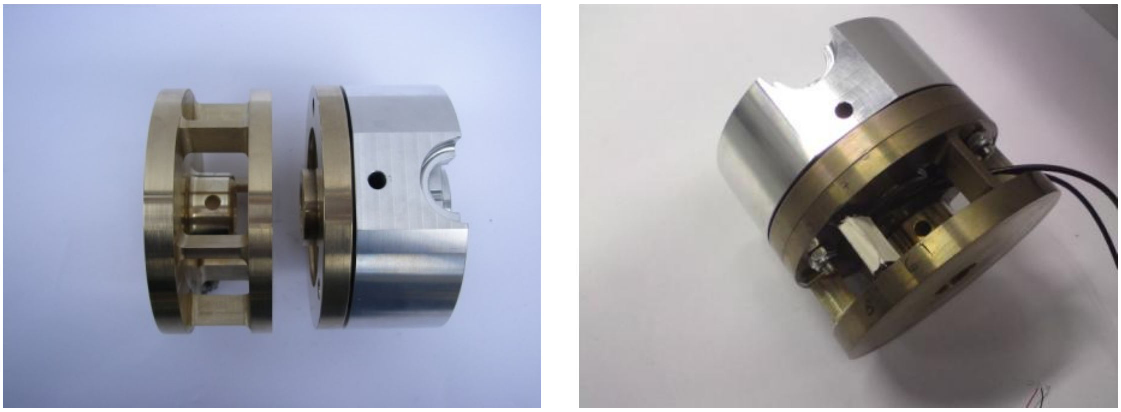

(a) Lower turbine hub attached to thrust part with torque part separate

(b) Completed dynamometer (with gauging)

Figure 5.7: Assembled 2-Part Model Turbine Dynamometer

effective flexure length of 19mm (neglecting fillets). The estimated maximum strain at flexure ends (when bending in contraflexure due to a torque of 46Nm) was 481$\mu\varepsilon$, equating to 16% of the yield stress. Rotational deflections and shear stresses were checked and found to be negligible (0.014mm and less than 1% of the yield stress respectively). The thrust part remained true to the original concept with four flexures. The assumed design stress levels for this part led to an effective flexure length of 13mm. The estimated maximum strain at flexure ends (when bending in contraflexure due to a thrust of 565N) was 250$\mu\varepsilon$, equating to 8% of the yield stress. Longitudinal deflections and rotational shear stresses were also checked and found to negligible (0.004mm and less than 6% of the yield stress respectively).

5.3.2 Designing a Blade for Measuring Imposed Loads

Dynamic blade loading is a complex topic as described in Section 2.5.3. The TST blades used in the experiments were based on a NACA 48XX profile with varying chord thickness and twist. They were milled from solid aluminium for high stiffness combined with a smooth surface finish. Only blade root bending could be scaled realistically with these blades since the blade bending modes were unlikely to relate to a full-scale composite TST blade. The use of scaled composite blades was discounted simply because of the difficulty in producing the sharp trailing edges required and correctly aligning and embedding a root section. In addition the numerical modelling would have become significantly more difficult since hydro-elastic effects would have to be considered for a more flexible blade.

The method adopted for measuring blade loading was to machine flat faces on the root of a single blade and strain gauge it to measure the strain in both the out-of-plane (thrust) and

(a) CNC machined model TST blade

(b) Anodised blade for gauging alongside normal blade (notice the square root section)

Figure 5.8: Blade root modification for strain gauging

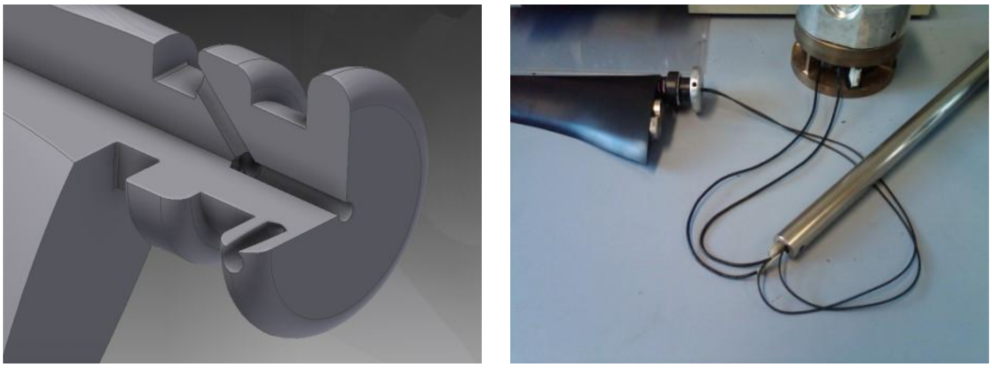

(a) CAD drawing showing detail of blade root section for gauging

(b) Gauged blade, dynamometer and shaft

Figure 5.9: Blade root strain gauging

in-plane (torque) directions. See Figure 5.8 for the changes in blade root design. The size of the machined section was arguably more important here than for the dynamometer design. The blade had to be sufficiently strong to resist the loads experienced during testing whilst also being flexible enough that any deformation could be recorded by the strain gauges. A square 14mm section, 8mm wide was found to provide sufficient sensitivity for the strain gauges whilst also resisting any static load from the experiments. A basic Finite-Element Analysis (FEA) was applied to a Computer Aided Design (CAD) model of the blade to verify the calculations. This resulted in a factor of safety of 3 for an assumed maximum out-of-plane bending moment calculated from basic BEM theory. For calculations see Appendix H.

It was unfeasible to have 3 blades manufactured with a modified root section and in addition there was no space to fit additional telemetry in the nacelle. A possible problem with using just a single gauged blade and two normal blades was that it could cause a rotor imbalance (due to the mass difference after machining) which could affect the results with an unwanted 1P oscillation and maybe even damage the turbine. The different mass-moments of the blade were calculated

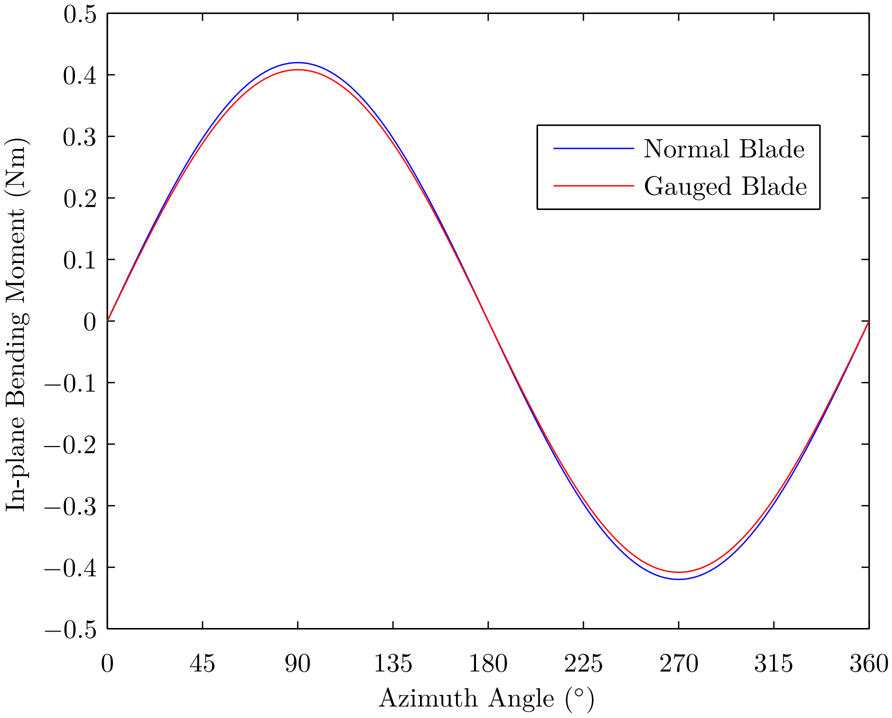

Figure 5.10: Comparing the theoretical mass-moments of an original blade against a newly modified, unbalanced blade for strain gauging

using CAD to determine the centre of mass. The difference in mass-moment (Figure 5.10) was adjusted with the addition of small stainless steel masses, as seen in Figure 5.9. These were designed to cause minimal hydrodynamic interference by locating in the flat milled region near the blade root.

5.3.3 Calibration Techniques

Calibration of the dynamometer and blade is required before use in the experiments to enable logical conversion of the acquired voltage data to equivalent load measurement. Calibration of the thrust part was achieved by inverting the turbine, placing known masses on the hub and measuring the subsequent output voltages from the telemetry equipment. Out-of-plane blade root bending was calibrated whilst the turbine was still inverted, using smaller masses suspended from near the blade tip at a known perpendicular distance from the root section. An example of the out-of-plane bending moment calibration is shown in Figure 5.11. This shows the loading graph as the mass increased and the unloading graph as the masses were subsequently removed. This process is important to ensure that they both follow the same linear path or interpreting the measured data is complicated with different calibration constants for the same measurement.

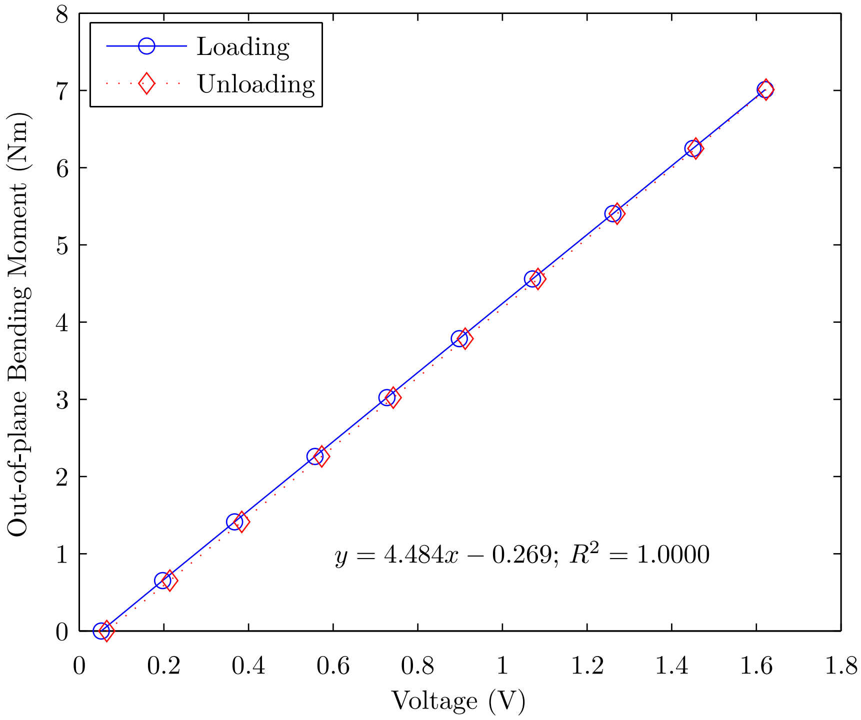

Figure 5.11: Example calibration plot for the out-of-plane blade root bending moment

The gradient of the lines forms the calibration constant. All the calibrations carried out during testing achieved a coefficient of determination (R^2) of at least 0.9998 therefore it was assumed that there was minimal systematic error in the calibration results.

Calibration of the torque part and in-plane root bending used the calibration rig is shown in Figure 5.12. This was designed to facilitate the process by rigidly clamping the turbine horizontally to the rig. The turbine shaft was locked in place and masses suspended from the blades to determine calibration constants for the torque part of the dynamometer and in-plane root bending. After calibrating the parts, the in-plane bending was measured at several key azimuth locations to determine the gravitational component of a blade.

5.4 Experimental Improvements

The turbine model required several design improvements after early tests revealed problems. The most difficult problem to solve was the ingress of water into the turbine nacelle. Leaks ended several rounds of testing due to water-damaged electronics. The turbine was made up of 3 hatches, a complex shaft seal arrangement and 3 cable glands (Figure 5.2 and Appendix C). Several attempts were made to improve certain seals, with the final solution being:

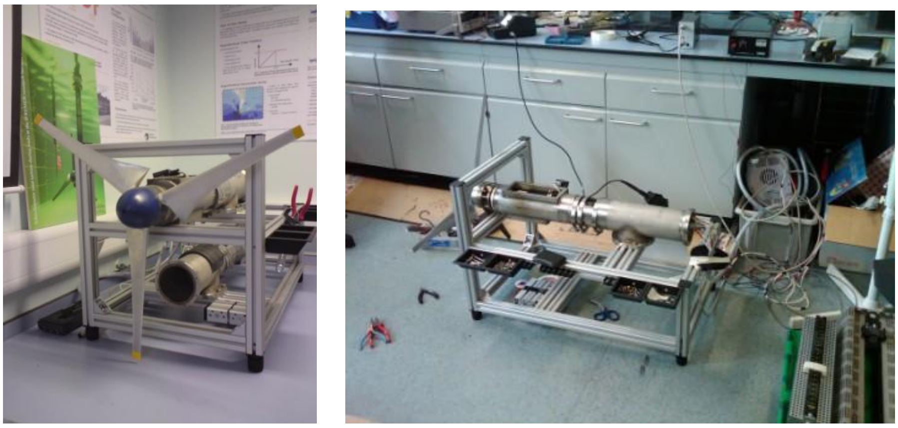

(a) Calibration rig, working platform and storage for two model turbines

(b) Circuit testing and calibration

Figure 5.12: Calibration rig with Turbines

- The main hatch gasket was upgraded to a high quality head gasket material. This was cut by hand using a pre-fabricated template. The housing was bolted in place using many stainless M5 bolts, tightened in sequence to avoid creasing the gasket
- A new front shaft seal housing was designed using a Viton rubber double-lip shaft seal. The housing itself was bolted and sealed using a machined O-ring to the front of the nacelle as a further precaution against leaks. Replacing the original aluminium turbine shaft with a stainless steel alternative prevented shaft wear by the seal, thus increasing durability and reliability of the system
- The central curved hatch was sealed using a liquid gasket sealant, which was clamped in place using 3 large hose-clips
- The rear hatch used a large machined O-ring and was bolted in place
- The cable glands fitted to the rear hatch were all certified water resistant. These were sealed using liquid gasket sealant as a further precaution
- The turbine umbilical was adapted with a Shraeder valve fitting and the nacelle pressurised during tests. Keeping a positive pressure helped to ensure a dry nacelle. Care was taken not to apply excessive pressure as the seals were not all designed to resist an internal pressure
- As a further precaution against any seal failures, all the sensitive electronics were sealed using a suitable non-corrosive silicon

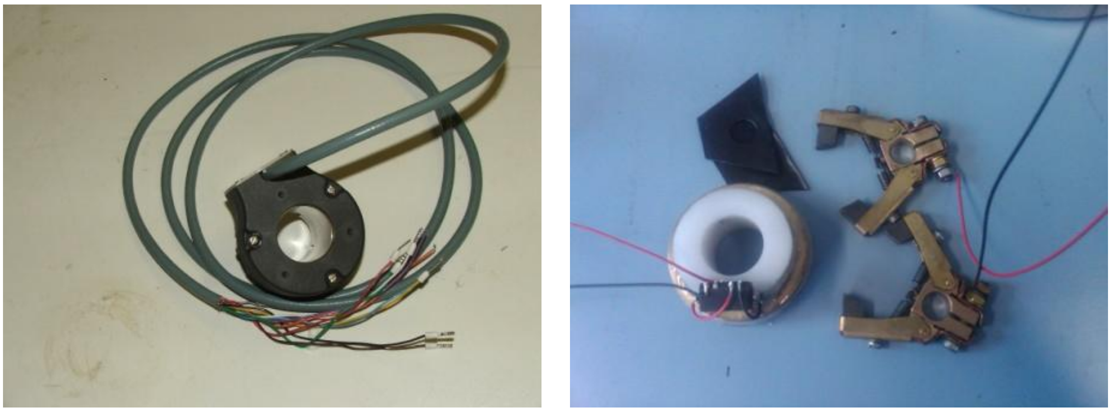

(a) New Shaft Encoder (b) Compact 2-Channel Slip-rings

Figure 5.13: Turbine Upgrades

A hollow-shaft encoder was used to replace infra-red optical RPM sensors. This provided much more reliable measurements and provided angular position data for the blades and more precise angular velocity measurements (Figure 5.13). The encoder had a resolution of 1200 counts per revolution. The unit was specially commissioned due to the compact size requirements of the nacelle. The encoder was still too large to fit in the nacelle without reducing the size of some other components. The shaft mounted amplifiers and the inductive pick-up could not be readily modified so the original slip-ring system was removed and replaced with a new, more compact design. A 2-channel system was designed and built by hand to suit the space envelope. The slip-rings were turned using a small billet of brass. The rings were fitted to an insulating nylon housing and used sprung carbon brushes as the electrical contacts. Finally, the bearings were replaced with more durable and more compact sealed units. These turbine upgrades improved the reliability of the system and permitted increased quality data capture.

5.5 Synchronised Data Acquisition

The different cables sending or receiving signals and power were composed of three separate, sealed umbilicals. The large central umbilical delivered power to the generator to overcome the start-up torque of the device, followed by a switch to a rheostat bank acting as an artificial load for speed control purposes (different TSRs were obtained in this way). Power to the system telemetry was delivered via a 5V supply linked to the slip-rings. This passed power to the rotating shaft through a 5V regulator to the telemetry circuitry. Amplified strain gauge signals were digitised and passed to a coil around the shaft where an inductive pickup collected the data from all the strain gauges simultaneously. The second umbilical transported the digital

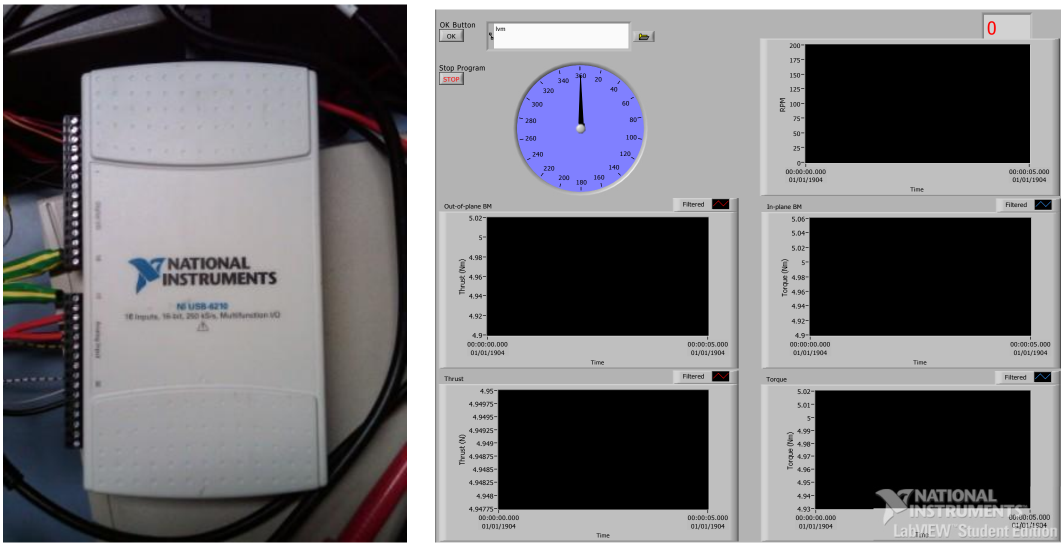

(a) National Instruments® DAQ Box

(b) LabVIEW® Front Panel

Figure 5.14: Data acquisition system

strain gauge data to a decoder box which transformed the data back into its original analogue form. The third umbilical controlled the shaft encoder. Power was supplied (5V) and digital shaft position data was transmitted to the water surface.

The four analogue outputs from the decoder box (thrust, torque, in-plane bending and out-of-plane bending) and the digital encoder outputs were connected to a National Instruments® DAQ (Data Acquisition) box. This synchronised the raw data using a LabVIEW® user interface designed for this work (Figure 5.14). The analogue signals were filtered at the DAQ connections by fitting capacitors (in parallel) across the terminals to reduce extraneous interference. The LabVIEW program was used to display current turbine loads, blade position and RPM whilst the raw voltage data was stored in ASCII format for post-processing in Matlab.

Chapter 6

Experimental Results

The experiments presented in this report were carried out at Solent University's wave-towing tank, which is jointly run with the University of Southampton. The model turbine used here, its specification and the experimental design are described in Chapter 5.

6.1 Results for a Typical Turbine Run

Rotor thrust data for a single run in the towing tank has been calibrated and presented in Figure 6.1. Several key features of this typical run are:

1. [0 to 9 seconds] Turbine spinning slowly using a power supply, hence the small negative thrust
2. [9 to 10 seconds] Carriage accelerates up to required tow speed, the turbine rpm also increases due to flow speed
3. [10 to 13 seconds] Carriage reaches required tow speed, power supply switched off
4. [13 to 14 seconds] Turbine motor/generator connected to rheostat bank, acting as a load on the generator, increasing thrust and controlling TSR. This increased drag causes the carriage to slow down, whereby the carriage speed controller accelerates to compensate, regaining the desired tow speed
5. [14 to 20 seconds] Towing carriage speed controller reduces carriage speed to original prescribed speed
6. [20 to 40 seconds] Region of useful experimental data

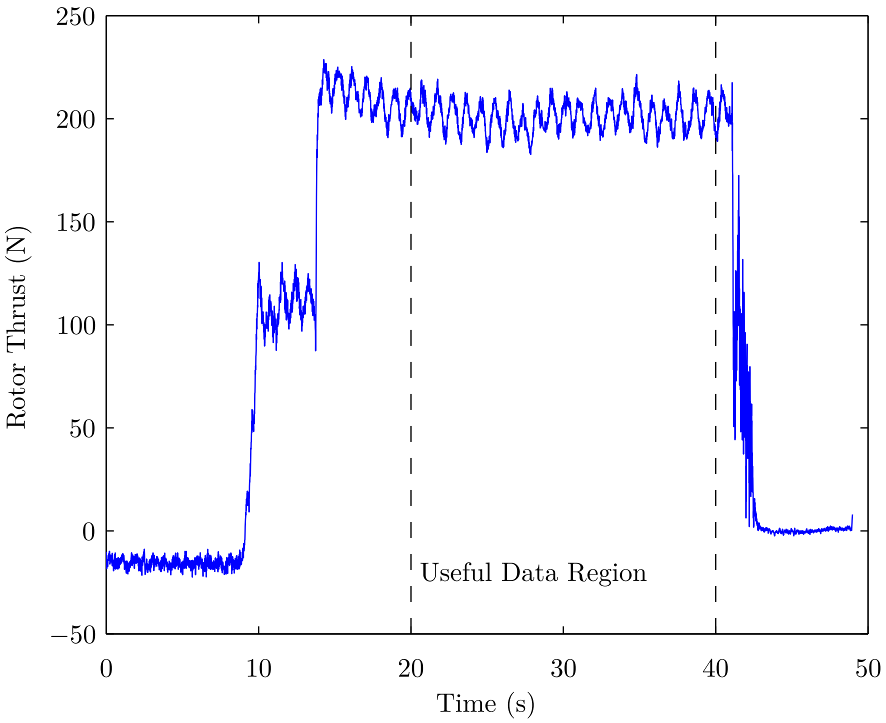

Figure 6.1: Model turbine thrust over a full test run $H = 0.08m$, $T_i = 1.33s$, $U = 0.9m/s$, $\gamma = 0°$, TSR $= 5$ and and $z_H = -0.9m$. Dashed lines denote region of useful data

7. [40 to 43 seconds] Automatic carriage stop triggered and carriage slows to a stop

8. [43 to 50 seconds] Rotor stopped, hence zero thrust

Only approximately 20 seconds of data was available per towed run, however this proved to be sufficient for the purposes of this research. Each towing run had the same features, but at different time intervals, therefore each run was individually inspected and the useful data cropped, calibrated, filtered and smoothed. The data was low-pass filtered to remove the electrical noise (+50Hz). Additional smoothing using a high-order polynomial fit, known as the Savitzky–Golay method (Orfanidis, 1996), improves the clarity of the data (important when comparing time-series data). The main advantage of this smoothing method is that it preserves important features of the distribution such as relative maxima and minima that are usually deformed by moving average smoothing techniques.

Speed Check - Longitudinal Velocity (m/s)				
Sample	Reverse mean speed	Standard deviation	Forward mean speed	Standard deviation
1	0.459	0.022	0.465	0.020
2	0.456	0.022	0.462	0.022
3	0.458	0.022	0.460	0.023
4	0.458	0.022	0.460	0.020
5	0.458	0.022	0.458	0.019
6	0.458	0.022	0.459	0.019
7	0.459	0.022	0.460	0.021
8	0.459	0.023	0.460	0.020
9	0.459	0.022	0.459	0.022
10	0.459	0.022	0.459	0.020

Table 6.1: Consistency of ADV velocity measurements (longitudinal velocity only)

6.2 Baseline Experimental Conditions

6.2.1 Measurement Consistency

Early experiments omitted the turbine and were focused on baseline measurements to test the consistency of the carriage speed and the wave maker. A Nortek® Vectrino® Acoustic Doppler Velocimeter (ADV) was used to measure velocity in three dimensions, sampling at a rate of 50Hz. The velocity range was set to ±0.3m/s which corresponds to the maximum velocity range of the largest waves used in the experiments. Transmit length was 2.4mm and *sample volume* length was 9.1mm. It would have been preferable to use a smaller sample volume but due to a lack of seeding particles this was not possible. Seeding is the addition of small particles to the water, in this case hollow glass spheres (Potters Industries Inc., 2012), to increase the ability of the ADV probe to gather velocity data. Towing tanks are notoriously difficult for ADVs because there is no suspended material in the water column for the high frequency sound waves to reflect against since they settle to the bottom of the tank and are hard to stir up from the bottom.

The first series of tests involved towing forwards and backwards into still water to establish the consistency of both the ADV measurements and carriage velocity (average carriage speed was found to be accurate after carrying out average speed runs by timing the carriage over a set distance). The carriage was found to have a fixed reverse speed of 0.46m/s which was adopted for the forward speed tests. Both tests were carried out 10 times as shown in Table 6.1.

The data clearly shows that the mean ADV velocity measurements and consequently carriage speed is sufficiently accurate in both directions. The component of longitudinal velocity of the ADV has been shown to be in greater error than the vertical velocity component, probably due

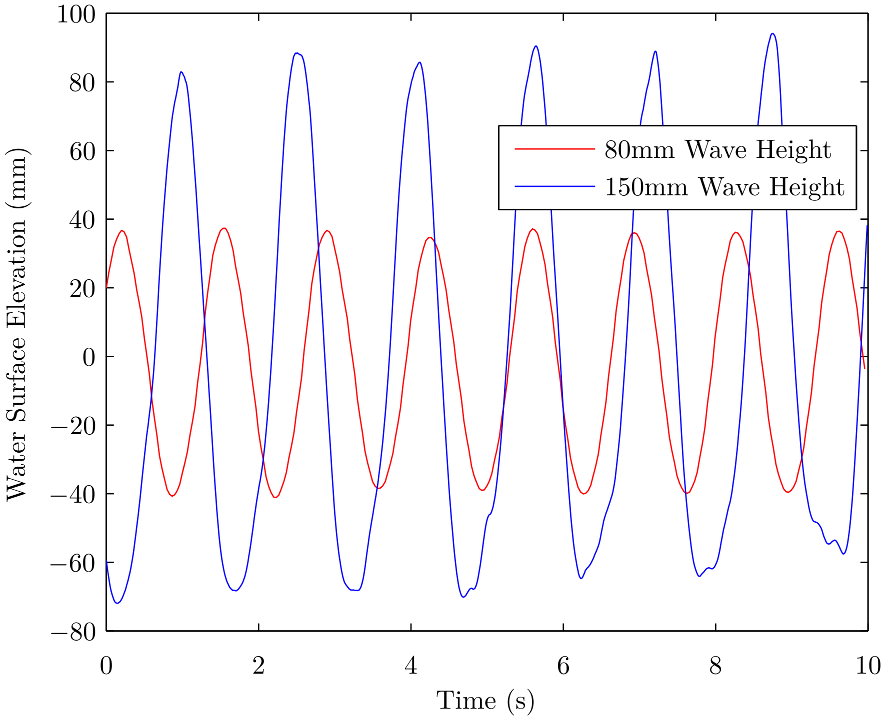

Figure 6.2: Time-series showing wave surface elevations from a wave probe

to the mounting method of the ADV on the carriage resulting in vibration in this direction. Standard deviations are also relatively small, being within ±5% of the mean standard deviation. The ADV probe was mounted in the water upstream of the carriage on a support structure capable of varying the submergence of the probe.

A single wave probe was also used alongside the ADV during the tests to monitor wave height, period and verify that the waves were truly linear as expected. The wave probe was calibrated twice daily and results were recorded for each run. The wave-maker was found to produce repeatable monochromatic waves, with minor nonlinearities towards the end of a towed run for large wave heights caused by poor damping of the wave paddle motion (Figure 6.2). The main difficulty was achieving the desired wave height using a gain setting, which happened to vary non-linearly with the chosen wave height. Since wave probes were used to determine precise wave heights, this was not envisaged as a problem providing the waves were close to the desired height.

6.2.2 Acoustic Velocimeter Data and Wave-Current Interaction

An ADV was attached to the carriage and towed in waves to observe one-dimensional wave-current interaction (Doppler shift). Equation 2.12 was verified against this data to ensure the

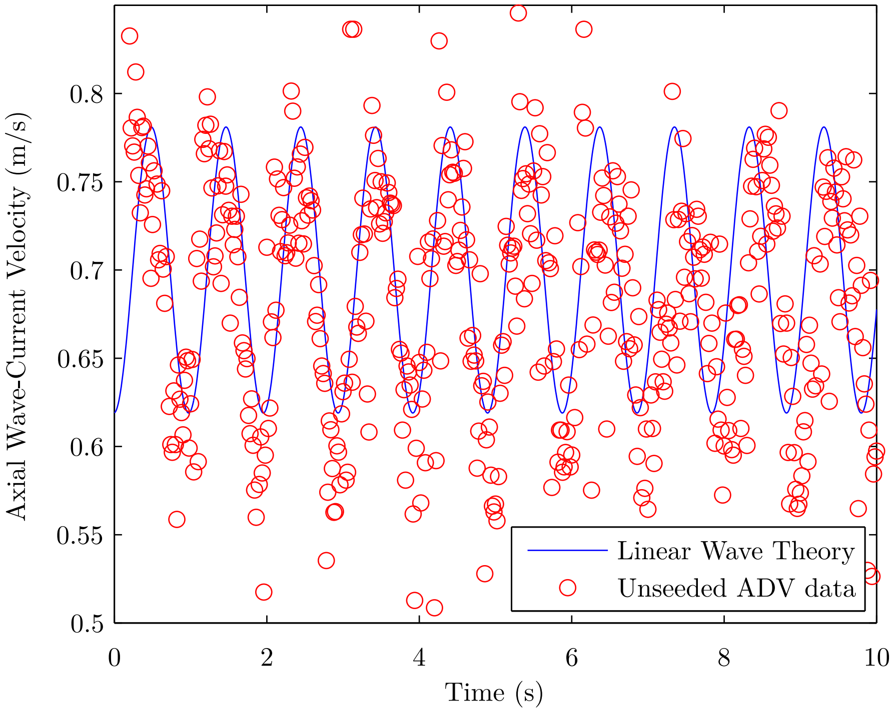

Figure 6.3: Unseeded, unfiltered acoustic velocimeter data compared against linear wave theory. $H = 0.08m$, $T_i = 1.33s$, $U = 0.7m/s$ (opposing current), $d = 1.88m$ and $z = -0.4m$

correct modifications were made to the BEM code. The effectiveness of the ADV velocity measurements were also evaluated to test whether the device was capable of measuring wave velocities. The device functioned well, but it was essential that the tank was well seeded to improve the returned ADV signals. Using a concentration of 5g/litre of seeding material in about 50 litres of water, mixed in at the start of every test session, proved sufficient to significantly increase the signal-to-noise ratio of the ADV above the manufacturers recommended limit for good data quality. A specific ADV filter was also applied to the data to remove extraneous noise. The velocity correlation filter developed by Cea et al. (2007) and implemented using Matlab proved to be effective, but only when combined with the use of seeding material.

Raw ADV data with no seeding has been presented alongside linear wave theory in Figure 6.3. This emphasised the need for the relatively large quantities of seeding material mentioned previously. The effects of the seeding can be seen in Figure 6.4. In addition to this seeding, a filtering technique by Cea et al. (2007) was applied to the data and found very effective at removing erroneous data points as shown by the ellipses in Figure 6.5. The points were then replaced using cubic interpolation. The x-velocity (axial flow direction) contains more spiking than the z-velocity (vertical direction). This can be attributed to the way that the ADV was

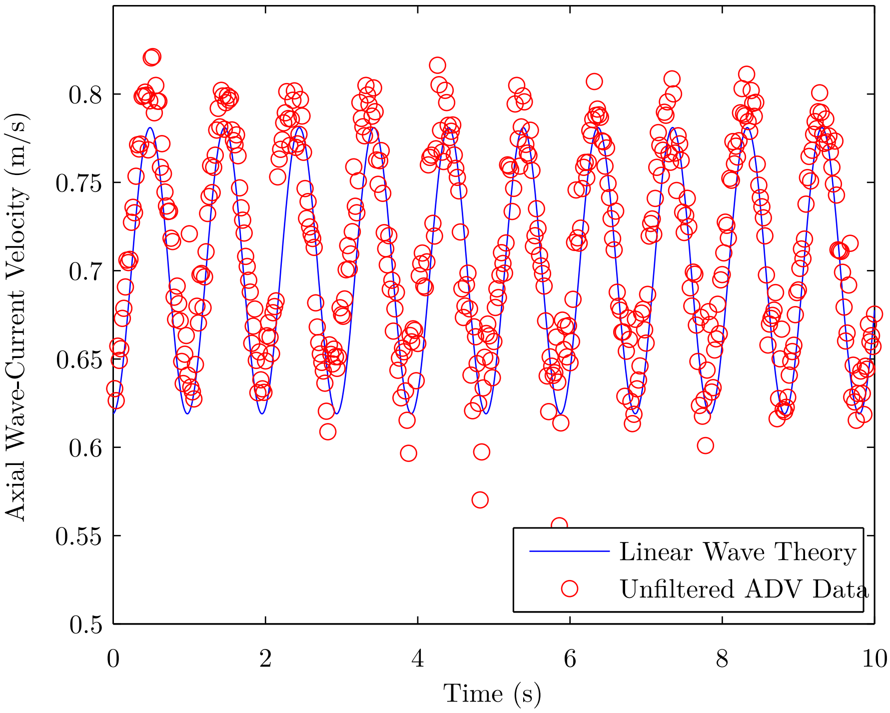

Figure 6.4: Seeded, unfiltered acoustic velocimeter data compared against linear wave theory. $H = 0.08m$, $T_i = 1.33s$, $U = 0.7m/s$ (opposing current), $d = 1.88m$ and $z = -0.4m$

used, with a greater average velocity in the axial flow direction. The y-velocity (lateral direction) is largely noise caused by structure/carriage vibration. Theoretically the y-velocity should approximate to zero. When the filter is applied to well seeded ADV data, as shown in Figure 6.5 the wave particle orbits can be observed in the x'-z' correlation plane. Applying a small amount of smoothing after filtering gives a very good approximation of the wave velocity at a particular depth location as shown in Figure 6.6. The Doppler shift is now evident in both the experimental and theoretical data. The intrinsic wave period created by the wave paddle was 1.33s, which was confirmed using a wave probe. The apparent wave period seen by the ADV, and hence the model turbine is 1.0s. This reduction is the expected Doppler shift caused by the appearance of more frequent wave crests as the probe travels against the wave direction (see Section 2.2). This effect will be reversed if travelling with the waves, resulting in a longer period of 2.0s.

6.2.3 Repeatability of Velocities

Repeatability is fundamental to all experiments. Normally the experimental variation should be smaller than a predefined range over a set of samples to ensure repeatability. Setting a limit is somewhat arbitrary, but when comparing three typical repeat runs (Figure 6.7) it is evident

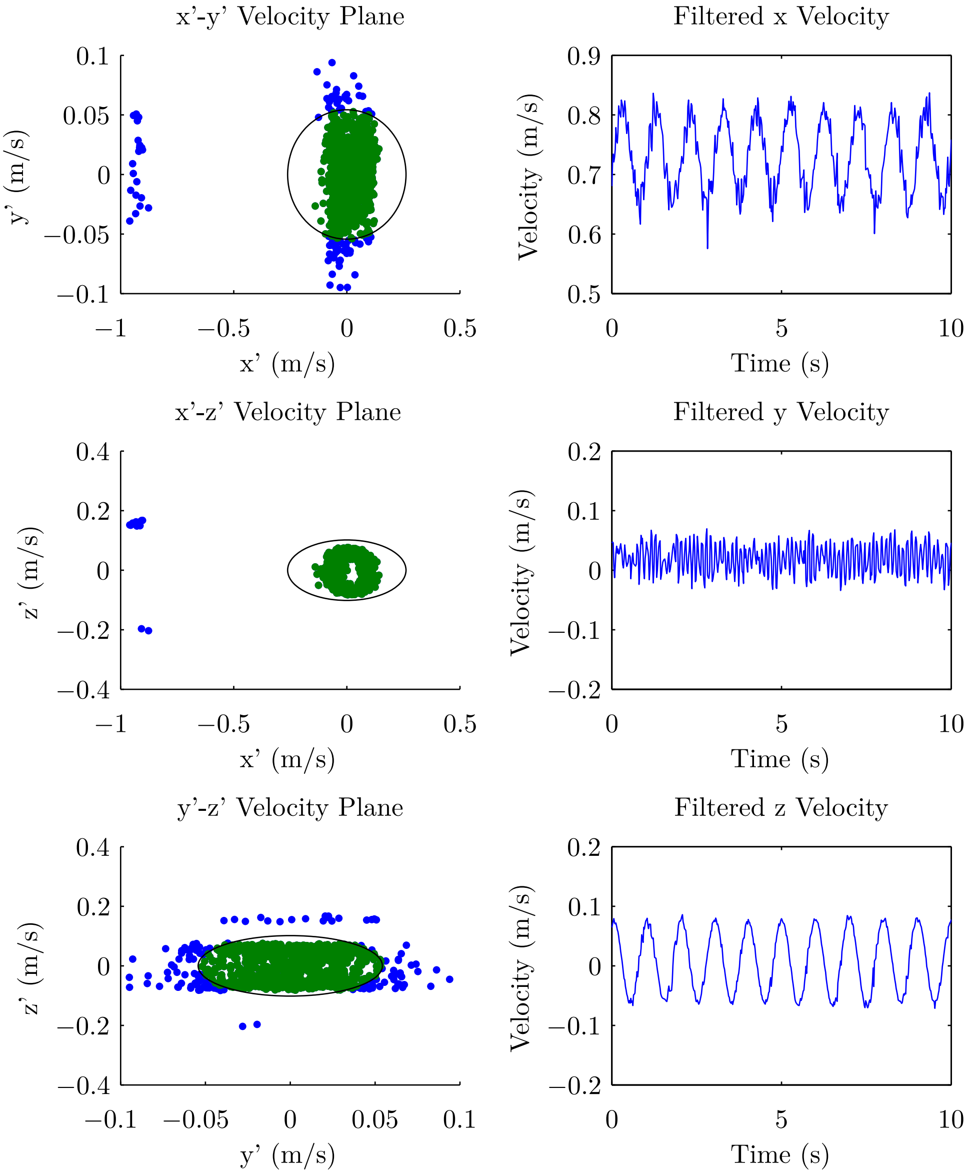

67

Figure 6.5: Application of the velocity correlation filter to seeded ADV data showing all correlation spaces and the resulting un-smoothed filtered time-domain velocities. $H = 0.08m$, $T_i = 1.33s$, $U = 0.7m/s$ (opposing current), $d = 1.88m$ and $z = -0.4m$

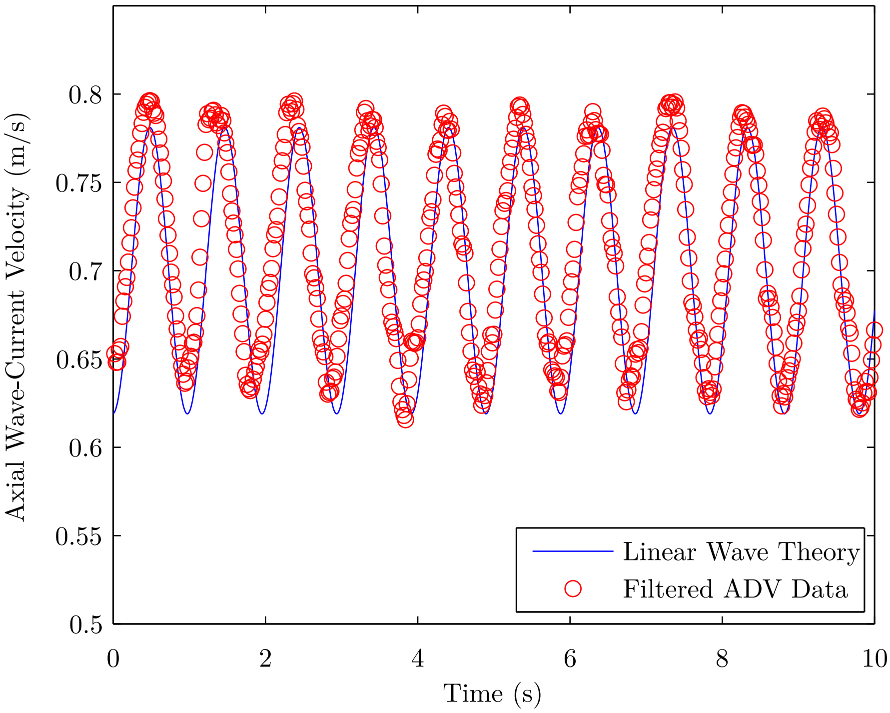

Figure 6.6: Seeded, filtered and smoothed acoustic velocimeter data compared against linear wave theory. $H = 0.08m$, $T_i = 1.33s$, $U = 0.7m/s$ (opposing current), $d = 1.88m$ and $z = -0.4m$

that the velocities are a close match with little variation apparent in either wave height or wave period. The same can be said of all the other velocity measurements carried out, so it was concluded that the inflow velocities were repeatable. The situation becomes more complicated when loading data is investigated in Section 6.2.4.

6.2.4 Repeatability of Load Measurements

Data repeatability is shown for out-of-plane and in-plane root bending moments in Figure 6.8 and Figure 6.9 respectively. The mean of each run is approximately the same, as is the load variation of the data. For these criteria the data can be described as repeatable. The periodic nature of the waves acting on the turbine blades is also shown to be repeatable, along with the less significant yawed loading component. The reason for the slight differences in the loading for these six similar runs was thought to be due to differences in blade azimuth position relative to the maximum wave crest elevation. Upon investigation this was found not to be very different, meaning that the loading discrepancies are likely to be a descriptor of the systematic experimental error.

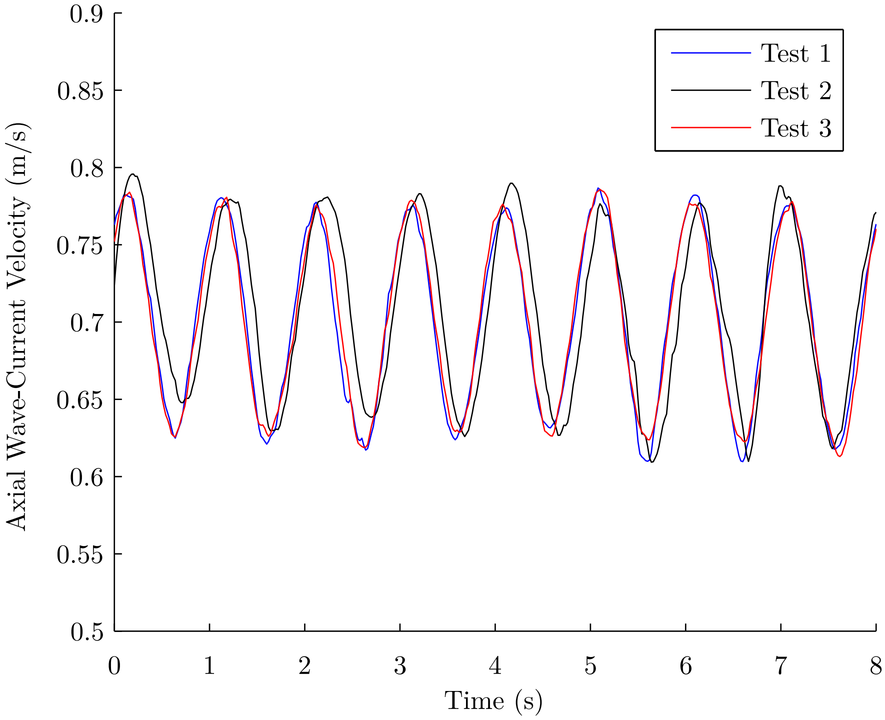

Figure 6.7: Repeatability of wave-carriage-ADV velocity measurements over three typical runs. $H = 0.08m$, $T_i = 1.33s$, $U = 0.7m/s$ (opposing current), $d = 1.88m$ and $z = -0.4m$

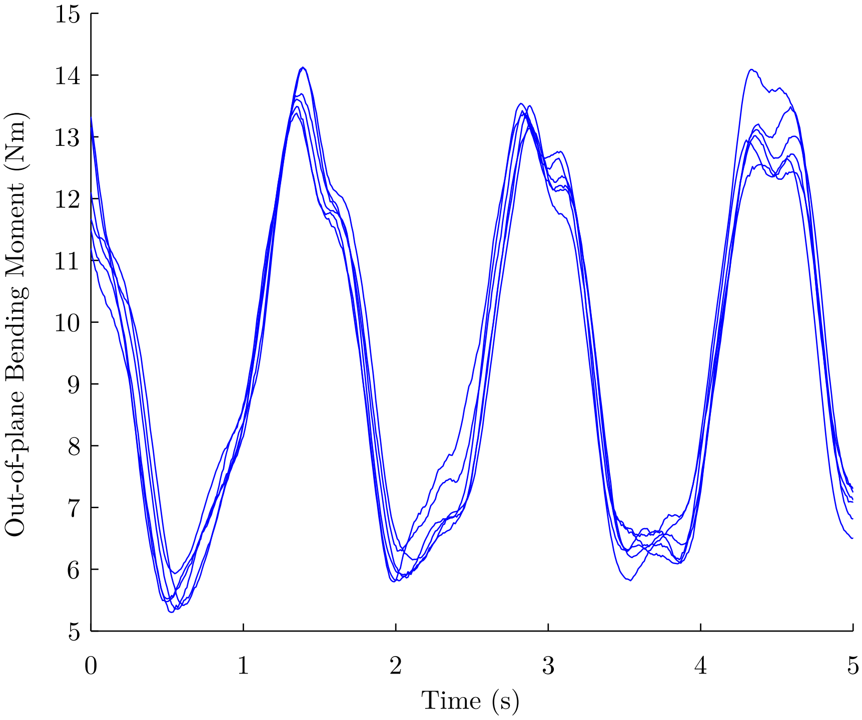

Figure 6.8: Repeatability of out-of-plane bending moments after phase-shifting. $H = 0.15m$, $T_i = 2s$, $U = 0.9m/s$, $\gamma = 15°$, mean TSR = 5.6 and $z_H = -0.9m$

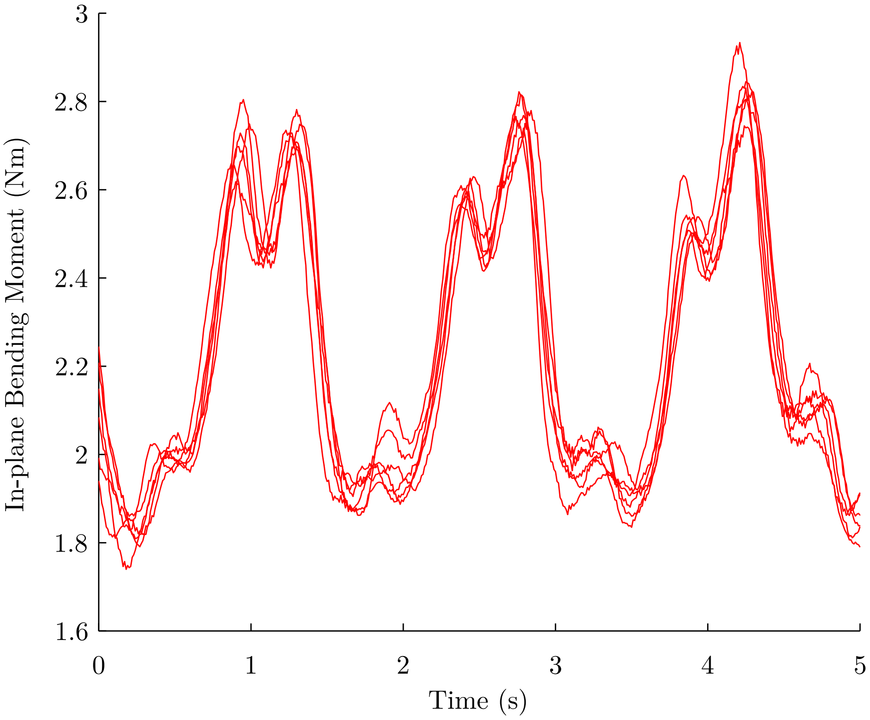

Figure 6.9: Repeatability of out-of-plane bending moments after phase-shifting. $H = 0.15m$, $T_i = 2s$, $U = 0.9m/s$, $\gamma = 15°$, mean TSR = 5.6 and $z_H = -0.9m$

6.3 Time-Series Blade Loads

Synchronised high-frequency blade data depicting water surface elevation, bending moment, azimuth blade angle and rpm is presented in Figure 6.10. The water surface elevation change is shown to be proportional to the change in turbine RPM, with the two being almost exactly in phase. What is less apparent is the influence of waves and yaw on the bending moments. In general the waves cause an approximately proportional fluctuation in the bending moments. This particular example also includes the effects of rotor yaw which creates a 1P frequency oscillation in both bending moment graphs. The in-plane bending moment also includes the gravitational bending moment component, hence why some of the 1P oscillations appear more pronounced. Inferring more from this figure leads us to understand that the presence of waves and yaw cause oscillations in the rotor power, which in-turn influences the quality of the electrical power production.

6.3.1 Load Comparison with Multiple TSRs

Experimental results from the turbine operating over the full range of TSRs is shown in Figure 6.11 for out-of-plane blade root bending moments and Figure 6.12 for in-plane bending

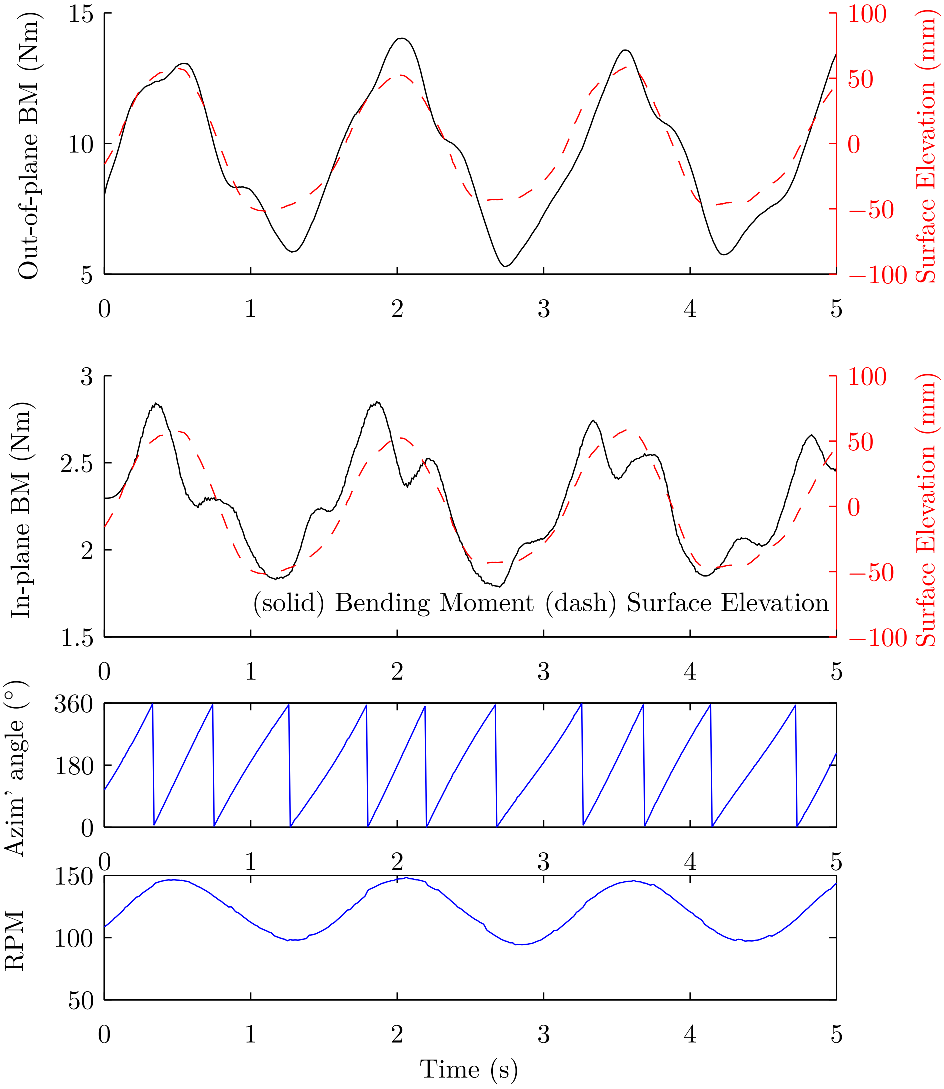

Figure 6.10: Experimental time-series blade data synchronised. $H = 0.1m$, $T_i = 2s$, $U = 0.9m/s$, $\gamma = 15°$, TSR = 5.7 and $z_H = -0.67m$

moments. These figures present turbine data under steady conditions with no waves or yaw i.e. the turbine is towed into still water with no yaw. As expected, increasing the TSR increases the out-of-plane loading and decreases the in-plane loading. Increasing the TSR also results in slightly more irregular loading in the out-of-plane direction. This could be attributed to several factors affected by increased turbine RPM, such as turbine structure stiffness, rotor/blade/shaft imbalances and the use of a rheostat as a speed controller. The fluctuations seen in the in-plane direction (Figure 6.12) represent the gravity bending moment component. The frequency of the gravity bending moment is component is proportional to the relative turbine TSR.

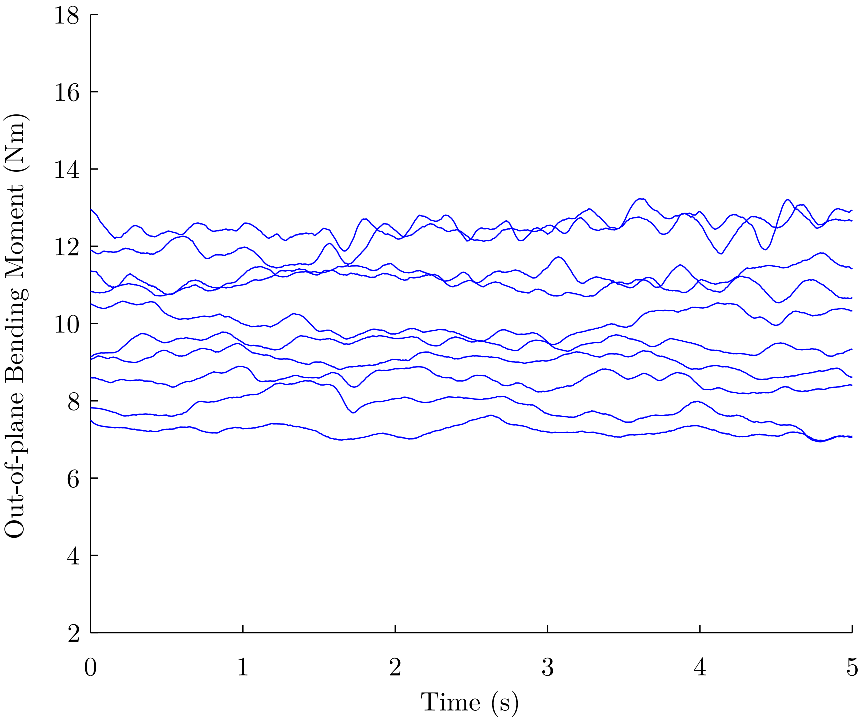

Figure 6.11: Filtered and smoothed out-of-plane bending moment data for TSR range of 4-7.5. No Waves and No Yaw. $U = 0.9m/s$, $z_H = -0.9m$

The effect of yawing the turbine is shown for out-of-plane bending in Figure 6.13 and in-plane bending in Figure 6.14. The load-time data has been manually phase-shifted in order to isolate the loading patterns on the gauged blade. The out-of-plane bending moment on a blade is shown to be effectively sinusoidal (with a 1P frequency component), however the in-plane bending moment is far less sinusoidal. This may mean that the in-plane bending moment is more sensitive to the individual blade position relative to the turbine RPM.

The effect of waves on the turbine is shown for out-of-plane bending in Figure 6.15 and in-plane bending in Figure 6.16. The large waves used in this series of experiments are likely

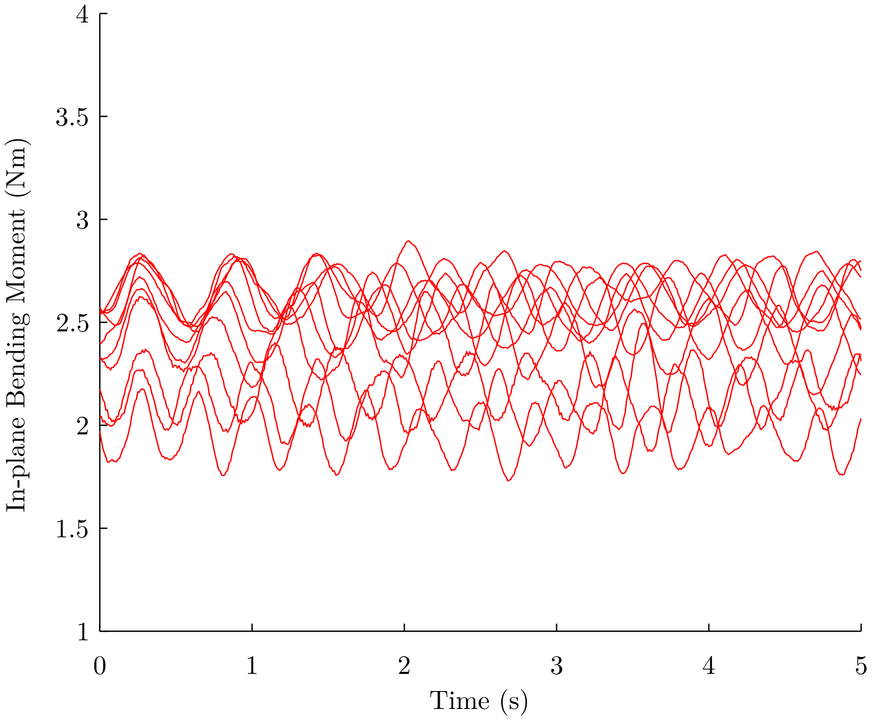

Figure 6.12: Filtered and smoothed in-plane bending moment data for TSR range of 4-7.5. No Waves and No Yaw. $U = 0.9m/s$, $z_H = -0.9m$

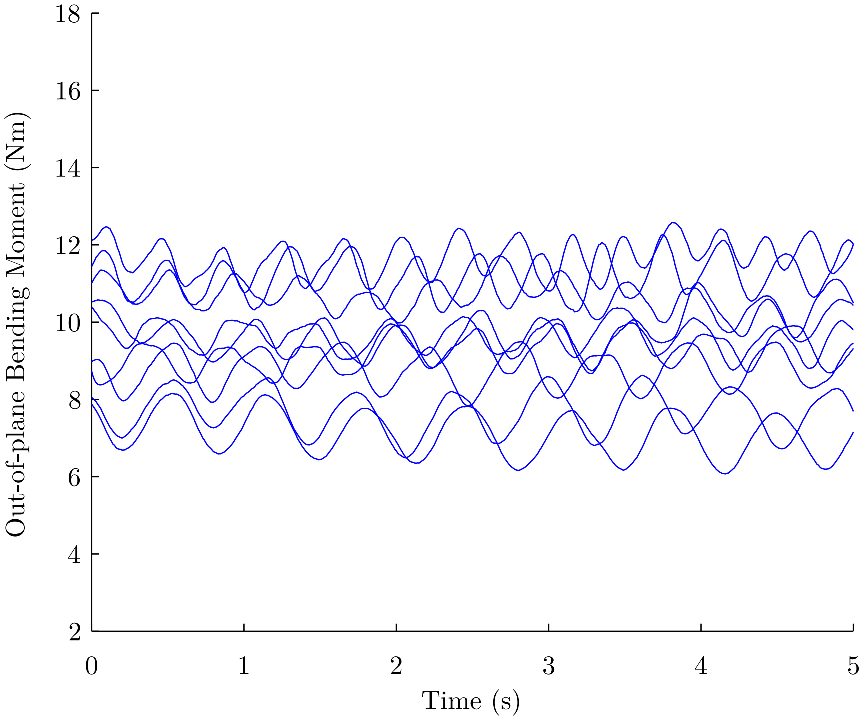

Figure 6.13: Filtered and smoothed out-of-plane bending moment data for TSR range of 4-7.5. No Waves. $U = 0.9m/s$, $z_H = -0.9m$ and $\gamma = 15°$

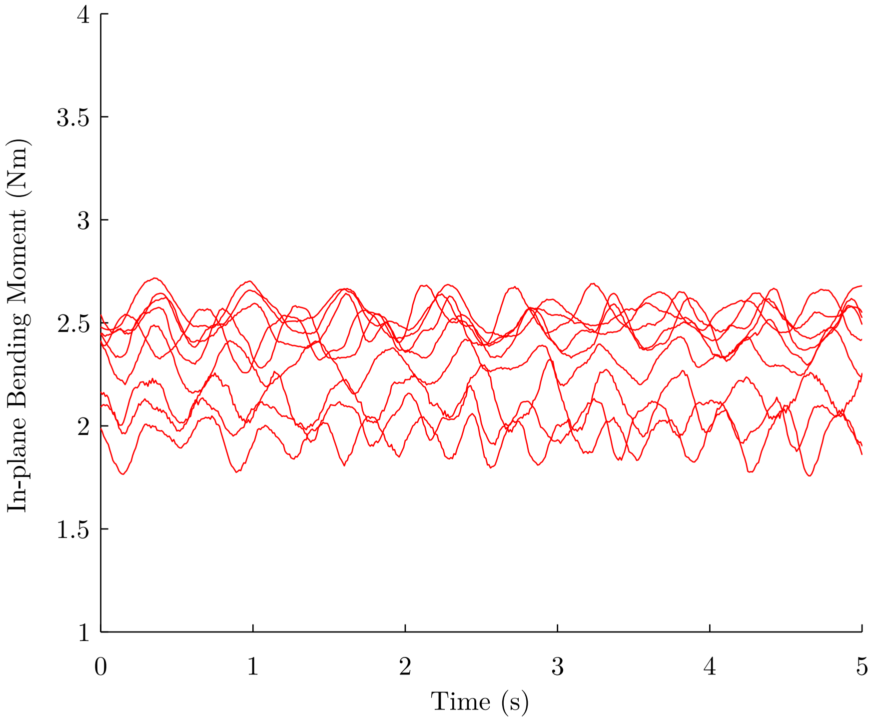

Figure 6.14: Filtered and smoothed in-plane bending moment data for TSR range of 4-7.5. No Waves. $U = 0.9m/s$, $z_H = -0.9m$ and $\gamma = 15°$

to be common in an exposed tidal site. 0.15m in the tank testing equates to 3m at full scale assuming a scale ratio of 1:20. Extreme waves at many sites will be much larger than this as shown by statistical data in ISO (2005), which describes 9.8m significant wave heights in the central North Sea with a return period of just 1 year. The in-plane bending moment shows many small fluctuations of shorter period (higher frequency) than the apparent wave period. This can be attributed to the mass-moment of the blade.

The effect of both waves and yaw on the turbine is shown for out-of-plane bending in Figure 6.17 and in-plane bending in Figure 6.18. The overall loading pattern across the full range of TSRs is dominated by the apparent wave period ($T_a = 1.54s$) and the wave height in these examples. The small fluctuations which can be observed for each TSR can be attributed to both the yawed inflow and the mass-moment of the blade for the in-plane loading. Another factor which cannot be controlled and may affect loading patterns, is the position of the wave crest relative to blade position. Ideally the crest maxima should arrive as the blade tip is vertically up to achieve maximum loading (for at least one of the blade revolutions during a test). This is not possible with the current experimental set-up, but nonetheless may be significant as shown in Section 6.2.4.

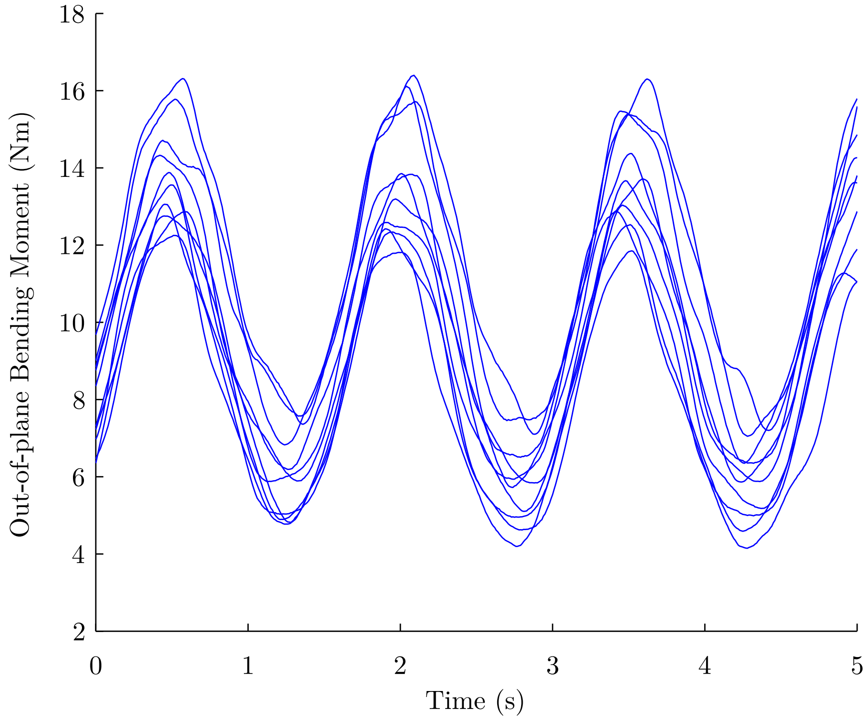

Figure 6.15: Filtered and smoothed out-of-plane bending moment data for TSR range of 4-7.5 $H = 0.15m$, $T_i = 2s$, $U = 0.9m/s$, $z_H = -0.9m$ and $\gamma = 0°$

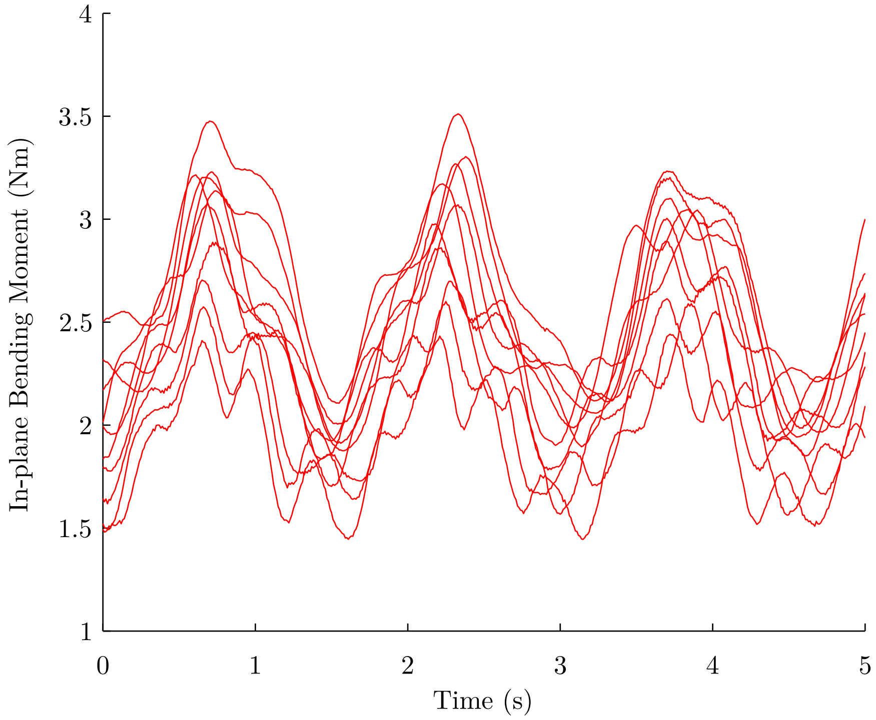

Figure 6.16: Filtered and smoothed in-plane bending moment data for TSR range of 4-7.5 $H = 0.15m$, $T_i = 2s$, $U = 0.9m/s$, $z_H = -0.9m$ and $\gamma = 0°$

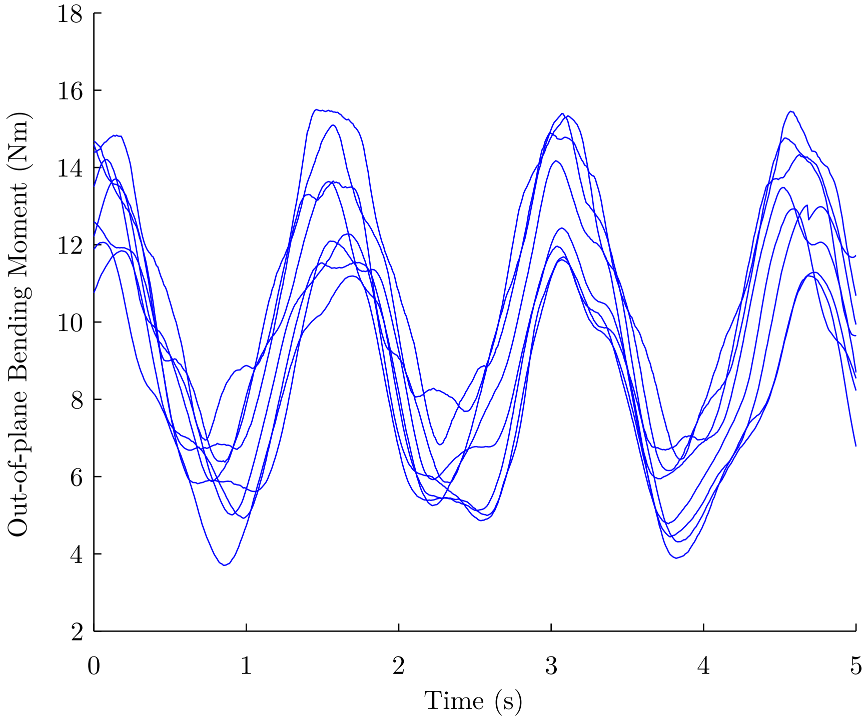

Figure 6.17: Filtered and smoothed out-of-plane bending moment data for TSR range of 4-7.5 $H = 0.15m$, $T_i = 2s$, $U = 0.9m/s$, $z_H = -0.9m$ and $\gamma = 15°$

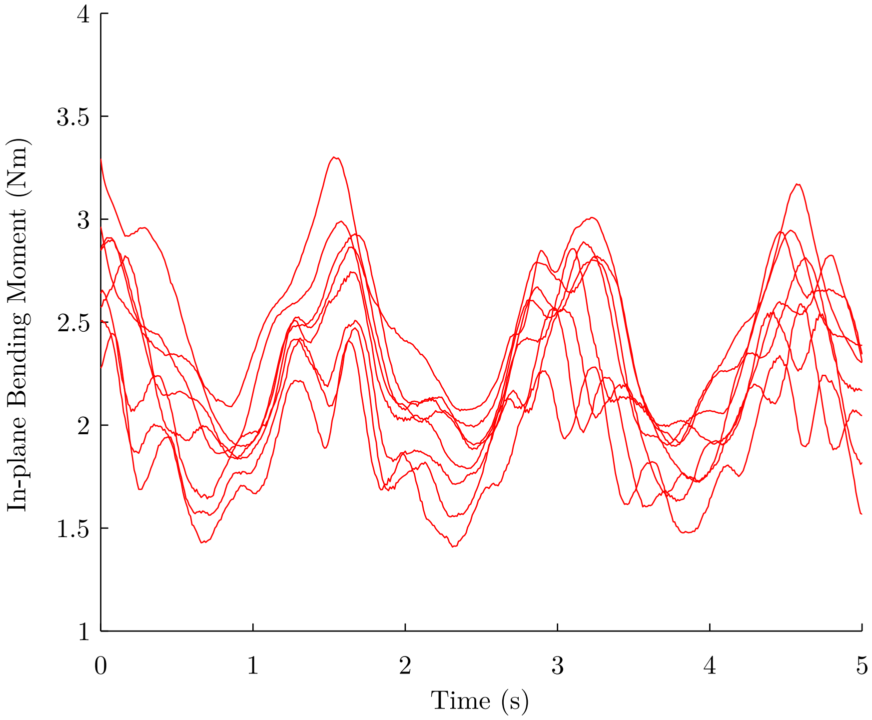

Figure 6.18: Filtered and smoothed in-plane bending moment data for TSR range of 4-7.5 $H = 0.15m$, $T_i = 2s$, $U = 0.9m/s$, $z_H = -0.9m$ and $\gamma = 15°$

Since the wave loading in general appears to be more dominant than the yawed inflow loading, the criteria of importance will be the apparent wave period. The wave period is related to the ratio of the range of $1Ta$ variation and the $1P$ turbine component, as described in Section 2.3. This means that for the towing tank conditions, the ratios will vary as shown in Figure 6.19. Interestingly for Figure 6.17 and Figure 6.18, the ratio is approximately 0.4 resulting in the dominance of the $1T_a$ component. If the ratio was greater than 1, the $1P$ component would dominate, placing more importance on the yaw loading, however this would require relatively short period waves, forcing the wave height to be small or the waves would break. The wave height is proportional to the loading range and has no dependence on the wave period, other than being within the limits for wave breaking i.e. steep waves are possible but exceeding the theoretical limit causes them to break, dissipating their energy ($H/L = 1/7$). This wave breaking creates an unknown loading force of potential significance but is beyond the scope of this research.

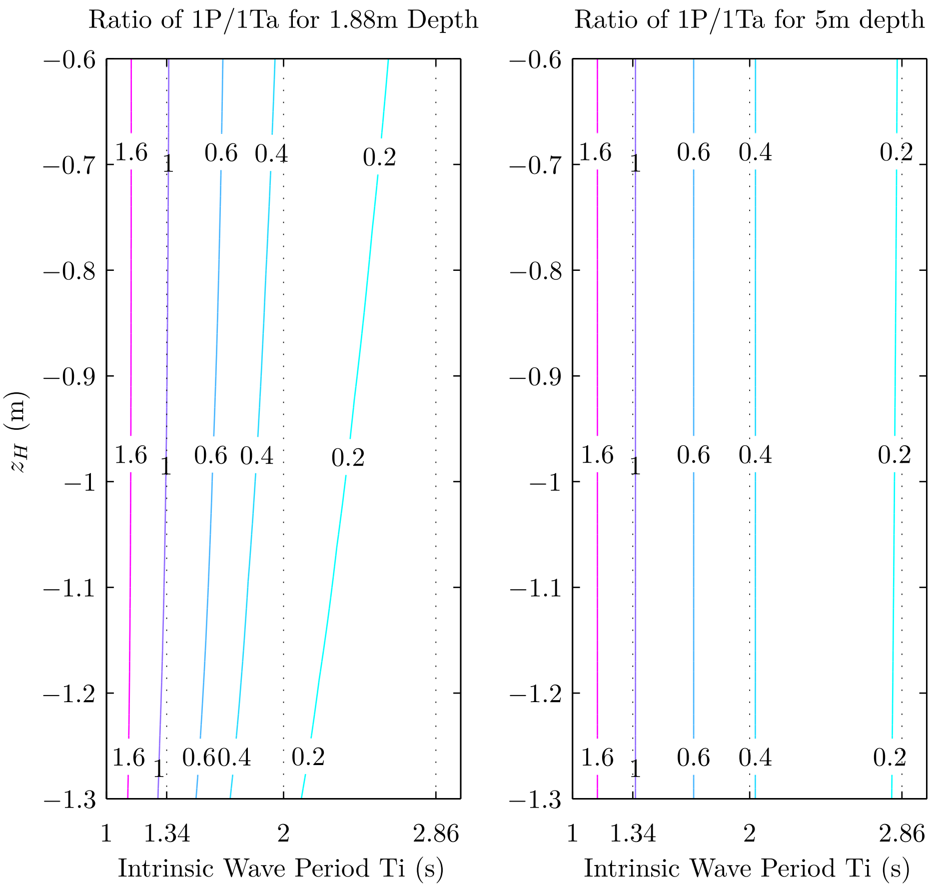

Figure 6.19: Ratio of longitudinal rotational wave induced velocity range (u_{rRange}) to the longitudinal velocity fluctuation range observed at the hub (u_{Range}) as a function of intrinsic period for the towing tank conditions. $r = 1R$, $R = 0.4m$

Setting the ratio equal to 1 places equal dependence on both the $1T_a$ component and the $1P$ component. This creates a much more complex loading pattern due to two equally significant loading components. This can be visualised in the blade loading data in Figure 6.20 and Figure 6.21. Phase-shifting the data finds no discernible loading pattern between the TSRs. This means that from numerical modelling standpoint, the mean/median loading and loading range are likely to be more reliable values than the blade azimuth or the time-domain loads.

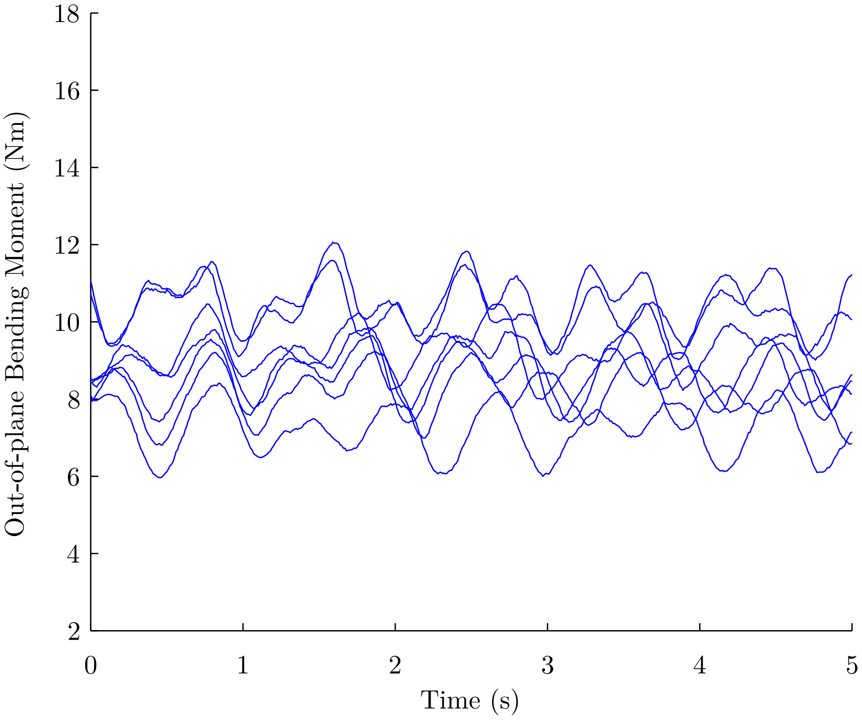

Figure 6.20: Filtered and smoothed out-of-plane bending moment data for TSR range of 4-7.5 $H = 0.08m$, $T_i = 1.33s$, $U = 0.9m/s$, $z_H = -0.9m$ and $\gamma = 15°$

6.4 Average Rotor and Blade Loads

The blade bending moments show very little variation of the median bending moment for an individual TSR across data with different wave and yaw parameters, as shown in Section 6.3. The median is used rather than the mean because it is less sensitive to outliers in the data set. The median out-of-plane bending moment increases with increasing TSR within the experimental range of the turbine (4.0 to 7.5 TSR) due to greater thrust on the rotor. This effect may change at higher blade pitch angles however, with a possible decrease in thrust at higher TSRs. The median in-plane bending moment reduces with increasing TSR over the same operating range. This is again expected since the rotor/shaft torque will reduce with increased TSR. On average

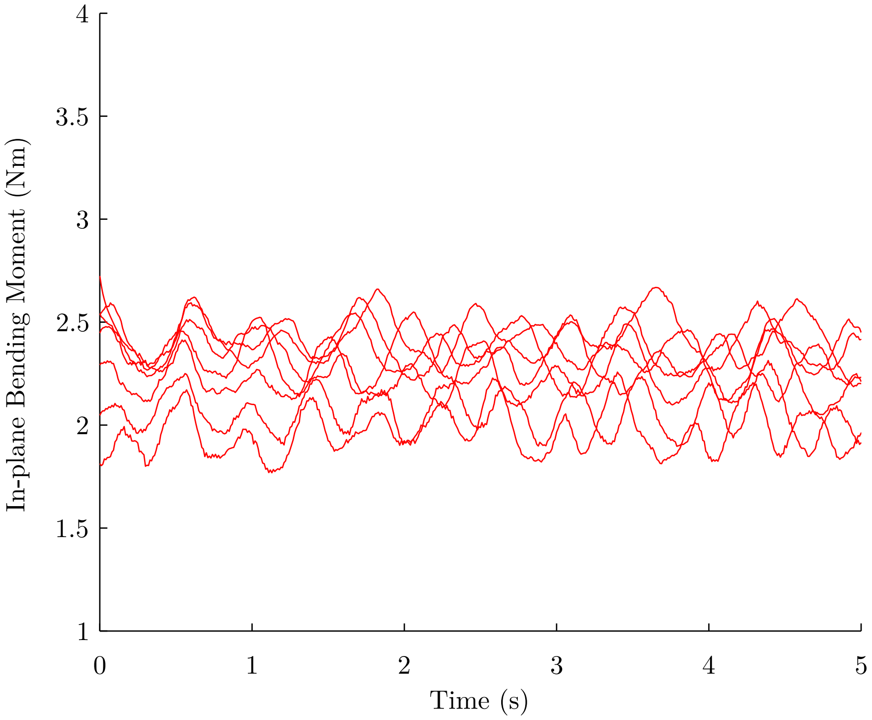

Figure 6.21: Filtered and smoothed in-plane bending moment data for TSR range of 4-7.5 $H = 0.08m$, $T_i = 1.33s$, $U = 0.9m/s$, $z_H = -0.9m$ and $\gamma = 15°$

the out-of-plane load is 4.1 times greater than the in-plane load. This effectively agrees with data derived from Barltrop et al. (2006) that shows a 3.8 times greater out-of-plane to in-plane load average (see Table 6.2). An aspect which has not been covered by Barltrop et al. (2006) is the comparison of instantaneous loads. Within these sets of experiments, instantaneous out-of-plane loading was found to be as much as 9.5 times greater than the in-plane load.

All the experimental data presented in Section 6.3.1 and further experimental data is presented in reduced form as boxplots in Figure 6.22, Figure 6.23 and Figure 6.24. For example, Figure 6.11 is condensed into a single boxplot (No Waves Yaw=0deg Mid-Depth) and can be seen in Figure 6.22.

A more important outcome from the experimental loading data is the range of loading experienced by the blade when looking at wave or yaw effects, rather than the average loading. The larger wave period used in the experiments ($Ti = 2.86s$) resulted in a loading range of 175% of the median out-of-plane load (Figure 6.22) and 100% of the median in-plane load (Figure 6.23). Barltrop et al. (2006) presented results which differ significantly; a loading range of 105% of the median value for out-of-plane bending moments and 250% of the median value for in-plane bending moments. The disparity in the out-of-plane load is likely to be a result of

Bending Direction	T_i (s)	H (m)	U (m/s)	max BM (Nm)	min BM (Nm)	mean BM (Nm)
Out-of-plane	2.0	0.15	0.3	-0.15	-0.75	-0.45
Out-of-plane	2.0	0.15	0.3	1.25	0.60	0.93
Out-of-plane	1.0	0.15	1.0	-0.13	-0.75	-0.44
Out-of-plane	1.0	0.15	1.0	1.20	0.55	0.88
Out-of-plane	0	0	?	0.89	0.89	0.89
In-plane	2.0	0.15	0.3	0.10	-0.30	-0.10
In-plane	2.0	0.15	0.3	0.50	0.00	0.25
In-plane	1.0	0.15	1.0	0.00	-0.25	-0.13
In-plane	1.0	0.15	1.0	0.50	0.00	0.25
In-plane	0	0	?	0.32	0.18	0.25

Table 6.2: Barltrop et al. (2006) data used for comparison (interpreted from graphs)

the different experimental scaling effects (larger waves in relation to the rotor diameter, blade type, Reynolds numbers etc.). The large fluctuation of in-plane bending moment could also be caused by the use of heavier blades relative to those used in these experiments. The maximum blade mass moment used here is 0.4Nm (Figure 5.10) which is approximately 17% of the median in-plane bending moment, unlike Barltrop et al. (2006) whose mass moment approximates 59% (this figure may include added mass effects, albeit these are likely to be negligible, Whelan et al., 2009b). This makes a case for careful investigation of the gravitational/buoyancy loads of full-scale TST blades (see Figure 6.27).

It can be seen that the median of each test run is approximately central to the interquartile loading range (Figure 6.22). This is expected in reality since the waves used are effectively sinusoidal (see Section 7.2), as is the loading effect caused by the yawed inflow. It appears that blade bending moments are affected approximately equally by changes in wave period and wave height. The effect of long wave length/large period waves will probably be exacerbated when the current is flowing in the same direction as the waves, effectively increasing the wavelength. Unfortunately it has not been possible to test this effect due to limitations of the towing carriage at the test facility. Should non-linear waves be encountered this effect is likely to change, probably resulting in a positive median shift due to waves exhibiting shallower troughs and sharper peaks. Barltrop et al. (2005) found that steeper waves impose lower bending moments in both directions about the roots of the rotor blade. This is logical given that there will be a reduced longitudinal velocity component, thus reducing the imposed loads in both planes, providing the waves are of equivalent energies. In order to obtain ultimate loads from Figure 6.22 and Figure 6.23, it would be sensible to use the maximum load (up to 1.5 times the interquartile

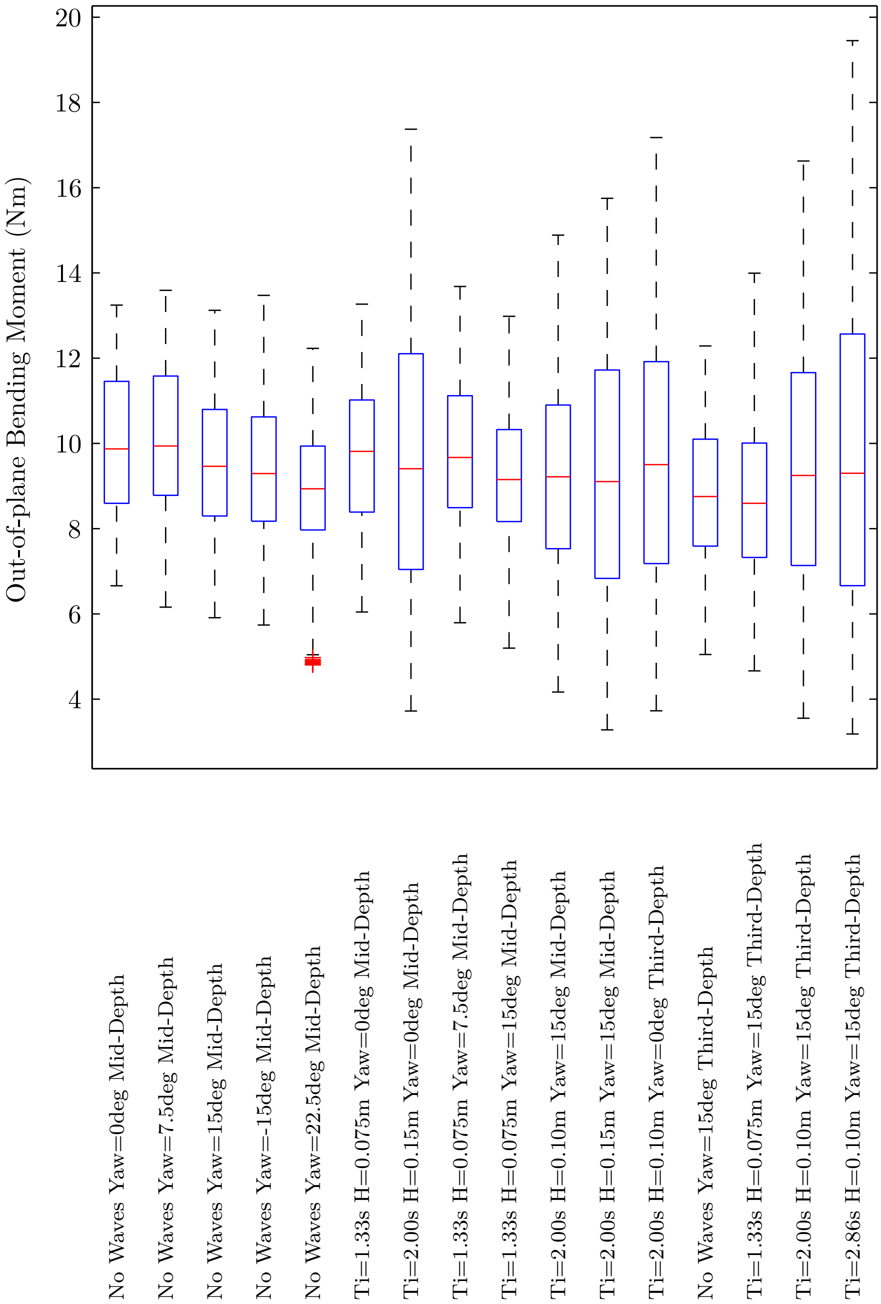

Figure 6.22: Out-of-plane blade root bending moment averages. Each boxplot represents statistics from all the TSRs of a unique test case (labelled). The vertical limits of the box are the interquartile range of the data and the red dividing line is the median of the data. The whiskers extend to the limits of the data (1.5 times the interquartile range) with any red crosses denoting outliers in the data set.

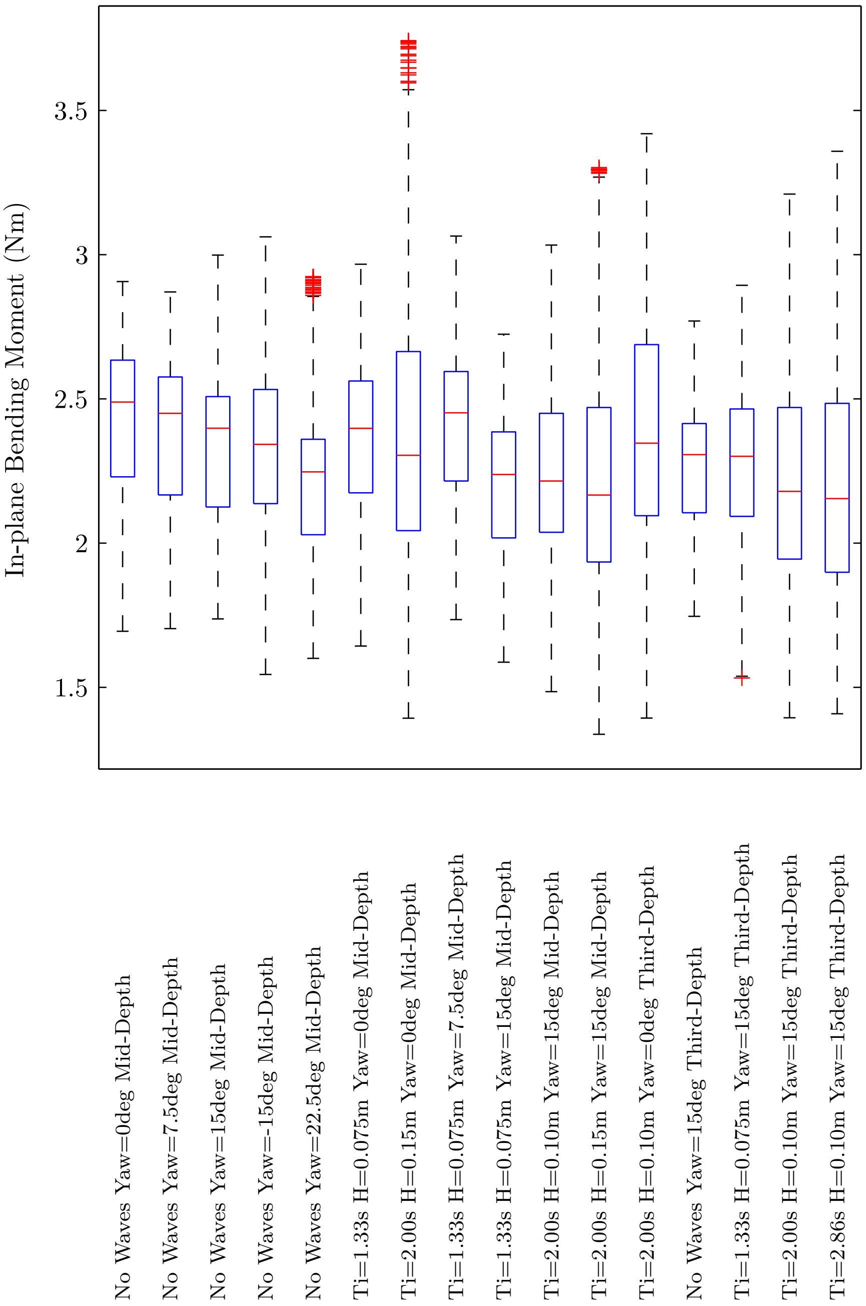

Figure 6.23: In-plane blade root bending moment averages. Each boxplot represents statistics from all the TSRs of a unique test case (labelled). The vertical limits of the box are the interquartile range of the data and the red dividing line is the median of the data. The whiskers extend to the limits of the data (1.5 times the interquartile range) with any red crosses denoting outliers in the data set.

range or 2.7 standard deviations, this will contain all the data up to a 98% confidence limit). Where the data exceeds the whiskers, as shown by crosses, it should be considered erroneous. In reality a factor of safety would be applied to any structural design.

When a turbine rotor is yawed to the flow, both median rotor torque (power) and median thrust are reduced, with an approximate 20% power reduction at 22.5° yaw (Galloway et al., 2010). Loading across the whole rotor when in yawed flow also reduces the interquartile range of loading, but the ultimate loading range remains unchanged (Figure 6.24). Interestingly, yaw loading on the rotor sees a positive skew for median thrust and a negative skew for median torque, an effect which is not readily apparent in the individual blade loading data. One could argue that in terms of ultimate loads, yaw has a negligible effect in comparison to waves. Wave loading is more difficult to quantify on the rotor, where it appears that reducing the depth of rotor immersion (see Figure 5.3 for tested immersion depths), increases the range of loading but both decreases and increases the median load. This is contrary to the expected constant median load with changing rotor immersion. This effect is replicated slightly in Figure 6.22 and Figure 6.23 and could be attributed to a reduced pressure across the turbine disc combined with a deformation of the streamtube if it begins to interact with the water surface boundary.

In order to better understand the loading effect of waves and yaw, the out-of-plane and in-plane bending was presented in the blade azimuth domain. Figure 6.25 shows data for a single towed run, with each line showing the loading experienced over a single blade revolution and how the bending moment is affected by waves and yaw. For the out-of-plane bending moment the range is not constant throughout the rotational cycle, there is a slight increase in the region of 225 degrees. This is due to the yawed flow creating an additional bending moment oscillation of once-per-revolution (1P). The in-plane bending moment case is more complicated with the inclusion of the gravitational component (Figure 6.26). The range is now no longer constant with a minimum bending moment at 180 degree location. It should be noted here that tower influence (pressure change upstream of the tower) is unlikely to be a factor in these experiments since the tower is situated almost one diameter (0.8m) downstream of the rotor plane at 0.7m. This is only likely to be important for rotors mounted downstream/close to any supporting structure.

Figure 6.27 reproduces Figure 6.25, binning the data every 8 degrees. This was done to show more clearly how the loading varies when the dynamic effects have been averaged. It is now more evident how the 15° yaw influences the out-of-plane bending moment resulting in a

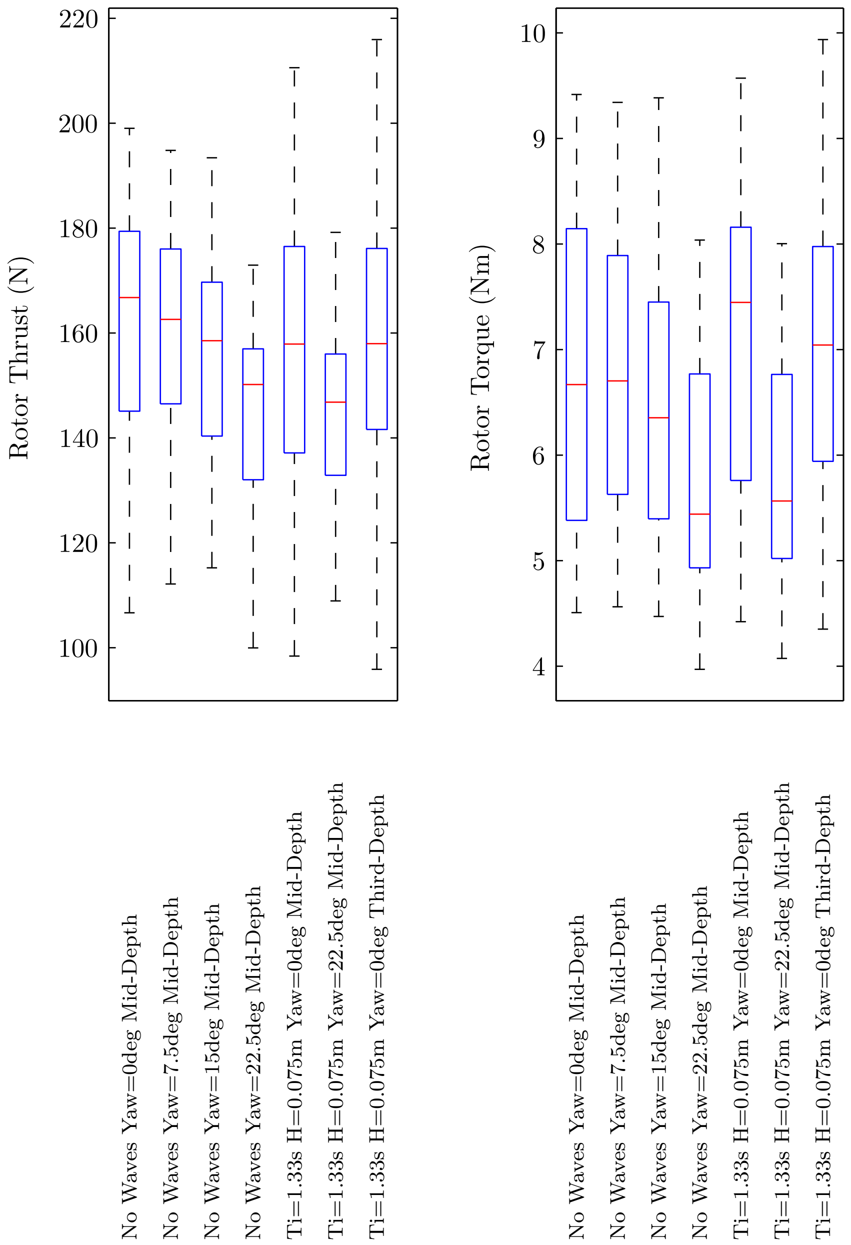

Figure 6.24: Full rotor thrust and torque averages. Each boxplot represents statistics from all the TSRs of a unique test case (labelled). The vertical limits of the box are the interquartile range of the data and the red dividing line is the median of the data. The whiskers extend to the limits of the data (1.5 times the interquartile range) with any red crosses denoting outliers in the data set.

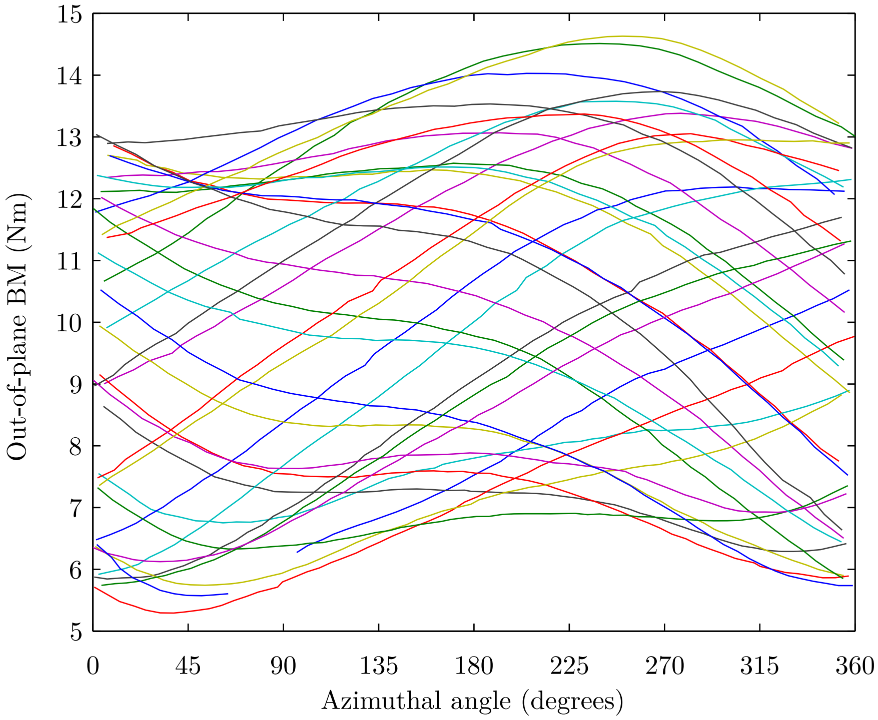

Figure 6.25: Measured out-of-plane blade root bending moments for a single turbine blade during a single towed run. $H = 0.1m$, $T_i = 2s$, $U = 0.9m/s$, $\gamma = 15°$, TSR $= 5.7$ and $z_H = -0.67m$. Each line denotes a full blade revolution

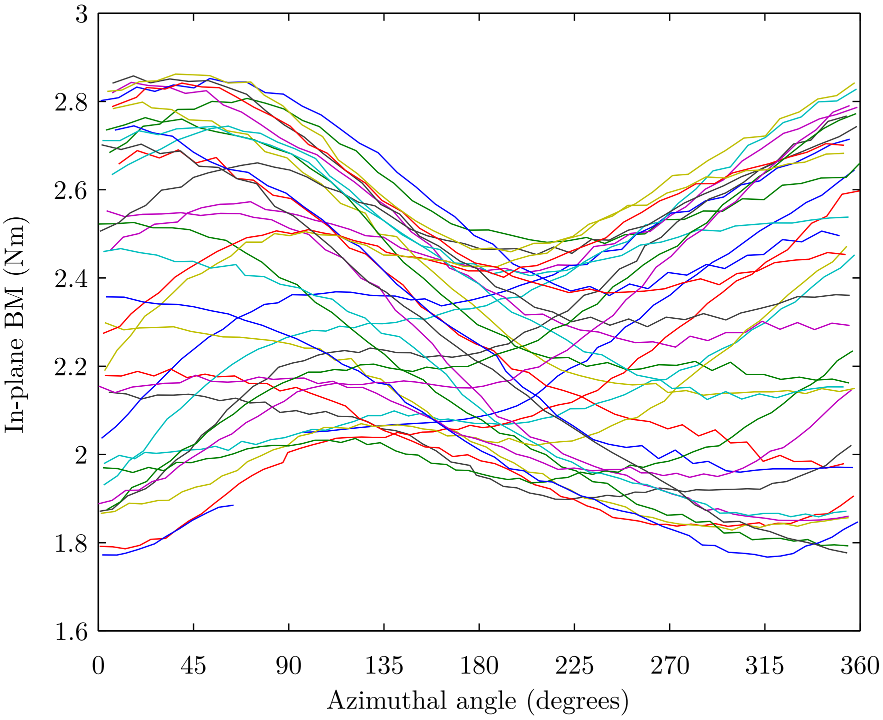

Figure 6.26: Measured in-plane blade root bending moments for a single turbine blade during a single towed run. $H = 0.1m$, $T_i = 2s$, $U = 0.9m/s$, $\gamma = 15°$, TSR $= 5.7$ and $z_H = -0.67m$. Each line denotes a full blade revolution

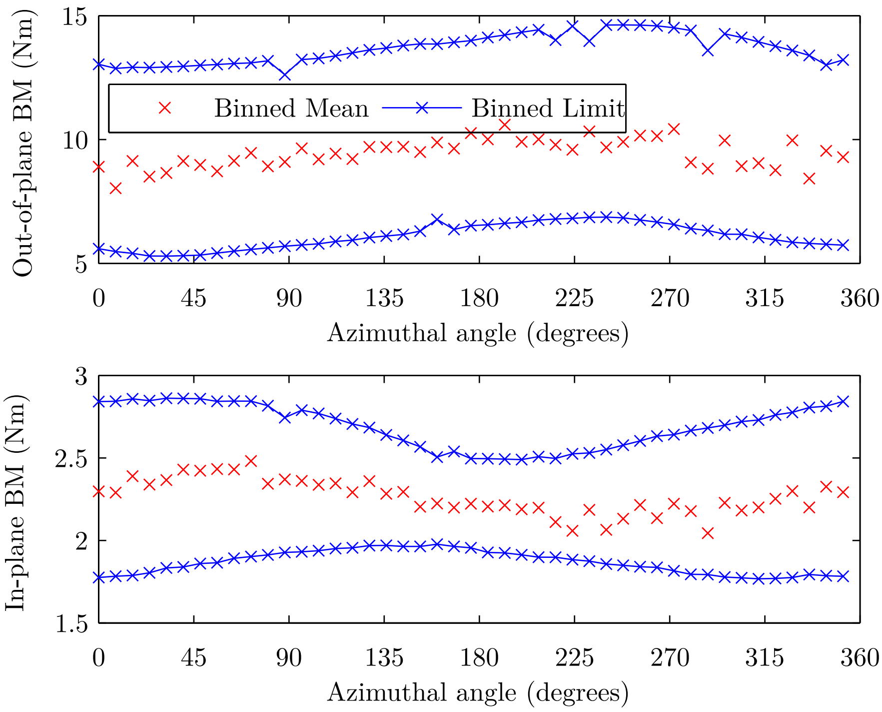

Figure 6.27: Azimuth binned blade root bending moments every 8°. (see Figure 6.26 for testing parameters)

1P oscillation with maximum load at 225° and minimum load at 45°. The wave-depth effects can be observed from the in-plane bending moments due to the maximum range occurring at 0° (blade up) and the minimum occurring at 180° (blade down). The gravitational component influences the in-plane bending moment and is evident from the in-plane bending moment data, with maximum and minimum loads occurring at approximately 90° and 270° respectively.

6.5 Summary of Experimental Results

The quality and repeatability of the experiments has led to several important quantitative and qualitative results:

- The median out-of-plane root bending moment is, on average, 4.1 times greater than the in-plane blade root bending moment for waves and yawed conditions.
- The out-of-plane bending moment has been shown to be as much as 9.5 times the in-plane bending moment (for a full-scale wave period of 12.8s). A maximum loading range of 175% of the median out-of-plane bending moment and 100% of the median in-plane bending moment was observed for this test case.

- The gravitational/buoyancy component of a blade can be significant to the in-plane blade root bending moment
- The apparent wave period was found to be equally significant to the wave height in terms of loading range of a blade
- Steady nacelle yaw loading on an individual blade is negligible in comparison to wave loading
- Steady nacelle yaw will reduce total
- rotor power capture and mean rotor thrust loading. Below 7.5° the reduction in power/thrust is, however, negligible
- Reduced hub depth may lead to interaction with the water surface boundary, leading to uncharacteristic rotor/blade loads. There will be a complex relationship between the modified turbine streamtube, possibly resulting in reduced thrust loads and increased wave loading due to surface proximity

Chapter 7

Comparative Modelling

7.1 BEM Numerical Model

The modified BEM model uses equations from Chapter 4 along with those from Chapter 3 to approximate the various hydrodynamic velocities and loads experienced by the turbine blades. NACA 48XX blades of varying twist and chord-thickness ratio were used, whose geometry is described in Figure 7.1. Using two-dimensional lift and drag data obtained from Xfoil (Drela and Youngren, 2001) for the correct scaled blade Reynolds number (Appendix A), it was possible to extrapolate the lift and drag coefficients over the full range of angles of attack of a blade (Figure 7.2). This was considered important since extreme angles of attack are experienced during code iteration, particularly at low TSRs. A flow diagram showing the process modules used in the code is shown in Figure 4.4. Since waves and rotor misalignment were included in the model, the velocity seen at each blade, at an individual time instant, is different. This required all three blades to be modelled for a more accurate prediction of the rotor effects. Surface plots in Figure 7.3 have been included to show how the axial inflow factor and the angle of attack vary over ten blade revolutions for one of the blades and the corresponding coefficients of lift and drag which directly affect the forces on the blades and rotor. The overall range in which the variables change is effectively the same for each blade. This is a useful result if the aim is to test individual blade characteristics, however all blades must be modelled in order to obtain a more accurate, time-domain model of total rotor thrust and torque/power.

The inclusion of the dynamic stall model by Tarzanin (1971), as described in Section 2.6 has been shown to have a negligible effect on the hydrodynamics of a blade. Whilst the dynamic angle of attack has an increased range in variation and a time delay component (Figure 7.4),

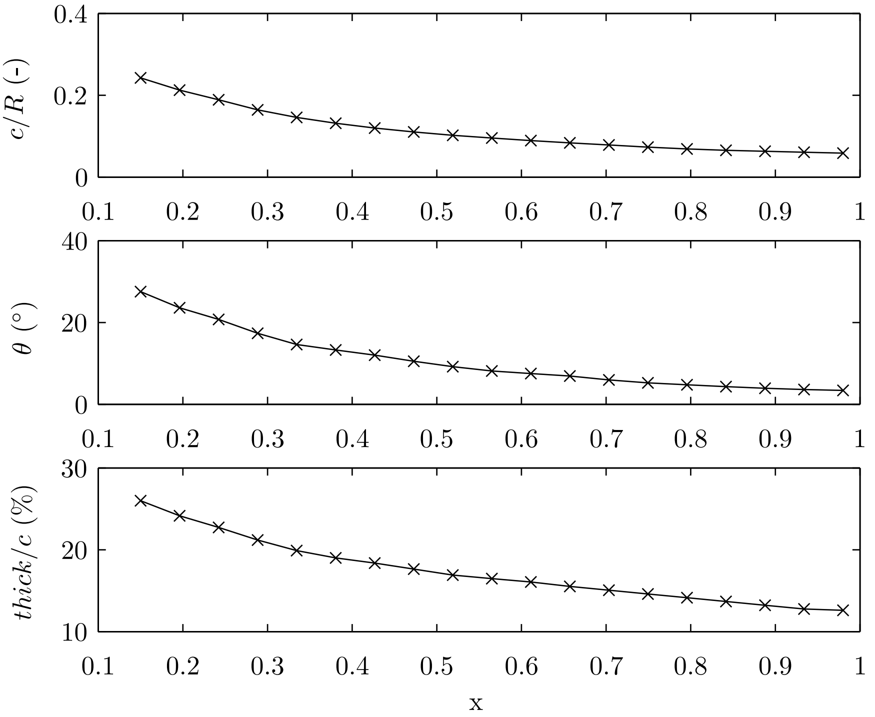

Figure 7.1: NACA 48XX blade geometry. c/R is chord to length ratio, θ is blade twist angle and t/c is thickness to chord ratio

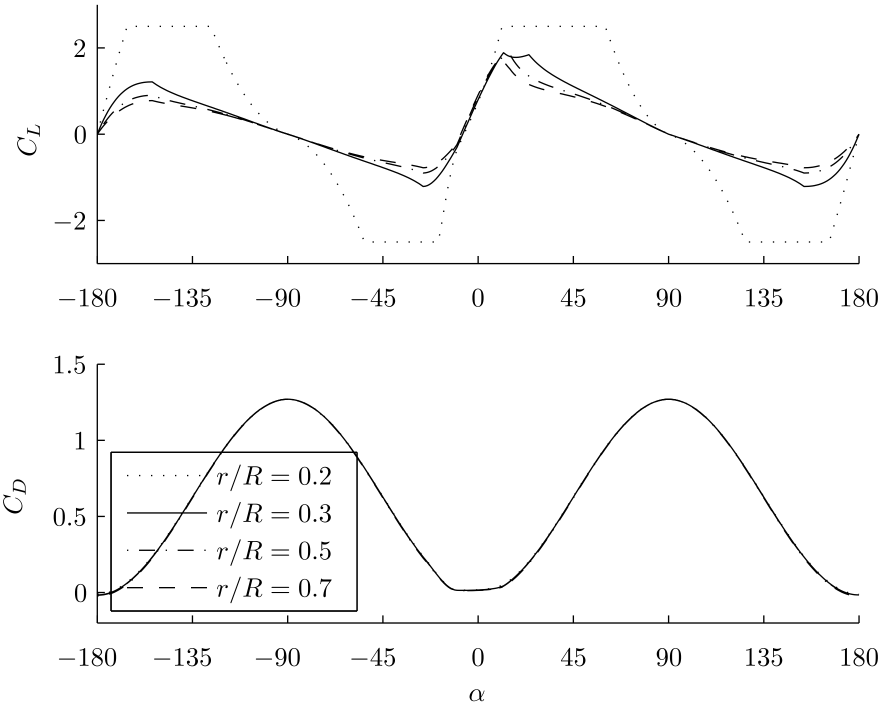

Figure 7.2: Hydrodynamic lift and drag coefficients extended to all possible angles of attack for NACA48XX blade. r/R is the dimensionless blade radius, x

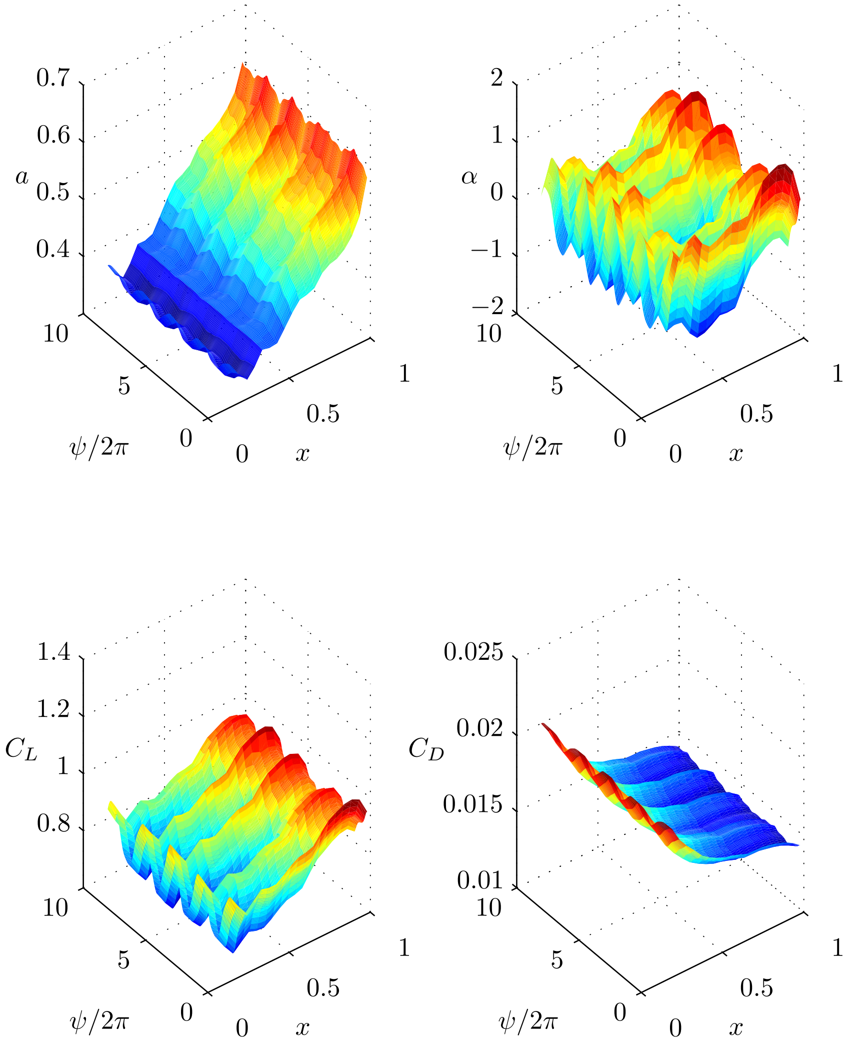

Figure 7.3: BEM variables (a, α, C_L C_D) shown as surface plots over blade length (x) and blade rotations ($\psi/2\pi$). $H = 0.08m$, $T_i = 1.33s$, $\gamma = 15°$, mean TSR $= 7.0$ and $z_H = -0.67m$

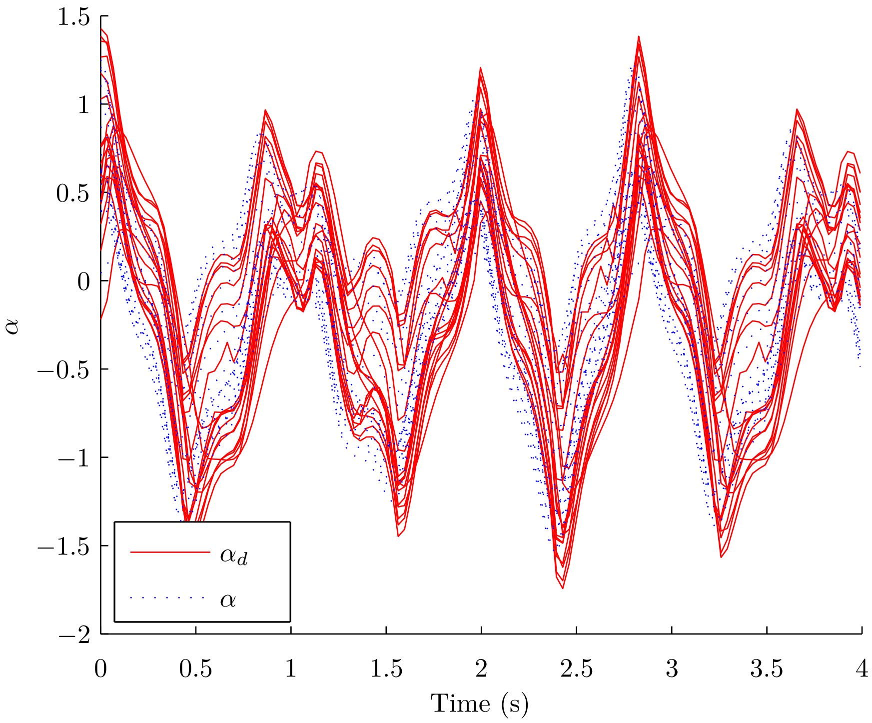

Figure 7.4: Dynamic angle of attack (α_d) alongside normal angle of attack (α). $H = 0.08m$, $T_i = 1.33s$, $\gamma = 15°$, mean TSR = 7.0 and $z_H = -0.67m$. Each line represents a blade element position

this has no effect on the dynamic coefficient of lift (Figure 7.5). This result is likely due to the fact that dynamic stall is not a significant effect for TST blades during normal operation. Dynamic stall is likely to be most significant in turbulent flow conditions as well as steep wave environments with the inclusion of misaligned flow since this will result in the greatest range and rapid changes in blade angle of attack. In reality it seems more important to include the effect of dynamic inflow rather than dynamic stall, as shown by the comparison in Figure 7.7. A possible reason for dynamic inflow being a dominant effect in the results may be due to the low Reynolds numbers in the experiments. It is postulated that this may lead to greater inertial rotor/blade effects than would otherwise be expected due to low turbulence in the flow.

The modified BEM model had been compared to the FAST model (described in Section 4.5) and experimental data as shown in Figure 7.6, both with and without dynamic inflow. It is clear that none of the models come close to adequately predicting the blade root bending moments, although the mean loading is good for both modified BEM models. It transpires that the many corrections applied to BEM theory, to correct what it is simply not designed to do, interfere with each other. This is a particularly difficult case since the ratio of $1T_a$ and $1P$ components is equal to one. The result is an incorrect load amplitude in proportion to the $1P$ variation

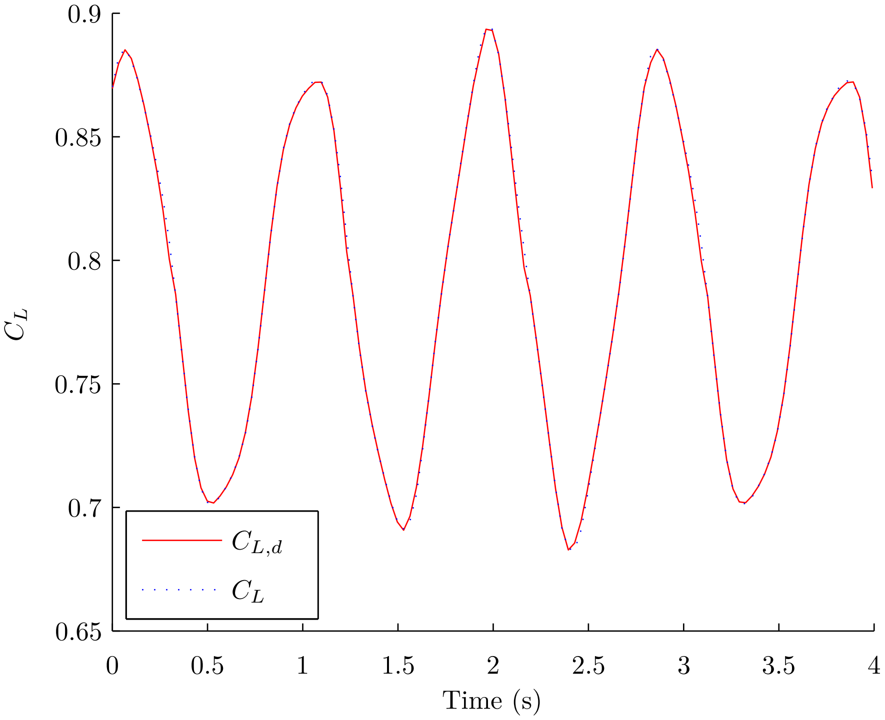

Figure 7.5: Dynamic coefficient of lift ($C_{L,d}$) alongside normal coefficient of lift (C_L), note there is no change, indicating no dynamic stall. $H = 0.08m$, $T_i = 1.33s$, $\gamma = 15°$, mean TSR = 7.0 and $z_H = -0.67m$. Each line represents a blade element position

(and $1T_a$ in this case). Re-running the same comparison, with the skewed axial inflow correction disabled (Equation 4.3) results in a significantly better load prediction as seen in Figure 7.7. It is thought that correcting the relative inflow velocities to the blades is sufficient without the need to correct the axial inflow factors because these are recalculated during the iterative process. Further research will be required to determine whether the remaining discrepancies are caused by a lack of correction for skewed axial inflow. It is possible that a new empirical skewed axial inflow correction is needed, which can function alongside the other model inclusions. The current model retains the use of the skewed axial inflow correction for situations when there are no waves present.

7.2 Model Verification with Experimental Coefficients

No numerical model can be considered complete without some verification prior to its validation. In the case of BEM theory, experimental data verification is invariably the most appropriate method since any other computational techniques have their own issues. Verifying a complex model in the time-domain is subject to many irregularities therefore a logical solution is to begin

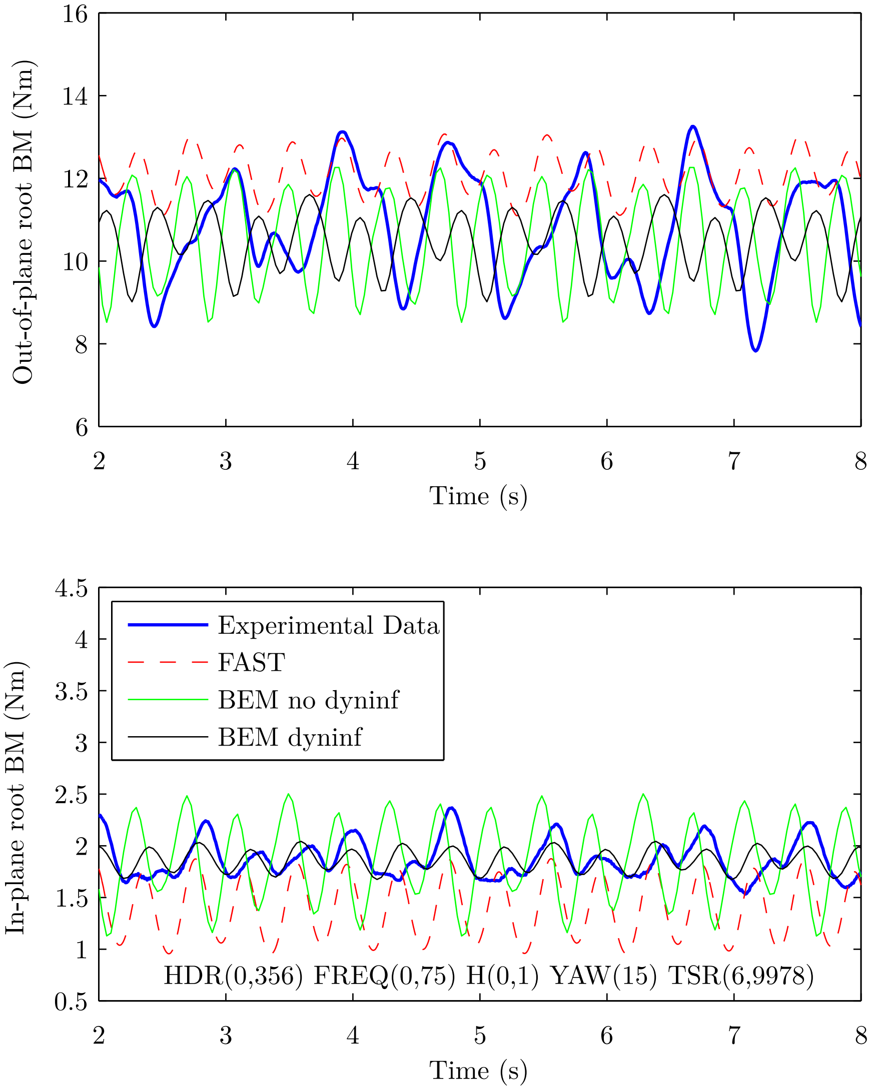

Figure 7.6: Comparing experimental data with FAST and modified BEM, note the poor load prediction in all cases due to exaggerated $1P$ loading. $H = 0.08m$, $T_i = 1.33s$, $\gamma = 15°$, mean TSR $= 7.0$ and $z_H = -0.67m$

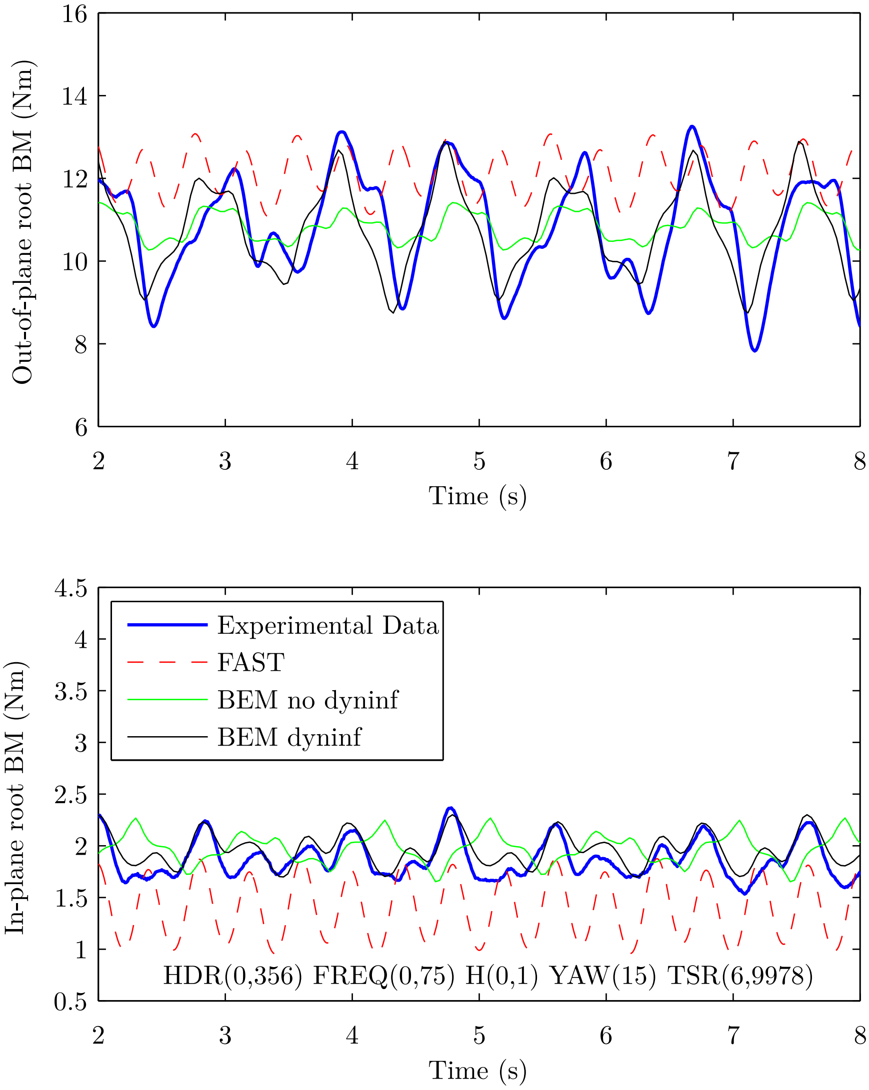

Figure 7.7: Comparing experimental data with FAST and modified BEM, note the dramatic improvement in the BEM predictions compared to Figure 7.6. $H = 0.08m$, $T_i = 1.33s$, $\gamma = 15°$, mean TSR $= 7.0$ and $z_H = -0.67m$

with the use of dimensionless coefficients, obtained by averaging a set of repeat experimental runs. The coefficients used depend on TSR, nacelle yaw angle and blade pitch angle. They remain mostly unaffected by waves since the waves used in the experiments are sinusoidal (effectively no non-linearities) and the wave particle velocities are always a small percentage of the current velocity. The coefficients all contain a squared or cubed component of the total velocity, the mean of which equates to $U + \frac{1}{2}u_a^2$. The assumption is that the $\frac{1}{2}u_a^2$ term is negligible when U is an order of magnitude greater, which is the case in these experiments (see Figure 4.2, ensuring to further divide the ratios by 2). The greater this ratio, the more load the turbine will experience on average, and theoretically deliver more power, although this will depend on the control system. The experimental coefficients are all calculated as a ratio of the measured variable divided by its theoretical maximum e.g.:

$$C_P = \frac{Power}{\frac{1}{2}\rho A U^3}$$

The numerical equivalent is calculated from the theory based on the initial coefficients of lift and drag as shown in Equation 4.6 and requires integrating along the blade and azimuthal values to determine the average coefficient. Blade designs are generally compared in terms of their coefficients of power and thrust against TSR, resulting in a non-dimensionalised plot, a useful feature when scaling a TST. The values of the coefficients are obtained by integrating the corresponding blade element values along the blade length and then integrating azimuthally. Essentially they can be seen as average power and thrust here since they are time independent. Figure 7.8 shows power and thrust curves for the NACA 48XX blades used in these experiments. In general, at low TSRs the code struggles to converge near the root of the blade (TSR < 4). This is due to a breakdown of the theory and is a common feature of BEM codes. At high TSRs the code relies heavily on empirical corrections for high axial inflow factors, which is a source of error if the empirical correction is not matched to the blade type. It is clear from the figure that the modified BEM code provides very good agreement of the results around the optimum TSR region, however the code struggles towards the extremities when matched against the experimental coefficients. This is unlikely to be a problem because a TST will be operated as near to the optimum TSR as possible for maximum power extraction. The model was verified against further published data by Bahaj et al. (2005), who used NACA 63-8XX blades in a towing tank. Figure 7.9 shows the coefficients from these different experiments with

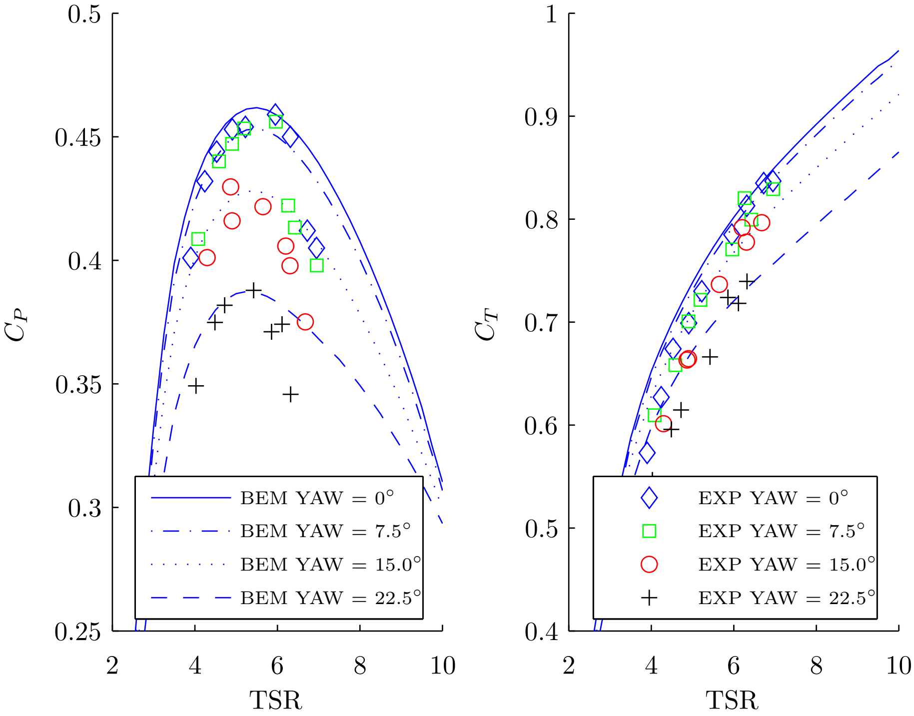

Figure 7.8: C_P and C_T BEM predictions plotted with experimental data points for NACA 48XX

new blade geometry and coefficients of lift and drag inputs for the BEM code. The turbine in this experiment was able to operate at higher TSRs than the model used herein due to the use of a higher towing speed ($1.4ms^{-1}$ as opposed to $0.9ms^{-1}$) resulting in better hydrodynamics across the blades (higher blade Reynolds number). This does make the full-scale flow speed (assuming 1:20 scale) somewhat high at $6.3m/s$ compared to a more realistic $4.0m/s$ used for the present research. There is a clear discrepancy between the model and experiment for the coefficients of thrust of the NACA 63-8XX blade. A fixed blade pitch angle of 5° was used in the BEM model as stated by Bahaj et al. (2005), however it is possible that the pitch setting in the experiment was slightly lower at 4°, resulting in much better agreement, as shown in Figure 7.9. There is basically no change in the coefficient of power, however the change in blade thrust is significant. The NACA 48XX blades were pinned in the hub at the exact pitch angle required, preventing any blade pitch error.

The towing tank data generally shows a reasonably large scatter in results, mainly due to the brief time window available for measurements. The predictions from both experiments demonstrate general agreement for TSRs of 4.5–6.5 for all cases of the coefficient of power. The closest agreement was found at the highest value of power coefficient, showing that steady yaw is only significant above 7.5° with an approximate 20% power reduction at 22.5° yaw (optimum

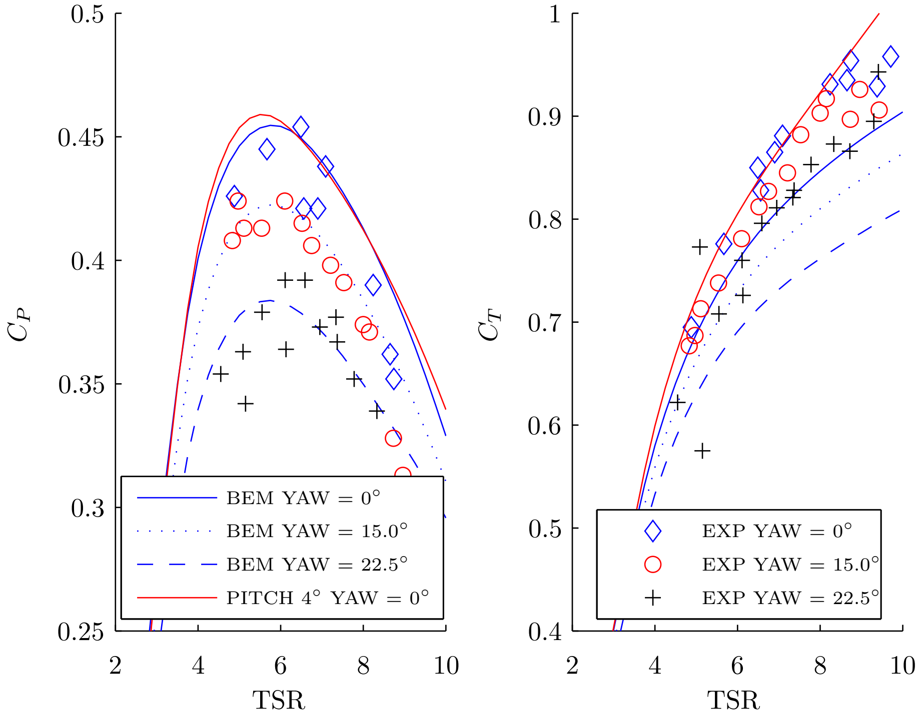

Figure 7.9: C_P and C_T BEM predictions plotted with experimental data points for NACA 63-8XX (Bahaj et al., 2005)

TSR of 6). When a turbine is yawed to the flow, both mean power and thrust are reduced as shown by the experimental coefficients. Comparing the coefficients of thrust is difficult however, because Figure 7.8 under predicts thrust at low TSR, whilst Figure 7.9 over predicts thrust if the pitch angle of 5° is assumed correct.

On the whole, it has been shown that the modified BEM code provides a reasonably good prediction of thrust and torque, but this does not infer that that the prediction of blade root bending moments will be accurate. In order to verify that this was the case, the root bending moment coefficients were calculated from experimental runs and compared against the BEM code shown in Figure 7.10 and Figure 7.11 for out-of-plane (C_{MY}) and in-plane (C_{MX}) blade root bending moments respectively. All the experimental coefficients have been presented with the predicted yaw coefficients from the BEM model. TSRs of 4-5.5 show good agreement with the model, however the model under-predicts the bending moment coefficients for TSRs of 5.5-7.5. The agreement of the model with the experimental coefficients is considered acceptable and permits further prediction of loads in the time-domain.

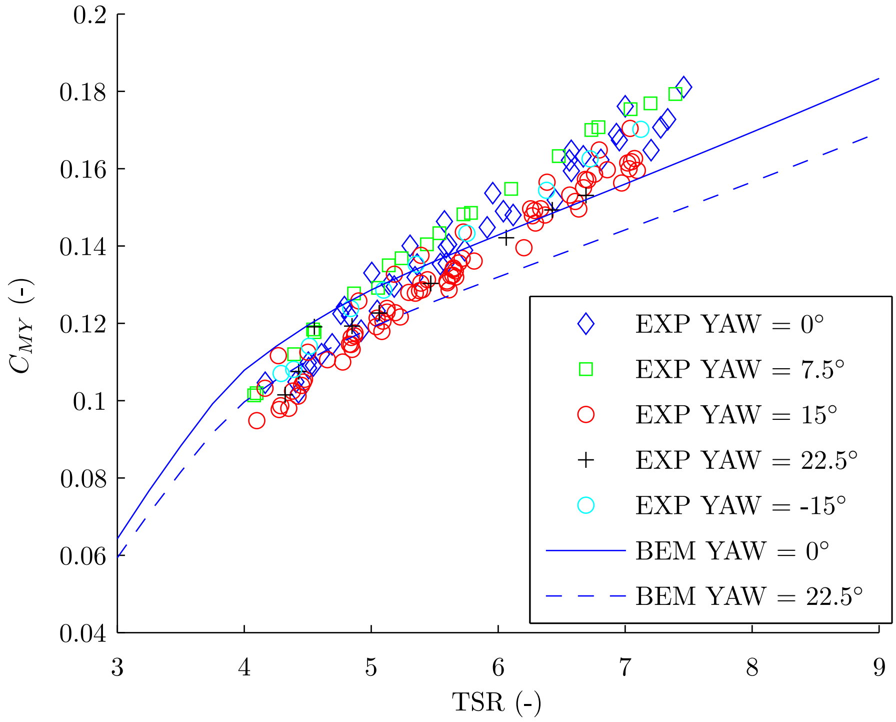

Figure 7.10: C_{MY} BEM predictions plotted with experimental data points for NACA 48XX

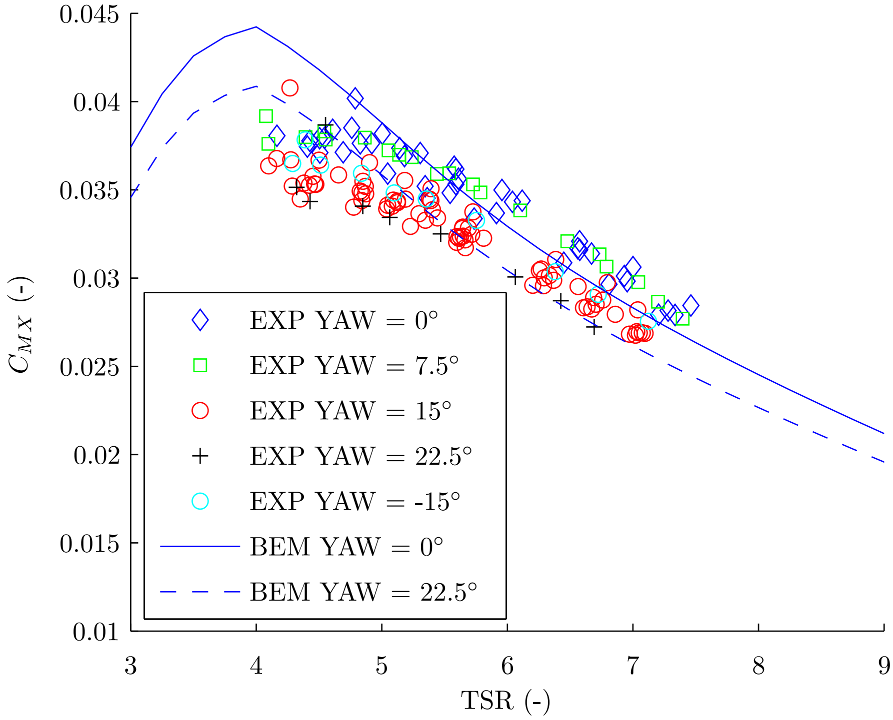

Figure 7.11: C_{MX} BEM predictions plotted with experimental data points for NACA 48XX

7.3 Time-Series Comparison of Numerical and Experimental Data

The experimental blade root bending moment data from the towing tank experiments was compared to the modified BEM code and to FAST (Jonkman, 2012) (both are described in Chapter 4). The conditions modelled experimentally and numerically have been chosen to be representative of full-scale moderate-extreme conditions. Assuming a scaling factor of 1:20; the full-scale depth is 36m, rotor diameter 16m, maximum wave height is 3m and maximum wave period is 12.8s. The results in this section all use the same axes limits for added clarity when comparing the results.

7.3.1 Waves Only

Figure 7.12 shows good agreement between the experiment and the modified BEM model for a case with relatively large waves (no yaw). The slight over estimation of the in-plane bending moment can be attributed to less precise numerical prediction at lower values of TSR (see Figure 7.11). FAST agrees well with the in-plane bending moment but struggles to predict the out-of-plane bending moment. This may be due to the dynamic inflow model used in FAST being inapplicable for the case of a TST. The periodic load fluctuations are very well represented by both numerical models. The amplitude fluctuations are well predicted in the BEM code but are significantly under-predicted in the out-of-plane case and over-predicted in the in-plane case. In addition, the median load prediction of FAST does not agree favourably. These discrepancies emphasise the danger of using wind turbine specific codes for dynamic TST load prediction.

7.3.2 Yaw Only

Figure 7.13 shows the turbine nacelle yawed at 15° to the incoming flow field, with no waves. Whilst the yaw misalignment is relatively high, the load fluctuations are comparatively small when compared against those in Figure 7.12. Again the load predictions from the BEM model are closer than those of FAST. Both the numerical models have the same periodic component, which interestingly goes out of phase with the experimental loads. This happens more quickly for the in-plane loads, signifying greater non-linearity than out-of-plane. This effect may be one of the reasons that the skewed axial inflow correction is really only suitable for a simple steady yaw case such as this, with no inclusion of waves (see Section 7.1).

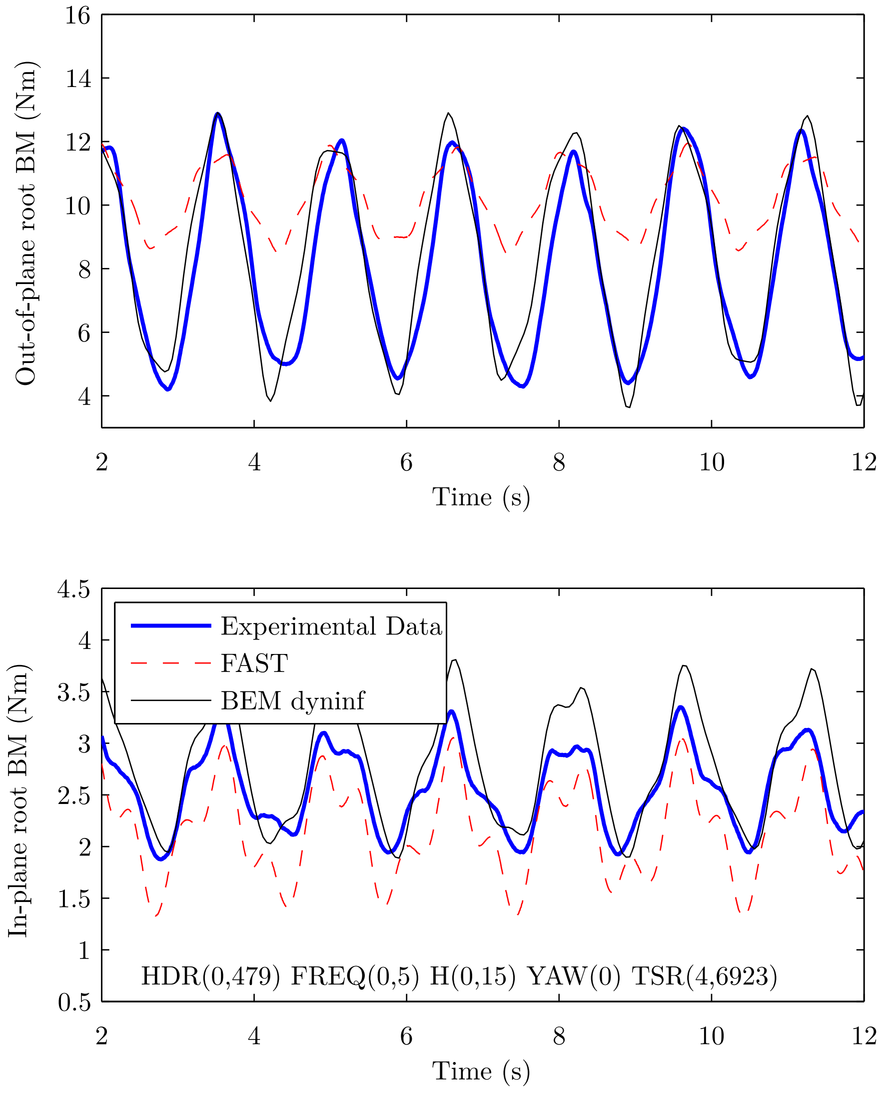

Figure 7.12: Comparing time-series experimental data with FAST and modified BEM. $H = 0.15m$, $T_i = 2s$, $\gamma = 0°$, mean TSR = 4.7 and $z_H = -0.9m$

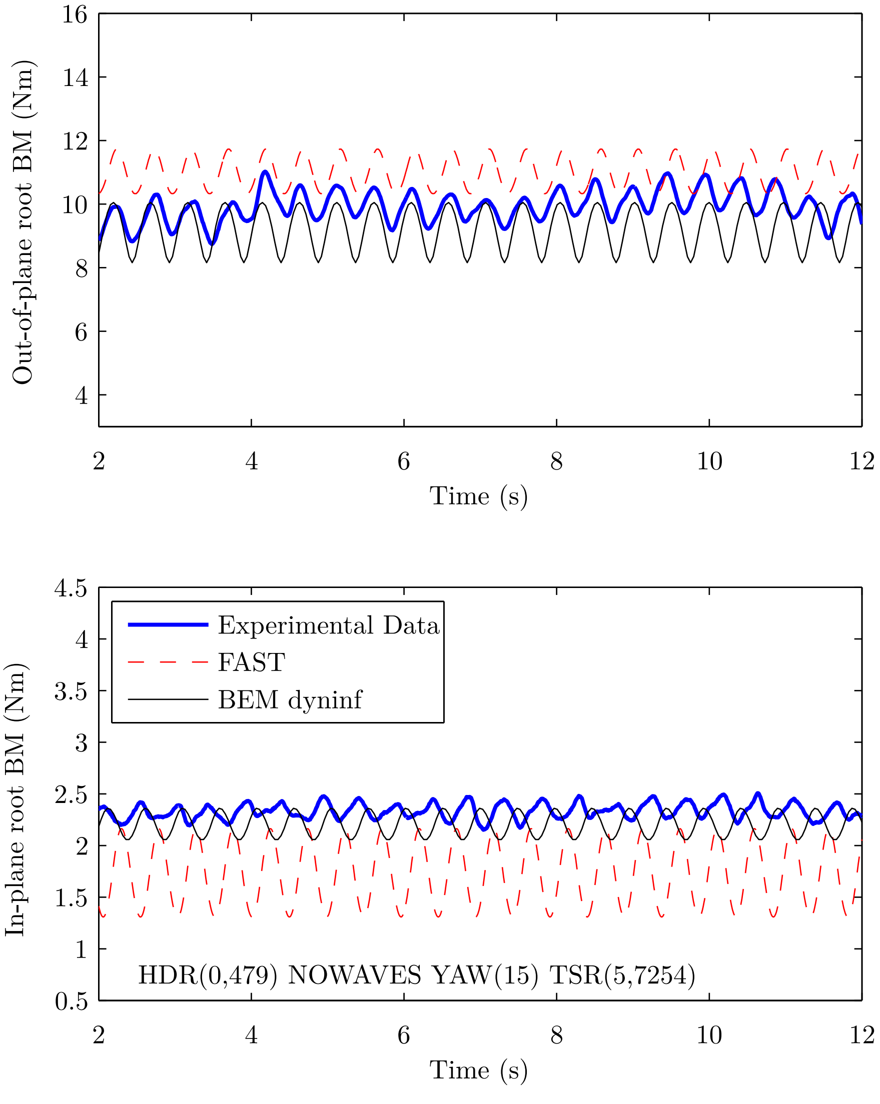

Figure 7.13: Comparing time-series experimental data with FAST and modified BEM. $H = 0m$, $T_i = 0$s, $\gamma = 0°$, mean TSR = 5.7 and $z_H = -0.9m$

7.3.3 Waves and Yaw

Figure 7.14 and Figure 7.15 show the inclusion of both waves and yaw misalignment on TST blade loading. The only variable to change between the two figures is the wave period, being 2.86s and 2s respectively. In both cases the patterns are very similar. The in-plane bending moment prediction with the BEM model is a good match. The out-of-plane bending moment prediction is less precise, probably as a result of not adequately modelling the yaw misalignment since the skewed axial inflow correction is inadequate in these conditions. The skewed inflow correction has been excluded for all but the simplest steady yaw cases (see Section 7.3.2). This may explain why the amplitude of the loading is generally well predicted with the exception of the higher frequency load components. Increasing the wave period increases the load amplitude, but the median load remains unchanged. This is an expected result caused by the increased wave particle excursion.

FAST was used in this research purely for verification purposes; to test that the experimental and numerical results were of the correct magnitude. FAST was designed for wind turbine applications therefore does not consider the kind of velocity inflow caused by waves. Whilst special input files have been made to include the effect of waves, undoubtedly the source code still requires further modification. In general FAST tends to over predict out-of-plane bending moments by about 25% and under predict in-plane bending moments by about 25%. This is not a blade pitch error and may simply be a result of using FAST in an application for which it was not designed.

7.3.4 Reduced Tidal Stream Turbine Immersion

Reducing turbine immersion could permit greater power extraction because of the greater energy in tidal flows near the surface (Dyer, 1986). This will also reduce the problems encountered with bottom effects from turbulence. If it is found that turbines can be placed nearer the surface, a more likely outcome is the increase in turbine diameter. This research is concerned primarily with the effect of wave loading so bottom effects are neglected.

Figure 7.16 and Figure 7.17 show the resulting effects of reducing the immersion depth of a TST device. Figure 7.16 shows the TST at 1/2 depth and Figure 7.17 at 1/3 depth (Figure 5.3). The results present a particularly non-linear experimental loading pattern, caused by the 1P variation closely matching the absolute wave period (1Ta). BEM predicts the majority of the peaks caused by wave loading out-of-plane, however struggles due to the omission of a yaw

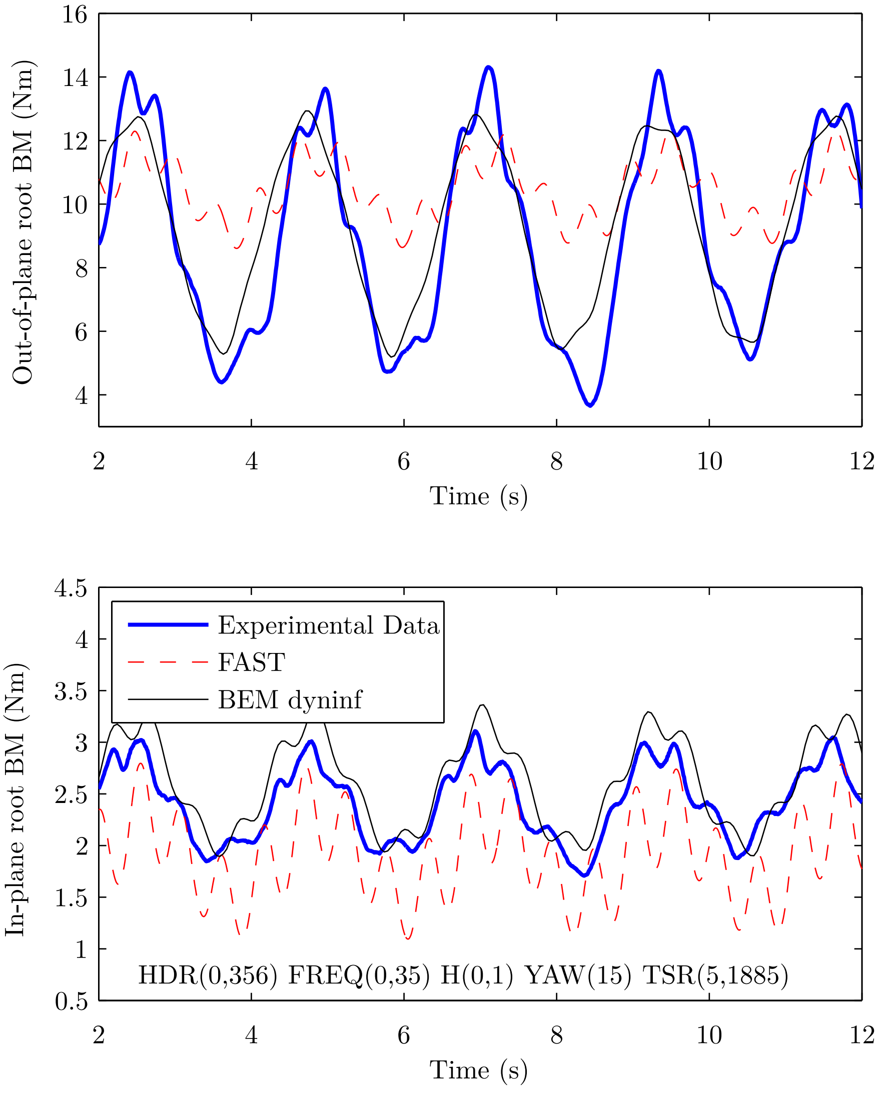

Figure 7.14: Comparing time-series experimental data with FAST and modified BEM. $H = 0.1m$, $T_i = 2.86s$, $\gamma = 15°$, mean TSR $= 5.2$ and $z_H = -0.67m$

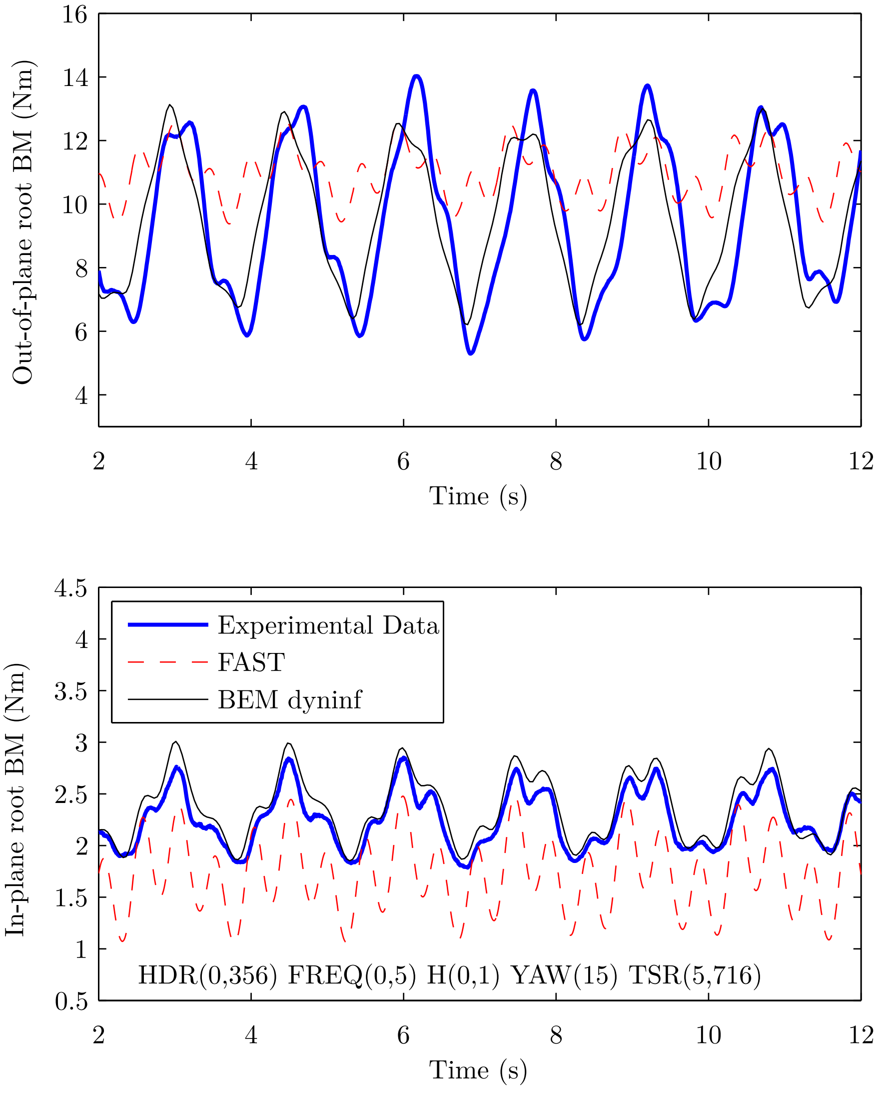

Figure 7.15: Comparing time-series experimental data with FAST and modified BEM. $H = 0.1m$, $T_i = 2s$, $\gamma = 15°$, mean TSR = 5.7 and $z_H = -0.67m$

correction to model the smaller amplitude fluctuations. Essentially reducing turbine immersion serves to increase the amplitude of the wave loading whilst the median load remains the same. Yawed loading with reduced immersion does not appear to change with immersion as can be seen by the smaller load fluctuations being of a similar amplitude. This may not be entirely accurate if the surface boundary effects become important i.e. the wake could be altered by a pressure change or modified streamtube shape. The increased amplitude loading has implications for fatigue loading and network integration due to the power fluctuations being greater.

7.4 Summary of Comparative Study

Generally it can be said that there is good agreement between the BEM numerical model and the experimental data. The model agrees with experimental data and proves that the combination of BEM theory and linear wave theory and yaw misalignment is possible. The main area for improvement is the thrust/out-of-plane predictions which appear to be more complex to predict than the torque/power/in-plane loads. Results have shown that waves will be very important in the design of future TST blades due to the significant variance in the loading. Steady yaw loading may be neglected altogether at low yaw angles of less than 7.5°, however its effect becomes more significant above this value. Placing the turbine nearer the surface will increase the amplitude of the loading but not the mean loading. The numerical model has a tendency to under-predict thrust and over-predict power at high TSRs, hence should be used with caution if modelling in this region.

Most of the conclusions drawn so far agree with those of Barltrop et al. (2005). Barltrop claims however, that mean thrust remains unchanged but that mean torque is increased by waves. Experiments have shown that both mean thrust and torque remain unaffected by waves. The reason Barltrop may have obtained such data is as a result of surface boundary effects since the turbine was towed very near the surface of the water and apparently no allowance was made for this. This is an important consideration for TST developers because although there may be greater energy density near the surface (higher flow velocity), the turbine may become less efficient when subject to water surface boundary effects. An alternative explanation may relate to the velocity ratio described in Section 2.2 and Section 7.2. Barltrop used some wave-current velocity ratios that were much higher than those used in these experiments, caused by the use of a lower tow speed and the proximity of the turbine hub to the free surface. This should have

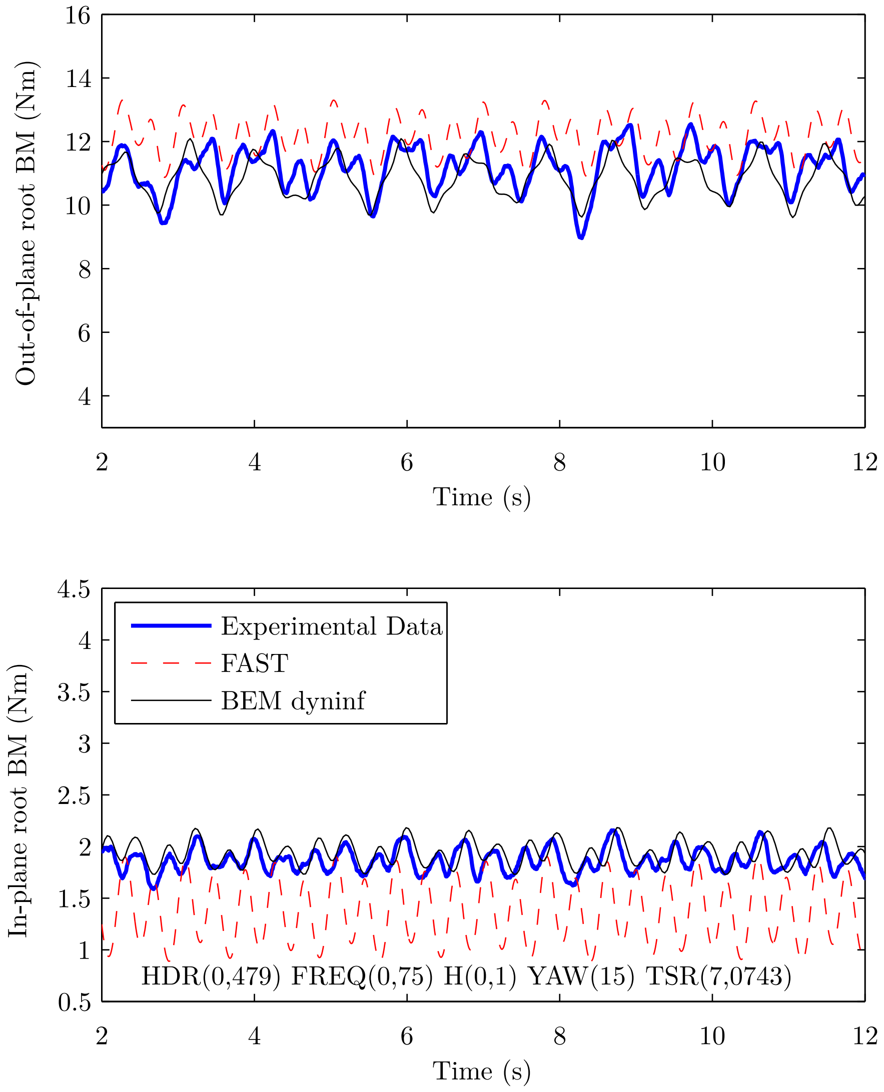

Figure 7.16: Comparing time-series experimental data with FAST and modified BEM. $H = 0.08m$, $T_i = 1.33s$, $\gamma = 15°$, mean TSR = 7.1 and $z_H = -0.9m$

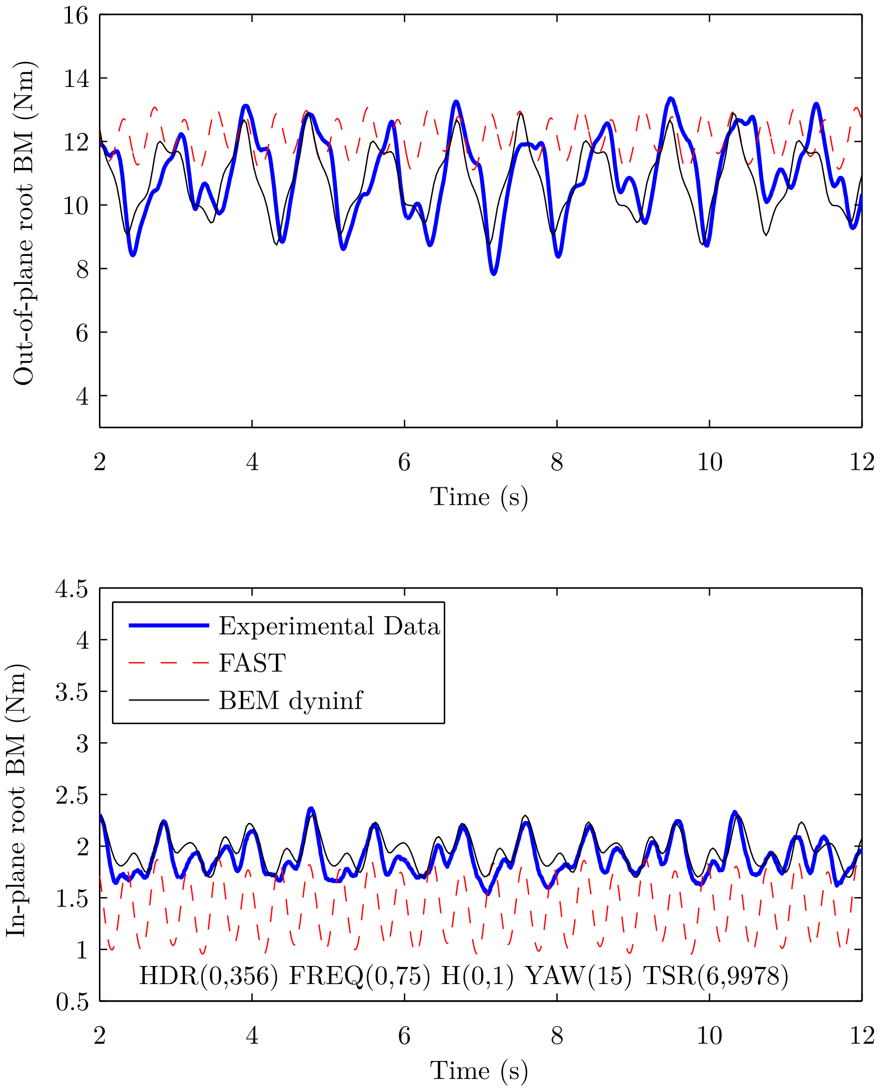

Figure 7.17: Comparing time-series experimental data with FAST and modified BEM. $H = 0.08m$, $T_i = 1.33s$, $\gamma = 15°$, mean TSR = 7.0 and $z_H = -0.67m$

resulted in an increased thrust as well as increased torque, however if the thrust increase was very slight it may not have been apparent?

In general it can be seen that the modified BEM code provides good predictions of the complex blade loadings experienced by a TST under wave and yawed flow conditions. In-plane bending moments are well predicted apart from a slight over prediction at the lower TSRs. Out-of-plane bending moments give a very good indication of the loading pattern, however they have been found to under predict the loading range. The inclusion of a suitable yaw correction will improve calculation prediction. FAST has served to verify the results, but cannot be used as a genuine comparison due to its specific application to wind turbines.

Chapter 8

Full-Scale Dynamic Blade Loading

An important area for this research is the applicability of the findings to a full-scale TST device. No developers have published device information therefore many assumptions were required for the purpose of this study. Table 8.1 shows some of the most important parameters, along with references if necessary. It was also assumed that the turbine would be stationary below 1m/s (Fraenkel, 2010) and the only loads applied to the blades would be as a result of drag (Morison's equation, $C_{D_{mor}} \approx 2$).

8.1 Site Data: St. Catherine's Point, Isle of Wight, UK

The site data was measured off the south coast of the Isle of Wight. The site was chosen because it is an area with high tidal current velocity, as shown by Figure 8.1, where the daily current speed is in excess of 1m/s. The current resource is one of the most important considerations for the installation of a successful TST device. The data was obtained using an AWAC (Acoustic Wave And Current) mounted on the seabed. The device had the capability of measuring current velocity, directionality, wave height and wave period. The device was not capable of multiplexing so the current data is recorded for about 45 minutes, binning data at different depths, followed 15 minutes monitoring wave characteristics. This was not considered a problem since the data sampling occurred at relatively short time intervals (data was gathered for a whole month), therefore wave and current effects could be considered synchronised. The significant wave height (Figure 8.2) and apparent wave period (Figure 8.3) were sampled hourly, whilst the current velocity was sampled every minute. The hourly averages were combined (neglecting the wave and current directionality for reduced complexity) and used to create a 26 day data set for use

Parameter	Description	Format	Units	Values
γ	Yaw Angle	Singular	°	0
Ti	Intrinsic Wave Period	1D Array	s	Site Data
H	Wave Height	1D Array	m	Site Data
z_H	Hub Depth	Singular	m	-20
d	Water Depth	Singular	m	40
U	Mean Current Velocity	1D Array	m/s	Site Data
R	Blade Radius	Singular	m	8.5
B	No. of Blades	Integer	-	3
SET_PITCH	Fixed Pitch Setting	Singular	°	7
PSIi	No. Azimuthal Nodes	Integer	-	15
BladeMass	Blade Mass	Singular	kg	2200 (Wadia et al., 2011)
WaterMass	Displaced Water - Blade	Singular	kg	1400
LeverArm	Blade Lever Arm	Singular	-	$R/3$
Density	Fluid Density	Singular	kg/m^3	1026
StrainPos	Blade Strain Position	Singular	-	0.95 (Root)
r/R	Dimensionless Blade Radius	1D Array	-	(Burton et al., 2001)
c/R	Dimensionless Chord Length	1D Array	-	(Burton et al., 2001)
TWIST	Blade Twist Angle	1D Array	°	(Burton et al., 2001)'
THICK	Thickness to Chord Ratio	1D Array	%	(Burton et al., 2001)
$\alpha - C_L - C_D$	Angle of Attack vs. Lift/Drag	2D Array	°, -, -	(Burton et al., 2001)

Table 8.1: Inputs to the modified BEM code for full-scale TST blade loading predictions

with the modified BEM code.

8.2 BEM Load Analysis

The modified BEM code was fed by the site data and other parameters described in Table 8.1. The resulting out-of-plane and in-plane loads are shown in Figure 8.4. The current speed was assumed bi-directional and the TST device capable of generating in both directions. The full-scale out-of-plane load is on average 4.3 times greater than the in-plane load, which agrees with the results from the comparative small-scale study (Chapter 7). The data has been reduced in Figure 8.5 and Figure 8.6 to show median and range loading per day. In both cases the median loads and the interquartile ranges follow a very similar pattern, albeit at a different magnitude. The whiskers and outliers are a little misleading. The lower whisker/outliers are influenced in most cases by the blade drag when the TST is stationary. The data is often positively skewed, which can be seen by the median value shifting to the lower quartile on some days followed by many outliers from the upper whisker. It is unclear from these boxplots whether the upper outliers are caused by error in the BEM code or that the whisker length is too short for the

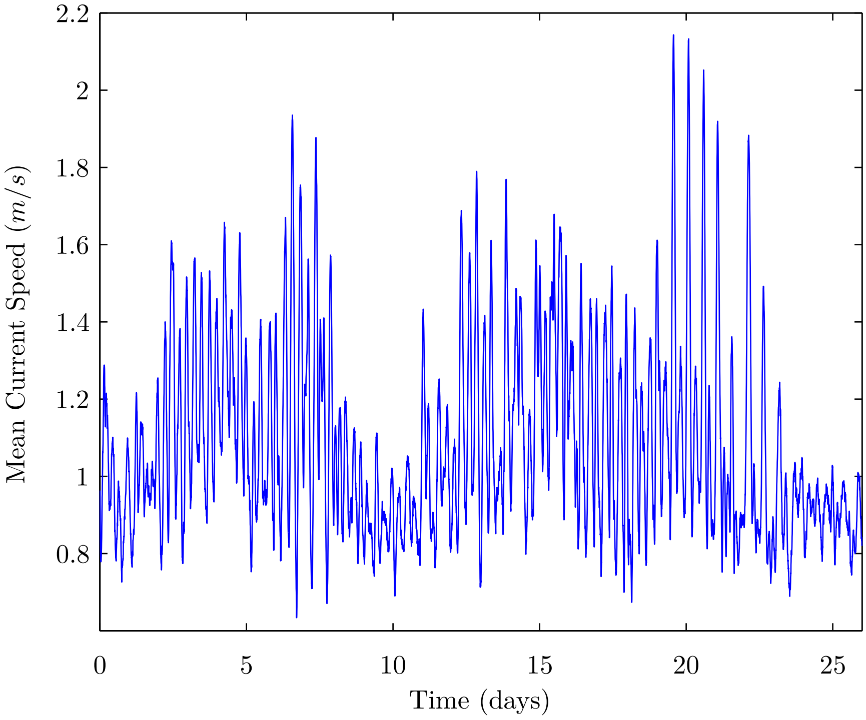

Figure 8.1: Mean current speed data (U) gathered using an AWAC sited at St. Catherine's Point, Isle of Wight, UK

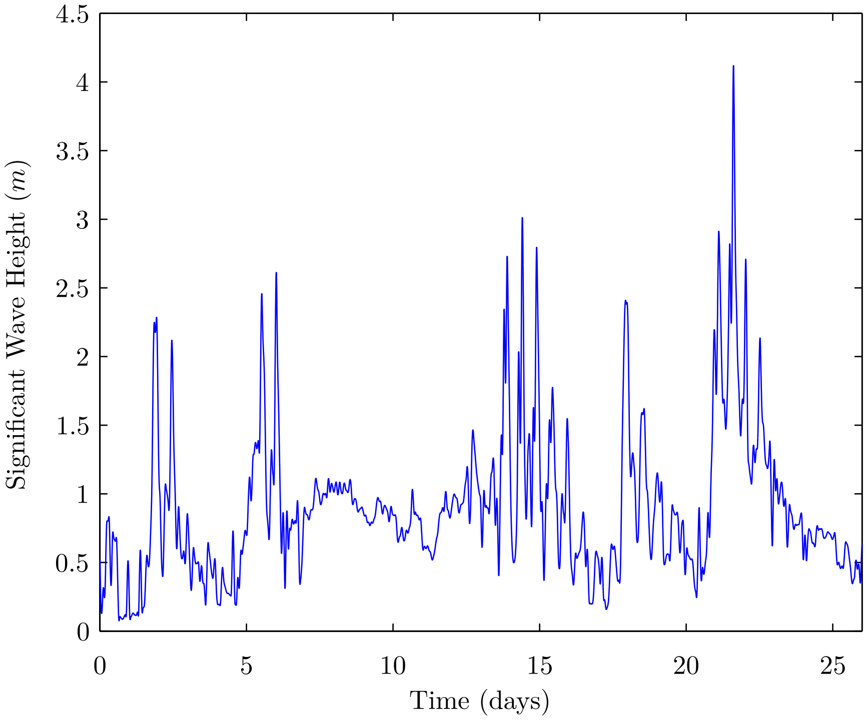

Figure 8.2: Significant wave height data (H_S) gathered using an AWAC sited at St. Catherine's Point, Isle of Wight, UK

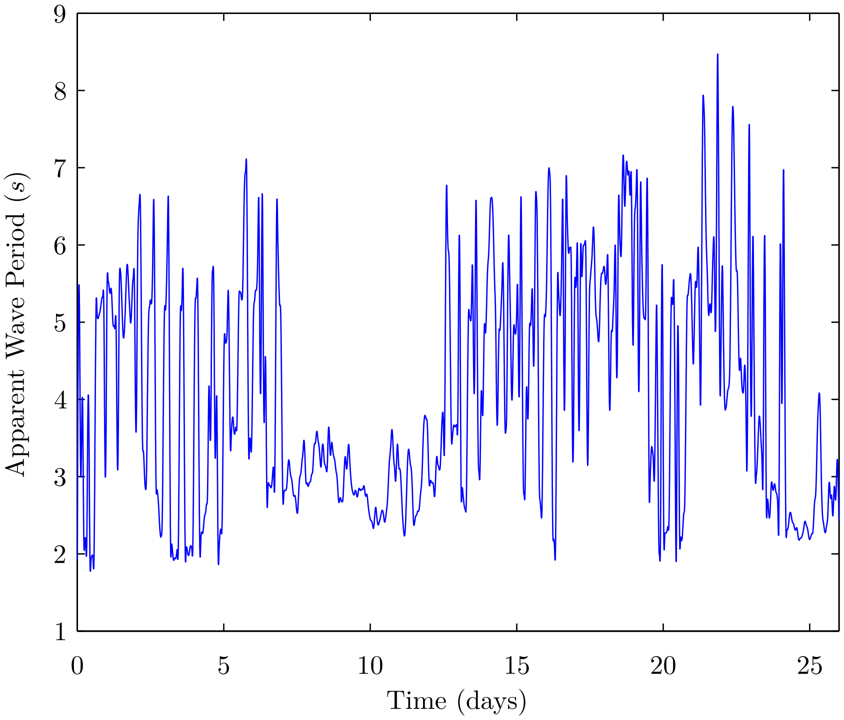

Figure 8.3: Wave period data (T_a) gathered using an AWAC sited at St. Catherine's Point, Isle of Wight, UK

statistical interpretation of the data. This is important because a maximum load will be required in order to design for ultimate limit strength of a blade. These statistics provide a brief overview of the results, however to draw more meaningful results from this data requires carrying out detailed fatigue calculations, which are beyond the scope of this research. Section 8.3 provides a brief overview of a basic fatigue calculation.

8.3 Rainflow Counting and Fatigue

The loading shown in Figure 8.4 is very high resolution, containing 830,000 data points. As a result this data also contains a high number of loading fluctuations or stress reversals. It is these stress reversals that can cause fatigue failures to occur, with the onset of crack propagation in the material (Freebury and Musial, 2000), and this can occur with cyclic loading significantly below the ultimate load. In order to calculate the fatigue loading at a basic level, the Palmgren-Miner rule (Equation 8.1) can be applied to a data set to assess what proportion of life is consumed by stress reversal at each load magnitude (Kong et al., 2006). Each of these magnitudes can be referred to as a Damage Equivalent Load (DEL). The sum of these damage equivalent loads (C) should be less than 1 for design purposes i.e. if it exceeds 1 the design will likely fail before its

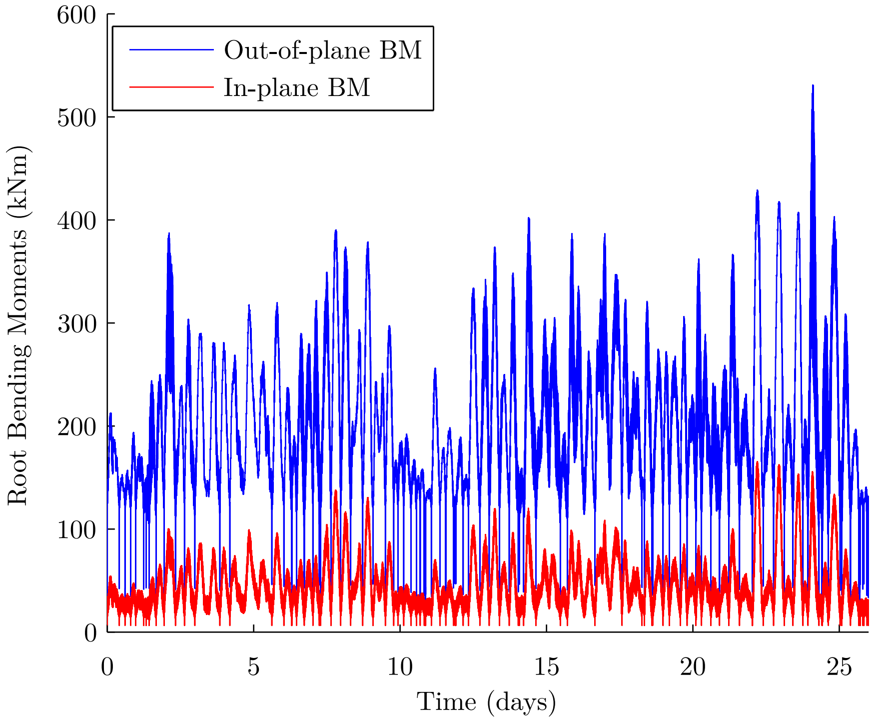

Figure 8.4: Modified BEM code applied to site data. Out-of-plane and in-plane loads are shown over a tidal cycle

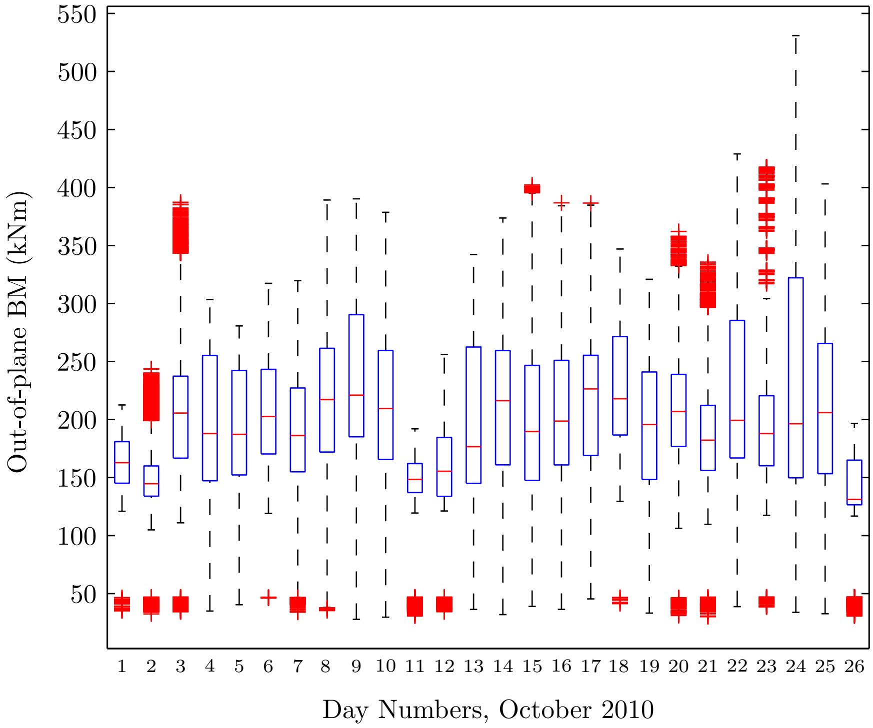

Figure 8.5: Out-of-plane blade root bending moment daily averages across full TSR range

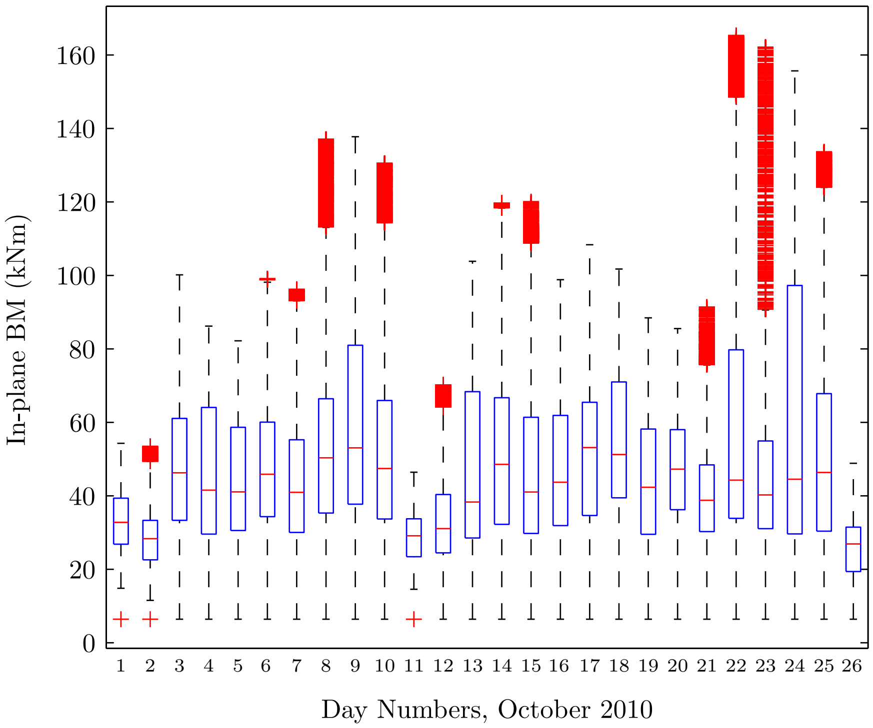

Figure 8.6: In-plane blade root bending moment daily averages across full TSR range

required cycle life-time:

$$\sum_{i=1}^{I} \frac{n_i}{N_i} = C \tag{8.1}$$

I is the number of load magnitudes, with n_i the number of load cycles and N_i the number of cycles to failure at each magnitude. n_i can be calculated from an experimental data sets using a technique called rainflow counting (Garrad Hassan Ltd., 2008). This has been carried out for Figure 8.4 and shown as fatigue damage spectra for out-of-plane and in-plane bending moments (Figure 8.7 and Figure 8.8 respectively)

Calculating N_i is more difficult because it usually requires experimental data to verify any theoretical S-N curves at different stress ratios. The choice of composite material used for TST blades is not yet certain, so a single fictitious M-N curve has been created in order to demonstrate the application of the Palmgren-Miner rule on the full-scale TST blade loading data (Figure 8.9). The unknown quantity is the precise number of cycles to failure for a given load magnitude. The use of M-N curves as opposed to S-N curves is suggested by Freebury and Musial (2000), and shown to be effective for wind turbine blades. Applying the Palmgren-Miner rule to the

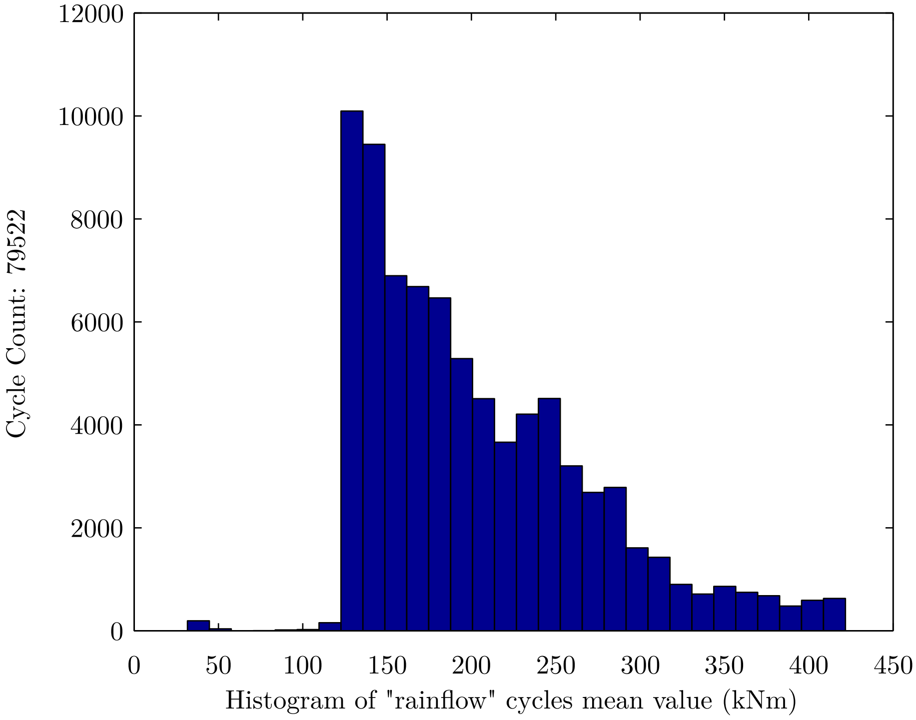

Figure 8.7: Fatigue damage spectrum from “Rainflow” cycle counting of out-of-plane loads of Figure 8.4

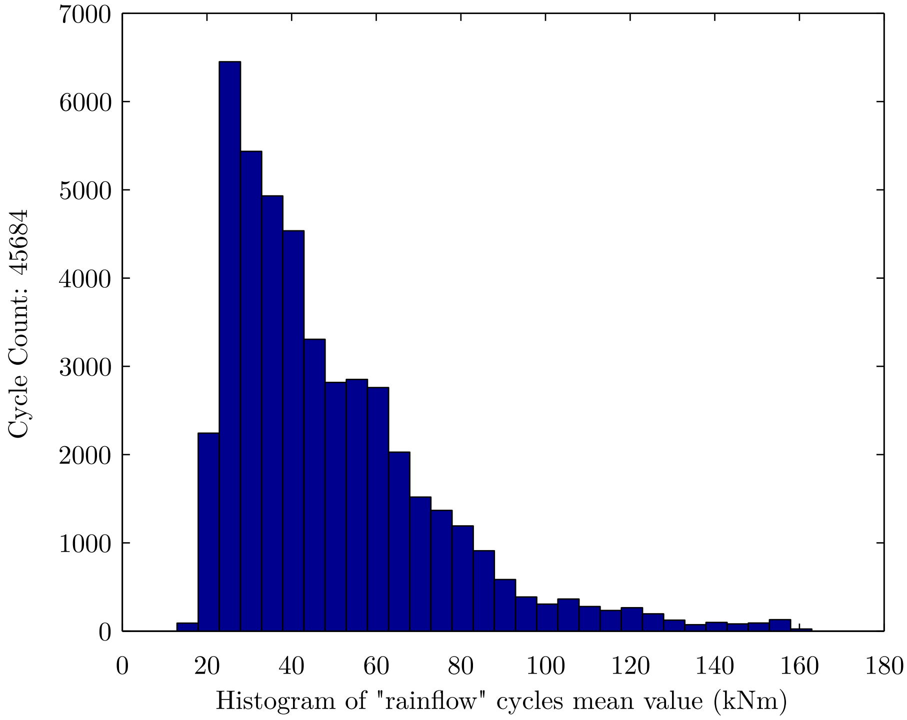

Figure 8.8: Fatigue damage spectrum from “Rainflow” cycle counting of in-plane loads of Figure 8.4

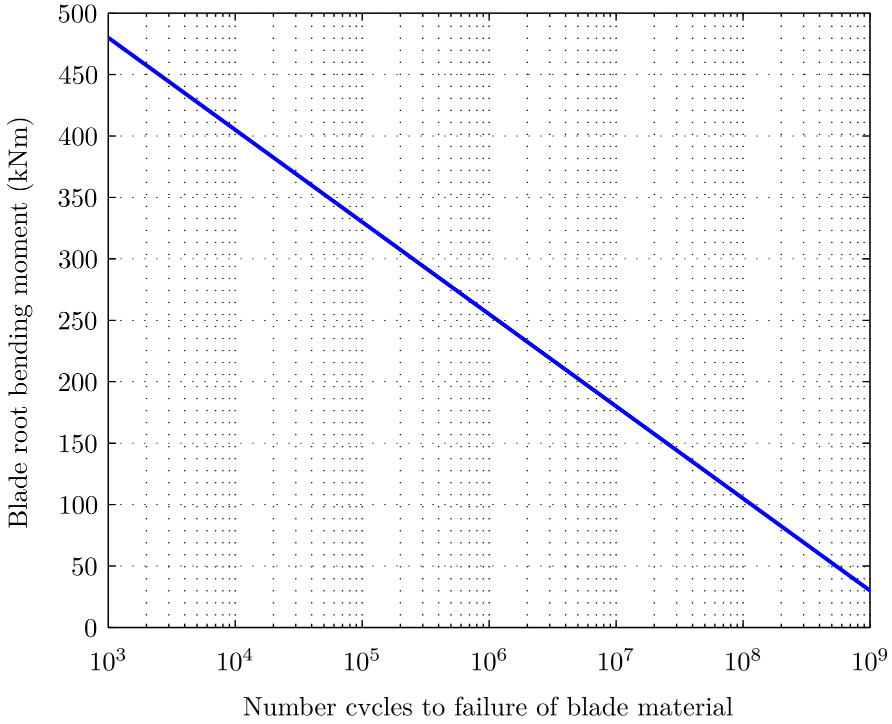

Figure 8.9: Fictitious blade material M-N curve (rather than S-N curve) used in fatigue life calculations

data from Figure 8.7 and Figure 8.8 results in a blade lifetime of 5.05 years out-of-plane and 7.12 years in-plane, assuming the load spectra remain unchanged for the life of the blade. This lifetime was estimated using Equation 8.2, where L_{years} is the estimated lifetime of the part. Y is the year sample time ratio e.g. 26/365 for this load study and C_{des} is the design limit set to 1 for this example.

$$L_{years} = 100Y\left(C_{des} - C\right) \tag{8.2}$$

In reality, this 5 year blade lifetime can only be used to justify that the method is acceptable. To calculate the fatigue life of a blade correctly would require extensive S-N data curves with the use of a detailed Goodman diagram (Sutherland and Mandell, 2005). This does however demonstrate the possible consequences for neglecting fatigue loading in a TST design, even at an early stage of device development. Fatigue is likely to be one of the main drivers in the quest to commercialise TST technology.

Chapter 9

Conclusions

The need for this work arose from the lack of understanding of waves and misaligned flows on TST rotors and blades. The aim of the research was to increase device reliability through informed laboratory experiments and numerical modelling, with a view to facilitating the installation of devices in more energetic sites, permitting greater power capture.

An existing scale model, three bladed, horizontal axis turbine was modified as part of this work to measure thrust and torque with a new rotor hub dynamometer (see Section 5.3). The material used for the main shaft was changed from aluminium to stainless steel for increased durability and the lower rotor hub was re-designed to suit the new dynamometer system along with adequate cable holes for an additional strain gauged blade (see Section 5.3.2). Blade position was measured using a specially commissioned hollow shaft encoder, which consequently provided speed and acceleration data. A wireless telemetry system provided amplified voltage signals from the various strain gauge bridges mounted on the dynamometer and blade. Data was then transmitted via a sealed umbilical cable to a custom LabVIEW program that synchronised the data and provided a live-feed of all loads. Experiments were conducted successfully in a large wave-towing tank facility in Southampton. Many test runs were carried out to investigate wave and misaligned flow conditions on a TST rotor and blades. The misaligned flow conditions were simulated with the yawing of the turbine nacelle to the incident flow.

Experimental data was compared to a detailed BEM numerical model which included many new additions. The basic modifications such as static stall and tip-losses were modelled with the inclusion of new modifications for yaw and blade azimuth, linear waves on a uniform current and dynamic inflow and dynamic stall models. These modifications were combined to create a functional Matlab tool for comparing with the varied experimental tests. By way of further comparison, an existing certified and open source wind turbine code, FAST from NREL (Jonkman, 2012) was modified with the inclusion of waves. This proved very useful for the verification of some of the conclusions drawn.

It has been demonstrated that the presence of waves and the effect of rotor misalignment is likely to have a detrimental impact on TSTs. This is not a significant problem in terms of power output, other than to further complicate the power electronics required for smoothing the power/flicker. The main issue with wave interaction around a TST is the cyclic loading, which will likely result in accelerated fatigue to the rotor and blades, as shown with the basic full-scale simulation in Chapter 8. This is particularly evident in the axial flow direction. Another important consideration is whether a rotor yaw drive is required at any specific tidal site. Large amounts of directional swing will occur around headlands and can cause a significant reduction in power as well as increase the dynamic loading if a yaw drive is omitted.

Outside the optimum operating range of the TST, the BEM code rapidly loses its applicability. This is less important for low TSR values since the turbine cannot usually operate in these conditions. The high TSR region is more of a problem and should a turbine operate beyond a TSR of 8, the load predictions become gradually less accurate (in part due to the high axial inflow factor correction), a common feature of all BEM codes. Results have shown that waves and yawed flow will be very important in the design of future TST blades due to the significant amplitudes in the loading. Placing the turbine nearer the surface should increase the amplitude of wave loading, but it is postulated that a reduction in the overall thrust due to streamtube deformation, results in no significant increase in loading, only confusion of the load interpretation. Experiments here have shown that both the mean thrust and torque remain unaffected by the linear waves used in the experiments (Section 7.2). Blade loading experiments have shown the same discrepancies in the load coefficients at high TSR. The time-series data has been reproduced effectively for most of the data sets using the modified BEM theory and new dynamic inflow method presented in Section 4.3.

In summary, for a turbine in dynamic flow:

- The median out-of-plane root bending moment is, on average, 4.1 times greater than the in-plane blade root bending moment for waves and yawed conditions.
- The out-of-plane bending moment has been found to be as much as 9.5 times the in-

plane bending moment (for a full-scale wave period of 12.8s). A maximum loading range of 175% of the median out-of-plane bending moment and 100% of the median in-plane bending moment was observed for this test case.

- The gravitational/buoyancy component of a blade can be significant to the in-plane blade root bending moment
- The apparent wave period was found to be equally significant to the wave height in terms of loading range of a blade
- Steady nacelle yaw loading on an individual blade is negligible in comparison to wave loading
- Steady nacelle yaw will reduce total rotor power capture and mean rotor thrust loading. Below 7.5° the reduction in power/thrust is, however, negligible
- Reduced hub depth may lead to interaction with the water surface boundary, leading to uncharacteristic rotor/blade loads. There is likely to be a complex relationship between the modified turbine streamtube and increased wave loading due to surface proximity

Numerical modelling summary:

- The modification of BEM theory to include the effects of linear waves and nacelle yaw misalignment has been shown to be effective at reproducing load histories
- Dynamic inflow must be included for the calculation of TST loads.
- An effective dynamic inflow model has been created and used to improve BEM blade load prediction
- The closest agreement between all experimental results and numerical predictions was in the optimum operating range of the turbine (i.e. 5-6 TSR)
- Dynamic stall may be neglected in some cases since its effect here was limited. This may not be the case for turbulent flows or non-linear waves
- The inclusion of steady yaw effects (using the skewed axial inflow correction) in a BEM model should be used with caution when waves are also modelled. Omitting the skewed axial inflow correction results in significantly improved load prediction

- The gravitational/buoyancy component is significant to the in-plane blade bending moment and should be included in any BEM model

The research presented in this thesis was carried out to further understand the dynamic loading effects of waves and misaligned flows on tidal stream turbine devices. Further research in this area should be focused on the creation of detailed data sets to support the conclusions presented and for the validation of any other numerical models. Further data could be used to improve the corrections applied to the BEM theory, especially for loading predictions at higher TSRs. Wave spectra or sheared currents have not been tested on the scale model TST. It is not possible to simulate a real sea state in a towing tank due to the limited towing time available, however this may be possible in a large flume. A more fundamental blockage correction is also required as the current empirical corrections tend to be quite varied and also inapplicable to the case of an individual blade.

The author hopes that this research and following works assist in the development of a fundamentally sound and important technology for future sustainable energy demand.

References

Abbott, I. H. and von Doenhoff, A. E. (1949). *Theory of Wing Sections*, Dover Publications, Inc.

Andritz Hydro Hammerfest (2012). HS300.
URL: *www.hammerfeststrom.com*

Bahaj, A. S., Batten, W. M. J., Molland, A. F. and Chaplin, J. R. (2005). Experimental Investigation into the Hydrodynamic Performance of Marine Current Turbines, *Technical Report March 2005*.

Bahaj, A. S. and Myers, L. E. (2001). Cavitation prediction in operating marine current turbines.

Barltrop, N., Grant, A. D., Varyani, K. S. and Pham, X. P. (2005). Wave-current interactions in marine current turbines, *6th European Wave and Tidal Energy Conference, Glasgow, UK*, pp. 33–38.

Barltrop, N., Varyani, K. S., Grant, A. D., Clelland, D. and Pham, X. P. (2006). Wave-current interactions in marine current turbines, *Proceedings of the Institution of Mechanical Engineers, Part M: Journal of Engineering for the Maritime Environment* **220**(4): 195–203.

Batten, W. M. J., Bahaj, A. S., Molland, A. F. and Blunden, L. S. (2006). Yawed performance of horizontal axis marine current turbines, *International Solar Energy Society*, Vol. 85, p. 151.

Batten, W. M. J., Bahaj, A. S., Molland, A. F. and Chaplin, J. R. (2007). Experimentally validated numerical method for the hydrodynamic design of horizontal axis tidal turbines, *Ocean Engineering* **34**: 1013–1020.

Bechly, M. E. and Clausen, P. D. (1999). Some Dynamic Strain Measurements from the Blade of a Small Wind Turbine, *Wind Engineering* **23**(1): 15–22.

Bedard, R., Previsic, M., Polagye, B., Hagerman, G. and Casavant, A. (2006). EPRI TP-008-NA North America Tidal In-Stream Energy Conversion Technology Feasibility Study, *Technical report*.

BERR (2008). Atlas of UK marine renewable energy resources, *Technical report*, Department For Business Enterprise And Regulatory Reform.

Betz, A. (1920). Das Maximum der theoretisch möglichen Ausnötzung des Windes durch Windmotoren, *Gesamte Turbinenwesen* (17): 307–309.

Black and Veatch (2005). Phase II UK Tidal Stream Energy Resource Assessment, *Technical report*, Carbon Trust.

Bossanyi, E. A. (2007). GH Tidal Bladed Theory Manual.

Buckland, H. C., Masters, I., Chapman, J. C. and Orme, J. A. C. (2010). Blade Element Momentum Theory in Modelling Tidal Stream Turbines, *18th UK Conference on Computational Mechanics*.

Buhl, M. L. (2005). A New Empirical Relationship between Thrust Coefficient and Induction Factor for the Turbulent Windmill State, *Technical Report August*, NREL.

Burton, T., Sharpe, D., Jenkins, N. and Bossanyi, E. A. (2001). *Wind Energy Handbook*, Wiley.

Carbon Trust (2011). Accelerating Marine Energy, *Technical report*, Carbon Trust.
URL: *www.carbontrust.com*

Cea, L., Puertas, J. and Pena, L. (2007). Velocity measurements on highly turbulent free surface flow using ADV, *Experiments in Fluids* **42**(3): 333–348.

Chaplin, J. R. (1984). Nonlinear forces on a horizontal cylinder beneath waves, *Journal of Fluid Mechanics* **147**: 449–464.

Clarke, J. A., Connor, G., Grant, A. D. and Johnstone, C. M. (2005). Desing and Initial Testing of a Contra-Rotating Tidal Current Turbine, *6th European Wave and Tidal Energy Conference, Glasgow, UK*, pp. 73–80.

Dean, R. G. and Dalrymple, R. A. (1991). *Water wave mechanics for engineers and scientists*, World Scientific Pub. Co. Inc.

DECC (2011). Consultation on proposals for the levels of banded support under the Renewables Obligation for the period 2013-17 and the Renewables Obligation Order 2012, *Technical Report October 2011*, Department of Energy and Climate Change.
URL: *www.decc.gov.uk*

Drela, M. and Youngren, H. (2001). XFOIL 6.9 User Guide.

Dunn, P. (1986). *Renewable Energies: Sources, Conversion, Application*, Peter Peregrinus Ltd., UK.

Dyer, K. (1986). *Coastal and estuarine sediment dynamics*, John Wiley and Sons, Sussex, UK.

Eastwood, J. W., Townend, I. H. and Watson, C. J. H. (1987). The Modelling of Wave-Current Velocity Profiles in the Offshore Design Process, *Advances in Underwater Technology, Ocean Science and Offshore Engineering* **12**: 327–341.

ENSG (2012). Our Electricity Transmission Network: A Vision For 2020, *Technical Report February*, Electricity Networks Strategy Group.
URL: *www.decc.gov.uk*

ETI (2010). Marine Energy Technology Roadmap, *Technical report*, Energy Technologies Institute & UK Energy Research Centre.

European Marine Energy Centre (2012). A global centre of excellence in marine energy testing and research.
URL: *www.emec.org.uk*

Fenton, J. D. (1985). A fifth-order stokes theory for steady waves, *Journal of Waterway, Port, Coastal and Ocean Engineering* **111**(2).

Fingersh, L., Hand, M. and Laxson, A. (2006). Wind Turbine Design Cost and Scaling Model, *Technical Report December*, NREL.

Fraenkel, P. L. (2005). Progress with marine current turbines, *6th European Wave and Tidal Energy Conference, Glasgow, UK*, pp. 141–148.

Fraenkel, P. L. (2010). Development and testing of Marine Current Turbine's SeaGen 1.2MW tidal stream turbine, *3rd International Conference on Ocean Energy.*

Francis, M. and Hamilton, M. (2007). Floating Tidal Stream Turbine, *Technical report*, BERR.

Freebury, G. and Musial, W. (2000). Determining Equivalent Damage Loading for Full-Scale Wind Turbine Blade Fatigue Tests, *19th American Society of Mechanical Engineers, Wind Energy Symposium, Reno, Nevada.*

Galloway, P. W., Myers, L. E. and Bahaj, A. S. (2010). Studies of a scale tidal turbine in close proximity to waves, *3rd International Conference on Ocean Energy*, Bilbao, Spain.

Galloway, P. W., Myers, L. E. and Bahaj, A. S. (2011). Experimental and numerical results of rotor power and thrust of a tidal turbine operating at yaw and in waves, *World Renewable Energy Congress*, Linköping, Sweden.

Garrad Hassan Ltd. (2008). Development of a design tool for axial flow tidal stream devices, *Technical report*, Department for Business Enterprise and Regulatory Reform.

Garrett, C. and Cummins, P. (2007). The efficiency of a turbine in a tidal channel, *Journal of Fluid Mechanics* **588**: 243–251.

GL Garrad Hassan (2012). Tidal Bladed.
URL: *www.gl-garradhassan.com*

Gooch, S., Thomson, J., Polagye, B. and Meggitt, D. (2009). Site Characterization for Tidal Power, *OCEANS 2009, MTS/IEEE Biloxi - Marine Technology for Our Future: Global and Local Challenges*, Seattle, USA.

Hahn, G. D. (1994). Influences of wave stretching on the response of wave-excited offshore platforms, *Ocean Engineering* **21**(6): 507–517.

Hedges, T. S., Anastasiou, K. and Gabriel, D. (1985). Interaction of Random Waves and Currents, *Waterway, Port, Coastal and Ocean Engineering* **111**(2): 275–288.

ISO (2005). Petroleum and natural gas industries - Specific requirements for offshore structures, *Technical report.*

Jo, C. H., Lee, K. H. and Rho, Y. H. (2010). Recent TCP (Tidal Current Power) projects in Korea, *Science in China Series E: Technological Sciences* **53**(1): 57–61.

Jonkman, J. (2012). NREL-NWTC Design Codes: FAST.
URL: *www.nrel.gov*

Kamphuis, J. W. (2010). *Introduction to coastal engineering and management*, 2nd editio edn, World Scientific Publishing Co. Pte. Ltd., Singapore.

Kong, C., Kim, T., Han, D. and Sugiyama, Y. (2006). Investigation of fatigue life for a medium scale composite wind turbine blade, *International Journal of Fatigue* **28**(10): 1382–1388.

Larsen, J. W., Nielsen, S. R. K. and Krenk, S. (2007). Dynamic stall model for wind turbine airfoils, *Journal of Fluids and Structures* **23**(7): 959–982.

Leishman, J. G. and Beddoes, T. S. (1986). A Semi-Empirical Model for Dynamic Stall, *Journal of the American Helicopter Society* **34**(3-17).

Mackay, D. J. C. (2009). *Sustainable Energy - Without The Hot Air*, 3.5.2 e1.4 edn, UIT Cambridge Ltd., Cambridge.

Macpherson, D. M., Puleo, V. R. and Packard, M. B. (2007). Estimation of Entrained Water Added Mass Properties for Vibration Analysis, *Technical Report June*.
URL: *www.hydrocompinc.com*

Maganga, F., Germain, G., King, J., Pinon, G. and Rivoalen, E. (2009). Experimental study to determine flow characteristic effects on marine current turbine behaviour, *8th European Wave and Tidal Energy Conference, Uppsala, Sweden*, pp. 661–667.

Manwell, J. F., McGowan, J. G. and Rogers, A. L. (2009). *Wind Energy Explained*, 2nd edn, Wiley.

Marine Current Turbines (2012). SeaGen Technology.
URL: *www.marineturbines.com*

Masters, I., Orme, J. A. C. and Chapman, J. C. (2007). Towards realistic marine flow conditions for tidal stream turbines, *7th European Wave and Tidal Energy Conference, Porto, Portugal*.

McCann, G. (2007). Tidal current turbine fatigue loading sensitivity to waves and turbulence - a parametric study, *7th European Wave and Tidal Energy Conference, Porto, Portugal*.

McCann, G., Hitchcock, S. and Lane, S. (2008). Implications of Site-Specific Conditions on the Prediction of Loading and Power Performance of a Tidal Stream Device St Vincent's Works, *2nd International Conference on Ocean Energy*, number October.

McCombes, T., Johnstone, C. M. and Grant, A. D. (2009). Unsteady 3D Wake Modelling for Marine Current Turbines, *8th European Wave and Tidal Energy Conference, Uppsala, Sweden*, pp. 548–557.

Milne, I. A., Day, A. H., Sharma, R. N., Flay, R. G. J. and Bickerton, S. (2011). Tidal Turbine Blade Load Experiments for Oscillatory Motion, *9th European Wave and Tidal Energy Conference*, Southampton.

Milne, I. A., Sharma, R. N., Flay, R. G. J. and Bickerton, S. (2010). The Role of Waves on Tidal Turbine Unsteady Blade Loading, *3rd International Conference on Ocean Energy*.

Molland, A. F. (1976). Strain gauge force ballances, dynamometers and transducers, *Technical report*.

Molland, A. F. and Turnock, S. R. (2002). A Propeller Thrust and Torque Dynamometer for Wind Tunnel Models, *Strain* **38**(1): 3–10.

Moriarty, P. J. and Hansen, A. C. (2005). AeroDyn theory manual, *Technical Report January*.

Myers, L. E. (2005). *Operational parameters of horizontal axis marine current turbines*, Phd thesis, University of Southampton.

Myers, L. E. and Bahaj, A. S. (2008). Scale reproduction of the flow field for tidal energy converters, *10th World Renewable Energy Congress, Glasgow*, Vol. 44.

Myers, L. E. and Bahaj, A. S. (2009). Near wake properties of horizontal axis marine current turbines, *8th European Wave and Tidal Energy Conference, Uppsala, Sweden* pp. 558–565.

Nicholls-Lee, R. F. and Turnock, S. R. (2007). Enhancing Performance of a Horizontal Axis Tidal Turbine using Adaptive Blades, *OCEANS 2007* .

Nicholls-Lee, R. F., Turnock, S. R. and Boyd, S. W. (2008). Performance prediction of a free stream tidal turbine with composite bend-twist coupled blades, *2nd International Conference on Ocean Energy*, number October, pp. 1–9.

Norris, J. V. and Droniou, E. (2007). Update on EMEC activities, resource description, and characterisation of wave-induced velocities in a tidal flow., *7th European Wave and Tidal Energy Conference, Porto, Portugal*.

OpenHydro Group (2012). Development: EMEC.
URL: *www.openhydro.com*

Ordonez-Sanchez, S., Grant, A. D. and Johnstone, C. M. (2010). Contra Rotating Marine Turbines Tank Tests to Analyse System Dynamic Response, *3rd International Conference on Ocean Energy*.

Orfanidis, S. J. (1996). *Introduction to Signal Processing*, Upper Saddle River, NJ: Prentice Hall.

Orme, J. A. C., Chapman, J. C. and Masters, I. (2007). Aspects of the performance prediction of tidal stream turbines in yawed flow, *NAFEMS World Congress, Vancouver, Canada, May 22-25*.

Papadopoulos, K., Morfiadakis, E., Philippidis, T. P. and Lekou, D. J. (2000). Assessment of the Strain Gauge Technique for Measurement of Wind Turbine Blade Loads, *Wind Energy* **3**: 35–65.

Pedersen, K. O. H., Hansen, K. S., Paulsen, U. S. and Sorensen, P. (2008). Wind Turbine Measurement Technique - an Open Laboratory for Educational Purposes, *Wind Energy* (September 2007): 281–295.

Peters, D. A., Boyd, D. D. and He, C. J. (1987). Finite-State Induced-Flow Model for Rotors in Hover and Forward Flight, *Journal of the American Helicopter Society* **34**(4): 5–17.

Pitt, D. M. and Peters, D. A. (1981). Theoretical prediction of dynamic-inflow derivatives, *Vertica* **5**: 21–34.

Polinder, H., van Der Pijl, F. F. A., De Vilder, G. J. and Tavner, P. J. (2006). Comparison of Direct-Drive and Geared Generator Concepts for Wind Turbines, *IEEE Transactions on Energy Conversion* **21**(3): 725–733.

Potters Industries Inc. (2012). Sphericel Hollow Glass Spheres.
URL: *www.pottersbeads.com*

Scottishpower Renewables (2012). Sound of Islay.
URL: *www.scottishpowerrenewables.com*

Shen, W. Z., Mikkelsen, R., Sorensen, J. N. and Bak, C. (2005). Tip Loss Corrections for Wind Turbine Computations, *Wind Energy* **8**(4): 457–475.

Shimizu, Y., Shunsuke, N., Takahashi, M. and Azuma, A. (1987). Fluctuation of a Bending Moment Acting on the Rotating blade of a Horizontal Axis Wind Turbine (Comparison of Experimental Results and Annular Momentum Theory), *The Japan Society of Mechanical Engineers* **30**(260): 288–295.

Smith, J. A. (2006). Wave-Current Interactions in Finite Depth, *Journal of Physical Oceanography* **36**(7): 1403–1419.

Snel, H., Houwink, R. and Bosschers, J. (1994). Sectional prediction of lift coefficients on rotating wind turbine blades in stall, *Technical report*.

Sorensen, R. M. (2006). *Basic Coastal Engineering*, third edit edn, Springer, New York.

Srokosz, M. A. (1987). Models of Wave-Current Interaction, *Advances in Underwater Technology, Ocean Science and Offshore Engineering* **12**: 313–325.

Sumer, B. M. and Fredsoe, J. (2006). *Hydrodynamics around cylindrical structures*, Vol. 26, revised edn, World Scientific Publishing Co. Pte. Ltd., Singapore.

Sutherland, H. J. and Mandell, J. F. (2005). Updated Goodman diagrams for fiberglass composite materials using the DOE/MSU fatigue database, *Technical report*.

Swan, C., Cummins, I. P. and James, R. L. (2001). An experimental study of two-dimensional surface water waves propagating on depth-varying currents. Part 1. Regular waves, *Journal of Fluid Mechanics* **428**: 273–304.

Swan, C. and James, R. L. (2001). A simple analytical model for surface water waves on a depth-varying current, *Applied Ocean Research* **22**: 331–347.

Tarzanin, F. J. (1971). Prediction of Control Loads due to Blade Stall, *Journal of the American Helicopter Society* **17**(2): 33–46.

The Crown Estate (2010). Pentland Firth and Orkney Waters Round 1 Development Sites, *Technical report*.
URL: *www.thecrownestate.co.uk*

Theodorsen, T. (1954). Theory of Propellors.

Thomson, J., Polagye, B., Richmond, M. and Durgesh, V. (2010). Quantifying turbulence for tidal power applications, *Oceans 2010 MTS/IEEE Seattle*, IEEE.

Turner, N. E. and Owen, A. (2009). The Effect of Boundary Conditions on Performance Prediction Model Results for Tidal Turbines, *8th European Wave and Tidal Energy Conference, Uppsala, Sweden*, pp. 842–848.

Twidell, J., Weir, A. D. and Weir, T. (2006). *Renewable Energy Resources*, Spon Press.

van Wingerden, J. W., Hulskamp, A. W., Barlas, T., Marrant, B., van Kuik, G. A. M., Molenaar, D. P. and Verhaegen, M. (2008). On the Proof of Concept of a 'Smart' Wind Turbine Rotor Blade for Load Alleviation, *Wind Energy* **11**: 265–280.

Viterna, L. A. and Corrigan, R. D. (1981). Fixed Pitch Rotor Performance of Large Horizontal Axis Wind Turbines, *Technical report*, NASA, Ohio.

Wadia, M., Meunier, M., Olsen, D. and McEwen, L. (2011). Composite Blades for Tidal Turbines Versus Wind Turbines at Multi-Megawatt Scale, *9th European Wave and Tidal Energy Conference*.

Whelan, J. I., Graham, J. M. R. and Peiró, J. (2009a). A free-surface and blockage correction for tidal turbines, *Journal of Fluid Mechanics* **624**: 281–291.

Whelan, J. I., Graham, J. M. R. and Peiró, J. (2009b). Inertia Effects on Horizontal Axis Tidal-Stream Turbines, *8th European Wave and Tidal Energy Conference, Uppsala, Sweden*.

Wolf, J. and Prandle, D. (1999). Some observations of wave-current interaction, *Coastal Engineering* **37**(3-4): 471–485.

Young, Y. L., Motley, M. R. and Yeung, R. W. (2010). Three-Dimensional Numerical Modeling of the Transient Fluid-Structural Interaction Response of Tidal Turbines, *Journal of Offshore Mechanics and Arctic Engineering* **132**(1).

Zaman, M. H. (2008). Suppression of ocean waves by uniform forced currents, *27th International Conference on Offshore Mechanics and Arctic Engineering*.

Zheng, J., Li, T., Yan, Y. and Hu, J. (2008). Experimental study on mean velocity profiles under wave-current interactions, *International Conference on Offshore Mechanics and Arctic Engineering*.

Appendix A

Scaling

The model turbine experiment was 1:20th scale relative to a full-scale SeaGen device (Marine Current Turbines, 2012) e.g. the turbine scale factor was 1/20. By using realistic full-scale site conditions it was possible to apply Froude scaling to determine the relative wave height, wave period and current speed range for the experiment. Froude scaling was using rather than Reynolds scaling because of the inclusion of waves; gravity being more important than viscosity. The Reynolds number is still important but it was not possible to increase this without adversely affecting the Froude scaling e.g. using an unrealistically high current speed. To scale length, one multiplies the full-scale value by the scale factor. Time and speed are scaled by multiplying by the square root of the scale factor. The wavelength is found by solving the water surface phase speed equated to the depth-dependent phase speed (dispersion relation divided by the wave number). See Table A.1 for an example of scaled monochromatic waves.

Real Sea	Value	Unit	Scale	Towing Tank	Value	Unit
wave height	1.6	m	0.05	**wave height**	**0.080**	m
wave period	6.0	s		**wave period**	**1.342**	s
wave length	56.2	m		wave length	2.809	m
water depth	37.0	m		water depth	1.880	m
current speed	4.0	ms^{-1}		**current speed**	**0.894**	ms^{-1}
wave number	0.1118	m^{-1}		wave number	2.2367	m^{-1}
wave frequency	0.1667	Hz		wave frequency	0.7454	Hz
phase speed: $c = \frac{2\pi f}{k}$ (water surface)	9.3631	ms^{-1}		phase speed	2.0938	ms^{-1}
phase speed: $c = \sqrt{\frac{g}{k}\tanh{(kh)}}$ (intermediate depth)	9.3631	ms^{-1}		phase speed	2.0938	ms^{-1}
$\lvert(c - c)\rvert$	0	-	check	abs(c-c)	0	-
Froude number	0.210	-		Froude number	0.208	-
approx. width of channel	10000	m		width of channel	3.70	m
hydraulic diameter	147	m		hydraulic diameter	3.73	m
tank Reynolds number	3.9E+08	-		tank Reynolds number	2.2E+06	-
approx. mean chord length	0.7000	m		mean chord length	0.0350	m
blade Reynolds number	1.8E+06	-		blade Reynolds number	2.1E+04	-

Table A.1: Experimental Scaling: Froude number Scaling with Calculation of Reynolds Numbers

Appendix B

Blockage Correction

Blockage corrections were not applied to any of the data presented. The reason is a lack of agreement between the blockage corrections. Blockage comparisons have been presented based on work by Barnsley and Wellicome in Bahaj et al. (2005), Garrett and Cummins (2007) and Whelan et al. (2009a) showing the relative disparity between the methods (Figure B.1 and Figure B.2). Knowing which, if any, of the corrections is suitable for application to experimental data is unclear. Normally the blockage corrections would be applied only to experimental data which has been subject to blockage e.g. a turbine in a towing tank (the blockage here was 7%), BEM data was used here only for the sake of clarity, showing a greater range of TSR than possible by experiment.

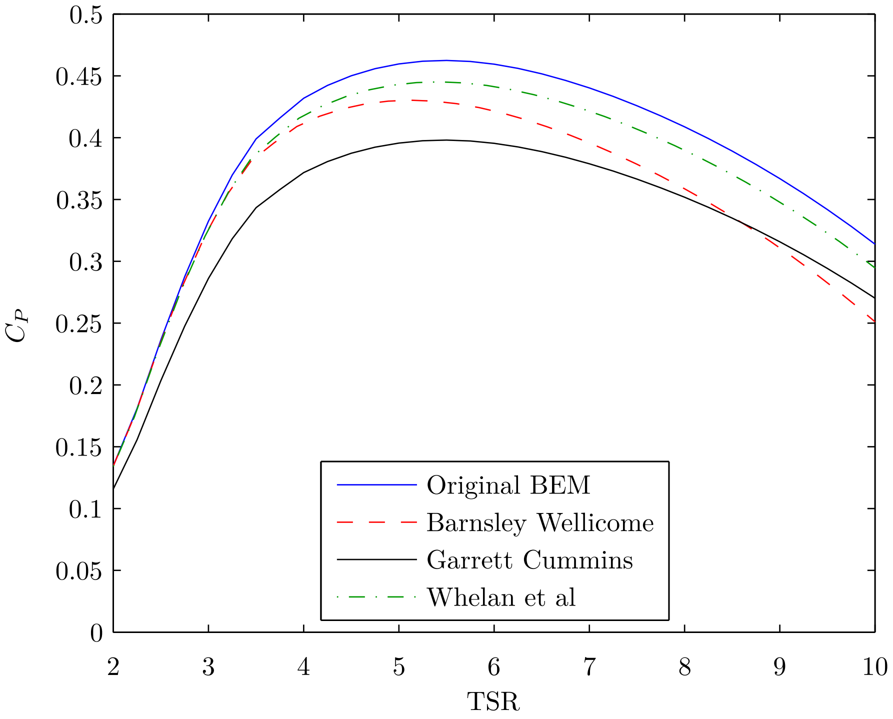

Figure B.1: Examples of blockage corrections for the coefficient of Power

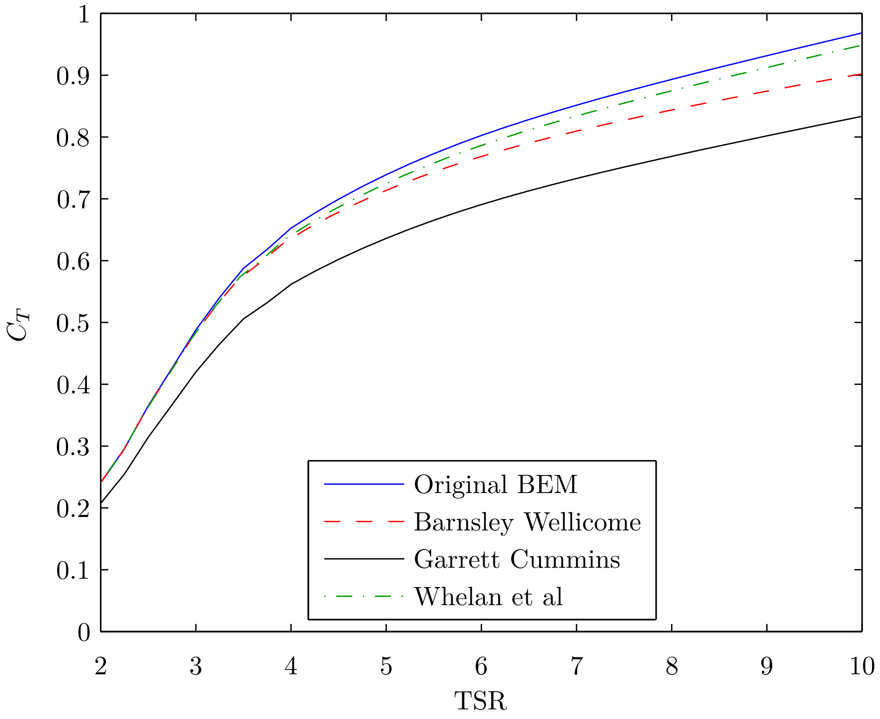

Figure B.2: Examples of blockage corrections for the coefficient of Thrust

Appendix C

Model Turbine Assembly Photos

Additional photographs depicting model turbine assembly, monitoring equipment and experimental set-up.

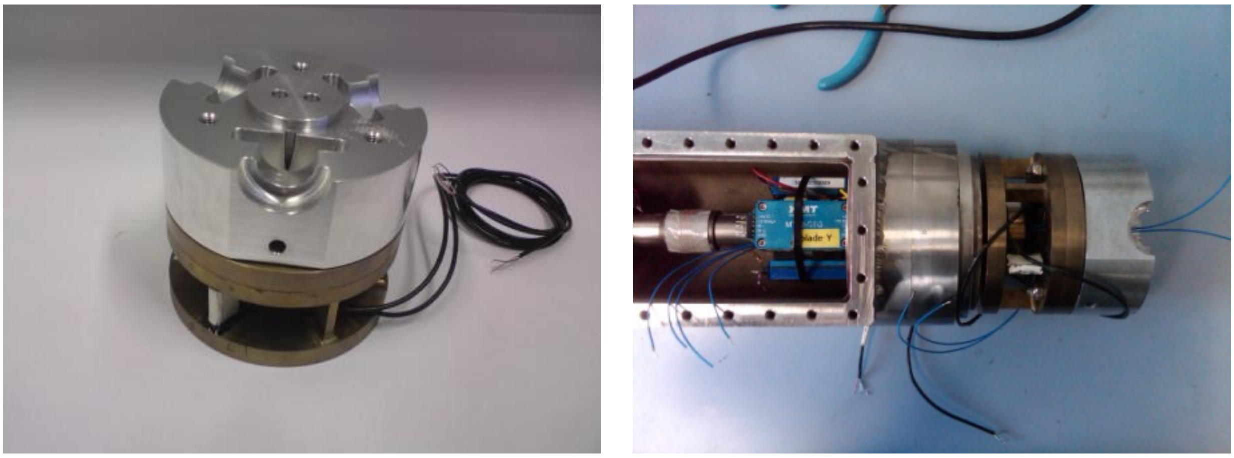

(a) Dynamometer with Lower Hub (b) Threading the strain gauge wiring through the shaft

Figure C.1: Dynamometer

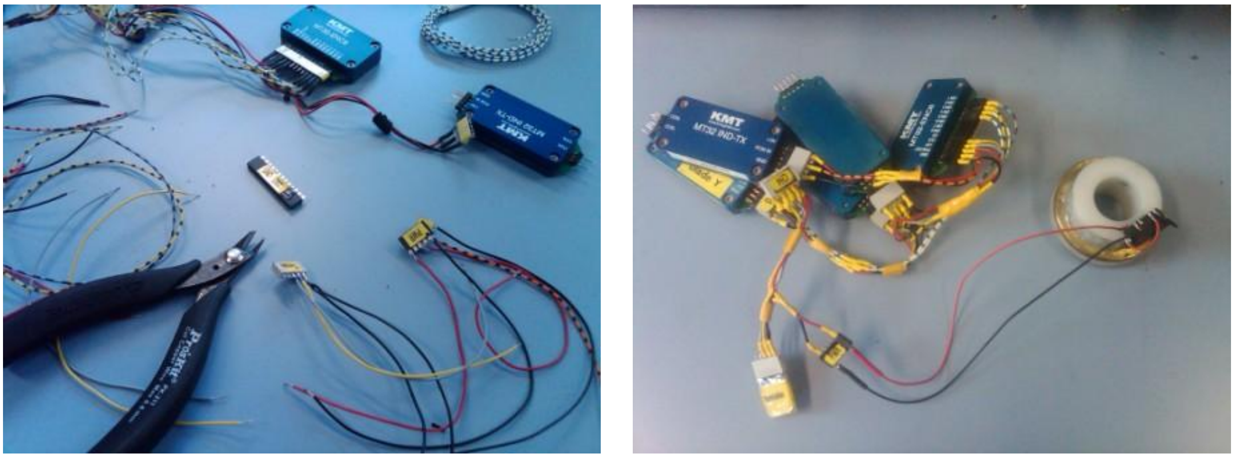

(a) Wiring Loom (b) Amplifier boxes connected to Slip-Rings

Figure C.2: Strain Gauge Amplifiers

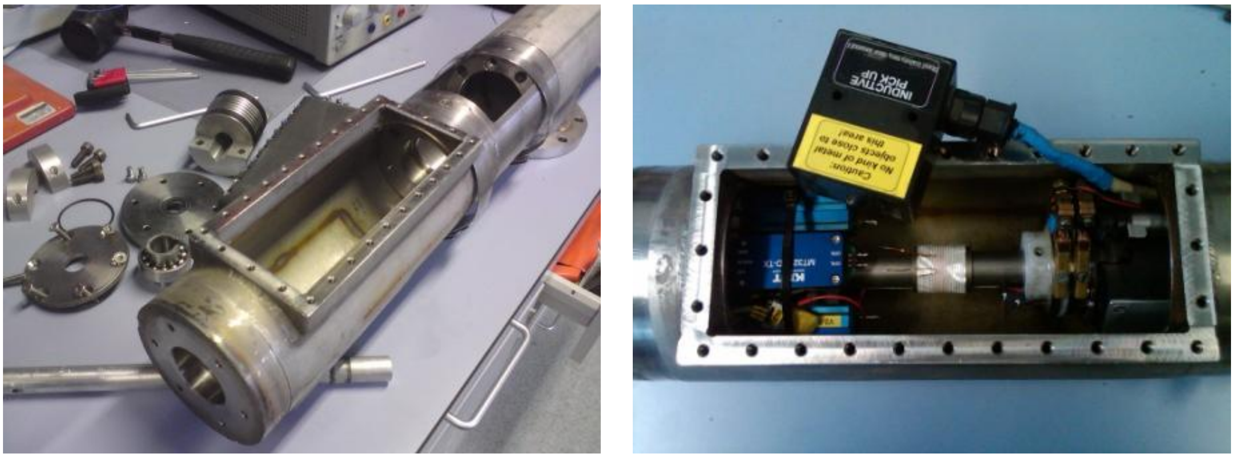

(a) Nacelle and Drive-Train Parts (b) Nacelle Monitoring Equipment

Figure C.3: Nacelle Drive-Train and Electronics

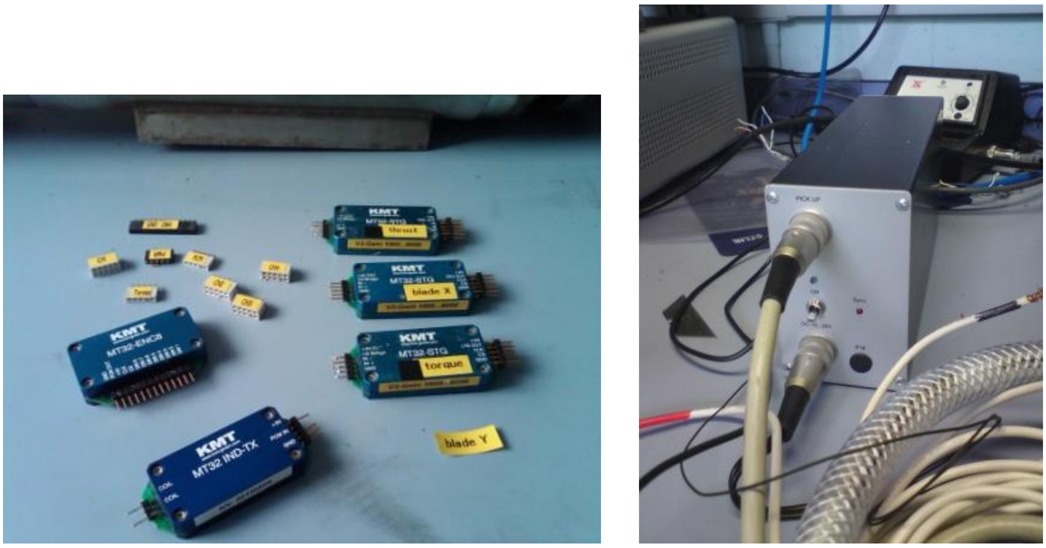

(a) Strain Gauge Amplifiers (b) Telemetry Decoding Box

Figure C.4: Wireless Telemetry System

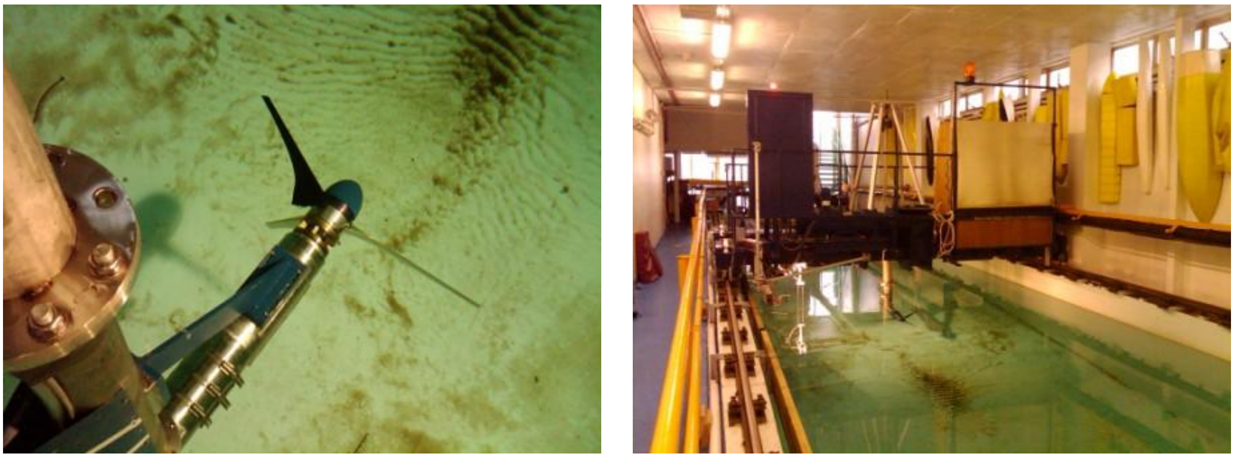

(a) Turbine Mounted on Carriage (b) View of Turbine and Carriage above Towing Tank

Figure C.5: View of Experimental Set-up

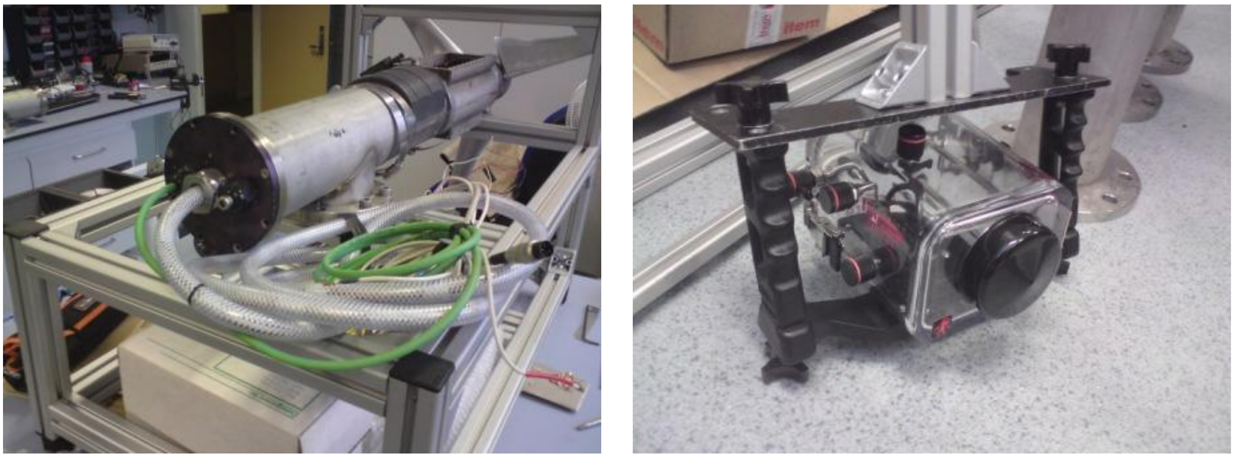

(a) Waterproof Turbine Umbilical (b) Underwater Camera Housing

Figure C.6: Data transmission and Digital Image Capture

Appendix D

Modified BEM Matlab Code

Full reproduction of modified blade element-momentum code. BEM_FAST is the main code, the rest being sub-routines or functions. Example input parameters have been provide in Appendix E.

```
% Numerical Model to compare experimental data
% with modified BEM theory and FAST
% 10/07/11. Pascal Galloway.

clear all;
close all;

%% Load a post-processed experimental data file
% for a unique TSR, YAW and WAVE height and period

tic

[FileList] = getfilelist(...
    'C:\Documents and Settings\pwg204\My Documents\MATLAB\LabVIEW\'...
    ,'mat','false');
%extract location of measurement from filename and store filelist array
[FileListFAST] = getfilelist(...
    'C:\Documents and Settings\pwg204\My Documents\MATLAB\FAST_BEM_comp\'...
    ,'out','false');
%extract location of measurement from filename and store filelist array

for p = [6 46 61 76 86]
    %blockage correction
    % A = pi*0.4^2; %turbine area
    % Ac = 1.88*3.7; %channel area
    % CTT = CT;
    % fact = blockage_BandW(CTT,A,Ac); %Barnsley & Wellicome
    % F1 = F1.*(fact^2); %blockage correction
    % F2 = F2.*(fact^3); %blockage correction

    load(FileList{p})

    % calibration corrections for blade loading
    Sflap = Sflap*1; %out-of-plane bending moment (Nm)
    Sedge = Sedge*1; %in-plane bending moment (Nm)

    FS3 = FS3*(3/2); %out-of-plane blade load (N)
    FS4 = FS4*(3/2); %in-plane blade load (N)
```

```
% V = 3M/2L (triangular cantilever with max load at end)
% These loads to be used with caution! Triangular load assumption not
% particularly accurate

file = (FileList{p});
file = file(62:end-4); %crops out relevant filename
fnamebreak = textscan(file, '%s', 'delimiter', '_');
YAW = textscan(fnamebreak{1,1}{3,1}, '%[^yaw]');
YAW = str2double(strrep(YAW{1,1}{1,1},',','.'));
timeEXP = time;
if length(fnamebreak{1,1}) == 5
    WAVES = 0;
    Ti = 6;
    H = 2;
    if strcmp(fnamebreak{1,1}{5,1},'middepth') == 1
        zh = -0.9;
    elseif strcmp(fnamebreak{1,1}{5,1},'thirddepth') == 1
        zh = -0.67;
    else
        disp(' hub depth error: check variable ''zh''')
        return
    end
elseif length(fnamebreak{1,1}) == 6
    WAVES = 1;
    Ti = textscan(fnamebreak{1,1}{4,1}, '%[^Hz]');
    Ti = 1/str2double(strrep(Ti{1,1}{1,1},',','.')); %Hz -> Ti
    H = textscan(fnamebreak{1,1}{5,1}, '%[^mm]');
    H = str2double(strrep(H{1,1}{1,1},',','.'))/1000; %mm -> m
    if strcmp(fnamebreak{1,1}{6,1},'middepth') == 1
        zh = -0.9;
    elseif strcmp(fnamebreak{1,1}{6,1},'thirddepth') == 1
        zh = -0.67;
    else
        disp(' hub depth error: check variable ''zh''')
        return
    end
else
    disp(' filename error: check variable ''file''')
    return
end

%% Running BEM code based on experimental data parameters
d = 1.88; %water depth
U = 0.9; %carriage speed
R = 0.4; %rotor radius
B = 3; %No. blades
BLADE = 'LUKE'; %blade type (LUKE, WILL or WEH)
blade = 1; %blade ref (LUKE=1, WILL=2 or WEH=3)
% NOTE - adjust mass moment if not using blade 1
SET_PITCH = 0.25; %blade pitch (LUKE=0.25, WILL=5.0 or WEH=7.0)

PSIi = 30; %number of azimuthal nodes (integer)
% e.g. 30 gives node every 12 degrees
no_rev = 50; %number of full blade revolutions (integer)

%%%% PERMANENT FIX TO PREVENT ERROR WITH SKEWED INFLOW %%%%
if WAVES == 1
    origYAW = YAW;
    YAW = 0;
end

%%%%%%%%%%%%%%%%%%%%%%%%%%%%%%%%%%%%%%%%%%%%%%%%%%%%%%%
DATA_bem_compiler_wave_yaw_3Blade %Script to run BEM
% re-write this as a function later
%%%%%%%%%%%%%%%%%%%%%%%%%%%%%%%%%%%%%%%%%%%%%%%%%%%%%%%

% in-plane gravitational bending (LUKE'S blade)
BMASS = 1; %set to 0 to ignore gravitational component, 1 to include
MassMom = 0;
```

```
if BMASS == 1
    LeverArm = (97.57 + 21)/1000; %metres
    % 97.57mm is center of mass of blade (length wise)
    % 21mm is to hub centre from root section
    BladeMass = 0.351; %kg
    MassMom = (LeverArm*BladeMass*9.81*sin(PSI))/3; %Nm
end

W = (U.*(1-AA))./sin(PHIn);
W2 = (U.*(1-AA2))./sin(PHI2n);
W3 = (U.*(1-AA3))./sin(PHI3n);
% irregularities in AA and PHI cause large discrepancies in W,
% affecting calculations. errors are removed and smoothing applied
for j = 1:length(W(:,1))
    for i = 1:length(W(1,:))
        if W(j,i) > 12
            W(j,i) = NaN;
        end
        if W2(j,i) > 12
            W2(j,i) = NaN;
        end
        if W3(j,i) > 12
            W3(j,i) = NaN;
        end
        if W(j,i) < 0
            W(j,i) = NaN;
        end
        if W2(j,i) < 0
            W2(j,i) = NaN;
        end
        if W3(j,i) < 0
            W3(j,i) = NaN;
        end
        if W(j,i) == 0
            W(j,i) = NaN;
        end
        if W2(j,i) == 0
            W2(j,i) = NaN;
        end
        if W3(j,i) == 0
            W3(j,i) = NaN;
        end
    end
end
W = naninterp(W,'cubic'); %cubic interpolation of removed data
W2 = naninterp(W2,'cubic'); %cubic interpolation of removed data
W3 = naninterp(W3,'cubic'); %cubic interpolation of removed data
W = sgolayfilt(W,3,31); %extra smoothing
W2 = sgolayfilt(W2,3,31); %extra smoothing
W3 = sgolayfilt(W3,3,31); %extra smoothing
for J = 1:length(PSI)
    CXi(J) = simprule(DCXDXn(J,:),X(1),X(end));
    CYi(J) = simprule(DCYDXn(J,:),X(1),X(end));
    CXi2(J) = simprule(DCX2DXn(J,:),X(1),X(end));
    CYi2(J) = simprule(DCY2DXn(J,:),X(1),X(end));
    CXi3(J) = simprule(DCX3DXn(J,:),X(1),X(end));
    CYi3(J) = simprule(DCY3DXn(J,:),X(1),X(end));
end

% blade dynamic inflow coefficients
[CXD1,CXD2,CXD3,CXDT] = dynamic_inflow_GALL_W(U,R,W,W2,W3,PSI,TSR);

for J = 1:length(PSI)
    for I = 1:length(X)
        %WEH 3.140 (N) - axial blade force
        FX(J,I) =  0.5*1000*(W(J,I)^2)*CR(I)*(R^1)*CXi(J)*0.34;
        %DYNAMIC CORRECTION
        FXD(J,I) = 0.5*1000*(W(J,I)^2)*CR(I)*(R^1)*CXD1(J,I)*0.34;
        %WEH 3.140 (N) - tangential blade force
```

```
        FY(J,I) =  0.5*1000*(W(J,I)^2)*CR(I)*(R^1)*CYi(J)*0.34;
        %WEH 3.141 (Nm) – blade torque
        Q(J,I)  =  0.5*1000*(W(J,I)^2)*CR(I)*(R^2)*X(I)*CYi(J)*0.34;
        %WEH 3.142 (Nm)
        MZ(J,I) =  0.5*1000*(W(J,I)^2)*CR(I)*(R^1)*X(I)...
            *sin(PHIn(J,I))*CXi(J)*(0.34^2)*cos(THETA(I));
        %WEH 3.143 (Nm)
        MY(J,I) =  0.5*1000*(W(J,I)^2)*CR(I)*(R^1)*X(I)...
            *cos(PHIn(J,I))*CXi(J)*(0.34^2)*cos(THETA(I));
        %DYNAMIC CORRECTION
        MYD(J,I) =  0.5*1000*(W(J,I)^2)*CR(I)*(R^1)*X(I)...
            *CXD1(J,I)*(0.34^2)*cos(THETA(I));

        FX2(J,I) = 0.5*1000*(W2(J,I)^2)*CR(I)*(R^1)*CXi2(J)*0.34;
        FXD2(J,I) = 0.5*1000*(W2(J,I)^2)*CR(I)*(R^1)*CXD2(J,I)*0.34;
        FY2(J,I) = 0.5*1000*(W2(J,I)^2)*CR(I)*(R^1)*CYi2(J)*0.34;
        Q2(J,I) =  0.5*1000*(W2(J,I)^2)*CR(I)*(R^2)*X(I)*CYi2(J)*0.34;
        MZ2(J,I) = 0.5*1000*(W2(J,I)^2)*CR(I)*(R^1)*X(I)...
            *sin(PHI2n(J,I))*CXi2(J)*(0.34^2)*cos(THETA(I));
        MY2(J,I) = 0.5*1000*(W2(J,I)^2)*CR(I)*(R^1)*X(I)...
            *cos(PHI2n(J,I))*CXi2(J)*(0.34^2)*cos(THETA(I));
        MYD2(J,I) =  0.5*1000*(W2(J,I)^2)*CR(I)*(R^1)*X(I)...
            *CXD2(J,I)*(0.34^2)*cos(THETA(I));

        FX3(J,I) = 0.5*1000*(W3(J,I)^2)*CR(I)*(R^1)*CXi3(J)*0.34;
        FXD3(J,I) = 0.5*1000*(W3(J,I)^2)*CR(I)*(R^1)*CXD3(J,I)*0.34;
        FY3(J,I) = 0.5*1000*(W3(J,I)^2)*CR(I)*(R^1)*CYi3(J)*0.34;
        Q3(J,I) =  0.5*1000*(W3(J,I)^2)*CR(I)*(R^2)*X(I)*CYi3(J)*0.34;
        MZ3(J,I) = 0.5*1000*(W3(J,I)^2)*CR(I)*(R^1)*X(I)...
            *sin(PHI3n(J,I))*CXi3(J)*(0.34^2)*cos(THETA(I));
        MY3(J,I) = 0.5*1000*(W3(J,I)^2)*CR(I)*(R^1)*X(I)...
            *cos(PHI3n(J,I))*CXi3(J)*(0.34^2)*cos(THETA(I));
        MYD3(J,I) =  0.5*1000*(W3(J,I)^2)*CR(I)*(R^1)*X(I)...
            *CXD3(J,I)*(0.34^2)*cos(THETA(I));
    end
end
for J = 1:length(PSI)
    FXi(J) = simprule(FX(J,:),X(1),X(end)); %(N)
    FXDi(J) = simprule(FXD(J,:),X(1),X(end));

    FYi(J) = simprule(FY(J,:),X(1),X(end)); %(N)
    Qi(J) =  simprule(Q(J,:),X(1),X(end)); %(Nm)
    MZi(J) = simprule(MZ(J,:),X(1),X(end)); %(Nm)
    MYi(J) = simprule(MY(J,:),X(1),X(end)); %(Nm)
    MYDi(J) = simprule(MYD(J,:),X(1),X(end)); %(Nm)

    FXi2(J) = simprule(FX2(J,:),X(1),X(end));
    FYi2(J) = simprule(FY2(J,:),X(1),X(end));
    Qi2(J) =  simprule(Q2(J,:),X(1),X(end));
    MZi2(J) = simprule(MZ2(J,:),X(1),X(end));
    MYi2(J) = simprule(MY2(J,:),X(1),X(end));
    FXi3(J) = simprule(FX3(J,:),X(1),X(end));
    FYi3(J) = simprule(FY3(J,:),X(1),X(end));
    Qi3(J) =  simprule(Q3(J,:),X(1),X(end));
    MZi3(J) = simprule(MZ3(J,:),X(1),X(end));
    MYi3(J) = simprule(MY3(J,:),X(1),X(end));
end

% figure(1)
% plot(time,FX,'b'); hold on; plot(time,FXD,'r'); hold off;
% plot(time,FXi); hold on; plot(time,mean(FXi)+FXDi,'r'); hold off;
% figure(2)
% plot(time,MY,'b'); hold on; plot(time,MYD,'r'); hold off;
% plot(time,MYi); hold on; plot(time,mean(MYi)+MYDi,'r'); hold off;


%% Comparison
```

```
%     % PSDs of data: [Pxx,f] = pwelch(x,window,noverlap,nfft,fs)
%     samprate = 1/(time(2)-time(1)); %Hz
%     LW1 = length(MYi);
%     LW2 = length(Sflap);
%     window1 = hamming(LW1);
%     window2 = hamming(LW2);
%     [pFFLAP,psdFLAP] = pwelch(MYi-mean(MYi),window1,[],[],samprate);
%     [pFEDGE,psdEDGE] = ...
%         pwelch(MZi+MassMom-mean(MZi+MassMom),window1,[],[],samprate);
%     [pFTHRU,psdTHRU] = pwelch(Tt-mean(Tt),window1,[],[],samprate);
%     [pFTORQ,psdTORQ] = pwelch(Qt-mean(Qt),window1,[],[],samprate);
%     [pFFLAPe,psdFLAPe] = pwelch(Sflap-mean(Sflap),window2,[],[],sr);
%     [pFEDGEe,psdEDGEe] = pwelch(Sedge-mean(Sedge),window2,[],[],sr);
%     [pFTHRUe,psdTHRUe] = pwelch(F1-mean(F1),window2,[],[],sr);
%     [pFTORQe,psdTORQe] = pwelch(F2-mean(F2),window2,[],[],sr);

% closing figures
close(10); close(11); close(12); close(13); close(20); close(30);

figure(p+99)
% include figure set-up for matlabfrag here

subplot(2,1,1);
hold on;
plot(timeEXP,Sflap,'b','linewidth',2);
plot(time,mean(MYi)+MYDi,'c')
hold off;
ylim([3 16]); xlim([2 14])
xlabel('Time (s)'); ylabel('Out-of-plane root BM  (Nm)');
title('Out-of-plane blade root bending moment time series')

subplot(2,1,2);
%plot(time,Qi+MassMom,'--r'); hold on; %plot(time,Qt/B,'g');
plot(timeEXP,Sedge,'b','linewidth',2); %hold off;
ylim([0.5 4.5]); xlim([2 14])
text(2.5,0.75,strrep(fname,'_',' '));
xlabel('Time (s)'); ylabel('In-plane root BM (Nm)');
title('In-plane blade root bending moment time series');
%set(gca,'XTickLabel',[])

%     subplot(4,1,3)
%     hold on
%     plot(psdFLAP,pFFLAP,'--r');
%     plot(psdFLAPe,pFFLAPe,'b','linewidth',2);
%     % ylim([0 0.01]);
%     xlim([0 6]);
%     hold off;
%     % legend('Numerical','Experimental','Location','East',...
%     'Orientation','horizontal')
%     title('PSD of out-of-plane signals')
%     xlabel('Frequency (Hz)'); ylabel('Pa^2/Hz')
%     maxa = max(pFFLAP); maxb = max(pFFLAPe); maxc = max(maxa,maxb);
%     line([rps rps],[0 maxc],'linestyle',':','color','black');
%     %rotational frequency
%     text(rps+0.05, maxc,'1P','HorizontalAlignment','left');
%     %annotate the point (rps, maxc)
%     line([2*rps 2*rps],[0 maxc],'linestyle',':','color','black');
%     %rotational frequency
%     text(2*rps+0.05, maxc,'2P','HorizontalAlignment','left');
%     %annotate the point (rps, maxc)
%     line([3*rps 3*rps],[0 maxc],'linestyle',':','color','black');
%     %rotational frequency
%     text(3*rps+0.05, maxc,'3P','HorizontalAlignment','left');
%     %annotate the point (rps, maxc)
%     if WAVES ~= 0
%         k = (2*pi)/L; %wavenumber
%         Ta = (2*pi*Ti)/(2*pi + Ti*k*U); %apparent wave period
%         line([1/Ta 1/Ta],[0 maxc],'linestyle',':','color','black');
%         %wave frequency
```

```
%         text(1/Ta+0.05, maxc,'1Ta','HorizontalAlignment','left');
%         %annotate the point (rps, maxc)
%     end
%
%     subplot(4,1,4)
%     hold on
%     plot(psdEDGE,pFEDGE,'--r');
%     plot(psdEDGEe,pFEDGEe,'b','linewidth',2);
%     % ylim([0 0.01]);
%     xlim([0 6]);
%     hold off;
%     title('PSD of in-plane signals')
%     xlabel('Frequency (Hz)'); ylabel('Pa^2/Hz')
%     maxa = max(pFEDGE); maxb = max(pFEDGEe); maxc = max(maxa,maxb);
%     line([rps rps],[0 maxc],'linestyle',':','color','black');
%     text(rps+0.05, maxc,'1P','HorizontalAlignment','left');
%     line([2*rps 2*rps],[0 maxc],'linestyle',':','color','black');
%     text(2*rps+0.05, maxc,'2P','HorizontalAlignment','left');
%     line([3*rps 3*rps],[0 maxc],'linestyle',':','color','black');
%     text(3*rps+0.05, maxc,'3P','HorizontalAlignment','left');
%     if WAVES ~= 0
%         line([1/Ta 1/Ta],[0 maxc],'linestyle',':','color','black');
%         text(1/Ta+0.05, maxc,'1Ta','HorizontalAlignment','left');
%     end

%% FAST output data
out = importdata(FileListFAST{p});
FASTt = out.data(:,1); %time (FAST)
RootMyc1 = out.data(:,16);
%Blade 1 out-of-plane moment
%at the blade root About the yc,1-axis  (kNm)
RootMxc1 = out.data(:,17);
%Blade 1 in-plane moment
%at the blade root About the xc,1-axis  (kNm)
RootMyb1 = out.data(:,22);
%Blade 1 flapwise moment
%at the blade root About the yb,1-axis  (kNm)
RootMxb1 = out.data(:,23);
%Blade 1 edgewise moment
%at the blade root About the xb,1-axis  (kNm)
RotThrust = out.data(:,24);
%shaft thrust (kN)
RotTorq = out.data(:,25);
%shaft torque About the xa- and xs-axes (kNm)

% This while loop phase shifts the data for matching
% (requires user input)
l1 = 0;
shift = 0;
int1 = 5; %step change (increase this for faster phase shifting)
while shift == 0
    subplot(2,1,1);
    hold on
    RootF = circshift(RootMyc1*1000,l1);
    flap = plot(FASTt,RootF,'--r');
    hold off;

    subplot(2,1,2);
    hold on;
    RootE = circshift(RootMxc1*1000,l1);
    edge = plot(FASTt,RootE,'--r');
    hold off;
    shift = input('good fit? yes [1], no [] : ');
    if isempty(shift) == 1
        shift = 0;
        delete(flap)
        delete(edge)
    end
```

```
    l1 = l1 - int1;
end

samprateFAST = 1/(FASTt(2)-FASTt(1));
LW3 = length(RootMyc1);
window3 = hamming(LW3);
[pfast_outplane,psdfast_outplane] = pwelch((RootMyc1*1000)...
    -mean(RootMyc1*1000),window3,[],[],samprateFAST);
[pfast_inplane,psdfast_inplane] = pwelch((RootMxc1*1000)...
    -mean(RootMxc1*1000),window3,[],[],samprateFAST);

%     subplot(4,1,3)
%     hold on
%     plot(psdfast_outplane,pfast_outplane,'g');
%     xlim([0 6]);
%     hold off;
%
%     subplot(4,1,4)
%     hold on
%     plot(psdfast_inplane,pfast_inplane,'g');
%     xlim([0 6]);
%     hold off;

delete([fname,'.mat']);

%% dynamic inflow

[FXPn,FXP2n,FXP3n,FXPTn] = ...
    dynamic_inflow_GALL_C(U,R,X,PSI,DCXDXn,DCX2DXn,DCX3DXn);
[FYPn,FYP2n,FYP3n,FYPTn] = ...
    dynamic_inflow_GALL_C(U,R,X,PSI,DCYDXn,DCY2DXn,DCY3DXn);
MYi = FXPn+mean(MYi);
MZi = FYPn/3+mean(MZi);
Qi = FYPn/3+mean(Qi);
Qi = Qi';

% [FXP,FXP2,FXP3,FXPT] = ...
% dynamic_inflow_PITT(U,R,X,PSI,DCTDXn,DCT2DXn,DCT3DXn);
% Tt_new = FXPT+mean(Tt);
% MYi_new_pitt = FXPT/6+mean(MYi);

figure(p+99)
l2 = 0;
shift2 = 0;
int2 = 2; %step change
while shift2 == 0
    subplot(2,1,1);
    hold on
    MYin = MYi';
    MYinn = circshift(MYin,l2);
    flap2 = plot(time,MYinn,'k');
    hold off

    subplot(2,1,2);
    hold on
    Qin = Qi+MassMom;
    Qinn = Qin';
    Qinnn = circshift(Qinn,l2);
    edge2 = plot(time,Qinnn,'k');
    hold off
    shift2 = input('good fit? yes [1], no [] : ');
    legend('Experimental Data','NWTC-FAST','Modified BEM',...
        'Location','NorthEast','Orientation','horizontal')
    if isempty(shift2) == 1
        shift2 = 0;
        delete(flap2)
        delete(edge2)
    end
```

```
        l2 = l2 - int2;
    end
    %         subplot(4,1,3)
    %         hold on
    %         plot(psdFLAPn,pFFLAPn,'k');
    %         hold off
    %         subplot(4,1,4)
    %         hold on
    %         plot(psdEDGEn,pFEDGEn,'k');
    %         hold off


    %% Printing .eps and .tex
    %     matlabfrag('filename');

    %% Delete saved BEM data
    disp(['  ',fname])
    delete([fname,'.mat']);

end

tElapsed = toc;
%display run time
disp(['  Run Time (seconds): ',num2str(round(tElapsed))])




% Blade Element-Momentum code for Tidal Turbines
% 08/03/11. Pascal Galloway.

% Program details
disp(' ')
disp(' Tidal Turbine Prediction Program');
disp(' --------------------------------')
disp(' By P. W. Galloway');
disp(' BEM Theory with the inclusion of wave and yaw capability');
disp(' Dynamic Stall and Dynamic Inflow can be modelled');
disp(' ');

DRAG_FACT = 1; %drag factor???
DTOR = 0.017453292; %degrees to radians
RTOD = 1.0/DTOR; %radians to degrees

L = Airy_Wavelength(d,Ti); %derive wavelength

if blade == 2; % WILL'S BLADE DATA
    rR = [0.2 0.25 0.3 0.35 0.4 0.45 0.5 0.55 0.6 0.65 0.7 0.75...
        0.8 0.85 0.9 0.95 1.0]; %r/R
    cR = [0.125 0.1203 0.1156 0.1109 0.1063 0.1016 0.0969 0.0922...
        0.0875 0.0828 0.0781 0.0734 0.0688 0.0641 0.0594 0.0547 0.05]; %c/R
    twist = [15 12.1 9.5 7.6 6.1 4.9 3.9 3.1 2.4 1.9 1.5 1.2 0.9...
        0.6 0.4 0.2 0]; %degrees relative to blade tip
    thick = [24.0 22.5 20.7 19.5 18.7 18.1 17.6 17.1 16.6 16.1 15.6...
        15.1 14.6 14.1 13.6 13.1 12.6]; %max thickness relative to rR
elseif blade == 1; % LUKE'S BLADE DATA
    rR = [0.15 0.2 0.25 0.3 0.35 0.4 0.45 0.5 0.55 0.6 0.65 0.7 0.75...
        0.8 0.85 0.9 0.95 1];
    cR = [0.2425 0.2105 0.185 0.15875 0.141 0.12625 0.115 0.10525...
        0.09775 0.09075 0.0845 0.079 0.07325 0.0685 0.065 0.0625...
        0.06 0.05775];
    twist = [27.3 23.1 20 16.3 13.8 12.6 11 9.5 8.2 7.4 6.8 5.8...
        5 4.5 4 3.6 3.3 3.1];
    thick = [26 24 22.5 20.8 19.5 18.7 18.1 17.1 16.6 16.2 15.6...
        15.1 14.6 14.1 13.6 13.1 12.61 12.6];
elseif blade == 3; % W.E.H. BLADE DATA
    rR = [0.20 0.25 0.30 0.35 0.40 0.45 0.50 0.55 0.60 0.65 0.70...
        0.75 0.80 0.85 0.90 0.95 1.00];
    cR = [0.1276 0.1229 0.1182 0.1135 0.1088 0.1041 0.0994 0.0947...
```

```
        0.0900 0.0853 0.0806 0.0759 0.0712 0.0665 0.0618 0.0571 0.0524];
    twist = [15.0 12.1 9.5 7.6 6.1 4.9 3.9 3.1 2.4 1.9 1.5 1.2 0.9...
        0.6 0.4 0.2 0.0];
    thick = [24.6 22.5 20.7 19.5 18.7 18.1 17.6 17.1 16.6 16.1 15.6...
        15.1 14.6 14.1 13.6 13.1 12.6];
end

err = 1;
while err == 1
    if exist('PSIi','var') == 1
        break
    else
        PSIi = input(' Rotational Increments (degrees), default 15 = ');
        %rotational increments (degrees)
    end
    if isempty(PSIi) == 1
        PSIi = 15;
        err = 0;
    elseif sum(isletter(PSIi)) > 0
        err = 1;
        msgbox('must be a number','BEM (waves & yaw)')
    elseif PSIi > 0 && PSIi < 10
        err = 0;
        msgbox('WARNING: small rotational increments increase run time',...
            'BEM (waves & yaw)','warn')
    elseif PSIi <= 0
        err = 1;
        msgbox('rotational increments must be greater than zero',...
            'BEM (waves & yaw)')
    else
        err = 0;
    end
end

err = 1;
while err == 1
    if exist('no_rev','var') == 1
        break
    else
        no_rev = input(' Number of Blade Revolutions (-), default 50 = ');
        %number of revs
    end
    if isempty(no_rev) == 1
        no_rev = 50;
        err = 0;
    elseif sum(isletter(no_rev)) > 0
        err = 1;
        msgbox('must be a number','BEM (waves & yaw)')
    elseif no_rev < 1
        err = 1;
        msgbox('must complete at least one revolution','BEM (waves & yaw)')
    elseif no_rev > 100
        err = 0;
        msgbox('WARNING: many revoltions increases run time',...
            'BEM (waves & yaw)','warn')
    elseif no_rev*360 < PSIi
        err = 1;
        msgbox('increase number of revolutions','BEM (waves & yaw)')
    else
        err = 0;
    end
end

rps = (TSR.*(U/R))/(2*pi); %revs per sec
rpm = rps*60; %revs per min
PSIL = no_rev*360+1; %must be 'odd' for 'simprule' to work
PSI = (0:PSIi*(pi/180):PSIL*(pi/180)); %azimuth values (radians)

BX = rR;
```

```
BCR = cR;
BTHICK = thick;
BTHETA = twist;
disp([BX' BCR' BTHICK' BTHETA'])

% SET VARIABLES
no_TSR = length(TSR); %No. TSR used
no_YAW = length(YAW); %No. yaw angles used
no_WAVES = length(WAVES);
no_PSI = length(PSI);
ALPHA = zeros(19,no_TSR,no_YAW);
DCPDXA = zeros(19,no_TSR,no_YAW);
DCTDXA = zeros(19,no_TSR,no_YAW);
DCP2DXA = zeros(19,no_TSR,no_YAW);
DCT2DXA = zeros(19,no_TSR,no_YAW);
DCP3DXA = zeros(19,no_TSR,no_YAW);
DCT3DXA = zeros(19,no_TSR,no_YAW);
CL = zeros(19,no_TSR,no_YAW);
CD = zeros(19,no_TSR,no_YAW);
AA = zeros(19,no_TSR,no_YAW);
AT = zeros(19,no_TSR,no_YAW);
CP = zeros(no_TSR,no_YAW);
CT = zeros(no_TSR,no_YAW);
CX = zeros(no_TSR,no_YAW);
CY = zeros(no_TSR,no_YAW);
CP2 = zeros(no_TSR,no_YAW);
CT2 = zeros(no_TSR,no_YAW);
CX2 = zeros(no_TSR,no_YAW);
CY2 = zeros(no_TSR,no_YAW);
CP3 = zeros(no_TSR,no_YAW);
CT3 = zeros(no_TSR,no_YAW);
CX3 = zeros(no_TSR,no_YAW);
CY3 = zeros(no_TSR,no_YAW);
DCXDXA = zeros(19,no_TSR,no_YAW);
DCYDXA = zeros(19,no_TSR,no_YAW);
DCX2DXA = zeros(19,no_TSR,no_YAW);
DCY2DXA = zeros(19,no_TSR,no_YAW);
DCX3DXA = zeros(19,no_TSR,no_YAW);
DCY3DXA = zeros(19,no_TSR,no_YAW);
CKD = zeros(19,no_TSR,no_YAW);
CKD2 = zeros(19,no_TSR,no_YAW);
CKD3 = zeros(19,no_TSR,no_YAW);

%% GET THE BLADE DATA
[X, THETA, CR, THICK, AERO_ANG, AERO_CL, AERO_CD] =...
    get_aero_data_4(blade,BX,BCR,BTHICK,BTHETA);

% figure(1)
% % CHORD LENGTH TO RADIUS RATIO
% subplot(3,1,1)
% plot(X,CR,'xk-');
% ylabel('c/R');
% title('Blade Properties');
% % BLADE TWIST ANGLE
% subplot(3,1,2);
% plot(X,THETA,'xk-');
% ylabel('\theta (degrees)');
% % THICKNESS TO CHORD LENGTH RATIO
% subplot(3,1,3);
% plot(X,THICK,'xk-');
% ylabel('t/c')
% xlabel('X')

% figure(2)
% % LIFT DATA
% subplot(2,1,1)
% hold on;
% plot(AERO_ANG,AERO_CL(:,3),'k:'); %all columns of AERO_CL are identical???
% plot(AERO_ANG,AERO_CL(:,6),'k-');
```

```
% plot(AERO_ANG,AERO_CL(:,13),'k-.');
% plot(AERO_ANG,AERO_CL(:,19),'k--');
% axis([-180 180 -4 4]);
% title('a) Lift forces');
% ylabel('C_L');
% hold off;
% % DRAG DATA
% subplot(2,1,2)
% hold on;
% plot(AERO_ANG,AERO_CD(:,3),'k:');
% plot(AERO_ANG,AERO_CD(:,6),'k-');
% plot(AERO_ANG,AERO_CD(:,13),'k-.');
% plot(AERO_ANG,AERO_CD(:,19),'k--');
% axis([-180 180 -0.2 1.5]);
% legend('r/R ~0.2','r/R ~0.3','r/R ~0.5','r/R ~0.7');
% title('b) Drag forces');
% xlabel('\alpha');
% ylabel('C_D');
% hold off;

%% BEM CODE
for k = 1:no_WAVES
    for j = 1:no_TSR %loop over TSR range
        for i = 1:no_YAW %loop over pitch range
            disp(['  TSR = ' num2str(TSR(j))])
            disp(['  YAW = ' num2str(YAW(i))])
            [fname, CP(j,i), CT(j,i), CX(j,i), CY(j,i), DCPDXA(:,j,i),...
                DCTDXA(:,j,i), DCXDXA(:,j,i), DCYDXA(:,j,i)...
                CP2(j,i), CT2(j,i), CX2(j,i), CY2(j,i), DCP2DXA(:,j,i),...
                DCT2DXA(:,j,i), DCX2DXA(:,j,i), DCY2DXA(:,j,i)...
                CP3(j,i), CT3(j,i), CX3(j,i), CY3(j,i), DCP3DXA(:,j,i),...
                DCT3DXA(:,j,i), DCX3DXA(:,j,i), DCY3DXA(:,j,i)...
                CKD(:,j,i), CKD2(:,j,i), CKD3(:,j,i)] = ...
                my_bem_wave_yaw_3Blade(BLADE, WAVES(k), YAW(i), PSI, ...
                d, H, Ti, U, zh, R, X, THETA+SET_PITCH, CR, AERO_ANG,...
                AERO_CL, AERO_CD, TSR(j), B, L, THICK, no_rev);
        end
    end
end

for i = 1:no_YAW
    for j = 1:no_TSR
        %average coefficients over the three blades
        CPM(j,i) = nanmean([CP(j,i),CP2(j,i),CP3(j,i)]);
        CTM(j,i) = nanmean([CT(j,i),CT2(j,i),CT3(j,i)]);
        CXM(j,i) = nanmean([CX(j,i),CX2(j,i),CX3(j,i)]);
        CYM(j,i) = nanmean([CY(j,i),CY2(j,i),CY3(j,i)]);
    end
end
TSRM = TSR; %to retain values only

%% Loading Data for Unique TSR and YAW angle
load(fname) %load filename

% figure(6) %all 3 blades
% subplot(3,3,1);
% plot(X,ALPHA);
% grid on;
% xlabel('X'); ylabel('ALPHA1');
% subplot(3,3,4);
% plot(X,CL);
% grid on;
% xlabel('X'); ylabel('C_L1');
% subplot(3,3,7);
% plot(X,CD);
% grid on;
% xlabel('X'); ylabel('C_D1');
% subplot(3,3,2);
% plot(X,ALPHA2);
```

```
% grid on;
% xlabel('X'); ylabel('ALPHA2');
% subplot(3,3,5);
% plot(X,CL2);
% grid on;
% xlabel('X'); ylabel('C_L2');
% subplot(3,3,8);
% plot(X,CD2);
% grid on;
% xlabel('X'); ylabel('C_D2');
% subplot(3,3,3);
% plot(X,ALPHA3);
% grid on;
% xlabel('X'); ylabel('ALPHA3');
% subplot(3,3,6);
% plot(X,CL3);
% grid on;
% xlabel('X'); ylabel('C_L3');
% subplot(3,3,9);
% plot(X,CD3);
% grid on;
% xlabel('X'); ylabel('C_D3');

% figure(7) %all 3 blades
% subplot(3,3,1);
% plot(X,AA);
% grid on;
% xlabel('X'); ylabel('AA1');
% subplot(3,3,4);
% plot(X,AT);
% grid on;
% xlabel('X'); ylabel('AT1');
% subplot(3,3,7);
% plot(X,DCPDX);
% grid on;
% xlabel('X'); ylabel('C_P1');
% figure(7)
% subplot(3,3,2);
% plot(X,AA2);
% grid on;
% xlabel('X'); ylabel('AA2');
% subplot(3,3,5);
% plot(X,AT2);
% grid on;
% xlabel('X'); ylabel('AT2');
% subplot(3,3,8);
% plot(X,DCP2DX);
% grid on;
% xlabel('X'); ylabel('C_P2');
% figure(7)
% subplot(3,3,3);
% plot(X,AA3);
% grid on;
% xlabel('X'); ylabel('AA3');
% subplot(3,3,6);
% plot(X,AT3);
% grid on;
% xlabel('X'); ylabel('AT3');
% subplot(3,3,9);
% plot(X,DCP3DX);
% grid on;
% xlabel('X'); ylabel('C_P3');

% figure(8) %all 3 blades
% subplot(3,3,1);
% plot(X,DCTDX);
% grid on;
% xlabel('X'); ylabel('C_T1');
% subplot(3,3,4);
```

```
% plot(X,DCXDX);
% grid on;
% xlabel('X'); ylabel('C_X1');
% subplot(3,3,7);
% plot(X,DCYDX);
% grid on;
% xlabel('X'); ylabel('C_Y1');
% subplot(3,3,2);
% plot(X,DCT2DX);
% grid on;
% xlabel('X'); ylabel('C_T2');
% subplot(3,3,5);
% plot(X,DCX2DX);
% grid on;
% xlabel('X'); ylabel('C_X2');
% subplot(3,3,8);
% plot(X,DCY2DX);
% grid on;
% xlabel('X'); ylabel('C_Y2');
% subplot(3,3,3);
% plot(X,DCT3DX);
% grid on;
% xlabel('X'); ylabel('C_T3');
% subplot(3,3,6);
% plot(X,DCX3DX);
% grid on;
% xlabel('X'); ylabel('C_X3');
% subplot(3,3,9);
% plot(X,DCY3DX);
% grid on;
% xlabel('X'); ylabel('C_Y3');

% figure(9) %only for one blade 1
% subplot(2,4,1),surf(X,PSI/(2*pi),AA,'edgecolor','none'),...
% title('AA'); ylim([0 no_rev]); xlabel('X'); ylabel('Revs'); %view(-25,20)
% subplot(2,4,2),surf(X,PSI/(2*pi),ALPHA,'edgecolor','none'),...
% title('ALPHA'); ylim([0 no_rev]); xlabel('X'); ylabel('Revs');
% subplot(2,4,3),surf(X,PSI/(2*pi),CL,'edgecolor','none'),...
% title('C_L'); ylim([0 no_rev]); xlabel('X'); ylabel('Revs');
% subplot(2,4,4),surf(X,PSI/(2*pi),CD,'edgecolor','none'),...
% title('C_D'); ylim([0 no_rev]); xlabel('X'); ylabel('Revs');
% subplot(2,4,5),surf(X,PSI/(2*pi),DCPDX,'edgecolor','none'),...
% title('C_P'); ylim([0 no_rev]); xlabel('X'); ylabel('Revs');
% subplot(2,4,6),surf(X,PSI/(2*pi),DCTDX,'edgecolor','none'),...
% title('C_T'); ylim([0 no_rev]); xlabel('X'); ylabel('Revs');
% subplot(2,4,7),surf(X,PSI/(2*pi),DCXDX,'edgecolor','none'),...
% title('C_X'); ylim([0 no_rev]); xlabel('X'); ylabel('Revs');
% subplot(2,4,8),surf(X,PSI/(2*pi),DCYDX,'edgecolor','none'),...
% title('C_Y'); ylim([0 no_rev]); xlabel('X'); ylabel('Revs');

figure(10) %for detailed blade loading - all 3 blades
for J = 1:length(PSI)
    CXi(J)  = simprule(DCXDX(J,:),X(1),X(end));
    CYi(J)  = simprule(DCYDX(J,:),X(1),X(end));
    CPi(J)  = simprule(DCPDX(J,:),X(1),X(end));
    CTi(J)  = simprule(DCTDX(J,:),X(1),X(end));
    CXi2(J)  = simprule(DCX2DX(J,:),X(1),X(end));
    CYi2(J)  = simprule(DCY2DX(J,:),X(1),X(end));
    CPi2(J)  = simprule(DCP2DX(J,:),X(1),X(end));
    CTi2(J)  = simprule(DCT2DX(J,:),X(1),X(end));
    CXi3(J)  = simprule(DCX3DX(J,:),X(1),X(end));
    CYi3(J)  = simprule(DCY3DX(J,:),X(1),X(end));
    CPi3(J)  = simprule(DCP3DX(J,:),X(1),X(end));
    CTi3(J)  = simprule(DCT3DX(J,:),X(1),X(end));
end
time = (PSI.*R)/(TSR*U);
subplot(4,1,1);
plot(time,CPi); hold on; plot(time,CPi2,'r'); plot(time,CPi3,'g');
hold off;
```

```
xlabel('Time (s)'); ylabel('C_P'); title('Per Blade')
subplot(4,1,2);
plot(time,CTi); hold on; plot(time,CTi2,'r'); plot(time,CTi3,'g');
hold off;
xlabel('Time (s)'); ylabel('C_T');
subplot(4,1,3);
plot(time,CXi); hold on; plot(time,CXi2,'r'); plot(time,CXi3,'g');
hold off;
xlabel('Time (s)'); ylabel('C_X');
subplot(4,1,4);
plot(time,CYi); hold on; plot(time,CYi2,'r'); plot(time,CYi3,'g');
hold off;
xlabel('Time (s)'); ylabel('C_Y');

figure(11) %for detailed rotor loading
CPm = sum([CPi;CPi2;CPi3])/3;
CTm = sum([CTi;CTi2;CTi3])/3;
CXm = sum([CXi;CXi2;CXi3])/3;
CYm = sum([CYi;CYi2;CYi3])/3;
subplot(4,1,1);
plot(time,CPi); hold on;
plot(time,CPi2,'r');
plot(time,CPi3,'g');
plot(time,CPm,'k'); hold off;
xlabel('Time (s)'); ylabel('C_P');
title('Black line is total coefficient')
subplot(4,1,2);
plot(time,CTi); hold on;
plot(time,CTi2,'r');
plot(time,CTi3,'g');
plot(time,CTm,'k'); hold off;
xlabel('Time (s)'); ylabel('C_T');
subplot(4,1,3);
plot(time,CXi); hold on;
plot(time,CXi2,'r');
plot(time,CXi3,'g');
plot(time,CXm,'k'); hold off;
xlabel('Time (s)'); ylabel('C_X');
subplot(4,1,4);
plot(time,CYi); hold on;
plot(time,CYi2,'r');
plot(time,CYi3,'g');
plot(time,CYm,'k'); hold off;
xlabel('Time (s)'); ylabel('C_Y');

figure(12) %for detailed rotor loading
Pt = CPm*0.5*1000*pi*(R^2)*(U^3); %WEH 3.11
Qt = CPm*0.5*1000*pi*(R^2)*(U^3)/((TSR*U)/R);
%Qt = P/angular velocity where (TSR*U)/R is angular velocity
Tt = CTm*0.5*1000*pi*(R^2)*(U^2); %WEH 3.15
subplot(3,1,1);
plot(time,Pt);
ylabel('PWR (W)'); title('Rotor Power (W)'); set(gca,'XTickLabel',[])
subplot(3,1,2);
plot(time,Qt);
ylabel('TRQ (Nm)'); title('Rotor Torque (Nm)'); set(gca,'XTickLabel',[])
subplot(3,1,3);
plot(time,Tt);
xlabel('Time (s)'); ylabel('THR (N)'); title('Rotor Thrust (N)');

figure(13) %for detailed blade loading — only blade 1
W = (U.*(1—AA))./sin(PHI.*DTOR);
[W1,W2] = gradient(W);
for J = 1:length(PSI)
    for I = 1:length(X)
        if abs(W1(J,I)) > 1 && J > 1
            W(J,I) = W(J—1,I);
            %rough correction due to small sin(PHI) error
        end
```

```
        FX(J,I) = CXi(J)*0.5*1000*(W(J,I)^2)*CR(I)*(R^2); %WEH 3.140
        FY(J,I) = CYi(J)*0.5*1000*(W(J,I)^2)*CR(I)*(R^2);
        Q(J,I) = CYi(J)*0.5*1000*(W(J,I)^2)*CR(I)*(R^3)*X(I); %WEH 3.141
        MZ(J,I) = CXi(J)*0.5*1000*(W(J,I)^2)*CR(I)*(R^3)*X(I)...
            *sin(PHI(J,I).*DTOR); %WEH 3.142
        MY(J,I) = CXi(J)*0.5*1000*(W(J,I)^2)*CR(I)*(R^3)*X(I)...
            *cos(PHI(J,I).*DTOR);
    end
end
for J = 1:length(PSI)
    FXX(J) = simprule(FX(J,:),X(1),X(end));
    FYX(J) = simprule(FY(J,:),X(1),X(end));
    QX(J) = simprule(Q(J,:),X(1),X(end));
    MZX(J) = simprule(MZ(J,:),X(1),X(end));
    MYX(J) = simprule(MY(J,:),X(1),X(end));
end
subplot(5,1,1);
plot(time,FXX);
ylabel('F_X (N)'); title('Axial blade force (N)');
set(gca,'XTickLabel',[])
subplot(5,1,2);
plot(time,FYX);
ylabel('F_Y (N)'); title('Tangential blade force (N)');
set(gca,'XTickLabel',[])
subplot(5,1,3);
plot(time,QX);
ylabel('Q (Nm)'); title('Torque per blade (Nm)');
set(gca,'XTickLabel',[])
subplot(5,1,4);
plot(time,MZX);
ylabel('M_Z (Nm)'); title('Yawing moment (Nm)');
set(gca,'XTickLabel',[])
subplot(5,1,5);
plot(time,MYX);
xlabel('Time (s)'); ylabel('M_Y (Nm)'); title('Tilting moment (Nm)')

%% Dynamic Routine (Stall & Inflow Correction)

err = 1;
while err == 1
    if WAVES == 0 && YAW == 0
        noplot = 1;
        PHIn = PHI*DTOR;
        PHI2n = PHI2*DTOR;
        PHI3n = PHI3*DTOR;
        DCXDXn = DCXDX;
        DCX2DXn = DCX2DX;
        DCX3DXn = DCX3DX;
        DCYDXn = DCYDX;
        DCY2DXn = DCY2DX;
        DCY3DXn = DCY3DX;
        figure(20)
        figure(30)
        return
    end
    err = 0;
    Dynamic_Routine
end




% function contains main BEM code with modifications
% 28/09/11. Pascal Galloway.

function [fname, CP, CT, CX, CY, DCPDXA, DCTDXA, DCXDXA, DCYDXA, CP2,...
    CT2, CX2, CY2, DCP2DXA, DCT2DXA, DCX2DXA, DCY2DXA, CP3, CT3, CX3,...
    CY3, DCP3DXA, DCT3DXA, DCX3DXA, DCY3DXA, CKDi, CKD2i, CKD3i] =...
    my_bem_wave_yaw_3Blade(BLADE, WAVES, YAW, PSI, d, H, Ti, U, zh,...
```

```
    R, X, THETA, CR, AERO_ANG, AERO_CL, AERO_CD, TSR,  B, L, THICK, no_rev)

% INPUTS:
% X=r/R;
% THETA=blade twist angle;
% CR=c/R;
% AERO_ANG=range of attack angles;
% AERO_CL=lift coeff's with stall effects;
% AERO_CD=drag coeff's;
% TSR=tip speed ratio;
% B=number of blades;

% OUTPUTS:
% CP=coeff of power;
% CT=coeff of thrust;
% ALPHA=angle of attack;
% CL=coeff of lift;
% CD=coeff of drag;
% DCPDX=dCp/dX;
% AA=axial inflow factor;
% AT=tangential inflow factor

DTOR = 0.017453292; RTOD = 1/DTOR;
THETA = THETA*DTOR;
PSI2 = (PSI+(2*pi)/B);
PSI3 = (PSI2+(2*pi)/B);

SIGMA = zeros(1,19);
SIGMAR = zeros(1,19);

CL = zeros(length(PSI),19);
CD = zeros(length(PSI),19);
PHI = zeros(length(PSI),19);
CKD = zeros(length(PSI),19);
CKDi = zeros(1,19);
AA = zeros(length(PSI),19);
AT = zeros(length(PSI),19);
ALPHA = zeros(length(PSI),19);
DCPDX = zeros(length(PSI),19);
DCTDX = zeros(length(PSI),19);
DCXDX = zeros(length(PSI),19);
DCYDX = zeros(length(PSI),19);
DCXDXA = zeros(1,19);
DCYDXA = zeros(1,19);
DCPDXA = zeros(1,19);
DCTDXA = zeros(1,19);

CL2 = zeros(length(PSI),19);
CD2 = zeros(length(PSI),19);
PHI2 = zeros(length(PSI),19);
CKD2 = zeros(length(PSI),19);
CKD2i = zeros(1,19);
AA2 = zeros(length(PSI),19);
AT2 = zeros(length(PSI),19);
ALPHA2 = zeros(length(PSI),19);
DCP2DX = zeros(length(PSI),19);
DCT2DX = zeros(length(PSI),19);
DCX2DX = zeros(length(PSI),19);
DCY2DX = zeros(length(PSI),19);
DCX2DXA = zeros(1,19);
DCY2DXA = zeros(1,19);
DCP2DXA = zeros(1,19);
DCT2DXA = zeros(1,19);

CL3 = zeros(length(PSI),19);
CD3 = zeros(length(PSI),19);
PHI3 = zeros(length(PSI),19);
CKD3 = zeros(length(PSI),19);
CKD3i = zeros(1,19);
```

```
AA3 = zeros(length(PSI),19);
AT3 = zeros(length(PSI),19);
ALPHA3 = zeros(length(PSI),19);
DCP3DX = zeros(length(PSI),19);
DCT3DX = zeros(length(PSI),19);
DCX3DX = zeros(length(PSI),19);
DCY3DX = zeros(length(PSI),19);
DCX3DXA = zeros(1,19);
DCY3DXA = zeros(1,19);
DCP3DXA = zeros(1,19);
DCT3DXA = zeros(1,19);

%%%% BLADE 1 %%%%
for J = 1:length(PSI)
    for I = 1:19 %loop for each blade element
        SIGMA(I) = CR(I)*B/2; %blade solidity
        SIGMAR(I) = (CR(I)*B)/(2*pi*X(I)); %chord solidity
        if J == 1 && TSR >= 5
            ALPHA(J,I) = 0.1; %alpha iteration starting value
        elseif J == 1 && TSR < 5
            ALPHA(J,I) = 0.3; %alpha iteration starting value
        else
            ALPHA(J,I) = ALPHA(J-1,I);
            %alpha iteration starting value (increased code speed)
        end
        NUMITER = 0; %number of iterations starting value
        DIFF = 100; %see while loop
        AA(J,I) = 0; %axial inflow factor
        AT(J,I) = 0; %tangential inflow factor

        while DIFF > 0.0001,
            NUMITER = NUMITER+1;
            PHI(J,I)=ALPHA(J,I)+THETA(I);
            %flow angle relative to the plane of rotation
            CL(J,I) = interp1q(AERO_ANG,AERO_CL(:,I),ALPHA(J,I)*RTOD);
            CD(J,I) = interp1q(AERO_ANG,AERO_CD(:,I),ALPHA(J,I)*RTOD);
            DCXDX(J,I) = CL(J,I)*cos(PHI(J,I))+CD(J,I)*sin(PHI(J,I));
            %see chapter 3.5.3 WEH
            DCYDX(J,I) = CL(J,I)*sin(PHI(J,I))-CD(J,I)*cos(PHI(J,I));
            %see chapter 3.5.3 WEH

            %Shen correction factor
            %allows force to tend to zero near blade tip
            g = exp(-0.125*(B*TSR-21))+0.1;
            %g = 1; %to ignore Shen correction

            %K, Prandtl's approximation for tip-loss factor
            F = -B/2 * g * (1-X(I))/X(I) * ((1 + (TSR*X(I))^2)...
                / ((1-AA(J,I))^2))^0.5; %eqn 3.76 WEH
            exp(F);
            if exp(F) > -1 && exp(F) < 1
                KT = 2 / pi * acos(exp(F));
            else
                KT = 1;
            end
            %KT = 1; %when tip-loss is not included
            F = -B/2 * (X(I)-X(1))/X(I) * ((1 + (TSR*X(I))^2)...
                / ((1-AA(J,I))^2))^0.5; %eqn 3.76 WEH
            exp(F);
            if exp(F) > -1 && exp(F) < 1
                KR = 2 / pi * acos(exp(F));
            else
                KR = 1;
            end
            KR = 1; %when root-loss is not included
            K = KT*KR;

            % AA = Axial inflow factor - see eqn 3.51 WEH
            CONST = SIGMA(I)/(4*pi*X(I)*(sin(PHI(J,I)))^2);
```

```
        CA = CONST/K*(DCXDX(J,I)-CONST*(DCYDX(J,I))^2);
        AA(J,I) = CA/(1+CA);
        if AA(J,I) > 0.3539 %empirical correction for high axial inflow
            CA = CA*4*AA(J,I)*(1-AA(J,I))/...
                (0.6+0.61*AA(J,I)+0.79*AA(J,I)^2);
            %CA = CONST*DCXDX(J,I)*4*AA(J,I)*(1-AA(J,I))+...
            %(1.169*AA(J,I))-((1.670*AA(J,I))/(1-AA(J,I)));
            %alternative empirical model based on WEH (pp.67-68)
            AA(J,I) = CA/(1+CA);
        end
        % modified AA for YAW i.e. skewed axial inflow factor
        if YAW ~= 0
            SKEW0=(0.6*AA(J,I)+1)*YAW*DTOR;
            %initial approximation of skew - eqn [19] AeroDyn

            %fSKEW = @(SKEW) (U*(cos(YAW*DTOR)-AA(J,I))*tan(SKEW))...
            %-(U*(sin(YAW*DTOR)-AA(J,I)*tan(SKEW/2)));%eqn [18] AeroDyn
            %SKEW = fzero(fSKEW,SKEW0); %too slow to iterate
            AA(J,I) = AA(J,I)*(1+(((15*pi)/32)*X(I)*tan(SKEW0/2)...
                *cos(PSI(J)))); %eqn [29] AeroDyn
        end
        % AT = Tangential inflow factor - see eqn 3.52 WEH
        CB = SIGMA(I)*DCYDX(J,I)/(4*pi*K*X(I)*sin(PHI(J,I))...
            *cos(PHI(J,I)));
        AT(J,I) = CB/(1-CB);

        % modified PHI for wave and yaw effects
        if WAVES ~= 0
            tx = (X(I)*R*sin(PSI(J))*sin(YAW*DTOR))/U;
            %time change as a result of yaw
            ti = (PSI(J)*R)/(TSR*U) + tx;
            %time instant
            zx = X(I)*R*cos(PSI(J));
            %for 0 degrees with blade pointing down
            zi = zx+zh;
            %depth at blade element
            [u,w] = Airy(d,H,Ti,U,ti,zi,L);
            %wave induced velocities

            PHI(J,I)=atan(((1.0-AA(J,I))+u*(1.0-AA(J,I)))...
                /((1.0+AT(J,I))*TSR*X(I)+w));
        else
            PHI(J,I)=atan(((1.0-AA(J,I)))/((1.0+AT(J,I))*TSR*X(I)));
            %from velocity vector diagram and geometry
        end

        % A0 = Angle of attack derived from velocity vector diagram
        A0=PHI(J,I)-THETA(I);
        DIFF = abs(A0-ALPHA(J,I));
        CKD(J,I) = DIFF;
        ALPHA(J,I) = (A0+ALPHA(J,I))/2;

        NA0 = isnan(A0);
        if NA0 == 1 %breaks loop if angle of attack is NaN
            disp('ALPHA = NaN')
            CP = NaN; CT = NaN; CPA0 = NaN;
            DIFF = -10;
        end
        if NUMITER == 300 %breaks loop if too many iterations
            disp('Too many iterations')
            DIFF = -10;
        end
    end

    %%%% End of ALPHA loop %%%%

    if DIFF == -10 %(from while loop above)
        CPA0 = NaN;
        DCPDX(J,I) = 0;
```

```
            DCTDX(J,I) = 0;
            DCXDX(J,I) = 0;
            DCYDX(J,I) = 0;
        else
            CPA0 = 0;
            DCXDX(J,I) = DCXDX(J,I)*cos(YAW*DTOR);
            DCYDX(J,I) = DCYDX(J,I)*((cos(YAW*DTOR))^2);
            DCTDX(J,I) = (2*(1-AA(J,I))^2*SIGMA(I)*DCXDX(J,I)/...
                (pi*(sin(PHI(J,I)))^2));
            DCPDX(J,I) = (2*TSR*(1-AA(J,I))^2*SIGMA(I)*X(I)*DCYDX(J,I)/...
                (pi*(sin(PHI(J,I)))^2));
        end

        if DCPDX(J,I) < 0 %statement prevents DCPDX being negative
            DCPDX(J,I) = 0;
        end
        if DCTDX(J,I) < 0
            DCTDX(J,I) = 0;
        end
        if DCXDX(J,I) < 0
            DCXDX(J,I) = 0;
        end
        if DCYDX(J,I) < 0
            DCYDX(J,I) = 0;
        end
    end
end
% Integration over azimuthal range (Simpson's rule)
for I = 1:19
    DCXDXA(I) = simprule(DCXDX(:,I),PSI(1),PSI(end))/PSI(end);
    DCYDXA(I) = simprule(DCYDX(:,I),PSI(1),PSI(end))/PSI(end);
    DCPDXA(I) = simprule(DCPDX(:,I),PSI(1),PSI(end))/PSI(end);
    DCTDXA(I) = simprule(DCTDX(:,I),PSI(1),PSI(end))/PSI(end);
    CKDi(I) =  simprule(CKD(:,I),PSI(1),PSI(end))/PSI(end);
end
CPA0 = isnan(CPA0);
if CPA0 == 1;
    CP = NaN; CT = NaN; CX = NaN; CY = NaN; AA = NaN; AT = NaN;...
        ALPHA = NaN; DCPDX = NaN;
else
    CT=simprule(DCTDXA,X(1),X(end)); %Coeff' of Thrust
    CP=simprule(DCPDXA,X(1),X(end)); %Coeff' of Power
    CX=simprule(DCXDXA,X(1),X(end)); %Coeff' of Thrust Force
    CY=simprule(DCYDXA,X(1),X(end)); %Coeff' of Torque Force
end
ALPHA = ALPHA*RTOD;
PHI = PHI*RTOD;

%%%% BLADE 2 %%%%
for J = 1:length(PSI2)
    for I = 1:19
        SIGMA(I) = CR(I)*B/2;
        SIGMAR(I) = (CR(I)*B)/(2*pi*X(I));
        if J == 1 && TSR >= 5
            ALPHA2(J,I) = 0.1;
        elseif J == 1 && TSR < 5
            ALPHA2(J,I) = 0.3;
        else
            ALPHA2(J,I) = ALPHA2(J-1,I);
        end
        NUMITER = 0;
        DIFF = 100;
        AA2(J,I) = 0;
        AT2(J,I) = 0;

        while DIFF > 0.0001,
            NUMITER = NUMITER+1;
            PHI2(J,I)=ALPHA2(J,I)+THETA(I);
            CL2(J,I) = interp1q(AERO_ANG,AERO_CL(:,I),ALPHA2(J,I)*RTOD);
```

```
CD2(J,I) = interp1q(AERO_ANG,AERO_CD(:,I),ALPHA2(J,I)*RTOD);
DCX2DX(J,I) = CL2(J,I)*cos(PHI2(J,I))+CD2(J,I)*sin(PHI2(J,I));
DCY2DX(J,I) = CL2(J,I)*sin(PHI2(J,I))-CD2(J,I)*cos(PHI2(J,I));

%Shen correction factor
g = exp(-0.125*(B*TSR-21))+0.1;
%g = 1; %use to ignore Shen correction

%K = Prandtl's approximation for tip-loss factor
F = -B/2 * g * (1-X(I))/X(I) * ((1 + (TSR*X(I))^2) /...
    ((1-AA2(J,I))^2))^0.5; %eqn 3.76 WEH
exp(F);
if exp(F) > -1 && exp(F) < 1
    KT = 2 / pi * acos(exp(F));
else
    KT = 1;
end
%KT = 1; %when tip-loss is not included
F = -B/2 * (X(I)-X(1))/X(I) * ((1 + (TSR*X(I))^2) /...
    ((1-AA2(J,I))^2))^0.5; %eqn 3.76 WEH
exp(F);
if exp(F) > -1 && exp(F) < 1
    KR = 2 / pi * acos(exp(F));
else
    KR = 1;
end
KR = 1; %when root-loss is not included
K = KT*KR;

% AA2 = Axial inflow factor - see eqn 3.51 WEH
CONST = SIGMA(I)/(4*pi*X(I)*(sin(PHI2(J,I)))^2);
CA = CONST/K*(DCX2DX(J,I)-CONST*(DCY2DX(J,I))^2);
AA2(J,I) = CA/(1+CA);
if AA2(J,I) > 0.3539
    CA = CA*4*AA2(J,I)*(1-AA2(J,I))/(0.6+0.61*AA2(J,I)+...
        0.79*AA2(J,I)^2);
    AA2(J,I) = CA/(1+CA);
end
% modified AA2 for YAW i.e. skewed axial inflow factor
if YAW ~= 0
    SKEW0=(0.6*AA2(J,I)+1)*YAW*DTOR;
    %fSKEW = @(SKEW) (U*(cos(YAW*DTOR)-AA2(J,I))*tan(SKEW))...
    %-(U*(sin(YAW*DTOR)-AA2(J,I)*tan(SKEW/2)));
    %eqn [18] AeroDyn
    %SKEW = fzero(fSKEW,SKEW0);
    AA2(J,I) = AA2(J,I)*(1+(((15*pi)/32)*X(I)*...
        tan(SKEW0/2)*cos(PSI2(J)))); %eqn [29] AeroDyn
end
% AT2 = Tangential inflow factor - see eqn 3.52 WEH
CB = SIGMA(I)*DCY2DX(J,I)/(4*pi*K*X(I)*sin(PHI2(J,I))...
    *cos(PHI2(J,I)));
AT2(J,I)= CB/(1-CB);

% modified PHI2 for wave and yaw effects
if WAVES ~= 0
    tx = (X(I)*R*sin(PSI2(J))*sin(YAW*DTOR))/U;
    ti = (PSI(J)*R)/(TSR*U) + tx;
    zx = X(I)*R*cos(PSI2(J));
    zi = zx+zh;
    [u,w] = Airy(d,H,Ti,U,ti,zi,L);

    PHI2(J,I)=atan(((1.0-AA2(J,I))+u*(1.0-AA2(J,I)))/...
        ((1.0+AT2(J,I))*TSR*X(I)+w));
else
    PHI2(J,I)=atan(((1.0-AA2(J,I)))/((1.0+AT2(J,I))*TSR*X(I)));
end

% A0 = Angle of attack derived from velocity vector diagram
A0=PHI2(J,I)-THETA(I);
```

```
            DIFF = abs(A0-ALPHA2(J,I));
            CKD2(J,I) = DIFF;
            ALPHA2(J,I) = (A0+ALPHA2(J,I))/2;

            NA0 = isnan(A0);
            if NA0 == 1
                disp('ALPHA2 = NaN')
                CP2 = NaN; CT2 = NaN; CP2A0 = NaN;
                DIFF = -10;
            end
            if NUMITER == 300
                disp('Too many iterations')
                DIFF = -10;
            end
        end

        %%%% End of ALPHA2 loop %%%%

        if DIFF == -10
            CP2A0 = NaN;
            DCP2DX(J,I) = 0;
            DCT2DX(J,I) = 0;
            DCX2DX(J,I) = 0;
            DCY2DX(J,I) = 0;
        else
            CP2A0 = 0;
            DCX2DX(J,I) = DCX2DX(J,I)*cos(YAW*DTOR);
            DCY2DX(J,I) = DCY2DX(J,I)*((cos(YAW*DTOR))^2);
            DCT2DX(J,I) = (2*(1-AA2(J,I))^2*SIGMA(I)*DCX2DX(J,I)...
                /(pi*(sin(PHI2(J,I)))^2));
            DCP2DX(J,I) = (2*TSR*(1-AA2(J,I))^2*SIGMA(I)*X(I)*...
                DCY2DX(J,I)/(pi*(sin(PHI2(J,I)))^2));
        end

        if DCP2DX(J,I) < 0
            DCP2DX(J,I) = 0;
        end
        if DCT2DX(J,I) < 0
            DCT2DX(J,I) = 0;
        end
        if DCX2DX(J,I) < 0
            DCX2DX(J,I) = 0;
        end
        if DCY2DX(J,I) < 0
            DCY2DX(J,I) = 0;
        end
    end
end

for I = 1:19
    DCX2DXA(I) = simprule(DCX2DX(:,I),PSI(1),PSI(end))/PSI(end);
    DCY2DXA(I) = simprule(DCY2DX(:,I),PSI(1),PSI(end))/PSI(end);
    DCP2DXA(I) = simprule(DCP2DX(:,I),PSI(1),PSI(end))/PSI(end);
    DCT2DXA(I) = simprule(DCT2DX(:,I),PSI(1),PSI(end))/PSI(end);
    CKD2i(I) =  simprule(CKD2(:,I),PSI(1),PSI(end))/PSI(end);
end

CPA0 = isnan(CPA0);
if CPA0 == 1;
    CP2 = NaN; CT2 = NaN; CX2 = NaN; CY2 = NaN; AA2 = NaN;...
        AT2 = NaN; ALPHA2 = NaN; DCP2DX = NaN;
else
    CT2=simprule(DCT2DXA,X(1),X(end)); %Coeff' of Thrust
    CP2=simprule(DCP2DXA,X(1),X(end)); %Coeff' of Power
    CX2=simprule(DCX2DXA,X(1),X(end)); %Coeff' of Thrust Force
    CY2=simprule(DCY2DXA,X(1),X(end)); %Coeff' of Torque Force
end
ALPHA2 = ALPHA2*RTOD;
PHI2 = PHI2*RTOD;
```

```
%%%% BLADE 3 %%%%
for J = 1:length(PSI3)
    for I = 1:19
        SIGMA(I) = CR(I)*B/2;
        SIGMAR(I) = (CR(I)*B)/(2*pi*X(I));
        if J == 1 && TSR >= 5
            ALPHA3(J,I) = 0.1;
        elseif J == 1 && TSR < 5
            ALPHA3(J,I) = 0.3;
        else
            ALPHA3(J,I) = ALPHA3(J-1,I);
        end
        NUMITER = 0;
        DIFF = 100;
        AA3(J,I) = 0;
        AT3(J,I) = 0;

        while DIFF > 0.0001,
            NUMITER = NUMITER+1;
            PHI3(J,I)=ALPHA3(J,I)+THETA(I);
            CL3(J,I) = interp1q(AERO_ANG,AERO_CL(:,I),ALPHA3(J,I)*RTOD');
            CD3(J,I) = interp1q(AERO_ANG,AERO_CD(:,I),ALPHA3(J,I)*RTOD);
            DCX3DX(J,I) = CL3(J,I)*cos(PHI3(J,I))+CD3(J,I)*sin(PHI3(J,I));
            DCY3DX(J,I) = CL3(J,I)*sin(PHI3(J,I))-CD3(J,I)*cos(PHI3(J,I));

            %Shen correction factor
            g = exp(-0.125*(B*TSR-21))+0.1;
            %g = 1; %use to ignore Shen correction

            %K = Prandtl's approximation for tip-loss factor
            F = -B/2 * g * (1-X(I))/X(I) * ((1 + (TSR*X(I))^2)...
                / ((1-AA3(J,I))^2))^0.5; %eqn 3.76 WEH
            exp(F);
            if exp(F) > -1 && exp(F) < 1
                KT = 2 / pi * acos(exp(F));
            else
                KT = 1;
            end
            %KT = 1; %when tip-loss is not included
            F = -B/2 * (X(I)-X(1))/X(I) * ((1 + (TSR*X(I))^2)...
                / ((1-AA3(J,I))^2))^0.5; %eqn 3.76 WEH
            exp(F);
            if exp(F) > -1 && exp(F) < 1
                KR = 2 / pi * acos(exp(F));
            else
                KR = 1;
            end
            KR = 1; %when root-loss is not included
            K = KT*KR;

            % AA3 = Axial inflow factor - see eqn 3.51 WEH
            CONST = SIGMA(I)/(4*pi*X(I)*(sin(PHI3(J,I)))^2);
            CA = CONST/K*(DCX3DX(J,I)-CONST*(DCY3DX(J,I))^2);
            AA3(J,I) = CA/(1+CA);
            if AA3(J,I) > 0.3539
                CA = CA*4*AA3(J,I)*(1-AA3(J,I))/(0.6+0.61*AA3(J,I)+...
                    0.79*AA3(J,I)^2);
                AA3(J,I) = CA/(1+CA);
            end
            % modified AA3 for YAW i.e. skewed axial inflow factor
            if YAW ~= 0
                SKEW0=(0.6*AA3(J,I)+1)*YAW*DTOR;
                %initial approximation of skew - eqn [19] AeroDyn
                %fSKEW = @(SKEW) (U*(cos(YAW*DTOR)-AA3(J,I))*tan(SKEW))...
                %-(U*(sin(YAW*DTOR)-AA3(J,I)*tan(SKEW/2)));
                %eqn [18] AeroDyn
                %SKEW = fzero(fSKEW,SKEW0);
                AA3(J,I) = AA3(J,I)*(1+(((15*pi)/32)*X(I)*tan(SKEW0/2)*...
```

```
            cos(PSI3(J)))); %eqn [29] AeroDyn
        end
        % AT3 = Tangential inflow factor - see eqn 3.52 WEH
        CB = SIGMA(I)*DCY3DX(J,I)/(4*pi*K*X(I)*sin(PHI3(J,I))*...
            cos(PHI3(J,I)));
        AT3(J,I)= CB/(1-CB);

        % modified PHI3 for wave and yaw effects
        if WAVES ~= 0
            tx = (X(I)*R*sin(PSI3(J))*sin(YAW*DTOR))/U;
            ti = (PSI(J)*R)/(TSR*U) + tx;
            zx = X(I)*R*cos(PSI3(J));
            zi = zx+zh;
            [u,w] = Airy(d,H,Ti,U,ti,zi,L);

            PHI3(J,I)=atan(((1.0-AA3(J,I))+u*(1.0-AA3(J,I)))/...
                ((1.0+AT3(J,I))*TSR*X(I)+w));
        else
            PHI3(J,I)=atan(((1.0-AA3(J,I)))/((1.0+AT3(J,I))*TSR*X(I)));
        end

        % A0 = Angle of attack derived from velocity vector diagram
        A0=PHI3(J,I)-THETA(I);
        DIFF = abs(A0-ALPHA3(J,I));
        CKD3(J,I) = DIFF;
        ALPHA3(J,I) = (A0+ALPHA3(J,I))/2;

        NA0 = isnan(A0);
        if NA0 == 1
            disp('ALPHA3 = NaN')
            CP3 = NaN; CT3 = NaN; CP3A0 = NaN;
            DIFF = -10;
        end
        if NUMITER == 300
            disp('Too many iterations')
            DIFF = -10;
        end
    end

    %%%% End of ALPHA3 loop %%%%

    if DIFF == -10
        CP3A0 = NaN;
        DCP3DX(J,I) = 0;
        DCT3DX(J,I) = 0;
        DCX3DX(J,I) = 0;
        DCY3DX(J,I) = 0;
    else
        CP3A0 = 0;
        DCX3DX(J,I) = DCX3DX(J,I)*cos(YAW*DTOR);
        DCY3DX(J,I) = DCY3DX(J,I)*((cos(YAW*DTOR))^2);
        DCT3DX(J,I) = (2*(1-AA3(J,I))^2*SIGMA(I)*DCX3DX(J,I)/...
            (pi*(sin(PHI3(J,I)))^2));
        DCP3DX(J,I) = (2*TSR*(1-AA3(J,I))^2*SIGMA(I)*X(I)*...
            DCY3DX(J,I)/(pi*(sin(PHI3(J,I)))^2));
    end

    if DCP3DX(J,I) < 0
        DCP3DX(J,I) = 0;
    end
    if DCT3DX(J,I) < 0
        DCT3DX(J,I) = 0;
    end
    if DCX3DX(J,I) < 0
        DCX3DX(J,I) = 0;
    end
    if DCY3DX(J,I) < 0
        DCY3DX(J,I) = 0;
    end
```

```
    end
end

for I = 1:19
    DCX3DXA(I) = simprule(DCX3DX(:,I),PSI(1),PSI(end))/PSI(end);
    DCY3DXA(I) = simprule(DCY3DX(:,I),PSI(1),PSI(end))/PSI(end);
    DCP3DXA(I) = simprule(DCP3DX(:,I),PSI(1),PSI(end))/PSI(end);
    DCT3DXA(I) = simprule(DCT3DX(:,I),PSI(1),PSI(end))/PSI(end);
    CKD3i(I) =  simprule(CKD3(:,I),PSI(1),PSI(end))/PSI(end);
end

CPA0 = isnan(CPA0);
if CPA0 == 1;
    CP3 = NaN; CT3 = NaN; CX3 = NaN; CY3 = NaN;
    AA3 = NaN; AT3 = NaN; ALPHA3 = NaN; DCP3DX = NaN;
else
    CT3=simprule(DCT3DXA,X(1),X(end)); %Coeff' of Thrust
    CP3=simprule(DCP3DXA,X(1),X(end)); %Coeff' of Power
    CX3=simprule(DCX3DXA,X(1),X(end)); %Coeff' of Thrust Force
    CY3=simprule(DCY3DXA,X(1),X(end)); %Coeff' of Torque Force
end
ALPHA3 = ALPHA3*RTOD;
PHI3 = PHI3*RTOD;

%% SAVING DATA %%
if WAVES == 0
    WAV = 'NOWAVES';
else
    FREQ = 1/Ti; FREQ = round(FREQ*1000)/1000;
    WAV = ['FREQ(',num2str(FREQ),')','_H(',num2str(H),')'];
end

HDR = abs(zh/d); HDR = round(HDR*1000)/1000;
if strcmp(BLADE,'LUKE') == 1
    BLADE = 'NACA48XX';
end
fname=horzcat(BLADE,'_HDR(',num2str(HDR),')_',WAV,'_YAW(',num2str(YAW),...
    ')_','TSR(',num2str(TSR),')');
fname=strrep(fname,'.', ',');
save(fname);

return




% Dynamic Routine - dynamic stall and dynamic inflow
% 12/05/11. Pascal Galloway.

%% Dynamic Stall
c = CR*R; %chord length

A1 = 0.87; %empirical time delay coefficient from Larsen (2007)
[ALPHA_D,ALPHA_D2,ALPHA_D3,CL_D,CL_D2,CL_D3] = ...
    dynamic_stall(U,time,c,A1,AERO_ANG,AERO_CL,X,PSI,ALPHA,ALPHA2,ALPHA3);

figure(20)
hold on
h1 = plot(time,ALPHA_D,'r');
h2 = plot(time,ALPHA,'b');
xlabel('Time (s)'); ylabel('AoA (degrees)');
title('Angle of Attack (AoA) at blade elements')
legend([h1(1) h2(1)],{'Effective AoA','Original AoA'})
hold off

figure(21)
hold on
h1 = plot(time,CL_D(:,1),'r');
h2 = plot(time,CL(:,1),'b');
```

```
xlabel('Time (s)'); ylabel('C_L (-)');
title('Coefficient of Lift (C_L) at blade elements')
legend([h1(1) h2(1)],{'Effective C_L','Original C_L'})
hold off

for J = 1:length(PSI)
    for I = 1:19 %loop for each blade element
        PHIn(J,I) = THETA(I) + ALPHA_D(J,I)*DTOR;
        PHI2n(J,I) = THETA(I) + ALPHA_D2(J,I)*DTOR;
        PHI3n(J,I) = THETA(I) + ALPHA_D3(J,I)*DTOR;

        DCXDXn(J,I) = (CL_D(J,I)*cos(PHIn(J,I))+CD(J,I)...
            *sin(PHIn(J,I)))*cos(YAW*DTOR);
        DCX2DXn(J,I) = (CL_D2(J,I)*cos(PHI2n(J,I))+CD(J,I)...
            *sin(PHI2n(J,I)))*cos(YAW*DTOR);
        DCX3DXn(J,I) = (CL_D3(J,I)*cos(PHI3n(J,I))+CD(J,I)...
            *sin(PHI3n(J,I)))*cos(YAW*DTOR);

        DCYDXn(J,I) = (CL_D(J,I)*sin(PHIn(J,I))-CD(J,I)...
            *cos(PHIn(J,I)))*((cos(YAW*DTOR))^2);
        DCY2DXn(J,I) = (CL_D2(J,I)*sin(PHI2n(J,I))-CD(J,I)...
            *cos(PHI2n(J,I)))*((cos(YAW*DTOR))^2);
        DCY3DXn(J,I) = (CL_D3(J,I)*sin(PHI3n(J,I))-CD(J,I)...
            *cos(PHI3n(J,I)))*((cos(YAW*DTOR))^2);
    end
end

%blade 1
for J = 1:length(PSI)
    for I = 1:19 %loop for each blade element
            DCTDXn(J,I) = (2*(1-AA(J,I))^2*SIGMA(I)*...
                DCXDXn(J,I)/(pi*(sin(PHIn(J,I)))^2));
            DCPDXn(J,I) = (2*TSR*(1-AA(J,I))^2*SIGMA(I)...
                *X(I)*DCYDXn(J,I)/(pi*(sin(PHIn(J,I)))^2));
        if DCPDXn(J,I) < 0
            DCPDXn(J,I) = 0;
        end
        if DCTDXn(J,I) < 0
            DCTDXn(J,I) = 0;
        end
        if DCXDXn(J,I) < 0
            DCXDXn(J,I) = 0;
        end
        if DCYDXn(J,I) < 0
            DCYDXn(J,I) = 0;
        end
    end
end
for I = 1:19 %integration azimuthally
    DCXDXAn(I) = simprule(DCXDXn(:,I),PSI(1),PSI(end))/PSI(end);
    DCYDXAn(I) = simprule(DCYDXn(:,I),PSI(1),PSI(end))/PSI(end);
    DCPDXAn(I) = simprule(DCPDXn(:,I),PSI(1),PSI(end))/PSI(end);
    DCTDXAn(I) = simprule(DCTDXn(:,I),PSI(1),PSI(end))/PSI(end);
end
% integration along blade length
CTn=simprule(DCTDXAn,X(1),X(end)); %Coeff' of Thrust
CPn=simprule(DCPDXAn,X(1),X(end)); %Coeff' of Power
CXn=simprule(DCXDXAn,X(1),X(end)); %Coeff' of Thrust Force
CYn=simprule(DCYDXAn,X(1),X(end)); %Coeff' of Torque Force

%blade 2
for J = 1:length(PSI)
    for I = 1:19 %loop for each blade element
            DCT2DXn(J,I) = (2*(1-AA2(J,I))^2*SIGMA(I)...
                *DCX2DXn(J,I)/(pi*(sin(PHI2n(J,I)))^2));
            DCP2DXn(J,I) = (2*TSR*(1-AA2(J,I))^2*SIGMA(I)...
                *X(I)*DCY2DXn(J,I)/(pi*(sin(PHI2n(J,I)))^2));
        if DCP2DXn(J,I) < 0
            DCP2DXn(J,I) = 0;
```

```
        end
        if DCT2DXn(J,I) < 0
            DCT2DXn(J,I) = 0;
        end
        if DCX2DXn(J,I) < 0
            DCX2DXn(J,I) = 0;
        end
        if DCY2DXn(J,I) < 0
            DCY2DXn(J,I) = 0;
        end
    end
end
for I = 1:19 %
    DCX2DXAn(I) = simprule(DCX2DXn(:,I),PSI(1),PSI(end))/PSI(end);
    DCY2DXAn(I) = simprule(DCY2DXn(:,I),PSI(1),PSI(end))/PSI(end);
    DCP2DXAn(I) = simprule(DCP2DXn(:,I),PSI(1),PSI(end))/PSI(end);
    DCT2DXAn(I) = simprule(DCT2DXn(:,I),PSI(1),PSI(end))/PSI(end);
end
%
CT2n=simprule(DCT2DXAn,X(1),X(end)); %Coeff' of Thrust
CP2n=simprule(DCP2DXAn,X(1),X(end)); %Coeff' of Power
CX2n=simprule(DCX2DXAn,X(1),X(end)); %Coeff' of Thrust Force
CY2n=simprule(DCY2DXAn,X(1),X(end)); %Coeff' of Torque Force

%blade 3
for J = 1:length(PSI)
    for I = 1:19 %loop for each blade element
            DCT3DXn(J,I) = (2*(1-AA3(J,I))^2*SIGMA(I)...
                *DCX3DXn(J,I)/(pi*(sin(PHI3n(J,I)))^2));
            DCP3DXn(J,I) = (2*TSR*(1-AA3(J,I))^2*SIGMA(I)...
                *X(I)*DCY3DXn(J,I)/(pi*(sin(PHI3n(J,I)))^2));
        if DCP3DXn(J,I) < 0
            DCP3DXn(J,I) = 0;
        end
        if DCT3DXn(J,I) < 0
            DCT3DXn(J,I) = 0;
        end
        if DCX3DXn(J,I) < 0
            DCX3DXn(J,I) = 0;
        end
        if DCY3DXn(J,I) < 0
            DCY3DXn(J,I) = 0;
        end
    end
end
for I = 1:19 %
    DCX3DXAn(I) = simprule(DCX3DXn(:,I),PSI(1),PSI(end))/PSI(end);
    DCY3DXAn(I) = simprule(DCY3DXn(:,I),PSI(1),PSI(end))/PSI(end);
    DCP3DXAn(I) = simprule(DCP3DXn(:,I),PSI(1),PSI(end))/PSI(end);
    DCT3DXAn(I) = simprule(DCT3DXn(:,I),PSI(1),PSI(end))/PSI(end);
end
%
CT3n=simprule(DCT3DXAn,X(1),X(end)); %Coeff' of Thrust
CP3n=simprule(DCP3DXAn,X(1),X(end)); %Coeff' of Power
CX3n=simprule(DCX3DXAn,X(1),X(end)); %Coeff' of Thrust Force
CY3n=simprule(DCY3DXAn,X(1),X(end)); %Coeff' of Torque Force

%% Dynamic Inflow
[FXP,FXP2,FXP3,FXPT] = ...
    dynamic_inflow_PITT(U,R,X,PSI,DCTDXn,DCT2DXn,DCT3DXn);

figure(30)
hold on
plot(time,Tt, 'b')
plot(time,FXPT+mean(Tt), 'r')
xlabel('Time (s)'); ylabel('Rotor Thrust (N)');
title('Rotor thrust corrected for dynamic inflow')
legend('Original Thrust','Pitt Corr''')
```

```
% Dynamic Stall Model
% "Dynamic stall models for wind turbine aerofoils"
% Larsen et al. (2007) using Boeing-Vertol model, Tarzanin (1971)

% 05/06/11. Pascal Galloway.

function [ALPHA_D,ALPHA_D2,ALPHA_D3,CL_D,CL_D2,CL_D3] =...
    dynamic_stall(U,time,c,A1,AERO_ANG,AERO_CL,X,PSI,ALPHA,ALPHA2,ALPHA3)

% U = 0.9; %mean current velocity
% time = (PSI.*R)/(TSR*U); %time
% c = chord length
% A1 = empirical coefficient for the model describing time delay
% This is profile dependent
%     - Boeing-Vertol use 0.87
%     - Larsen et al. use 0.165
%     - Beddoes-Leishman use 0.3

diffx = time(2)-time(1); %step change in time
for I = 1:length(X)
    CL0(I) = interp1(AERO_ANG,AERO_CL(:,I),0);
    %static lift coefficient at zero angle of attack
end

[X1,Y1] = gradient(ALPHA); %change in ALPHA
adot = Y1/diffx; %rate of change of ALPHA
adotabs = abs(adot); %absolute rate of change
for J = 1:length(PSI)
    for I = 1:length(X)
        ALPHA_D(J,I) = ALPHA(J,I) - A1*(sqrt((c(I)*adotabs(J,I))...
            /(2*U)))*(adot(J,I)/adotabs(J,I)); %dynamic angle of attack
        CLS(J,I) = interp1(AERO_ANG,AERO_CL(:,I),...
            ALPHA_D(J,I)); %lift coefficient at dynamic stall angle
        CL_D(J,I) = CL0(I) + ((CLS(J,I)-CL0(I))...
            /ALPHA_D(J,I))*ALPHA(J,I); %corrected lift coefficient
    end
end

[X2,Y2] = gradient(ALPHA2);
adot2 = Y2/diffx;
adotabs2 = abs(adot2);
for J = 1:length(PSI)
    for I = 1:length(X)
        ALPHA_D2(J,I) = ALPHA2(J,I) - A1*(sqrt((c(I)*adotabs2(J,I))...
            /(2*U)))*(adot2(J,I)/adotabs2(J,I));
        CLS2(J,I) = interp1(AERO_ANG,AERO_CL(:,I),ALPHA_D2(J,I));
        CL_D2(J,I) = CL0(I) + ((CLS2(J,I)-CL0(I))...
            /ALPHA_D2(J,I))*ALPHA2(J,I);
    end
end

[X3,Y3] = gradient(ALPHA3);
adot3 = Y3/diffx;
adotabs3 = abs(adot3);
for J = 1:length(PSI)
    for I = 1:length(X)
        ALPHA_D3(J,I) = ALPHA3(J,I) - A1*(sqrt((c(I)*adotabs3(J,I))...
            /(2*U)))*(adot3(J,I)/adotabs3(J,I));
        CLS3(J,I) = interp1(AERO_ANG,AERO_CL(:,I),ALPHA_D3(J,I));
        CL_D3(J,I) = CL0(I) + ((CLS3(J,I)-CL0(I))...
            /ALPHA_D3(J,I))*ALPHA3(J,I);
    end
end

end
```

```
%Dynamic Inflow Model using Coefficients

% eqn 3.199 & 3.201 WEH heavily modified

function [FXP,FXP2,FXP3,FXPT] =...
    dynamic_inflow_GALL_C(U,R,X,PSI,DCXDXn,DCX2DXn,DCX3DXn)

% U current velocity
% R blade radius
% X normalised blade radial distance (array)
% PSI azimuthal position of blade 1
% DCXDX matrix of CX corresponding to each blade element position in time
% CX mean coefficient of thrust of blade 1

rho = 1000; %density of fluid (kg/m^3)

for J = 1:length(PSI)
    DCXDXA(J) = simprule(DCXDXn(J,:),X(1),X(end));
end
nonDimAcc1 = DCXDXA-mean(DCXDXA); %non-dimensional acceleration
Fxa = 0.5*rho*(R^3)*(U^2)*(pi)*nonDimAcc1;

for J = 1:length(PSI)
    DCX2DXA(J) = simprule(DCX2DXn(J,:),X(1),X(end));
end
nonDimAcc2 = DCX2DXA-mean(DCX2DXA); %non-dimensional acceleration
Fxa2 = 0.5*rho*(R^3)*(U^2)*(pi)*nonDimAcc2;

for J = 1:length(PSI)
    DCX3DXA(J) = simprule(DCX3DXn(J,:),X(1),X(end));
end
nonDimAcc3 = DCX3DXA-mean(DCX3DXA); %non-dimensional acceleration
Fxa3 = 0.5*rho*(R^3)*(U^2)*(pi)*nonDimAcc3;

FXP = Fxa*(1/3);
FXP2 = Fxa2*(1/3);
FXP3 = Fxa3*(1/3);

FXPT = (FXP+FXP2+FXP3); %total thrust (dynamic inflow)

FXP = FXP';
FXP2 = FXP2';
FXP3 = FXP3';
FXPT = FXPT';
end
```

```
%Dynamic Inflow Model

% this works in a similar fashion to GALL_C
% but is too reliant on smoothing of W to be as useful

function [CXD1,CXD2,CXD3,CXDT] = dynamic_inflow_GALL_W(U,R,W1,W2,W3,PSI,TSR)
% U current velocity
% R blade radius
% W1 relative blade 1 inflow velocity
% PSI azimuthal position
% TSR tip-speed-ratio

inerCoeff = 1; %inertia adjustment (1 if unused)

time = (PSI.*R)/(TSR*U);
diffx = time(2)-time(1);

for i = 1:length(W1)
    if i == length(W1)
        diffy(i,:) = diffy(i-1,:);
```

```
    else
        diffy(i,:) = W1(i+1,:)—W1(i,:);
    end
end
dW1dt = diffy./diffx;
CXD1 = (2*inerCoeff/pi)*(R/(U^2))*dW1dt;%blade 1 axial force coefficient


for i = 1:length(W2)
    if i == length(W2)
        diffy(i,:) = diffy(i—1,:);
    else
        diffy(i,:) = W2(i+1,:)—W2(i,:);
    end
end
dW2dt = diffy./diffx;
CXD2 = (2*inerCoeff/pi)*(R/(U^2))*dW2dt;%blade 2 axial force coefficient


for i = 1:length(W3)
    if i == length(W3)
        diffy(i,:) = diffy(i—1,:);
    else
        diffy(i,:) = W3(i+1,:)—W3(i,:);
    end
end
dW3dt = diffy./diffx;
CXD3 = (2*inerCoeff/pi)*(R/(U^2))*dW3dt;%blade 3 axial force coefficient

CXDT = (CXD1+CXD2+CXD3); %total axial force coefficient

end




%Dynamic Inflow Model

% eqn 3.199 & 3.201 WEH with modification
% based on Pitt & Peters (1981) for dynamic inflow

function [FXP,FXP2,FXP3,FXPT] = ...
    dynamic_inflow_PITT(U,R,X,PSI,DCTDXn,DCT2DXn,DCT3DXn)
% U = 0.9; %current velocity
% R = 0.4; %blade radius
% X = normalised blade radial distance (array)
% PSI = azimuthal position of blade 1
% DCTDX = matrix of CT corresponding to each blade element position in time
% CT = mean coefficient of thrust of blade 1

rho = 1000; %density of fluid (kg/m^3)
inerCoeff = 8/3; %inertia coefficient (originally Pitt&Peters used 128/75)

DCTDXA = mean(DCTDXn);
for J = 1:length(PSI)
    for I = 1:length(X)
        CTD1(J,I) = DCTDXn(J,I) — DCTDXA(I);
    end
end
nonDimAcc1 = (pi/(2*inerCoeff))*CTD1; %non—dimensional acceleration
meanAcc1 = nonDimAcc1*((U^2)/R);
Fxa = inerCoeff*rho*(R^3)*meanAcc1;

DCT2DXA = mean(DCT2DXn);
for J = 1:length(PSI)
    for I = 1:length(X)
        CTD2(J,I) = DCT2DXn(J,I) — DCT2DXA(I);
    end
end
```

```
nonDimAcc2 = (pi/(2*inerCoeff))*CTD2; %non−dimensional acceleration
meanAcc2 = nonDimAcc2*((U^2)/R);
Fxa2 = inerCoeff*rho*(R^3)*meanAcc2;

DCT3DXA = mean(DCT3DXn);
for J = 1:length(PSI)
    for I = 1:length(X)
        CTD3(J,I) = DCT3DXn(J,I) − DCT3DXA(I);
    end
end
nonDimAcc3 = (pi/(2*inerCoeff))*CTD3; %non−dimensional acceleration
meanAcc3 = nonDimAcc3*((U^2)/R);
Fxa3 = inerCoeff*rho*(R^3)*meanAcc3;

FXP = zeros(1,length(PSI));
FXP2 = zeros(1,length(PSI));
FXP3 = zeros(1,length(PSI));
for J = 1:length(PSI)
    FXP(J) = simprule(Fxa(J,:),X(1),X(end))/3;
    FXP2(J) = simprule(Fxa2(J,:),X(1),X(end))/3;
    FXP3(J) = simprule(Fxa3(J,:),X(1),X(end))/3;
end

FXPT = (FXP+FXP2+FXP3); %total

end




% A function for Simpsons 1/3 rule
% to numerically integrate an array (NOT a function) between a and b
% 01/02/09. Pascal Galloway.

function [integral] = simprule(data,a,b)
% number of intervals must be even
% therefore number of data points must be odd

if mod(length(data),2)
   n=length(data)−1;
else
   disp('Error: Number of data points must be odd')
end

h=(b−a)/n;  % interval width
ff=zeros(length(data),1);

for i=2:2:n;    % all even terms
    x  = data(i);
    ff(i) = 4*x;
end
for i=3:2:n;    % all odd terms
    x  = data(i);
    ff(i) = 2*x;
end

integral=(h/3)*(data(1)+sum(ff)+data(end));
%integral result with approximation to area under curve




function X = naninterp(X,method)
% Interpolate over NaNs
% See INTERP1 for more info
% method can be 'linear', 'cubic' etc.
% E. Rodriguez
X(isnan(X)) = ...
    interp1(find(~isnan(X)), X(~isnan(X)), find(isnan(X)),method,'extrap');
```

```
return



function [nCL,nCD] = stall_delay(nang,alpha,CL,CD,c_r,AR)

%Pascal Galloway and William Batten
%Stall delay model improves BEM theory by taking account of the rotating
%lift coefficients, hence increasing theoretical power output (stall delay)

nn = 1.4; aa = 3; bb = 2;
%used for calculating 3D rotating lift coefficients
DTOR = 0.017453292; RTOD = 1.0/DTOR;
%degree and radian conversions

[a1 b1] = min(CL); %a1 is min CL, b1 is location of min CL
[a2 b2] = max(CL);
alpha_stall = alpha(b2); %Xfoil's last value
alpha = alpha(b1:b2); CL = CL(b1:b2); CD = CD(b1:b2); %NaN removal
alpha_zero = interp1(CL,alpha,0,'spline'); %find alpha for zero CL
K =(0.1756/c_r)^0.9225; %velocity gradient - Tangler & Selig, NREL
fact = K*c_r/0.138; %see eqn A.8 SES
delay_ang = RTOD*(DTOR*(alpha_stall-alpha_zero)*((fact^nn)-1));
%stall delay angle, see eqn A.7 SES
nStall = round(delay_ang+alpha_stall); %rounded stall delay angle
[nCL, nCD] = viterna_corrigan(nang,alpha,CL,CD,AR);
%runs viterna_corrigan to correct BEM for static stall

dCL = zeros(length(nang),1);
dCD = nCD;
for i = 1:length(nang)
    angle = nang(i);
    if angle < nStall;
        dCL(i) = nCL(i)+aa*(c_r)^bb*(2*pi*(DTOR*(angle-alpha_zero))...
            -nCL(i)); %eqn 3.190 WEH
    else
        dCL(i) = 100; %used to crop lift coefficients
    end
end

[a b] = max(dCL); %a is max dCL, b is location of max dCL
[nCL, nCD] = viterna_corrigan(nang,nang(1:b-1),dCL(1:b-1),dCD(1:b-1),AR);
%new lift and drag coefficients taking account of stall and stall delay

return



function [nCL, nCD] = viterna_corrigan(nang,ang,CL,CD,AR,isST,isPlt)

%Pascal Galloway and William Batten
%Used for improving BEM theory at high angles of attack by assuming the
%aerofoil behaves like a flat plate. This measn the aerodynamic
%coefficients depend only on the aspect ratio of the plate

%[nCL, nCD] = viterna_corrigan(nang,ang,CL,CD,AR,isST,isPlt)
%nang = new angle range
%ang,CL,CD = old aero data;
%AR = aspect ratio of blade, mean(R/c)
%isST = 0 if the last point is not the stall angle;
%isPlt = 1 to plot the data in figure(101)

DTOR = 0.017453292; %deg to rad

narg = nargin; %number of function input arguments
if narg == 5
    isST = 0;
```

```
    isPlt = 0;
elseif narg == 6
    isPlt = 0;
elseif narg == 7
    disp('Ploting Graph figure 101');
else
    disp('Check number of inputs');
    nCL = CL; nCD = CD;
    return
end

CD_MAX = 1.11+0.018*AR; %eqn 13 Viterna & Corrigan 1982 (only approx.)
A1 = CD_MAX/2; %eqn 11 Viterna & Corrigan 1982
B1 = CD_MAX; %eqn 12 Viterna & Corrigan 1982

if isST == 0; %if the last point is not the stall angle
    [a IST] = max(CL);
    CL = CL(1:IST);
    CD = CD(1:IST);
    ang = ang(1:IST);
end

nonew = length(nang);
ANGS = ang(IST)*DTOR; CLS = CL(IST); CDS = CD(IST); %stall values
nCL = zeros(nonew,1); nCD = nCL; %initialise array
nnn = 0;
for i = 1:nonew
    alpha = nang(i)*DTOR;
    if nang(i) <= ang(IST); %before stall
        intCL = interp1(ang,CL,nang(i),'spline');
        intCD = interp1(ang,CD,nang(i),'spline');
        A2 = (intCL-CD_MAX*sin(alpha)*cos(alpha))...
            *(sin(alpha)/((cos(alpha))^2));
        %eqn 15 Viterna & Corrigan 1982
        B2 = (intCD-CD_MAX*((sin(alpha))^2))/(cos(alpha));
        %eqn 16 Viterna & Corrigan 1982
    else %after stall
        A2 = (CLS-CD_MAX*sin(ANGS)*cos(ANGS))*(sin(ANGS)/((cos(ANGS))^2));
        %eqn 17 Viterna & Corrigan 1982
        B2 = (CDS-CD_MAX*((sin(ANGS))^2))/(cos(ANGS));
        %eqn 18 Viterna & Corrigan 1982
    end
    nCL(i) = A1*sin(2*alpha)+A2*((cos(alpha))^2)/sin(alpha);
    %eqn 8 Viterna & Corrigan 1982
    nCD(i) = B1*((sin(alpha))^2)+B2*cos(alpha);
    %eqn 9 Viterna & Corrigan 1982
    if isnan(nCL(i)) == 1 %searching for NaN
        nnn = i; %position of NaN
    end
end

if nnn > 0; %interpolate NaN value
    angle = [nang(1:nnn-1) nang(nnn+1:end)];
    CLL = [nCL(1:nnn-1); nCL(nnn+1:end)]';
    nCL(nnn) = interp1(angle,CLL,nang(nnn),'spline');
end

if isPlt == 1; %plots the data in figure(101)
    figure(101);
    plot(ang,CL,'k-',nang,nCL,'k--');
    hold on;
    plot(ang,CD,'k-',nang,nCD,'k:');
    hold off;
end

return
```

```
%function calculates the aerodynamic parameters used in BEM code
%coefficients are corrected for static stall and stall delay, then
%extrapolated to include all values (helps iterations to converge in BEM)


% 08/03/09. Pascal Galloway.
function [X, THETA, CR, THICK, AERO_ANG, AERO_CL, AERO_CD] = ...
    get_aero_data_4(blade,BX,BCR,BTHICK,BTHETA)

% Interp foil shape from hub to tip
X = linspace(BX(1),0.98,19);
CR = interp1(BX',BCR',X,'spline');
THETA = interp1(BX',BTHETA',X,'spline');
THICK = interp1(BX',BTHICK',X,'linear','extrap');

% Read the foil shapes
if blade == 2 % WILL'S BLADE DATA
    NACA = ['63−812';'63−815';'63−818';'63−821';'63−824'];
    %part filename for data files
    th_foil = [12 15 18 21 24];
    %chord to thickness ratios of foil sections
elseif blade == 1 % LUKE'S BLADE DATA
    NACA = ['4812';'4815';'4818';'4821';'4824';'4827'];
    th_foil = [12 15 18 21 24 27];
elseif blade == 3; % W.E.H. BLADE DATA
    NACA = ['63212';'63215';'63218';'63221';'63225'];
    th_foil = [12 15 18 21 25];
end

num_thick = length(th_foil); %number of foil thicknesses used
alphamin = zeros(1,num_thick);
alphamax = zeros(1,num_thick);
for i = 1:num_thick
    data=dlmread([char(NACA(i,:)) '_trip_Re1000000']);
    %full filename reads txt file with Xfoil data
    alphamin(i) = min(data(:,1));
    alphamax(i) = max(data(:,1));
end
amax = max(alphamax); %maximum alpha from data
amin = min(alphamin); %minimum alpha from data

new_alpha = amin:1:90; %new range of alpha values
num_alpha = length(new_alpha);
FALPHA = zeros(141,num_thick)∗NaN;
FCL = zeros(141,num_thick)∗NaN;
FCD = zeros(141,num_thick)∗NaN;
for i = 1:num_thick %loop carried out for each thickness
    data=dlmread([char(NACA(i,:)) '_trip_Re1000000']);
    [xno yno] = size(data); %size of 'data'
    nn = 1;
    for j = 1:num_alpha;
        FALPHA(j,i) = new_alpha(j);
        if nn > xno
            %disp('got to end'); %end of loop iterations
        elseif data(nn,1) == new_alpha(j)
            FCL(nn,i) = data(nn,2);
            FCD(nn,i) = data(nn,3);
            nn = nn + 1;
        end
    end
end

THICK_dist = THICK;
CR_dist = CR;
X_dist = X;
CR_foil = interp1(THICK_dist,CR_dist,th_foil,'spline');
%chord ratio for each NACA foil
R_foil = interp1(THICK_dist,X_dist,th_foil,'spline');
%radial distance for each NACA foil
```

```
c_r = CR_foil./R_foil;
%chord length for each NACA foil

nang = -10:1:90; %new angle range (alpha)
AR = 1/mean(BCR); %blade aspect ratio (blade span/mean chord)
nCL = zeros(101,5);
nCD = zeros(101,5);

for i = 1:num_thick
    [nCL(:,i), nCD(:,i)] = ...
        stall_delay(nang,nang,FCL(:,i),FCD(:,i),c_r(i),AR);
end

AERO_ANG = nang;
AERO_CL = zeros(101,19);
AERO_CD = zeros(101,19);

for i = 1:19
    AERO_CL(:,i) = ...
        interp2(th_foil,AERO_ANG,nCL,THICK(i),AERO_ANG,'linear');
    AERO_CD(:,i) = ...
        interp2(th_foil,AERO_ANG,nCD,THICK(i),AERO_ANG,'linear');
end

%% Interpolating over the whole range of alpha -180 to +180 degrees

% method based on static aerofoil characteristics from AeroDyn, NREL
AERO_ANG = -180:1:180;
AERO_nCL = NaN(361,19);
AERO_nCD = NaN(361,19);
%Indexing
am90 = 91; %location of -90alpha
a90 = 271; %location of +90alpha
[r1 acrop] = find(AERO_ANG > amax);
%acrop is an indexing array for 'scaling and reflecting' lift and drag data
acrop = acrop(1:90-amax); %removing NaNs
acropl = length(acrop)-1; %ranging index used in for loop
aminL = 171;
%aminL in the index for the minimum available aero data point

AERO_nCL(aminL:a90,1:19) = AERO_CL(:,1:19);
AERO_nCD(aminL:a90,1:19) = AERO_CD(:,1:19);

%DRAG
for i = 1:19
sx = AERO_nCD(acrop,i);
sxr = (rot90(sx,2));
AERO_nCD(a90:a90+acropl,i) = sxr;
AERO_nCD(am90:am90+acropl,i) = sxr;
AERO_nCD(am90-acropl:am90,i) = sx;
AERO_nCD(:,i) = naninterp(AERO_nCD(:,i),'cubic');
%Aerodyn uses linear interpolation, however cubic seems more appropriate
end

%LIFT
for i = 1:19
sx = AERO_nCL(acrop,i);
sxc = sx*0.7;
sxr = (rot90(sx,2));
sxrc = (sxr(1)-sxr)*0.7;
AERO_nCL(a90:a90+acropl,i) = sxrc;
AERO_nCL(am90:am90+acropl,i) = sxrc;
AERO_nCL(am90-acropl:am90,i) = sxc;
AERO_nCL(1,i)=0; AERO_nCL(end,i)=0; %forces lift to zero at 180degree extents
AERO_nCL(:,i) = naninterp(AERO_nCL(:,i),'cubic');
end

AERO_CL = AERO_nCL;
AERO_CD = AERO_nCD;
```

```
%Empirical fix to CL (relevant to blade root only, therefore acceptable)
for i = 1:361
    for j = 1:19
        if AERO_CL(i,j) > 2.5
            AERO_CL(i,j) = 2.5;
        end
        if AERO_CL(i,j) < -2.5
            AERO_CL(i,j) = -2.5;
        end
    end
end

return



function [u,w] = Airy(d,H,Ti,U,ti,zi,L)
%
% With this function, you can get the horizontal and vertical velocity with
% time and depth of a uniform current with small amplitude waves
%
% Inputs:
%             d = water depth (m)
%             H = wave height (m)
%             Ti = intrinsic wave period (s)
%             U = uniform current speed (m/s)
%             ti = time instant (s)
%             zi = depth position (m) note that d=-z
%             L = wavelength (m)

phi = 0; %phase angle i.e. phase shift, use for moving along x-axis
mu = 0; %angle of inclination between wave and current

k = (2*pi)/L; %wavenumber
Ta = (2*pi*Ti)/(2*pi + Ti*k*U); %observed wave period at rotor
sigma = -((2*pi)/Ta)*ti + phi; %wave phase

steepness = H/L; %steepness of waves.
% when ratio reaches 1:7 waves break i.e. 0.14
if steepness > 0.14
    display 'WAVE BREAKING!'
end

u = ((pi*H)/Ti)*cos(mu)*(cosh(k*(d+zi))/sinh(k*d))*cos(sigma);
w = ((pi*H)/Ti)*(sinh(k*(d+zi))/sinh(k*d))*sin(sigma);

return



function [L] = Airy_Wavelength(d,Ti)
% ______________________________________________________
% With this function, you can get the horizontal and vertical velocity with
% time and depth of a uniform current with small amplitude waves
%
% Inputs:
%             d = water depth (m)
%             Ti = intrinsic wave period (s)

%%%%% Getting the value of wavelength, L %%%%%
g = 9.81;
fl = @(L) (L/Ti)-sqrt((g/((2*pi)/L))*tanh(d*((2*pi)/L)));
L = fzero(fl,5);

return
```

Appendix E

Example BEM Input Parameters

Normalised blade geometry and coefficients of lift and drag for varying thickness to chord ratio of the NACA 48XX blades used in the experiments (hydrodynamic data came from Xfoil - Drela and Youngren, 2001).

r/R	c/R	TWIST (deg)	THICK (%)
0.15	0.2425	27.3	26.0
0.20	0.2105	23.1	24.0
0.25	0.1850	20.0	22.5
0.30	0.1588	16.3	20.8
0.35	0.1410	13.8	19.5
0.40	0.1263	12.6	18.7
0.45	0.1150	11.0	18.1
0.50	0.1053	9.5	17.1
0.55	0.0978	8.2	16.6
0.60	0.0908	7.4	16.2
0.65	0.0845	6.8	15.6
0.70	0.0790	5.8	15.1
0.75	0.0733	5.0	14.6
0.80	0.0685	4.5	14.1
0.85	0.0650	4.0	13.6
0.90	0.0625	3.6	13.1
0.95	0.0600	3.3	12.6
1.00	0.0578	3.1	12.6

Table E.1: Blade Geometry Inputs to modified BEM code

α (deg)	C_L	C_D
-7	-0.1939	0.0128
-6	-0.0790	0.0124
-5	0.0358	0.0121
-4	0.1489	0.0120
-3	0.2613	0.0121
-2	0.3731	0.0122
-1	0.4848	0.0124
0	0.5957	0.0127
1	0.7052	0.0131
2	0.8131	0.0135
3	0.9192	0.0140
4	1.0232	0.0146
5	1.1248	0.0153
6	1.2221	0.0163
7	1.3147	0.0175
8	1.4028	0.0189
9	1.4860	0.0204
10	1.5628	0.0223
11	1.6327	0.0244
12	1.6944	0.0270
13	1.7474	0.0301
14	1.7896	0.0340

Table E.2: NACA 4812

α (deg)	C_L	C_D
-7	-0.2426	0.0133
-6	-0.1283	0.0130
-5	-0.0139	0.0129
-4	0.1010	0.0129
-3	0.2156	0.0129
-2	0.3293	0.0131
-1	0.4418	0.0133
0	0.5530	0.0136
1	0.6625	0.0140
2	0.7702	0.0145
3	0.8758	0.0150
4	0.9791	0.0156
5	1.0797	0.0164
6	1.1773	0.0172
7	1.2715	0.0182
8	1.3619	0.0193
9	1.4443	0.0209
10	1.5201	0.0228
11	1.5896	0.0250
12	1.6512	0.0276
13	1.7050	0.0308
14	1.7498	0.0348
15	1.7855	0.0398
16	1.8243	0.0461
17	1.8376	0.0550
18	1.8382	0.0665
19	1.8205	0.0813
20	1.7899	0.0989
21	1.7519	0.1185
22	1.6635	0.1619
23	1.6200	0.1846
24	1.5802	0.2074

Table E.3: NACA 4815

α (deg)	C_L	C_D
-7	-0.2942	0.0143
-6	-0.1792	0.0140
-5	-0.0639	0.0139
-4	0.0512	0.0139
-3	0.1658	0.0139
-2	0.2794	0.0141
-1	0.3917	0.0143
0	0.5025	0.0146
1	0.6117	0.0150
2	0.7187	0.0155
3	0.8234	0.0161
4	0.9255	0.0168
5	1.0247	0.0176
6	1.1205	0.0186
7	1.2127	0.0197
8	1.3008	0.0210
9	1.3844	0.0225
10	1.4628	0.0242
11	1.5355	0.0263
12	1.6012	0.0288
13	1.6544	0.0324
14	1.7000	0.0368
15	1.7371	0.0424

Table E.4: NACA 4818

α (deg)	C_L	C_D
-7	-0.3455	0.0155
-6	-0.2321	0.0152
-5	-0.1180	0.0150
-4	-0.0038	0.0150
-3	0.1101	0.0150
-2	0.2228	0.0152
-1	0.3344	0.0154
0	0.4444	0.0157
1	0.5524	0.0162
2	0.6583	0.0167
3	0.7615	0.0174
4	0.8618	0.0182
5	0.9589	0.0191
6	1.0524	0.0203
7	1.1418	0.0215
8	1.2268	0.0231
9	1.3072	0.0248
10	1.3823	0.0270
11	1.4521	0.0296
12	1.5161	0.0327
13	1.5737	0.0365
14	1.6244	0.0413
15	1.6674	0.0471
16	1.7015	0.0542

Table E.5: NACA 4821

α (deg)	C_L	C_D
-7	-0.3972	0.0170
-6	-0.2875	0.0166
-5	-0.1759	0.0164
-4	-0.0636	0.0162
-3	0.0484	0.0163
-2	0.1598	0.0164
-1	0.2698	0.0167
0	0.3783	0.0170
1	0.4845	0.0175
2	0.5885	0.0182
3	0.6896	0.0189
4	0.7875	0.0199
5	0.8819	0.0210
6	0.9723	0.0223
7	1.0584	0.0239
8	1.1402	0.0258
9	1.2170	0.0280
10	1.2885	0.0308
11	1.3543	0.0341
12	1.4144	0.0382
13	1.4679	0.0431
14	1.5140	0.0490
15	1.5516	0.0560
16	1.5802	0.0642
17	1.6002	0.0736
18	1.6126	0.0841
19	1.6348	0.0954
20	1.6377	0.1073
21	1.6403	0.1191
22	1.6424	0.1310
23	1.6410	0.1433
24	1.6349	0.1561
25	1.6296	0.1688

Table E.6: NACA 4824

α (deg)	C_L	C_D
-7	-0.4461	0.0188
-6	-0.3432	0.0182
-5	-0.2363	0.0179
-4	-0.1278	0.0177
-3	-0.0185	0.0177
-2	0.0901	0.0178
-1	0.1978	0.0181
0	0.3038	0.0185
1	0.4075	0.0191
2	0.5088	0.0198
3	0.6070	0.0207
4	0.7019	0.0219
5	0.7930	0.0232
6	0.8800	0.0249
7	0.9627	0.0269
8	1.0406	0.0293
9	1.1132	0.0323
10	1.1806	0.0359
11	1.2422	0.0402
12	1.2972	0.0453
13	1.3449	0.0513
14	1.3848	0.0584
15	1.4166	0.0664
16	1.4412	0.0755
17	1.4598	0.0853
18	1.4742	0.0958
19	1.4870	0.1064

Table E.7: NACA 4827

Appendix F

Creation of Binary Full-Field Wave-Current Velocity Files for FAST

Script used to create the four-dimensional input 'wind' velocity files for FAST. The script calculates wave particle velocity using linear wave theory in 3 dimensions in both space and time.

```
%Script to create a 4—D array for manipulation into a .wnd binary velocity
%full—field file to be used in FAST. 18/04/12. Pascal Galloway.

clear all
close all

FileName = '05Hz_150mm_09zHub';
% FileName = 'nowaves';
% NOTE — if no waves are desired, but full—field file still required,
% change u, v and w to zero in loops

total_time = 60; %run time (s)
dx = 0.05; %delta x in m
dy = 0.1; %lateral point spacing (m)
dz = 0.1; %vertical point spacing (m)
ny = 20; %number of lateral points
nz = 20; %number of vertical points

zHub = 1.21; %reference hubheight (m) — 0.9 > 0.95, 0.67 > 1.21
MFFWS = 0.9; %mean full field current speed (m/s)

d = 1.880; %water depth (m)
H = 0.150; %wave height (m)
Ti = 2; %intrinsic wave period (s) — 1.33(0.75), 2(0.5) or 2.85(0.35)

L = Airy_Wavelength(d,Ti); %calculating the wavelength

dt = dx/MFFWS; %time difference (s).
y = linspace(—ny/2*dy,ny/2*dy,ny); %equally spaced vector
z = linspace(—nz/2*dz,nz/2*dz,nz)+zHub; %equally spaced vector
z1 = z(1); %vertical location of bottom of grid [m above ground level]
```

```
time = 10:dt:total_time+10; %time vector
zi = -z; %depth position (m) note that d=-z
nt = (length(time)-1)/2; %half number of time steps

%format according to TurbSim
velocity = zeros(length(time),3,length(ny),length(nz));
for it = 1:length(time)
    for iz = 1:nz
        for iy = 1:ny
            [u,v,w] = Airy_Range_TurbSim(d,H,Ti,MFFWS,time(it),zi(iz),L);
            velocity(it,1,iy,iz) = u; %axial velocity (m/s)
            velocity(it,2,iy,iz) = v; %lateral velocity (m/s)
            velocity(it,3,iy,iz) = w; %vertical velocity (m/s)
        end
    end
end

%% initialize variables
fileFmt  = 'int16'; %file format 16-bit integer
ConvFact = 1.0; %results in meters and seconds (change conversion factor
% for other units)

str      = {'HUB HEIGHT','CLOCKWISE','UBAR','TI(U','TI(V','TI(W'};
%MUST be in UPPER case

numVars  = length(str);

%% -----------------------------------------
%  WRITING THE HEADER TO THE BINARY FILE
% -----------------------------------------
fid_wnd   = fopen( [ FileName '.wnd' ],'w');
if ( fid_wnd <= 0 )
   error( 'Wind file could not be opened.' );
end

nffc  = -99; fwrite( fid_wnd, nffc, 'int16' );
% number of components

fc    = 4;   fwrite( fid_wnd, fc,   'int16' );
% should be 4 to allow turbulence intensity to be stored in the header

nffc  = 3;   fwrite( fid_wnd, nffc, 'int32' );

lat = 0.0;      fwrite( fid_wnd, lat,     'float32' );
% latitude (deg)

z0 = 0.001;     fwrite( fid_wnd, z0,      'float32' );
% Roughness length (m)

fwrite( fid_wnd, zHub,     'float32' );
% Reference height (m) = Z(1) + GridHeight / 2.0

TI_U = 1;       fwrite( fid_wnd, TI_U,    'float32' );
% Turbulence Intensity of u component (%)

TI_V = 1;       fwrite( fid_wnd, TI_V,    'float32' );
% Turbulence Intensity of v component (%)

TI_W = 1;       fwrite( fid_wnd, TI_W,    'float32' );
% Turbulence Intensity of w component (%)

fwrite( fid_wnd, dz,    'float32' ); % delta z in m
fwrite( fid_wnd, dy,    'float32' ); % delta y in m
fwrite( fid_wnd, dx,    'float32' ); % delta x in m
fwrite( fid_wnd, nt,    'int32' );   % half the number of time steps
fwrite( fid_wnd, MFFWS, 'float32');  % mean full-field wind speed

fwrite( fid_wnd, 0, 'float32' );
fwrite( fid_wnd, 0, 'float32' );
```

```
fwrite( fid_wnd, 0, 'float32' ); %zLu,yLu,xLu:unused variables (for BLADED)
fwrite( fid_wnd, 0, 'int32' );
fwrite( fid_wnd, 0, 'int32' );   %unused variables (for BLADED)
fwrite( fid_wnd, nz, 'int32' );  %number of points in vertical direction
fwrite( fid_wnd, ny, 'int32' );  %number of points in horizontal direction
fwrite( fid_wnd, 0, 'int32' );
fwrite( fid_wnd, 0, 'int32' );
fwrite( fid_wnd, 0, 'int32' );
fwrite( fid_wnd, 0, 'int32' );
fwrite( fid_wnd, 0, 'int32' );
fwrite( fid_wnd, 0, 'int32' );
%other length scales: unused variables (for BLADED)

%% -----------------------------------------
%  WRITE THE GRID DATA TO THE BINARY FILE
%  -----------------------------------------
nt     = max([nt*2,1]); %number of time steps
nv       = nffc*ny*nz;  %the size of one time step

SummVars = [zHub; 1; MFFWS; 1; 1; 1];
%data from .sum file - SummVars(2) if '-1' anti-clockwise rotation

Scale    = 0.00001*SummVars(3)*SummVars(4:6);
Offset   = [SummVars(3) 0 0];

if SummVars(2) > 0 %clockwise rotation
    %flip the y direction
    y_ix = ny:-1:1;
else
    y_ix = 1:ny;
end

%changing the dimension of velocity so that it's 4-D instead of 3-D
velocity_norm = zeros(length(time),3,length(ny),length(nz));
for it = 1:nt
    for iz = 1:nz
        for iy = y_ix
            for k = 1:nffc
                velocity_norm(it,k,iy,iz) = velocity(it,k,iy,iz)...
                    /Scale(k) - Offset(k);
                fwrite( fid_wnd, velocity_norm(it,k,iy,iz), fileFmt );
            end %for k
        end %iy
    end % iz
end %it

fclose(fid_wnd);
```

```
% Linear Wave Theory accounting for Doppler shift of uniform current
% Outputs feed into 4Darray.m
% 18/04/12. Pascal Galloway.

% This function gives horizontal and vertical velocity in
% time and depth for a uniform current with small amplitude waves

function [u,v,w] = Airy_Range_TurbSim(d,H,Ti,U,ti,zi,L)

% Inputs:
% d = water depth (m)
% H = wave height (m)
% Ti = intrinsic wave period (s)
% U = uniform current speed (m/s)
% zi = depth position (m) note that d=-z

phi = 0; %phase angle i.e. phase shift, use for moving along x-axis
mu = 0; %angle of inclination between wave and current
```

```
k = (2*pi)/L; %wavenumber
Ta = (2*pi*Ti)/(2*pi + Ti*k*U); %observed wave period at rotor
sigma = ((2*pi)/Ta)*ti + phi; %wave phase

steepness = H/L;
%steepness of waves. when ratio reaches 1:7 waves break i.e. 0.14
if steepness > 0.14
    display 'WAVE BREAKING!'
end

u = ((pi*H)/Ti)*cos(mu)*(cosh(k*(d+zi))/sinh(k*d))*cos(sigma);
v = 0; %zero lateral velocity in towing tank
w = ((pi*H)/Ti)*(sinh(k*(d+zi))/sinh(k*d))*sin(sigma);

return
```

Appendix G

Dynamometer Design

Assumptions and calculations for the design of the turbine dynamometer are presented in Table G.1 and Table G.2. See Figure 5.6 for photos of the two-piece thrust-torque dynamometer. The two CNC machined, aluminium bronze parts were joined using fitted shoulder bolts and attached to the turbine shaft using spring pins to reduce vibration as much as possible. Strain gauging was done professionally to reduce the risk of failure when underwater.

DYNAMOMETER DESIGN	Value	Units
Thrust coefficient	1.00	-
Power coefficient	0.45	-
Max flow speed	1.50	$m.s^{-1}$
Min RPM	80	RPM
Rotor area	0.50	m^2
Power	382	W
Rotational velocity	8.38	$rad.s^{-1}$
Max thrust	565	N
Max torque	46	Nm
Max diameter	100	mm
Max strain at flexure ends	1000	$\mu\varepsilon$
Material	Aluminium Bronze CA104	-
Ultimate Tensile Strength	700	$N.mm^{-2}$
Yield stress	350	$N.mm^{-2}$
Young's Modulus	115000	$N.mm^{-2}$
Stress	115000	$N.mm^{-2}$
Percent of yield stress	33%	-

Table G.1: Basic assumptions for the design of the Turbine Dynamometer

THRUST	Value	Units	TORQUE	Value	Units
No. flexures	4	-	No. flexures	6	-
Flexure length	17	mm	Flexure length	25	mm
Flexure width	12	mm	Flexure width	12	mm
Flexure thickness	4	mm	Flexure thickness	4	mm
End radii	2	mm	End radii	3	mm
Thrust per flexure	141.4	N	Flexure offset from edge (including radii)	3.25	mm
			Mean flexure radius	40.8	mm
			Max force per flexure	186.3	N
Contraflexure:			Contraflexure:		
2nd moment area	64.00	mm^4	2nd moment area	64.00	mm^4
y_{max}	2.00	mm	y_{max}	2.00	mm
I/y	32.00	mm^3	I/y	32.00	mm^3
Root strain, ϵ	250	$\mu\varepsilon$	Root strain, ϵ	481	$\mu\varepsilon$
	29	$N.mm^{-2}$		55	$N.mm^{-2}$
Percent of yield stress	8%	-	Percent of yield stress	16%	-
Deflection, δ	0.004	mm	Deflection, δ	0.014	mm
Percent of effective length	0.03%	-	Percent of effective length	0.08%	-
Shear stress (axial)	2.95	$N.mm^{-2}$	Shear stress (axial)	1.96	$N.mm^{-2}$
Percent of yield stress	1%	-	Percent of yield stress	1%	-
Max force per flexure (rotation)	949	N	Max force per flexure (rotation)	633	N
Shear stress (rotation)	19.78	$N.mm^{-2}$	Shear stress (rotation)	3.88	$N.mm^{-2}$
Percent of yield stress	6%	-	Percent of yield stress	1%	-
Effective mean strain in gauges:			Effective mean strain in gauges:		
Gauge size	3	mm	Gauge size	3	mm
Effective flexure length	13	mm	Effective flexure length	19	mm
Gauge offset from edge	1.5	mm	Gauge offset from edge	1.5	mm
At mid gauge position, mean strain as a percentage of maximum at ends	53.8%	-	At mid gauge position, mean strain as a percentage of maximum at ends	68.4%	-
mean maximum strain at gauge location	134	$\mu\varepsilon$	mean maximum strain at gauge location	329	$\mu\varepsilon$

Table G.2: Calculations for the Thrust and Torque parts of the Turbine Dynamometer

Appendix H

Strain Gauged Blade Design

Assumptions and calculations for the design of the turbine dynamometer are presented in Table H.1 and Table H.2. See Figure 5.8 for photos of the machined blade root. The CNC machined, aluminium blade was strain gauged professionally to reduce the chance of failure when underwater. The strain gauge wiring was passed through the shaft along with the dynamometer wiring and sealed with a non-corrosive flexible silicon sealant.

BLADE DESIGN	Value	Units
Thrust coefficient	0.90	-
Power coefficient	0.45	-
Max flow speed	0.90	$m.s^{-1}$
Min RPM	80	RPM
Rotor area	0.50	m^2
Power	82	W
Rotational velocity	8.38	$rad.s^{-1}$
Max thrust	183	N
Max torque	8.6	Nm
Blade radius	0.4	mm
Hub radius	0.05	mm
Max strain at flexure ends	1000	$\mu\varepsilon$
Material	Aluminium 6082-T6	-
Ultimate Tensile Strength	325	$N.mm^{-2}$
Yield stress	260	$N.mm^{-2}$
Young's Modulus	70000	$N.mm^{-2}$
Stress	70000	$N.mm^{-2}$
Percent of yield stress	27%	-

Table H.1: Basic assumptions for the design of the Strain Gauged Blade

OUT-OF-PLANE	Value	Units	IN-PLANE	Value	Units
No. blades	3	-	No. blades	3	-
Flexure length	8	mm	Flexure length	8	mm
Flexure width	14	mm	Flexure width	14	mm
Flexure thickness	14	mm	Flexure thickness	14	mm
End radii	0	mm	End radii	0	mm
Force per blade/flexure	61.1	N	Torque per blade/flexure	2.9	Nm
Cantilever (uniform loading):			Cantilever (uniform loading):		
2nd moment area	3201	mm^4	2nd moment area	3201	mm^4
Uniformly distributed load	0.174	$N.m^{-1}$	Uniformly distributed load	0.24	$N.m^{-1}$
Effective blade length	0.35	m	Effective blade length	0.35	m
Max bending moment	10.7	$N.m$	Max bending moment	1.4	$N.m$
y_{max}	7.0	mm	y_{max}	7.0	mm
Root strain, ϵ	334	$\mu\varepsilon$	Root strain, ϵ	45	$\mu\varepsilon$
	23	$N.mm^{-2}$		3	$N.mm^{-2}$
Percent of yield stress	9%	-	Percent of yield stress	1%	-
Deflection, δ	1.5	mm	Deflection, δ	0.2	mm
Percent of effective length	0.42%	-	Percent of effective length	0.06%	-
Shear stress (in-line)	0.31	$N.mm^{-2}$	Shear stress (in-line)	0.04	$N.mm^{-2}$
Percent of yield stress	0.12%	-	Percent of yield stress	0.02%	-
Effective mean strain in gauges:			Effective mean strain in gauges:		
Gauge size	3	mm	Gauge size	3	mm
Effective flexure length	8	mm	Effective flexure length	8	mm
Gauge offset from edge	0	mm	Gauge offset from edge	0	mm
At mid gauge position, mean strain as a percentage of maximum at ends	~100%	-	At mid gauge position, mean strain as a percentage of maximum at ends	~100%	-
mean maximum strain at gauge location	334	$\mu\varepsilon$	mean maximum strain at gauge location	45	$\mu\varepsilon$

Table H.2: Calculations for the out-of-plane and in-plane bending of a strain gauged Turbine Blade

Appendix I

Experimental Log

The experimental log is described in Table I.1 with brief summary of key outcomes for each test date in Table I.2.

Date	Test	Waves T_i (s) H (mm)	Yaw (º)	Depth (mm)	RPM
07/04/09	Baseline (ADV)	$T_i = 0, 1.33$ $H = 0, 80$	-	200-350 (every 50mm)	-
08/04/09		$T_i = 0, 1.33$ $H = 0, 80$	-	200-1300 (every 100mm)	-
19/10/09	Seeding rig development	$T_i = 0, 1.33$ $H = 0, 80$	-	200	-
20/10/09		$T_i = 0, 1.33$ $H = 0, 80$	-	200,400,600	-
06/04/10 - 13/04/10	Commercial Turbine Testing (ARC)	—	—	—	—
07/06/10 - 08/06/10	Commercial Turbine Testing (ARC)	—	—	—	—
09/06/10	Model Turbine Experiment	$T_i = 0, 1.33$ $H = 0, 80$	0,7.5,15,22.5	900	90,100,120,140
10/06/10		$T_i = 0, 1.33$ $H = 0, 80$	0,7.5,15,22.5	900	80,110,130,150,160
11/06/10		$T_i = 1.33$ $H = 80$	0	630	90,100,110,120, 130,140,150,160
11/08/10	ADV-ADCP Comparison (Nortek)	$T_i = 0, 1.33$ $H = 0, 80$	-	200-1200 (every 200mm)	-
26/08/11	Model Turbine Experiment	-	-	-	-
30/08/11		-	-	-	-
31/08/11		-	-	-	-
21/11/11	Model Turbine Experiment	$T_i = 0$ $H = 0$	0	900	160-80 (approx. every 10)
22/11/11		$T_i = 0, 1.33$ $H = 0, 80$	0,15,22.5,-15,7.5	900	160-80 (approx. every 10)
23/11/11		$T_i = 0, 1.33, 2$ $H = 0, 80, 150$	0	900	160-80 (approx. every 10)
24/11/11		$T_i = 1.33, 2, 2.86$ $H = 80, 100, 150$	0,15	900,630	160-80 (approx. every 10)
25/11/11		$T_i = 0, 2$ $H = 0, 100$	15,0	630	160-80 (approx. every 10)

Table I.1: Experimental Log

Date	Summary
07/04/09	Carriage and instrument speed check. Wave paddle checked using wave probes. Shallow ADV data recorded with opposing and following waves (0.46m/s tow speed).
08/04/09	Deeper depths studied to test mounting rigidity and wave velocity decay. Repeatability study of carriage/wave paddle velocities carried out.
19/10/09	Seeding rig tested using different concentrations. Effects monitored in real time using Nortek ADV software (0.67m/s tow speed, minimum operational speed of turbine).
20/10/09	Optimum seeding (Potters Industries Inc., 2012) found to be ~2g/litre. Seeding rig considered unusable due to large lateral vibration, however concentration useful for future tank seeding using the turbine to mix in the seeding material.
06/04/10 - 13/04/10	Commercial testing for Atlantis Resources Corporation. 2 days for set-up. Half day to dismantle. Used Nortek High Frequency ADCP over 2 of the days.
07/06/10 - 08/06/10	Commercial testing for Atlantis Resources Corporation. Experimental set-up only took half a day rather than two based on experience.
09/06/10	Good results but slow acquisition due to minor leak. Turbine was winched up and dried out twice and left raised over night.
10/06/10	Leaks continued even after attempts to prevent them. Suspect rotary shaft seal requires re-design. Sample rate was reduced to 100 Hz to improve data quality after fears water ingress is resulting in electrical signal interference.
11/06/10	Underwater video of turbine in operation shows rotor rpm affected by wave action. Short tower fitted for immersion depth reduction with a noticeable increase in loading.
11/08/10	Re-run of data from previous ADCP tests. Velocity range exceeded for 0.67m/s. Data of very poor quality when at 0.2m/s (sample frequency of 1Hz is simply too low for the purposes of these experiments).
26/08/11	Experimental apparatus delivered to site with new straingauged blade and encoder. Structural elements installed.
30/08/11	Turbine wired up and tested. A few excellent test runs followed by erroneous readings. Turbine completely flooded due to a faulty cable glad at the rear of the turbine. Unfortunately some of telemetry was destroyed along with the encoder. A concept pressurisation system was designed and built after this incident as an additional future fail-safe.
31/08/11	The pressurisation system was tested successfully and lead to the discovery of an additional minor leak through the dynamometer cabling.
21/11/11	Turbine installed and tested successfully after refurbishment.
22/11/11	Data acquired for all yaw angles using the usual wave type.
23/11/11	Large wave height tested at the normal depth (mid-depth).
24/11/11	Longer wave periods tested and reduced turbine immersion depth. In addition, the LabVIEW program which synchronises the real-time data was modified to include wave-probe data alongside the loading data. Repeatability study carried out.
25/11/11	Final reduced immersion depth tests completed and experiment dismantled.

Table I.2: Summary of Experimental Log

Appendix J

Publications

- Galloway, P.W. and Myers, L.E. and Bahaj, A.S. (2014) “Quantifying wave and yaw effects on a scale tidal stream turbine”, *Renewable Energy* 63: 297-307
- Myers, L.E., Galloway, P.W. and Bahaj, A.S. (2011) “Operational issues surrounding the use of towing tanks for performance quantification of marine current energy converters”, *European Wave and Tidal Energy Conference, Southampton, UK*
- Galloway, P.W. and Myers, L.E. and Bahaj, A.S. (2011) “Experimental and numerical results of rotor power and thrust of a tidal turbine operating at yaw and in waves”, *World Renewable Energy Congress, Linköping, Sweden*
- Galloway, P.W. and Myers, L.E. and Bahaj, A.S. (2010) “Studies of a scale tidal turbine in close proximity to waves”, *3rd International Conference on Ocean Energy, Bilbao, Spain*

Renewable Energy 63 (2014) 297–307

Contents lists available at ScienceDirect

Renewable Energy

journal homepage: www.elsevier.com/locate/renene

Quantifying wave and yaw effects on a scale tidal stream turbine

Pascal W. Galloway*, Luke E. Myers, AbuBakr S. Bahaj

Sustainable Energy Research Group, Faculty of Engineering and the Environment, University of Southampton, Southampton SO17 1BJ, UK

ARTICLE INFO

Article history:
Received 20 September 2012
Accepted 20 September 2013
Available online

Keywords:
Tidal turbine
Dynamic
Loading
Yaw
Waves

ABSTRACT

The behaviour of Tidal Stream Turbines (TST) in the dynamic flow field caused by waves and rotor misalignment to the incoming flow (yaw) is currently unclear. The dynamic loading applied to the turbine could drive the structural design of the power capture and support subsystems, device size and its proximity to the water surface and sea bed. In addition, the strongly bi-directional nature of the flow encountered at many tidal energy sites may lead to devices omitting yaw drives; accepting the additional dynamic loading associated with rotor misalignment and reduced power production in return for a reduction in device capital cost. Therefore it is imperative to quantify potential unsteady rotor loads so that the TST device design accommodates the inflow conditions and avoids an unacceptable increase in maintenance action or, more seriously, suffers sudden structural failure.

The experiments presented in this paper were conducted using a 1:20th scale 3-bladed horizontal axis TST at a large towing tank facility. The turbine had the capability to measure rotor thrust and torque whilst one blade was instrumented to acquire blade root strain, azimuthal position and rotational speed all at high frequency. The maximum out-of-plane bending moment was found to be as much as 9.5 times the in-plane bending moment. A maximum loading range of 175% of the median out-of-plane bending moment and 100% of the median in-plane bending moment was observed for a turbine test case with zero rotor yaw, scaled wave height of 2 m and intrinsic wave period of 12.8 s.

A new tidal turbine-specific Blade-Element Momentum (BEM) numerical model has been developed to account for wave motion and yawed flow effects. This model includes a new dynamic inflow correction which is shown to be in close agreement with the measured experimental loads. The gravitational component was significant to the experimental in-plane blade bending moment and was also included in the BEM model. Steady loading on an individual blade at positive yaw angles was found to be negligible in comparison to wave loading (for the range of experiments conducted), but becomes important for the turbine rotor as a whole, reducing power capture and rotor thrust. The inclusion of steady yaw effects (using the often-applied skewed axial inflow correction) in a BEM model should be neglected when waves are present or will result in poor load prediction reflected by increased loading amplitude in the 1P (once per revolution) phase.

1. Introduction

Tidal Stream Turbine (TST) technology is currently at the prototype stage where unique devices are being deployed at specific sites or marine energy testing centres. The United Kingdom, United States, Canada and South Korea amongst others have been at the forefront of the evolution of freestream tidal energy technology. In many parts of the world freestream tidal energy presents a lucrative resource; estimates for the UK is that the technically extractable resource is 18 TWh/year [1] whilst in North America 1.6 TWh/year has been estimated from 7 specific locations [2]. South Korea has a number of locations on the south coast where it has been projected that several hundred MW of installed capacity could be deployed in order to reduce the country's reliance upon energy imports [3]. Historically there has been incidental data regarding flow velocities at sites with strong tidal flows often only stating spring peak and neap velocities for shipping and navigational purposes. With the advent of TST technology high quality data sets with increased temporal and spatial resolution are slowly being acquired at locations where technology is either installed or planned for deployment. Existing equipment (primarily Acoustic Doppler Current Profilers or ADCPs) used to measure tidal currents employs divergent acoustic beams in order to measure flow speed and direction

---

* Corresponding author. Tel.: +44 (0)23 80595458.
E-mail address: P.W.Galloway@soton.ac.uk (P.W. Galloway).

0960-1481/$ – see front matter © 2013 Elsevier Ltd. All rights reserved.
http://dx.doi.org/10.1016/j.renene.2013.09.030

vertically through the water column, often with the added capability to measure water surface elevation to determine characteristics of waves. Whilst binned data through the water column is advantageous, device geometry and principals of operation mean that standard deviation of acquired data over very short time intervals is significant, requiring time-averaging. In addition the measurement volumes (especially far from the instrument) are large. This means that short timescale effects cannot be accurately quantified (due to data averaging) and eddies and turbulence are poorly quantified although efforts have been made to correlate divergent and convergent acoustic instruments to provide better estimates of higher-order flow effects such as turbulence intensity [4]. Research carried out at the European Marine Energy Centre showed that in a water depth of 45 m, the orbital motion of the waves penetrated as far down as 20 m whilst a region of sheared turbulent flow propagated vertically upwards from the sea bed. This resulted in approximately the middle third of the water column remaining relatively stable [5]. The results from a single site cannot be considered general; however it is clear that the need for better understanding of the flow field at tidal energy extraction sites is vital for quantifying device loads and optimising energy capture from larger diameter rotors. Accurate quantification of higher-order flow effects and characterisation of turbulent length scales would prove a great benefit to the technology.

The effect that short-duration and length-scale flow features will have on TSTs is unclear, which will undoubtedly lead to prototype devices being over-engineered and installed at sheltered locations where such effects are minimised [6]. The state of the industry to date has predominantly seen deployment at relatively sheltered sites. MCT [7] have installed their TST in a loch in Ireland, Hammerfest Strom [8] in a fjord in Norway, Open Hydro [9] at the EMEC [10] test facility in Scotland and Scottish Power Renewables [11] have recently received consent for an array off the isle of Islay in a fjord protected from the Atlantic. The use of such sheltered sites is wise in the early stages of the technology where reliability and operability are key issues. However, the largest resource often lies at locations exposed to waves or with strong turbulent flow features due to varying bathymetry or eddies shed from land masses. Bearing in mind that TSTs of a given rated power typically experience four times the thrust of a wind turbine of the same rated power the need to quantitatively assess the dynamic blade loading under such unsteady flow conditions is essential if the technology is to move into the most energetic waters. At present, few experimental wave–current studies have been conducted in the presence of TSTs. One particular study combined Blade-Element Momentum (BEM) theory and linear wave theory to predict rotor torque and thrust and to assess the influence of waves on the dynamic properties of bending moments at the root of rotor blades [12]. The outcomes were limited, particularly those for the blade loading. This paper includes studies into yawed and dynamic load effects on a model turbine rotor and blades.

2. Methodologies

2.1. Wave-towing tank experiment

The experiments presented in this paper were conducted in a wave-towing tank (60 m long × 3.7 m wide × 1.8 m deep). A 1:20th scale tidal turbine with rotor diameter 0.8 m (Fig. 1a and Fig. 2b) was equipped with the capability to measure rotor thrust and torque utilising a custom waterproof dynamometer. This was installed ahead of any seals and bearings to increase accuracy. The design of the dynamometer was discussed previously [13] and was based on the extensive work carried out by Molland [14] for their research on ship propellers. Rotor velocity and acceleration was measured using a hollow shaft encoder mounted within the turbine nacelle. The encoder also provided precise azimuthal position for a strain gauged turbine blade measuring out-of-plane and in-plane root bending moments. A wireless telemetry system located inside the turbine nacelle collected filtered and amplified signals from the strain gauges before data was conveyed above the waterline via a sealed umbilical cable. All data was acquired simultaneously during each run on the towing carriage. The parameters varied included: Tip-Speed-Ratio (TSR), rotor yaw angle, characteristics of monochromatic waves and turbine proximity to the water surface. The blades utilised a NACA 48XX profile with varying thickness and twist along the chord length.

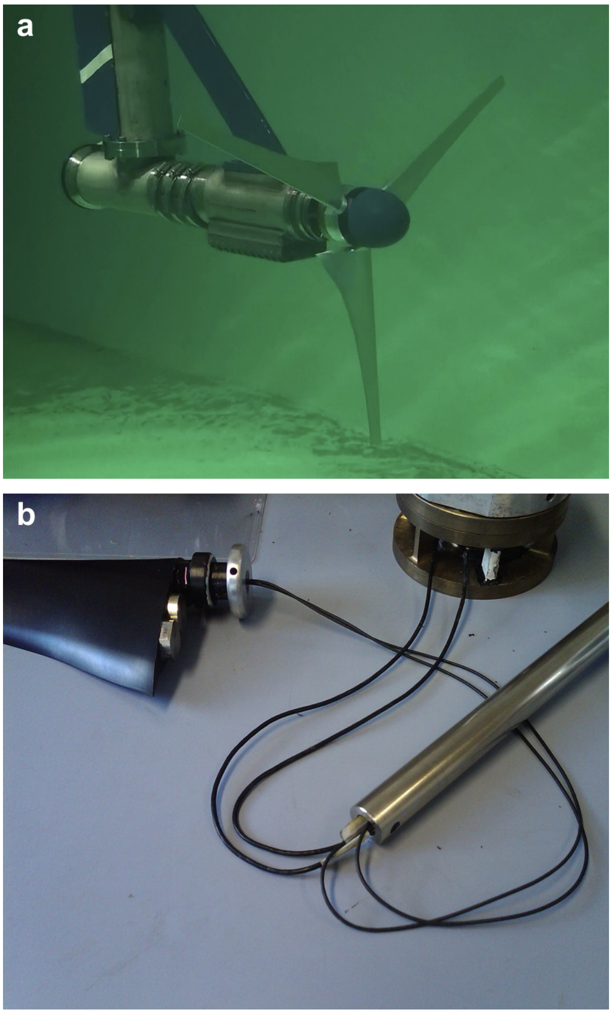

Fig. 1. a – Underwater photo of 1:20th-scale tidal turbine model with NACA 48XX blades. 1b – Strain gauged blade root and dynamometer wires feeding into shaft.

The model turbine was a Froude scaled representation of a 16 m diameter TST. Water waves are gravity dominated and since waves were used throughout the experiments, Froude scaling was the dominant scaling parameter. The fact that the yaw effect may be Reynolds number dominated is simply unfortunate in this case. The towing speed was kept constant at 0.9 ms^{-1}. This is equivalent to a full-scale uniform current speed of 4 ms^{-1}, which is significant for a suitable TST location; however it is significantly lower than the maximum current speed of 8.55 ms^{-1} used in the experiments conducted by Barltrop [11]. High velocities tend to be used in tidal turbine experiments because a low

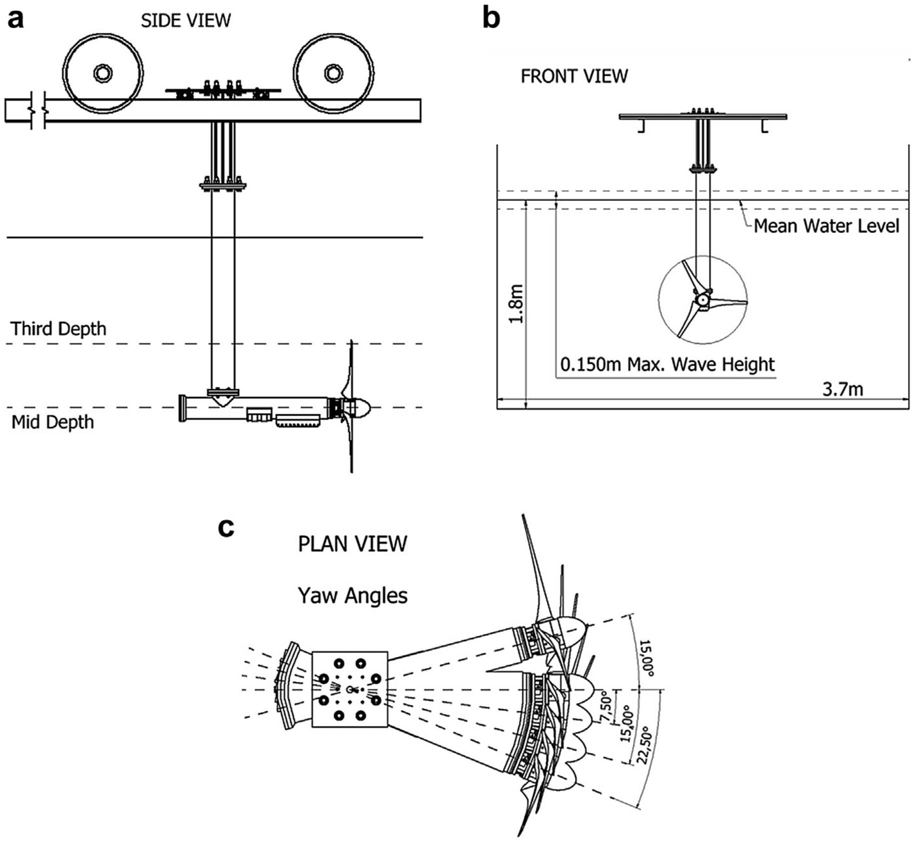

Fig. 2. a – Depth positions of turbine experiment. b – Dimensions of towing tank and maximum wave height. c – turbine yaw angles.

Reynolds number can degrade the dynamical properties of an aerofoil and can be a source of irregularity between the experimental data and simulation data [11]. Generally, turbine experiments are conducted at the lowest flow speed that will deliver the required range of TSR. The use of a towing tank provides one-dimensional wave–current interaction in the form of a Doppler shift. Whilst this is not truly representative of real conditions, this approach is considered more beneficial to understanding the complex wave and yaw interaction effects.

2.2. Numerical model

Blade-Element Momentum (BEM) theory is commonly used by wind turbine designers for predicting loads and power outputs for wind turbines [15–18]. Although this theory is readily applicable to TSTs there are some differences. Wind for example does not have a characteristic property that resembles wave–current interaction; therefore this must be taken into account when designing prototype TSTs. For this work basic BEM theory has been enhanced to include the effect of monochromatic waves on a uniform current with the inclusion of yawed flow if desired. The numerical model has assumed that there is no distortion to the incoming flow field or lateral velocity variation, no blade deflection and that turbine rotational speed is constant. All these conditions hold for the experiments conducted in the towing tank.

The numerical model is implemented in sequential subroutines. First the blade geometry and lift and drag are used to determine the aerodynamic data coupled with stall delay and static stall. This then feeds into an iterative BEM model which computes the inflow factors by convergence of the angle of attack. Skewed axial inflow correction (yaw) and the wave effects described in Section 2.2.1 are included in the iterative process. The resulting time-domain velocities and loads are used to inform the dynamic stall model (Section 2.2.2) and dynamic inflow model (Section 2.2.3), resulting in improved load prediction and coefficients.

2.2.1. Blade element-momentum modifications

BEM theory has some limitations because of its relative simplicity. One of the main limitations is its reliance on two dimensional section data for the lift and drag coefficients. The resulting axial inflow factors are strongly dependent on these values being accurate and poor data quality will obviously be transferred into the BEM output. Often these coefficients come from historic wind tunnel tests or from panel codes such as XFOIL [19]. Whilst these produce good results for steady state BEM simulations, the coefficients change under dynamic conditions. These changes can be determined experimentally but this is complex and expensive. A few of the modifications detailed herein go some way to reducing these errors. Another limitation comes from blade element theory, which assumes there is no span-wise flow along the blade [17]. This is not the case for heavily loaded rotors with large pressure gradients across the span, but empirical corrections have been implemented to account for this [15]. Another assumption is that the calculations are static, with the fluid around the aerofoil remaining in equilibrium and the passing flow accelerating instantly (see Section 2.2.3). In practice this is not the case with the aerofoil requiring time to adjust to the changing wake resulting from a dynamic inflow [20]. Dynamic stall (see Section 2.2.2) becomes a challenging problem since it is no longer possible to rely on the static stall coefficients because stall hysteresis can occur [21,22]. A further limitation is that BEM theory breaks down when the blades are subjected to large deflections outside the rotor plane.

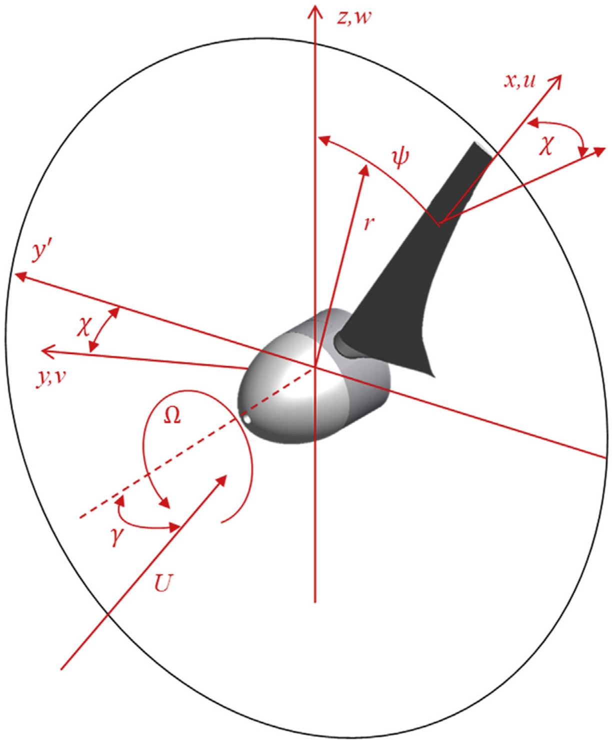

Fig. 3. Velocities on a yawed rotor. y' is the rotor plane in the horizontal direction before yaw, the new skewed plane is denoted by y (x' and x are perpendicular to these values in the horizontal plane).

Because the theory assumes momentum is conserved in a plane parallel to the rotor, any deflection will introduce aerodynamic errors [16].

In order to incorporate the effects of waves and yaw into BEM theory, the geometry of the problem needs to be understood. Firstly it becomes apparent that the azimuthal position of turbine blades is important because the velocity across the turbine rotor can no longer be considered uniform. This is the case for both the turbine in yawed flow and under wave conditions. Fig. 3 includes additional variables to describe this change in geometry. ψ is the azimuthal position, γ is the yaw angle of the upstream flow and χ is the skew angle of the wake, which is always slightly greater than the yaw angle due to flow accelerating around the turbine [15]. U is the current velocity (−ve when against the direction of wave propagation) and Ω is the rotational speed (rad/s).

To model the velocity at each blade element position, the problem becomes dependent on both time and azimuthal position. The wave particle velocity at each blade element position can be found using Equation (2.1) for horizontal velocity and Equation (2.2) for vertical velocity. The equations differ slightly from linear wave theory [23] in that there are two unknowns which are t_{i} (time instant) and z_{i} (elemental change in vertical distance). The wave phase has also been modified for a fixed location in space [24], which in this case is the vertical rotor plane of the TST.

$$u_{\mathrm{r}} = \frac{\pi H}{T_i}\frac{\cosh[k(d+z_i)]}{\sinh(kd)}\cos\left(\frac{2\pi}{T_{\mathrm{a}}}t_i\right) \tag{2.1}$$

$$w_{\mathrm{r}} = \frac{\pi H}{T_i}\frac{\sinh[k(d+z_i)]}{\sinh(kd)}\sin\left(\frac{2\pi}{T_{\mathrm{a}}}t_i\right) \tag{2.2}$$

H is the wave height, T is the wave period, k is the wave number, d is the water depth, z is the depth position and t is the time. Subscript i denotes ‘intrinsic’ (or absolute) and a is ‘apparent’ (or observed). T_{a} is of importance because it is this value that describes the Doppler shifted wave period.

Wave periods can appear different depending of the reference frame of the observer and the relative velocity of wave propagation. This is due to the Doppler shift. A simple example of this is for an observer travelling in the direction of the waves, the appearance of wave crests will be slower than if the observer was travelling against the waves. When waves are superimposed on a uniform current, the reference frame for the waves travels at the velocity of

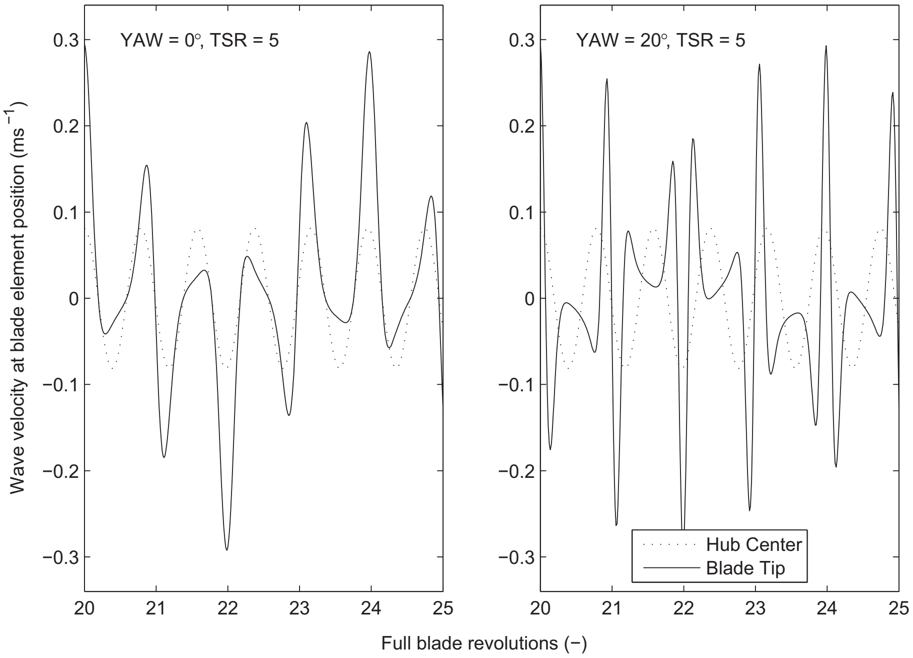

Fig. 4. 1st order wave–current interaction velocities as seen at individual blade elements over two revolutions. The left figure is for 0° yaw, the right figure is for 20° yaw. The dotted line represents hub velocity; the solid line represents tip-velocity. $H = 2$ m, $T_i = 5$ s, $U = -2$ m/s (−ve due to current opposing waves), $d = 40$ m, $z_{\mathrm{H}} = -17$ m and $R = 8$ m.

the underlying current [24]. A Doppler shift is valid in the case of a uniform current, but a more complex effect is noted in the case of sheared currents. Linear wave theory has been found to be a fairly accurate representation of wave–current interaction in depths of water greater than 12.5 m and with significant wave heights lower than 5 m for the purposes of dispersion [12]. This model is an approximation which neglects any change in the wavefield caused by the presence of the turbine rotor. If the modified wavefield could be determined, it would serve improve model reliability.

Time can be described by $t = \psi/\Omega$, so the time at a blade element position is

$$t_i = \frac{\psi R}{\lambda U} + t_X$$

R is the blade radius, λ is the Tip-Speed-Ratio (TSR). t_X is the time change caused by the yawed flow and can be described approximately by

$$t_X = \frac{r\sin(\psi)\sin(\gamma)}{U}$$

The change in vertical distance through the water column at each blade element position is

$$z_i = z_H + z_X$$

z_H represents the hub height of the turbine and z_X is the change in vertical position with blade rotation

$$z_X = r\cos(\psi)$$

Fig. 4 describes how the relative velocities vary as a result of waves and yaw for a single turbine blade. The largest fluctuations in velocity can be observed at the outer element i.e. at the tip of the blade. The hub velocity shows a sinusoidal change in velocity because there is no spatial displacement. The dotted line therefore represents the apparent wave period.

With a corrected value for velocity at each blade element position, the effect of waves can be included within BEM calculations based on the relative inflow angle to the blade

$$\tan(\phi) = \frac{(1-a) + u_r(1-a)}{\lambda(1+a') + w_r}$$

Unfortunately this does not account for the change in axial inflow factor resulting from the skewed wake. A correction for this is based on a method developed by Pitt and Peters [20] and used in the AeroDyn wind turbine BEM model [16]. a is replaced by a_{skew} which is defined in Equation (2.3)

$$a_{\text{skew}} = a\left[1 + \frac{15\pi x}{32}\tan\left(\frac{\chi}{2}\right)\cos(\psi)\right] \tag{2.3}$$

The skew angle χ, can be solved iteratively

$$\tan(\chi) = \frac{U\left[\sin(\gamma) - a\tan\left(\frac{\chi}{2}\right)\right]}{U[\cos(\gamma) - a]}$$

In order to complete the modifications to BEM for yawed flow, the effect of yaw must be included in the coefficients for C_P and C_T.

From momentum theory for a turbine rotor in steady yaw the coefficient of power can be defined

$$C_P = 4a(\cos(\gamma) - a)^2$$

Similarly a coefficient of thrust can be defined

$$C_T = 4a(\cos(\gamma) - a)$$

It can be said that C_P is a function of $\cos^2(\gamma)$ and similarly C_{YX} since they are coplanar

$$C_{YX} = [C_L\sin(\phi) - C_D\cos(\phi)]\cos^2(\gamma)$$

$$C_{PX} = \frac{2\lambda\left(1 - a_{(\psi,x)}\right)^2 \sigma x C_{YX}}{\pi\sin^2\phi_{(\psi,x)}}$$

$$C_P = \int_{x_0}^{x_n}\int_{\psi_0}^{\psi_n} C_{PX}\,d\psi\left(\frac{1}{\psi_n}\right)dx$$

C_{PX} is a power coefficient at a single elemental and azimuthal position and is a blade-element momentum formula, albeit not in the traditional sense. C_{YX} is the tangential force coefficient described by C_L (static lift coefficient) and C_D (static drag coefficient). These two coefficients can be obtained both experimentally and numerically. $x = r/R$, and the local solidity is $\sigma = cB/2R$ (where c is the blade chord length and B is the number of blades on the turbine). C_{XX} (axial force coefficient), C_{TX} (thrust coefficient at a single elemental and azimuthal position) and C_T are functions of $\cos(\gamma)$ and can be described using the same approach as above. In order to obtain a time-domain model for the turbine as a whole, the calculations must be repeated for each blade, whilst ensuring an appropriate phase shift for each blade position (ψ).

The dynamic and cyclic inflow velocities complicate the theoretical application of BEM theory as discussed in Section 2.2.2. Waves and yawed flow create a changing angle of attack at any span-wise position on the blade which also varies with azimuthal position. This leads to unsteady lift/drag forces that lead to undesired blade loading. Applying BEM theory at high angles of attack is problematic because of aerodynamic stall. Viterna and Corrigan [25] developed some modifications to the classical theory, which assume the aerofoil behaves like a flat plate at these high angles of attack. This means that the aerodynamic coefficients depend only on the aspect ratio of the plate (blade span/mean chord length). Another area of importance is that of stall delay. This is a phenomenon in which span-wise flow on a rotating blade delays the onset of stall usually observed in 2-dimensional or non-rotating wing applications. At high angles of attack, blade lift coefficients are found to significantly exceed that of static aerofoil tests [15]. Snel et al. [26] derived a correction which adjusts for the three-dimensional effects of this problem using two-dimensional static aerofoil data and has been shown to be quite effective. Aerodynamic stall can be modelled with stall delay using Viterna and Corrigan [25] within Snel et al. [26]. Moriarty and Hansen [16] suggest that it is prudent to extrapolate the lift and drag data over the range of ±180° to prevent any errors being returned when running a dynamic BEM model. Suitable methods are suggested for mirroring and modifying the data over this range. These effects have all been included in the current numerical model, along with high axial inflow correction and tip/hub loss correction.

2.2.2. Dynamic stall

An effect which has not yet been mentioned is that of dynamic stall. Dynamic stall events occur as a result of unsteady or oscillatory time histories which lead to a variation in velocity over the turbine rotor. Modifications to the lift and drag coefficients are needed to account for flow separation around the aerofoil. This is not a straight forward process since it is dependent on previous changes in the angle of attack. Wave and yaw misalignment are likely to cause dynamic stall, therefore its inclusion in BEM theory for TST technology is important. There are many models used to account for dynamic stall, the most common being the Leishman-Beddoes model originally used in the helicopter industry [21]. The model has twelve empirical parameters which require experimentation in order to calibrate, hence it was found more appropriate to use the Boeing-Vertol model developed by Tarzanin [22], which only has one tuning parameter, providing a more achievable route to experimental calibration as opposed to the impractical task of calibrating the Leishman-Beddoes model. The BEM model presented here includes modification of the lift coefficient for dynamic stall correction. This was implemented after a complete time series run in order to obtain values for the rate of change of angle of attack at a blade element position ($\dot{\alpha}$).

$$C_{\mathrm{L,d}} = C_{\mathrm{L}}(0) + \frac{C_{\mathrm{L}}(\alpha_{\mathrm{d}}) - C_{\mathrm{L}}(0)}{\alpha_{\mathrm{d}}}\alpha$$

$$\alpha_{\mathrm{d}} = \alpha - A_1\sqrt{\frac{c|\dot{\alpha}|}{2U}}\,\frac{\dot{\alpha}}{|\dot{\alpha}|}$$

α is the angle of attack of the aerofoil section, c is the chord length, A_1 is an empirical time delay coefficient and subscript d denotes a dynamic correction. In reality the inclusion of this particular dynamic stall model seemed to have a relatively minor effect.

2.2.3. *Dynamic inflow*

The inertia of TST blades/rotor and their reaction to dynamic conditions is a great challenge. Dynamic inflow refers to the reaction of the global flow field to turbulence and changes in rotor operation (such as variation in rotor speed or blade pitch angle). Steady state BEM theory shows us that increased flow speed results in an instantaneous increase in power. This also infers that there was an instantaneous increase in the axial induction factor and changes in the flow field upstream and downstream of the turbine. For rapid changes in the flow and rotor operation, the global flow field cannot respond quickly enough to instantly establish steady state conditions [15]. In order to account for what is normally described as the inertial response of the rotor, Pitt and Peters [20] dynamic inflow model has led to the creation of a new model for dynamic bending moment of a blade

$$M_{\mathrm{OP,d}} = \overline{M}_{\mathrm{OP}} + M_{\mathrm{OP,rel}}$$

$$M_{\mathrm{OP}} = \frac{1}{2}\rho W^2 crRC_{\mathrm{X}}$$

$$M_{\mathrm{OP,rel}} = \frac{1}{2}\rho R^3 U^2 \pi C_{\mathrm{X,d}}$$

$$C_{\mathrm{X,d}} = \int_{x_0}^{x_n}\left(C_{\mathrm{XX}_{(\psi,x)}} - \overline{C}_{\mathrm{XX}_{(x)}}\right)\mathrm{d}x$$

$$C_{\mathrm{XX}} = [C_{\mathrm{L}}\cos(\phi) - C_{\mathrm{D}}\sin(\phi)]\cos(\gamma)$$

The contribution to the loading coefficient from the dynamic acceleration has been approximated as $C_{\mathrm{X,d}}$, where C_{XX} is the axial force coefficient at an elemental and azimuthal position. $M_{\mathrm{OP,rel}}$ is the relative change in out-of-plane blade bending moment. M_{OP} is the steady state BEM out-of-plane bending moment, where W is the relative inflow velocity at a blade element and ρ is the fluid density. $M_{\mathrm{OP,d}}$ is the total dynamic out-of-plane bending moment.

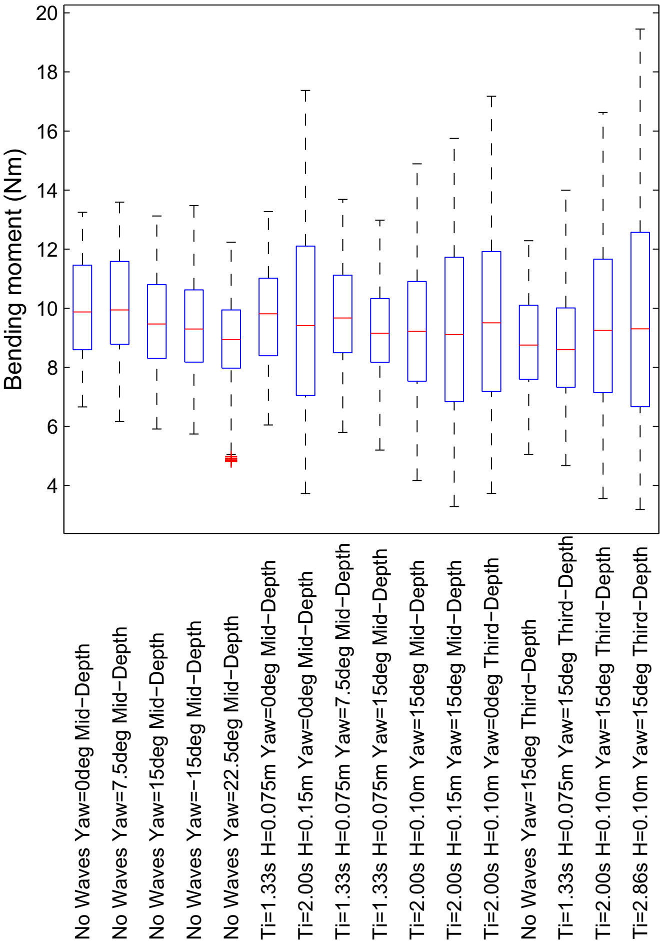

Fig. 5. Out-of-plane blade root bending moment averages across full TSR range (shown as statistical boxplots).

3. Experimental results

The model TST (Fig. 1) was used to acquire measurements of thrust, torque, blade bending, velocity and acceleration from a dynamic flow field. Blockage corrections by Barnsley and Wellicome [27], Garrett and Cummins [28] and Whelan et al. [29] were initially applied to the data; however the results were less than satisfactory. It has been deemed more suitable to neglect blockage until a more appropriate correction can be found. There is no accepted correction for these types of experiment, resulting in a certain disparity between them. This occurs especially around the optimum TSR for CP. The results vary by approximately 15%. This omission is acceptable if the blockage is small enough and 7% is assumed to be small enough here, however there does not appear to be any consensus on this. In addition, no blockage correction exists to deal with the blockage caused by an individual blade and the resulting effect on the blade root bending moments. Repeatability of test runs was good with TSR varying by 1%, out-of-plane load by 6% and in-plane load by 3%. Stall is predicted at a TSR of approximately 3 using a basic BEM code. In reality it occurs at about 4–5 TSR in the experiment due to drive train resistance. The optimum experimental TSR occurs at 5.5, rotor over-speed occurs between 7 and 7.5 TSR.

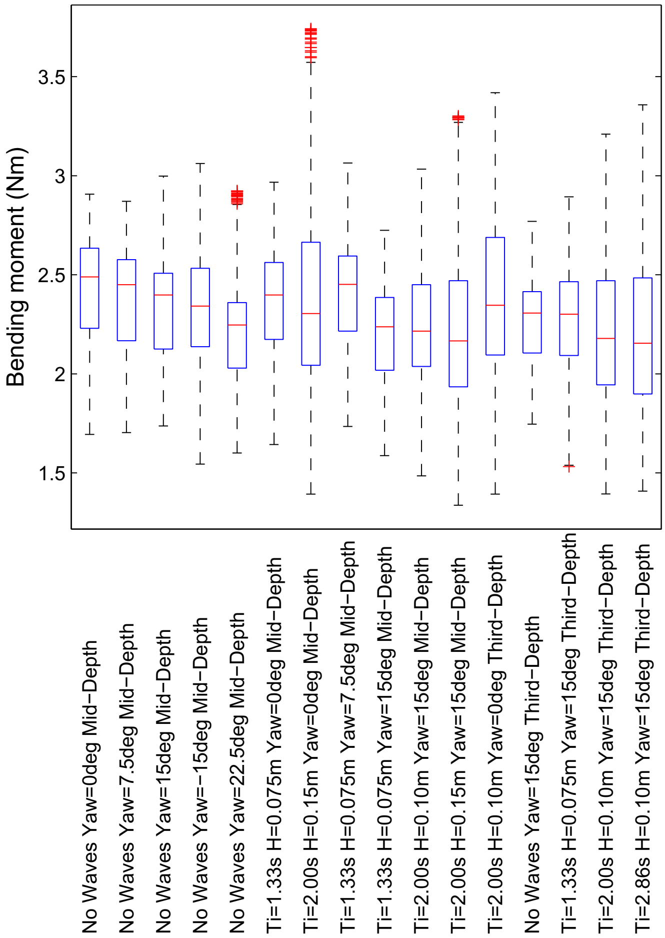

Fig. 6. In-plane blade root bending moment averages across full TSR range (shown as statistical boxplots).

3.1. *Time-averaged blade root out-of-plane and in-plane bending moments*

In general the data acquired for blade bending shows very little variation of the median bending moment at an individual TSR across data sets. The median out-of-plane bending moment increases with increasing TSR within the experimental range of the turbine (TSR 4–7.5) due to greater thrust on the rotor (this effect may change with increasing blade pitch angle however). The median in-plane bending moment reduces with increasing TSR over the same operating range. This is again expected since the rotor/shaft torque will reduce at higher TSRs. On average the out-of-plane load is 4.1 times greater than the in-plane load. This effectively agrees with Barltrop et al. [11] who showed a 3.8 times greater out-of-plane load prediction. Within these sets of experiments, instantaneous out-of-plane loading can be as much as 9.5 times greater than the in-plane loading.

A far more important effect is the range of loading experienced by the blade when looking at wave or yaw effects. The larger wave period used in the experiments resulted in a loading range of 175% of the median out-of-plane load and 100% of the median in-plane load (Figs. 5 and 6 – data presented as boxplots). Barltrop et al. [11] presented results which differ significantly; a loading range of 67% of the median value for out-of-plane bending moments and 200% of the median value for in-plane bending moments. This disparity is likely to be a result of the different experimental scaling effects (larger waves in relation to the rotor diameter, blade type etc.). The large fluctuation of in-plane bending moment could be caused by the use of heavier blades relative to those presented in this paper. The maximum blade mass moment used in this paper is 0.4Nm and is approximately 17% of the median in-plane bending moment, unlike Barltrop el al. whose mass moment approximates 50%. This makes a case for careful investigation of the gravitational/buoyancy loads of full-scale TST blades.

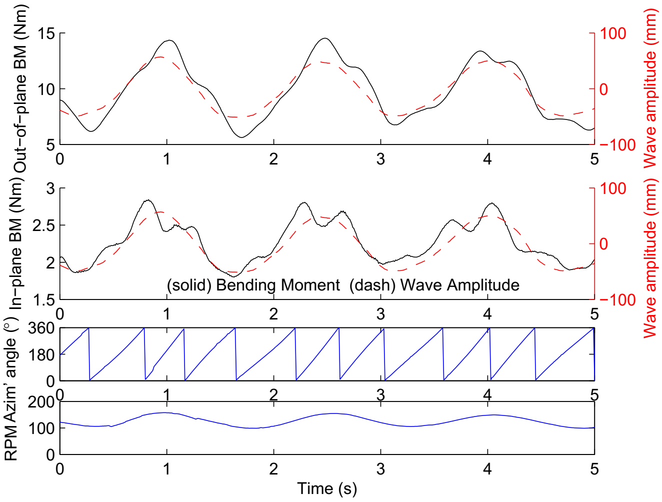

Fig. 7. Experimental time-series blade data acquired simultaneously. Third hub-depth, 0.5 Hz intrinsic wave frequency, 0.1 m wave height, 15° yaw angle and TSR of 5.7 (see Fig. 14 for time series).

Generally it can be said that the median of each test run is central to the interquartile loading range (see Figs. 5 and 6). This is expected in reality since the waves used are effectively sinusoidal, as is the loading effect caused by the yawed flow. Should non-linear waves be encountered this effect is likely to change, probably resulting in a positive median shift due to waves exhibiting shallower troughs and sharper peaks. Barltrop et al. [11] found that steeper waves impose lower bending moments in both directions about the roots of the rotor blade. This is logical given that there will be a reduced longitudinal velocity component, thus reducing the imposed loads in both planes.

In order to obtain ultimate loads from Figs. 5 and 6, it would be sensible to use the maximum load (up to 1.5 times the interquartile range or 2.7 standard deviations). Where the data exceeds the whiskers, as shown by crosses in Figs. 5 and 6, it should be considered erroneous. In reality a factor of safety should be applied to this ultimate load for design.

Non-zero values of rotor yaw have the effect of reducing the median loading and the interquartile range of loading, but the ultimate loading range remains unchanged. One could argue that in terms of ultimate loads, yaw has a negligible effect in comparison to waves. Wave loading is more difficult to quantify. It appears that in-plane bending is affected approximately equally by changes in wave frequency and wave height. This is not the case for out-of-plane bending where it appears that wave frequency is more dominant, particularly low frequency waves (see 2.86 s test case in Fig. 5). This cannot be explained by investigating the energy or power density of the waves since the test case at 2 s, 150 mm is 1.5 times more powerful than the test case of 2.86 s, 100 mm (in W/m^2). The effect of long wave length/large period waves will probably be exacerbated when the current is flowing in the same direction as the waves, effectively increasing the wavelength. Unfortunately it has not been possible to test this effect due to limitations of the towing carriage at the test facility.

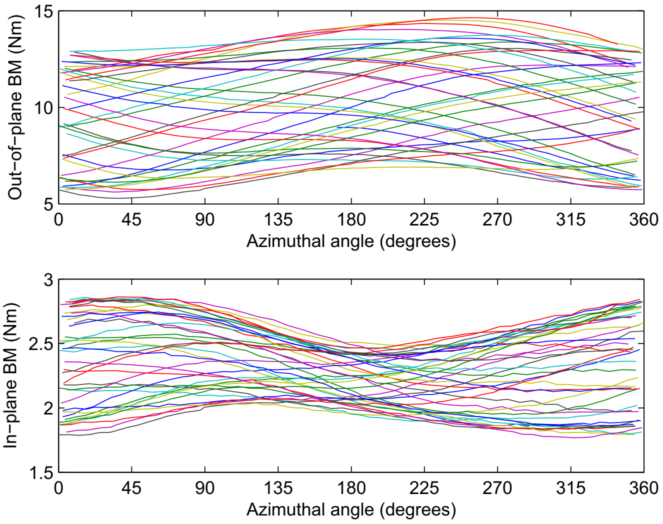

Fig. 8. Measured blade root bending moments for a single turbine blade during a single towed run. Third hub-depth, 0.5 Hz intrinsic wave frequency, 0.1 m wave height, 15° yaw angle and TSR of 5.7 (see Fig. 14 for time series).

When a turbine rotor is yawed to the flow, both median rotor torque (power) and median thrust are reduced, with an approximate 20% power reduction at 22.5° yaw [13]. This is a noticeable difference and is likely to be higher than the 20% suggested because the rotor experiences a reduced effective velocity in yawed flow, hence reduced TSR (assuming no pitch control). Reducing the depth of rotor immersion increases the range of loading, not the median load. This can be described by observing the increasing particle velocity range with reduced depth of immersion.

3.2. *Time-series blade root out-of-plane and in-plane bending moments*

The 1:20th-scale turbine shown in Fig. 1a was capable of acquiring data at high frequency during each towed run as demonstrated in Figs. 7–9. These results also produced the useful comparisons of mean loading shown previously in Section 3.1 and the time-series loading shown in Section 4.

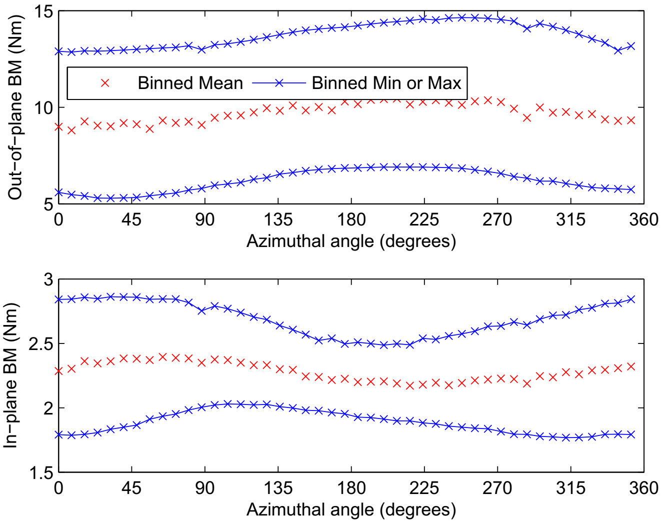

Fig. 9. Azimuthal binned average blade root bending moments (every 8°). Third hub-depth, 0.5 Hz intrinsic wave frequency, 0.1 m wave height, 15° yaw angle and TSR of 5.7 (see Fig. 14 for time series).

Fig. 7 shows high-frequency continuous blade data depicting wave amplitude, bending moment, azimuth blade angle and rpm. The bottom subplot of Fig. 7 shows how wave amplitude directly affects the RPM of the turbine, with the two being almost exactly in phase. What is less obvious is the influence of the waves on the bending moments. This particular example includes the effects of rotor yaw which creates a once-per-revolution (1P) frequency oscillation in both bending moment graphs. The in-plane BM also includes the gravitational bending moment component, hence why some of the 1P oscillations appear more pronounced. Inferring more from this figure leads us to understand that the presence of waves complicates the flow beyond simply adding turbulence. The waves cause oscillations in the rotor torque/power and thrust which in-turn influence the ‘quality’ of the electrical power production. High frequency oscillations (known as flicker) occur and it is thought that this flicker is caused by variations of the angle of attack under the influence of waves [30].

Fig. 8 shows data from the same experimental run. Each line is for a single blade revolution and shows how variable the bending moment is combined with waves and yaw. For the out-of-plane bending moment the range is not constant throughout the rotational cycle, there is a slight increase in the region of 225°. This is due to the yawed flow creating an additional bending moment oscillation. The in-plane bending moment case is more complicated with the inclusion of the gravitational component. The range is now no longer constant with a minimum bending moment at 180° location. It should be noted here that tower shadow is unlikely to be a factor in these experiments since the tower is situated almost one diameter downstream of the rotor plane (0.7 m).

Fig. 9 shows Fig. 8 reproduced with the data having been bin-averaged every 8°. This was done to show how the loading varies when the dynamic effects have been averaged (mean). It is now more evident how the 15° yaw influences the out-of-plane bending moment resulting in a 1P oscillation with maximum load at 225° and minimum load at 45°. The wave-depth effects can be observed from the in-plane bending moments due to the maximum range occurring a 0° (blade up) and the minimum occurring at 180° (blade down). The gravitational component influences the in-plane bending moment and is evident from the in-plane bending moment data maximum and minimum loads occurring at 90° and 270° respectively.

4. Experimental/numerical comparisons of time-series data

The experimental blade root bending moment data was compared to the BEM code described in this paper (using the modifications detailed herein) and to FAST, an industry certified wind turbine code from NWTC [31]. The FAST code was recompiled to remove an empirical correction which disabled dynamic inflow at lower wind speeds. This is irrelevant to the much lower flow speeds encountered by TSTs. A script was also designed to create new, full-field binary ‘wind’ velocity input files which contained wave velocities on a uniform current in both time and space.

The conditions modelled experimentally and numerically have been chosen to be representative of full-scale moderate-extreme conditions. Assuming a scaling factor of 1:20; the depth is 36 m, rotor diameter 16 m, maximum wave height is 3 m and maximum wave period is 12.8 s.

The inclusion of yaw in the numerical model was found to dramatically increase the range over which some of the parameters varied. It was deemed more appropriate to omit all but the simplest trigonometric corrections for yaw when waves were also present by removing the skewed axial inflow correction. The skewed

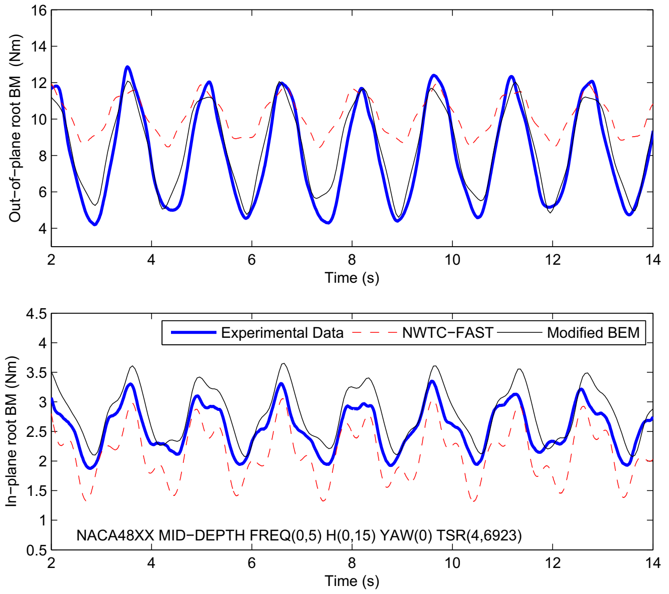

Fig. 10. Time series blade root bending moment comparison of experiment with NWTC-FAST and modified BEM codes. Mid-depth, 0.5 Hz intrinsic wave frequency, 0.15 m wave height, 0° yaw angle and TSR of 4.7.

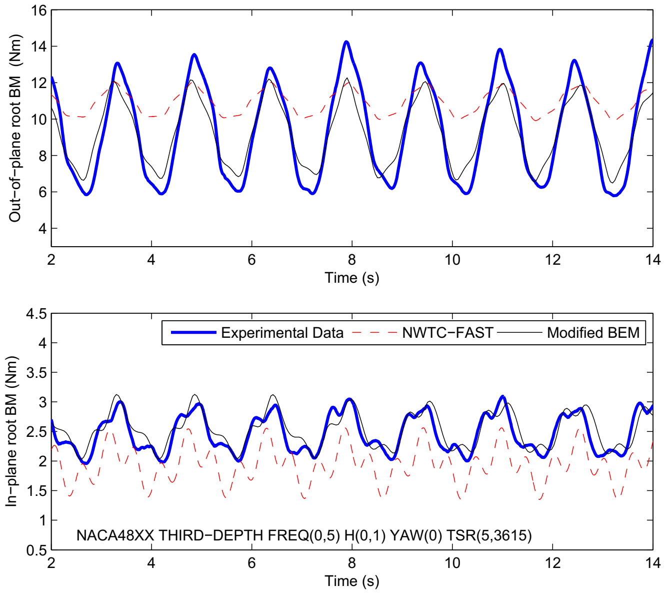

Fig. 11. Time series blade root bending moment comparison of experiment with NWTC-FAST and modified BEM codes. Third-depth, 0.5 Hz intrinsic wave frequency, 0.1 m wave height, 0° yaw angle and TSR of 5.4.

correction was found to be good when there the turbine was yawed but resulted in too much emphasis on the yaw loading (1P frequency) than the wave loading (apparent wave frequency). Omitting the skewed axial inflow correction resulted in significantly improved load prediction. FAST was used here for validation purposes, testing that the experimental and numerical results were of the correct magnitude.

FAST was designed for wind turbine applications therefore does not consider the kind of velocity inflow caused by waves. Therefore its use as a comparator here is purely a demonstration of how BEM codes designed for wind applications require modification for use in the tidal energy industry. Whilst special input files have been made to include the effect of waves, undoubtedly the source code still requires further modification.

Fig. 10 shows reasonably good agreement between the experiment and the modified BEM model. The slight over estimation of the in-plane bending moment can be attributed to less precise numerical prediction at lower values of TSR. FAST agrees well with the in-plane bending moment but struggles to predict the out-of-plane bending moment. This may be due to the dynamic inflow model being inapplicable for the case of a TST. Fig. 11 shows good prediction of the modified BEM with the experiment for in-plane bending moments in terms of phase and frequency, however the amplitude of the out-of-plane bending moment is slightly under predicted. This discrepancy could be improved with a suitable blockage correction (this is currently unavailable) or with further modification to the dynamic inflow correction. FAST predicts similar loading trends to that of Fig. 10. In general FAST tends to over predict out-of-plane bending moments by about 25% and under predict in-plane bending moments by about 25%. This is not a blade pitch error but may be a result of running FAST for what would normally be considered small scale.

Fig. 12 presents a particularly non-linear experimental loading pattern. Modified BEM predicts the majority of the peaks out-of-plane, however struggles due to the omission of a yaw correction. The inclusion of the skewed axial inflow factor results in a prediction not dissimilar to that of FAST but it is postulated that a new correction may be required in order to achieve more accurate prediction of the loads. This will be particularly important in cases where the 1P variation is similar to that of the absolute wave period (1Ta).

Fig. 13 shows the worst test case experimentally. The low frequency waves generated high out-of-plane bending moments which the modified BEM code under predicts. Again, it is postulated that using a more appropriate yaw correction will go some way to alleviating this problem. Fig. 14 presents very similar findings albeit at a slightly higher wave frequency. An interesting point to note from Figs. 13 and 14 is the slight phase shift in the out-of-plane bending moment between modified BEM and experiment. This is probably caused by numerical error in the dynamic stall correction since this imparts a slight time-delay to the results [21,22].

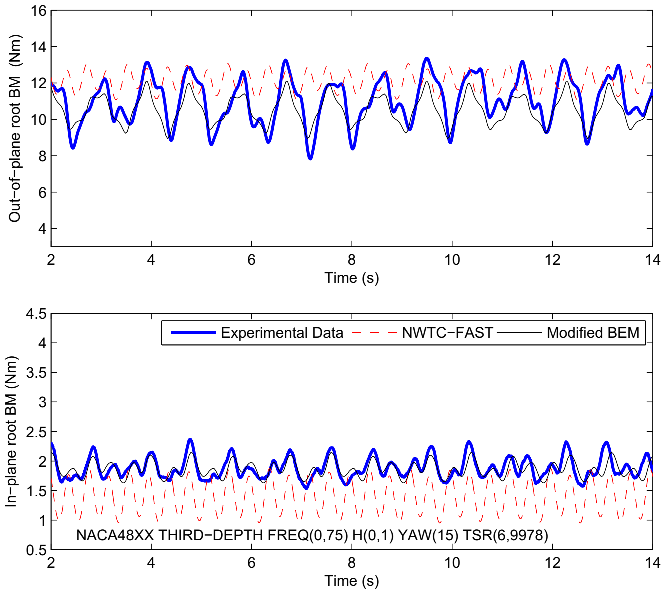

Fig. 12. Time series blade root bending moment comparison of experiment with NWTC-FAST and modified BEM codes. Third-depth, 0.75 Hz intrinsic wave frequency, 0.1 m wave height, 15° yaw angle and TSR of 7.

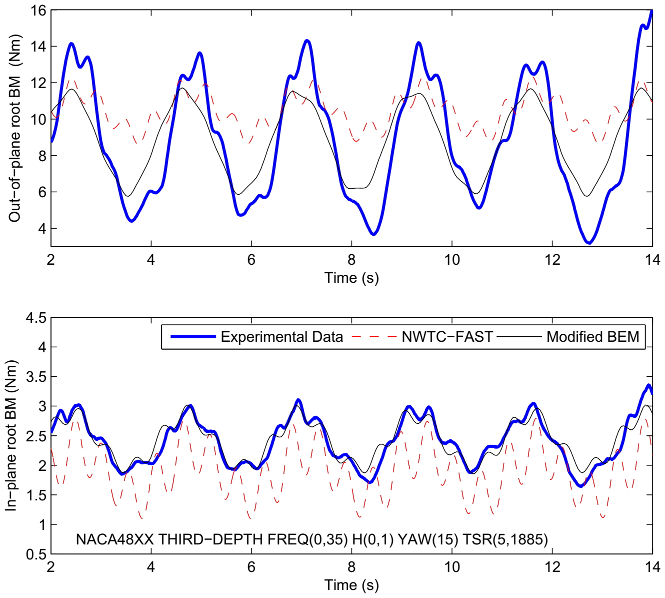

Fig. 13. Time series blade root bending moment comparison of experiment with NWTC-FAST and modified BEM codes. Third-depth, 0.35 Hz intrinsic wave frequency, 0.1 m wave height, 15° yaw angle and TSR of 5.2.

FAST has served to validate the results here, but cannot be used as a genuine comparison due to its application as a wind turbine specific code. Maniaci and Li [32] carried out some interesting research pertaining to modifying FAST for a TST application. The inclusion of added mass effects with AeroDyn, one of the main subroutines behind FAST, showed that added mass (inertia) effects could be important for the structural loading of tidal turbine blades. Their work will be used to feed into a new version of FAST suitable for TST applications.

In general it can be seen that the modified BEM code provides good predictions of the complex blade loadings experienced by a TST under wave and yawed flow conditions. In-plane bending moments are well predicted apart from a slight over prediction at the lower TSRs. Out-of-plane bending moments give a very good indication of the loading pattern, however they have been found to under predict the loading range.

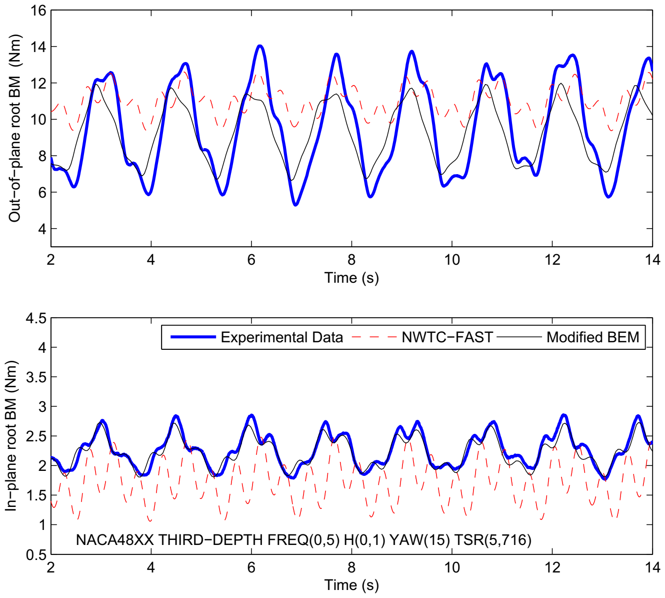

Fig. 14. Time series blade root bending moment comparison of experiment with NWTC-FAST and modified BEM codes. Third-depth, 0.5 Hz intrinsic wave frequency, 0.1 m wave height, 15° yaw angle and TSR of 5.7.

5. Conclusions

It has been demonstrated that the presence of waves and the effect of rotor misalignment is likely to have a detrimental impact on TSTs. This is not a significant problem in terms of power output, other than to further complicate the power electronics required for smoothing the power/flicker. The main issue with wave–current interaction around a TST is the cyclic loading, which will likely result in accelerated fatigue to the rotor and blades. This is particularly evident in the axial flow direction. Another important consideration is whether a rotor yaw drive is required at any specific tidal site. Large amounts of directional swing will occur around headlands and can cause a significant reduction in power as well as increase the dynamic loading if a yaw drive is omitted.

In summary, for a turbine in dynamic flow:

- The out-of-plane bending moment has been shown to be as much as 9.5 times the in-plane bending moment (for a full-scale wave period of 12.8 s). A maximum loading range of 175% of the median out-of-plane bending moment and 100% of the median in-plane bending moment was observed for this test case
- The wave frequency was found to be more significant than the wave height in terms of loading range of a blade (compared based on wave power in W/m)
- Steady yaw loading on an individual blade is negligible in comparison to wave loading (for the range of experiments carried out)
- Steady yaw loading is important for the turbine rotor as a whole, resulting in reduced power capture and reduced thrust

Numerical modelling summary:

- Dynamic inflow must be included for the calculation of TST loads otherwise loading amplitudes will be significantly under predicted especially for axial thrust force and out-of-plane bending moments.
- An effective dynamic inflow model has been created and used to improve BEM blade load prediction
- Dynamic stall may be neglected in some cases since its effect here was limited. This may not be the case for turbulent flows or non-linear waves where the inflow angle to the blades is subject to rapid change.
- The inclusion of steady yaw effects (using the skewed axial inflow correction) in a BEM model should be used with caution when waves are also modelled. Omitting the skewed axial inflow correction results in significantly improved load prediction.
- The gravitational/buoyancy component is significant to the in-plane blade bending moment and should be included in any BEM model developed for TSTs. Omitting such a source will result in under prediction of forces and also temporal errors in loading prediction.

The continuing work presented in this paper will assist in the structural design of TST rotor blades, quantification of dynamic loading effects and maximisation of rotor diameter to achieve a robust, high energy yield device.

6. Further work

The inclusion of a more suitable yaw correction and possibly a blockage correction for tank experiments will improve the modelling results. This research is on-going and further work will include more detailed experiments of waves and yawed flow effects using a non-uniform current. Dynamic yaw experiments will be included at a later date. Blockage and wake studies will be performed. The modelling of blade acceleration and inertial effects should provide a basis for fatigue analysis in future work when rpm/TSR is implemented as a variable. This could be validated using blade mounted accelerometers and actuator fence/disc studies. This modelling could then be used for the design of optimised TST blades for tidal stream turbine application at precise geographical locations.

Acknowledgements

Funding from EPSRC, grant number: EP/P504740/1

References

[1] Black and Veatch. Phase II UK tidal stream energy resource assessment. carbon trust; 2005.

[2] Bedard R, Previsic M, Polagye B, Hagerman G, Casavant A. North America tidal in-stream energy conversion technology feasibility study. EPRI TP-008-NA; 2006.

[3] Jo CH, Lee KH, Rho YH. Recent TCP (Tidal current power) projects in Korea. Sci China Ser E Technol Sci 2010;53(1):57–61.

[4] Thomson J, Polagye B, Richmond M, Durgesh V. Quantifying turbulence for tidal power applications. In: Oceans 2010 MTS/IEEE Seattle 2010.

[5] Norris JV, Droniou E. Update on EMEC activities, resource description, and characterisation of wave-induced velocities in a tidal flow. In: Proc. 7th European wave and tidal energy Conference, Porto, Portugal 2007.

[6] Myers LE, Bahaj AS. Scale reproduction of the flow field for tidal energy converters. In: Proc. 10th world renewable energy congress, Glasgow, UK 2008.

[7] MCT. Available from: http://www.marineturbines.com/, 2012, [accessed 21.02.12].

[8] Andritz Hydro Hammerfest HS300. Available from: www.hammerfeststrom.com, 2012, [accessed 26.06.12].

[9] OpenHydro Group. Development: EMEC. Available from: www.openhydro.com, 2012, [accessed 26.06.12].

[10] EMEC. Available from: http://www.emec.org.uk/, 2012, [accessed 22.03.12].

[11] Scottishpower Renewables. Sound of Islay. Available from: www.scottishpowerrenewables.com; 2012 [accessed 26.06.12].

[12] Barltrop N, Varyani KS, Grant A, Clelland D, Pham X. Wave-current interactions in marine current turbines. Proc IMechE 2006;220. Part M: J. Engineering for the Maritime Environment.

[13] Galloway PW, Myers LE, Bahaj AS. Studies of a scale tidal turbine in close proximity to waves. In: Proc. 3rd international conference on ocean energy, Bilbao, Spain 2010.

[14] Molland AF. The design, construction and calibration of a five-component strain gauge wind tunnel dynamometer. University of Southampton; 1976. Ship Science Report, 1/77, ISSN: 0140-3818.

[15] Burton T, Sharpe D, Jenkins N, Bossanyi E. Wind energy handbook. UK: John Wiley & Sons Ltd; 2001.

[16] Moriarty PJ, Hansen AC. AeroDyn theory manual. National Renewable Energy Laboratory; 2005. NREL/TP-500-36881, Available from: http://wind.nrel.gov/ [accessed 31.01.11, accessed 01.02.11].

[17] Manwell JF, McGowan JG, Rogers AL. Wind energy explained: theory design and application. 2nd ed. UK: John Wiley & Sons Ltd; 2009, ISBN 978-0-470-01500-1; 2009.

[18] GL-Garrad Hassan. Available from: http://www.gl-garradhassan.com/, 2012, [accessed 27.05.11].

[19] Drela M, Youngren H. XFOIL 6.9. Available from: http://web.mit.edu/drela/Public/web/xfoil/; 2001 [accessed 01.02.10].

[20] Pitt DM, Peters DA. Theoretical prediction of dynamic-inflow derivatives. Vertica 1981;5:21–34.

[21] Leishman JG, Beddoes TS. A semi-empirical model for dynamic stall. J Am Helicopter Soc 1986;34:3–17.

[22] Tarzanin FJ. Prediction of control loads. J Am Helicopter Soc 1972;17:33–46.

[23] Dean RG, Dalrymple RA. Water wave mechanics for engineers and scientists. UK: World Scientific Publishing Co. Pte. Ltd; 1984.

[24] ISO.. Petroleum and natural gas industries – specific requirements for offshore structures – part 1: metocean design and operating conditions. 1st ed.; 2005. EN ISO 19901-1:2005.

[25] Viterna LA, Corrigan RD. Fixed pitch rotor performance of large horizontal axis wind turbines. NASA technical reports server: 19830010962. Available from:, http://ntrs.nasa.gov/; 1982.

[26] Snel H, Houwink R, Bosschers J. Sectional prediction of rotating lift coefficients on rotating wind turbine blades in stall. ECN-C–;93–052; 1994.

[27] Barnsley and Wellicome. Final report on the 2nd phase of development and testing of a horizontal axis wind turbine test rig for the investigation of stall regulation aerodynamics, carried out under ETSU agreement E.5A/CON5103/1746; 1990.

[28] Garrett C, Cummins P. The efficiency of a turbine in a tidal channel. J Fluid Mech 2007;588:243–51.

[29] Whelan JI, Graham JMR, Peiro J. Inertia effects on horizontal axis tidal-stream turbines. In: Proc. 8th European wave and tidal energy conference, Uppsala, Sweden 2009.

[30] Abonnel C, Achard J, Archer A, Buvat C, Guittet L, Lenes A, et al. Some aspects of EDF modelling and testing activities, within its marine current energy research and development project. In: Proc. 6th European wave and tidal conference, Glasgow, UK 2005. p. 1–10.

[31] Jonkman J. FAST, NWTC design codes. Available from: http://wind.nrel.gov/designcodes/simulators/fast/; 2012 [accessed 01.09.11].

[32] Maniaci D, Li Y. Preliminary investigation of introducing added mass effect into the general dynamic wake theory for tidal current turbines. Mar Technol Soc J 2012;46(4):71.

Operational issues surrounding the use of towing tanks for performance quantification of marine current energy converters

Luke Myers, Pascal Galloway, AbuBakr Bahaj

Sustainable energy Research Group, Faculty of Engineering and the Environment
University of Southampton, SO171BJ, UK.
luke@soton.ac.uk
P.W.Galloway@soton.ac.uk

Abstract— **Towing tanks are being utilised far more frequently for the performance quantification of Marine Current Energy Converters (MCECs) due to their relatively low cost and ease of use. In this paper a number of issues are addressed that arose during a series of experimental campaigns investigating the performance of both static and dynamic MCEC models. These include the lack of ambient turbulence, carriage vibration, repeatability, carriage advance speed, vortex-induced-vibration and blockage. Results of experiments are also compared to those in circulating flumes and the relative merits of each type of facility are presented. Recommendations are that specific types of experiments such as wake measurements, power capture etc. are better suited to a specific type of facility although it is acknowledged that facility availability is often the overriding factor. It is difficult to judge previous published and ongoing work but the authors believe that many of the issues quantified in the paper through real world MCEC experimental studies are easy to overlook and could lead to less accurate experimental results. Recommendations for measurement of experimental parameters through the various stages of experimentation are given in order that future studies can be more comprehensive and accurate.**

Keywords— **Towing tank, Measurement, Accuracy, Error**

I. INTRODUCTION

Despite the seeming advanced nature of many Marine Current Energy Converters smaller-scale experimental studies are still highly valued for concept, device design and even for testing deployment and operational actions. Small-scale testing offers lower risk and lower cost testing that can generally be conducted in a shorter time period than at sea [1].

A key difference between tank or flume work compared to in-situ ocean testing is that of control and acceptance. At smaller indoor facilities conditions can be accurately controlled such that steady state experimental work can be conducted. Quantification of performance across a pre-defined envelope of operating conditions can be planned and executed in minimal time. Both water conditions and device operational parameters can be modified in relatively short time. At sea the testing regime is governed by acceptance. The resource varies in both a spatial and temporal manner. You must wait for a specific metocean condition to occur and whilst this is predictable for velocity and direction other issues such as wave conditions might not be. Therefore small-scale testing is still seen as a valuable proving ground for a wide range of design concepts, parameters and processes.

II. CHARACTERISTICS OF TOWING TANKS AND FLUMES

In order to characterize the performance of small-scale marine current energy converters (MCECs) there are two potential methods; a) move the device through a static fluid field or b) keep the device static and move the fluid. Both concepts are depicted in Fig. 1.

Towing tanks have been used extensively in scale MCEC studies [2-5]. The facilities generally have relatively low operating costs with the largest proportion of this associated with the towing mechanism and wave-maker. All towing tanks have an intrinsic ‘working’ length characterized by the distance that can be maintained at a steady, set towing speed. Buffer zones at either end are for safety and for acceleration/deceleration of the carriage. This working length is reduced for faster towing speeds to enable safe acceleration and braking. Most wave makers are capable of generating regular and irregular waves. The most basic tanks have the wave makers situated at the downstream end with varying carriage velocity only ‘into’ the waves. Following waves can be generated if the reverse carriage speed is also variable.

For MCEC experiments the generation of waves whist towing is advantageous although a true-combined wave-current interaction is not observed. Turbulence in towing tanks is zero as the water is still hence downstream wakes observed by any other flow structures will not be as representative as flumes or water channels. Data acquisition is also more cumbersome with time lost accelerating, slowing, reversing the carriage and waiting for the tank to settle between towing runs. However the lower costs of towing tanks compared to water channels, wave-making facilities and good cross sectional area properties ensure that they are utilised for aspects of MCEC research.

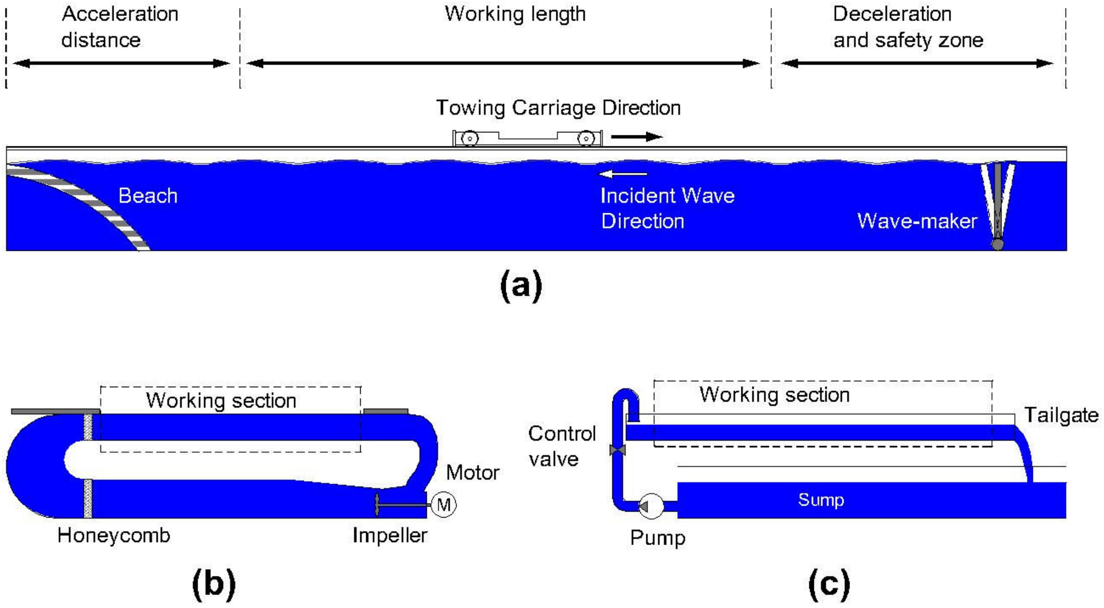

Fig. 1 - Side elevation of towing tank (a), circulating water channel (b) and circulating flume (c)

Flumes can be forced loops or an 'open' gravity driven design herein defined as 'water channel' or 'flume' respectively. Circulating water channels are permanently flooded and so can move large volumes of water easily thus working sections can be wide and deep. Disadvantages include installation of equipment (due to difficulty associated with draining down the flume) and varying water depth (again requires drainage). Gravity-fed flumes lift water from a sump and deposit at the upstream end of the working section. Flow rates and depths are often controlled via valves and a weir located at the end of the working section to create a backwater profile. These flumes are often long in length and the working section is dry when not in use so installation of equipment is simple. However, volumetric flow rates and cross sectional areas are generally significantly lower than circulating channels.

The ratio of device area to the channel cross-sectional area (commonly known as the blockage ratio) is important when quantifying the thrust force and power generated from a model MCEC's hydrodynamic (energy-capture) subsystem. For higher blockage ratios fluid cannot expand naturally around the device (as it would in an unconstrained flow field) and thus more fluid is entrained through the energy-capture area and measured thrust and power is increased. Methods have been developed to correct for this effect [6] and studies have demonstrated that the corrections hold when converting between different blockage ratios and also when changing the type of facility from a circulating channel to static towing tank [7]. In general it is good practice to minimise the blockage ratio but not at the expense of device performance and other scaling issues. Examples include operation in laminar flow or insufficient kinetic energy flux to replicate an operational envelope commensurate with a larger or full-scale device.

III. TYPES OF MEASUREMENT REQUIRED FOR QUANATIFICATION OF MARINE CURENT ENERGY CONVERTER PERFORMANCE ASSESSMENT

Measurements can be divided in a number of arbitrary ways. For the purpose of this work they will be classified as:

1) Inflow / natural environment
2) Device
3) Device-affected flow field

Herein we will principally address item 1 which shares some common issues with item 3. Measurements addressed herein include the quantification of towing speed, wave climates and the general flow field around the model MCEC. Other practical issues such as repeatability, ambient noise and base line condition are also addressed.

Due to the wide range of MCEC devices, modes of operation and device parameters that can be measured the reader is referred to Part IIB of the EquiMar protocols [8]. This gives valuable guidance on device measurement in addition to measurement of other test parameters. This paper shares the common aim with EquiMar to ensure the highest quality of small-scale testing possible and to this end some of the work addressed in this paper is represented in part IIB of the protocols. Specific aspects concern *Experimental Design*, *Quality and Accuracy of results* and *Calibration of sensors*. All are addressed in the final protocol (part IIB) and also in project deliverable D3.4 [9].

IV. EXPERIMENTAL SETUP

The experiments presented in this paper were carried out at Solent University's wave/towing tank (60m long x 3.7m wide x 1.8m deep – see Fig 2). A full-spanning motorised carriage can traverse down the tank at a maximum speed of 4m/s; Reversing speed is fixed at approximately 0.46m/s. A mid-depth-hinged wave maker is situated at the downstream end of the tank with the capability of generating both regular and irregular waves. The experimental issues addressed in the paper arose during a series of experiments involving a 1/15th-scale tidal turbine model (see Fig.3) that was equipped with the capability to measure rotor thrust and torque (utilising a dynamometer) and rate of rotation (via optical sensors). The parameters of the model varied included: TSR (tip-speed-ratio), turbine yaw and turbine submergence depth. Testing was conducted over a range of tow speeds and wave climates.

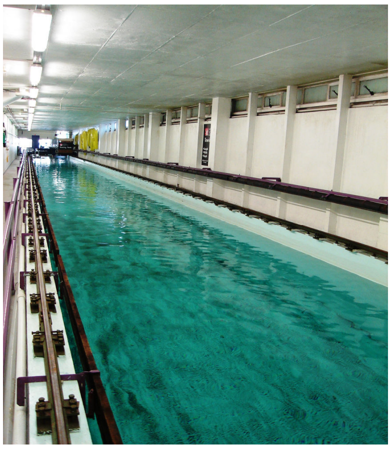

Fig. 2 - Towing tank facility

V. ISSUES RELEVANT TO ACCURATE PERFORMANCE ASSESSMENT IN TOWING TANKS

A. *Verification of Carriage Speed*

The repeatability of the towing carriage was verified. Sample 1 in Table 1 was omitted since the carriage motor and gearbox would need to be warm before the results could be representative. The variance in speed for subsequent runs was far lower.

Sample	**Forward average speed (m/s)**	**Reverse average speed (m/s)**
1	0.460	0.463
2	0.455	0.459
3	0.453	0.457
4	0.453	0.458
5	0.455	0.457
6	0.454	0.458
7	0.453	0.455
8	0.456	0.456
9	0.455	0.457
10	0.456	0.456

TABLE I
VERIFICATION OF TOWING CARRIAGE SPEEDS

The standard error of the mean;

$$= \sigma \Big/ \sqrt{N} \qquad (1)$$

for the carriage speed was essentially zero (to three decimal places) where σ is the standard deviation and N is the number of samples. Care must also be taken when towing models that impose a significant drag force upon the carriage. A brief check that the carriage set speed remains the same for towing with/without the model is recommended. Speed can be measured simply by timing the carriage over the working section (Fig. 1) or by using a device which has been independently verified i.e. a Doppler velocimeter or pitot tube.

B. *Flow field measurement*

There are a number of instruments that can be employed to characterize the flow field around a model MCEC. Pitot tubes, propeller meters, Doppler devices and wave probes will be addressed herein. In all cases the effective length of the towing tank and the rate of data acquisition will determine the quantity of data that can be collected. A sound judgement should be made as to the number of towing runs required to produce a robust and accurate data set. Repeatability of measurements is addressed in section V.D.

1) *Pitot tubes*

Pitot tubes offer a robust method of acquiring velocity data. Used in parallel several can be employed in a rake or array to facilitate fast data collection. They can only acquire in the principal direction of flow and at a single point. The determination of the forward velocity is based upon solid physical principals; the tube head has two tappings that measure the dynamic and static pressures.

$$V = \sqrt{2g(\Delta h)} \qquad (2)$$

Where g is the acceleration due to gravity and Δh is the differential pressure (dynamic to static) measured at the manometer or pressure transducer. If Δh is large enough then the accuracy of a pitot tube is very high assuming pressure measurements can be read to a good degree of precision. Generally in steady flow the height of fluid in a monometer can be read to ±1mm. If the pitot tube is situated upstream of a model then this should be the case. In the wake of the device the damping caused by the inertia of water in the tubes may manifest as an oscillating value read by the transducer or a slowly oscillating column of fluid in the manometer. An average value should be recorded and the repeatability should ideally be checked with further towing runs.

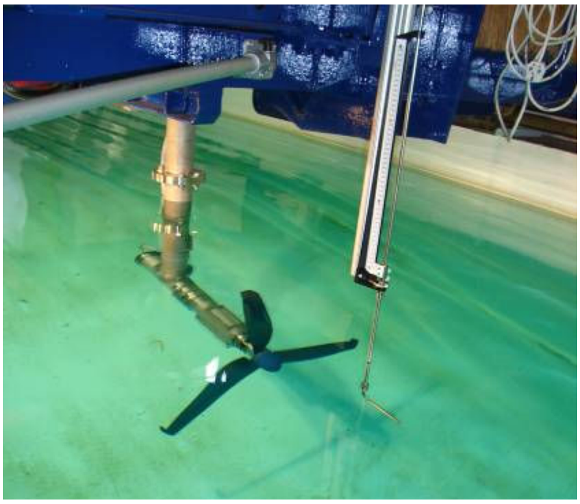

Fig. 3 - Pitot tube installed upstream of 1/15th – scale MCEC for verification of inflow velocity

There are a number of issues surrounding the setup of pitot tubes. The first is that all air is removed or bled from the flexible tubing between the pitot tube and the equipment used to measure the differential pressures (generally a manometer). The water in the tubes will lead to small changes in velocity being damped out due to the inertia of the water in the tubes and therefore pitot tubes can only really be employed to measure mean flow velocity over a towing run; faster sampling will not resolve rapidly changing flow structures. Ideally the manometer should be placed below the level of the tubes or as close as possible. This is often difficult as the tank is generally recessed below the carriage or general working area. At higher carriage speeds the pressures in the pitot tubes should be sufficient to overcome small differential heights between the tube heads and manometer. However, a calibration check against the set carriage speed or another device capable of measuring velocity should be conducted.

2) *Propeller meters*:

Propeller meters are simple devices that rotate in a plane orthogonal to the flow direction. The propeller creates a low voltage DC voltage output that varies linearly with flow speed. Implementation in towing tanks holds few practical issues. A recent calibration of the instrument should always be conducted before and after the testing period. Propeller meters often have an appreciable size meaning that use upstream of small models sensitive to disturbance is not advisable when acquiring other data. Voltage outputs can be acquired using a number of means but care should be taken not to sample at high frequency and expect coherent resolution of higher order flow effects such as turbulence. As with pitot tubes propeller meters are best employed for mean flow measurements. Their strength lies in having a simple output, low cost and ability to deploy in an array for multiple point measurement.

3) *Doppler Velocimenters*

Doppler velocimeters utilize the phase shift of light or sound as it is emitted from an instrument and is reflected from particles in the water back to a receiver. Measurements are taken in a small finite volume of fluid displaced below the sensor head. Generally at least 2 and usually 3 axes are resolved at high frequency allowing the quantification of both mean velocity and higher order flow effects. The principles of operation and accuracy issues are well documented for general use [10-12]. A key issue for the use of Doppler velocimeters is the amount of backscattering material suspended in the water. As the water in a towing tank is not regularly disturbed or circulated nearly all suspended matter will settle to the bottom. Therefore it is necessary to seed the water with small particles to provide strong return acoustic or light signals back to the Doppler velocimeter. Failure to seed the water will result in the acquisition of incoherent data as the device struggles to achieve sufficiently high return signal strengths. Circulating water channels and flumes generally return good results without the need for seeding; however results can normally be improved with a relatively small amount of seeding material.

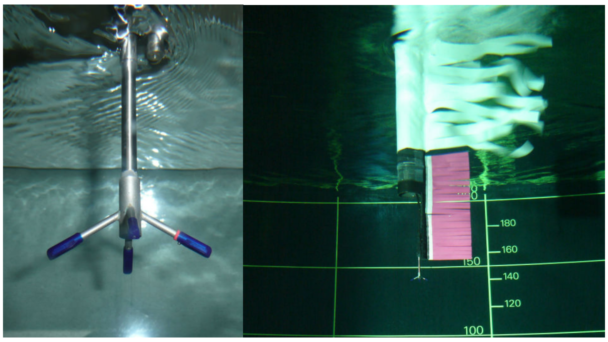

Fig. 4 - Acoustic Doppler Velocimeter head unit (left) and installed in turbulent flow (right)

Fig. 5 illustrates the reduction in data variability with even a modest amount of seeding material added to the tank. Data is shown for a steady towing speed over a period of 20 seconds sampling at 50Hz. The percentage occurrence is expressed as a decimal fraction.

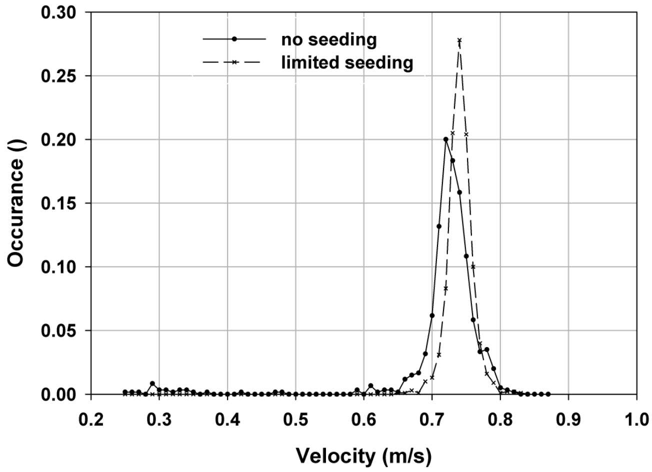

Fig. 5 – Increasing measurement accuracy for velocity for a single towing run by use of seeding particles (20 seconds data at 50Hz)

It can be seen that the variability in the received data is much reduced when more suspended matter is added to the tank. Aliasing errors and spiking prevalent in the clean water condition are removed. Seeding material should have a specific gravity close to 1. In the case of this work 13 micron hollow glass spheres were used with a specific gravity of 1.1. During testing it was necessary to partly re-seed the tank each morning. Seeding was added until instrument measurement quality parameters rose to acceptable levels. The amount of seeding required will vary depending upon:

- the size of the tank
- frequency of the emitted sound/light pulse
- any internal instrument data processing
- manufacturer recommended data quality

The first point is quite obvious. A useful mixing aid to distribute seeding throughout a static body of water is the operating model MCEC itself. The second issue pertaining to frequency is important as higher emitted frequencies will attenuate more rapidly in water according to Stokes' law and thus may require higher concentrations of backscattering material compared to a lower frequency instrument. Many devices return data quality indicators such as received signal strength (transmit signal divided by ambient noise level) and correlation scores. Some are more useful than others in defining data quality. For example the correlation score can often appear low in turbulent flows despite the data being good quality [13]. Other instruments perform internal data quality assessments and only output data above a specific threshold of accuracy. Users of Doppler devices should fully understand the working of the instrument before use. Some device manufacturers indicate lower bound values of parameters such as instrument signal to noise ratio or correlation to ensure good quality data. In the authors' experience this is not a definitive limit and should be exceeded to ensure maximum data quality. Often data requires further post processing but by maximising parameters such as device signal to noise ratio and correlation scores any data loss due to processing should be minimal.

Post processing can increase the data quality by removing spurious points. The precise method of filtering can sometimes appear quite arbitrary. There are a number of statistical methods and filtering techniques based upon physical phenomenon and the choice and inter-comparison is best left to the individual. Statistical methods include simple minimum/maximum thresholds. Fig. 5 above is a good example as the data can be seen to hold a roughly normal distribution. An example filtering criterion could be based upon the fact that 99.7% of data should lie within 3 standard deviations from the mean. Often significant spikes reach far beyond this limit so removal is sound.

Physical filters can be employed such as deleting sample points where the acceleration from or to the surrounding points is greater than g. The authors' preference is the velocity cross-correlation filter as proposed by Cea et. al [14]. This works by defining an ellipsoid around the varying velocity components of the sample in 3 dimensions. Data outside the ellipsoid is removed as shown in Fig 6. This filter works especially well when towing into waves and thus has been employed during studies of the 1/15th - scale model MCEC. Data shown is for wave amplitude of 0.088m, Period 1.34 sec, forward velocity 0.67m/s and depth 0.4m.

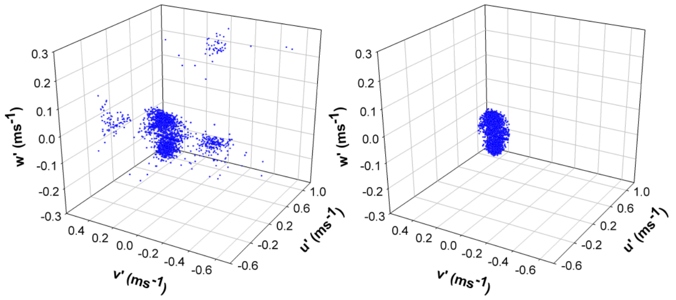

Fig. 6 - Effect of filtering Doppler velocimeter data. Raw sample set (left) and filtered data (right)

Fig 7. shows the time series data corresponding to that shown in Fig 6. Removed data points were replaced using shape-preserving cubic interpolation.

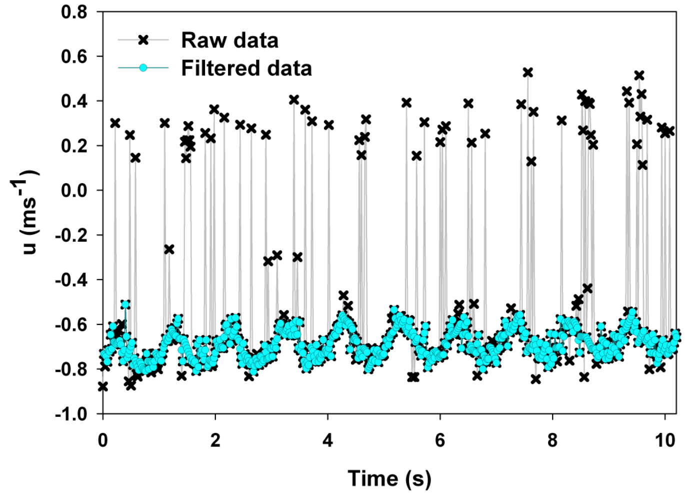

Fig. 7 - Time series velocity data for unfiltered and filtered conditions

Again it must be stressed that adequate seeding of towing tanks will facilitate the use of Doppler velocimeters and the multiple axis, rapid sampling that they can achieve with an associated reduction or even eliminating of post processing. In other cases more simple instruments are often better employed to measure axial mean velocities.

4) *Wave probes*

It is good practice to verify the input to the wave maker with a separate wave probe measurement and not to solely rely upon the settings stated on the driving software. A simple resistive wave probe can be employed a reasonable distance upstream of the wave maker to verify the output wave parameters. Wave probes should be regularly calibrated. Fig. 8 shows a typical wave series propagating up the towing tank.

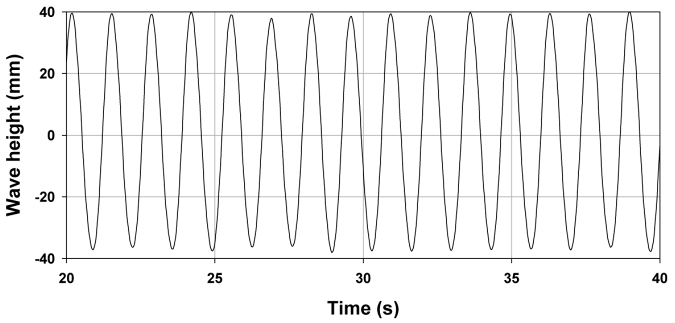

Fig. 8 - Wave height reading from resistive wave probe in towing tank

Data was collected over a 90-second period for the wave conditions specified at the wave maker of 1.34s period and 0.088m amplitude. Measured data gave an average period of 1.34s and average wave height of 0.076m. Whilst data in Fig.8 appears quite regular the wave height is not close to that specified. The discrepancy was remedied by adjusting gain parameters at the wave maker but this again highlights the importance of the quantification of baseline conditions.

If towing into waves the carriage should commence moving once the waves have reached the turbine. This will ensure that one the carriage is up to speed the initial waves (which are often not representative of the remaining series) have passed. Similarly, reflected waves from the beach must be avoided.

C. *Carriage motion and Vortex Induced vibrations*

Baseline conditions are an important aspect of any testing. In towing tanks it is probably unrealistic to assume that the carriage motion is perfectly steady. We can easily determine the forward speed with time using a number of instruments addressed above in section VB. Towing tank carriages generally run on rails of relatively short length. Despite best efforts in aligning the rails there is always the likelihood that the carriage will move vertically (or laterally) along the passage down the tank. If this occurs it is likely to affect many of the device measurements recorded. Quantification can be made by utilising accelerometers mounded upon the support structure of the model MCEC. Placement is important as the model is likely to be supported away from the main carriage and carriage/tank contact point (rails) thus the magnitude of any vibration is likely to be amplified whilst frequency may be reduced. Doppler velocimeters are another useful instrument to quantify any such vibration with travel (assuming the water is well seeded).

It is recommended that any carriage shake or rumble be identified ahead of the testing phase. This will allow an assessment to be made as to the duration and severity for each towed run. Also it might be that the problem manifests at or above certain speeds. Mitigation could include using elastomers or similar to damp down any oscillations transferred from the carriage to the MCEC device.

When water passes a submerged bluff body, vortex shedding can occur causing regular or random vibration. The generation and remediation of this Vortex Induced Vibration (VIV) is an entire subject in its own right and is of great concern in many heavy industries, most notably offshore hydrocarbons.

The propensity for VIV will depend upon a number of factors including inflow direction, velocity and the shape and sectional stiffness of the body in the water. Sequential shedding of vortices often lead to a lateral oscillation commonly referred to as ‘bowing’. Fig. 9 shows the energy spectra from an acoustic Doppler velocimeter attached to a bowing stainless steel tube. The lateral oscillations are evident as a peak in the energy spectra at approximately 4Hz (centre trace).

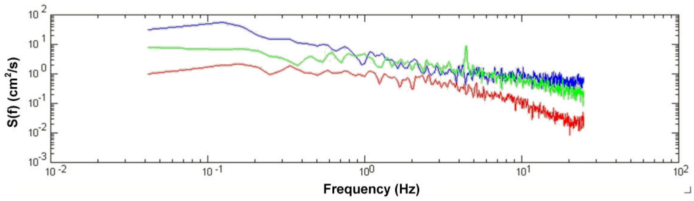

Fig. 9 – Lateral resonance of cylindrical support arm holding ADV instrument.

There are a number of solutions to this issue. Often resisting the motion by increasing the stiffness of the body in the water will only result in a small decrease (if any) of motion. A better approach is to either change the section shape to avoid vortex shedding or to damp down the vortices using strakes or feathered material as depicted in Fig 4. (right).

D. *Measurement Repeatability*

Repeatability of the tank conditions is an important aspect of any experimental programme. Testing in towing tanks does involve a good deal of lost time spent accelerating, decelerating, reversing and waiting for the tank to settle between runs. Therefore ascertaining the limits for the number of runs required to accurately quantify each point of MCEC device performance is essential.

For example, in section VA above the steadiness of the carriage forward tow speed is demonstrated. Similarly the waves generated from the wave maker also demonstrated very low variance between each run. If the baseline conditions are relatively steady then there is a good chance that the MCEC will operate in a steady fashion (when carriage is up to speed) and thus a small number of runs will suffice to accurately quantify performance at any operational point. Evidently the more levels of parameters that are recorded, the greater the systematic error e.g. it is likely that velocity measurements will be more repeatable than load measurements since the load measurements are also reliant upon the incident velocity.

Whilst there are no absolute standard prescribed for the accuracy and repeatability for experiments there is a very strong need for the maximisation of accuracy. This will be dependant upon the nature of the experiments and any constraints but it should be noted that for robust results all practical measures should be taken to minimise errors and ensure a high degree of accuracy. Section IIB of the EquiMar protocols [8,9] gives guidance on the reporting of data accuracy and this should always be provided so that independent assessment of the experimental accuracy can be made.

VI. CONCLUSIONS

This paper has addressed a number of issues pertaining to the accuracy and repeatability of experiments to quantify MCEC device performance in towing tanks. Such facilities generally have lower operational expenditure compared to large circulating flumes hence they are commonly utilised for the quantification of performance parameters of Marine Current Energy Converters (MCECs).

Whilst towing tanks offer a lower cost and wave-making capabilities this has to be balanced against the lack of ambient turbulence and a greater time required for data acquisition due to the discrete length of a towing run compared to the time required for acceleration, deceleration, reversing and tank settlement.

This paper has highlighted a number of issues that should always be considered in any towing tank to assess the baseline conditions. These include verification of carriage speed, wave properties and carriage shake (unsteady motion). Once the Model MCEC is in place measurement systems and instruments should also be carefully checked for setup parameters and signal feedback strengths/accuracy. These include onboard systems (e.g. rotor thrust/torque) and any peripheral measurements such as those used to quantify the characteristics of the surrounding flow field. Care should be taken with Doppler instruments to ensure strong return signals and pitot tubes require a careful setup and may be inappropriate for some tanks or for low advance speeds.

Once the setup and baseline conditions have been verified an assessment of the accuracy and repeatability of measurements associated with the operation of the model MCEC should be conducted. Whilst there are no absolute limits the operator should ensure that the highest practical level of accuracy is achieved and that this is quantified in any reporting. Examples are given in this paper and also in part IIB of the EquiMar protocols [8,9].

Post processing of data can be employed to further increase accuracy of results. Once again details should be provided in any experimental report and the operator must ensure that both the raw acquired data is always saved and that any filtering/post processing techniques are understood and fit for purpose. If the above techniques and actions are employed then the quality of work conducted in towing tanks for the performance quantification of MCECs should be enhanced benefitting both the person(s) conducting the testing, the wider marine energy community and any further development/up-scaling of the MCEC device in question.

REFERENCES

[1] Department for Energy and Climate Change (2008). Tidal-current Energy Device Development and Evaluation Protocol. URN 08/1317. Available at: http://www.berr.gov.uk/files/file48401.pdf

[2] Barltrop, N., Grant, A., Varyani, K.S. & Pham, X.P. (2005) Wave-current interactions in marine current turbines. In Proc. 6th European Wave and Tidal Conference, Glasgow, UK, 2005. pp. 33-38.

[3] Galloway, P.W., Myers, L.E. & Bahaj, A.S., (2010). Studies of a scale tidal turbine in close proximity to waves. In 3rd International Conference on Ocean Energy, Bilbao, Spain.

[4] Bahaj, A.S., Batten, W.M.J. & McCann, G. (2007) Experimental verifications of numerical predictions for the hydrodynamic performance of horizontal axis marine current turbines. In Renewable Energy, 15(32), pp. 2479-2490.

[5] Grant, A. & Johnstone, C., (2010). Contra Rotating Marine Turbines Tank Tests to Analyse System Dynamic Response. In 3rd International Conference on Ocean Energy.

[6] Barnsley MJ, Wellicome JF. Final report on the 2nd phase of development and testing of a horizontal axis wind turbine test rig for the investigation of stall regulation aerodynamics. Carried out under ETSU Agreement E.5A/CON5103/1746, April 1990.

[7] Bahaj A.S., Molland A.F., Chaplin J.R. and Batten W.M.J. (2007) Power and thrust measurements of marine current turbines under various hydrodynamic flow conditions in a cavitation tunnel and a towing tank. *Renewable Energy*, Volume 32, Issue 3, March 2007, pp 407-426.

[8] D. Ingram, G. Smith, C. Bittencourt-Ferreira and H. Smith, *Protocols for the Equitable Assessment of Marine Energy Converters*, University of Edinburgh, School of Engineering, Edinburgh, United Kingdom, 2011. ISBN: 978-0-9508920-2-3

[9] Equimar deliverable 3.4. (2011) Project homepage [Online]. Available: http://www.equimar.org/

[10] Voulgaris G., Trowbridge J.H. (1998) Evaluation of the acoustic Doppler velocimeter (ADV) for turbulence measurements. J Atmos Ocean Technol Vol. 15, pp. 272–289.

[11] Lohrmann A., Cabrera R., Kraus N.C. (1994) Acoustic Doppler velocimeter (ADV) for laboratory use. In: Proceedings of symposium on fundamentals and advancements on hydraulic measurements and experimentation. ASCE, pp 351–365.

[12] Skeivalas, J., Giniotis, V., (2003) Analysis of accuracy of measurement by Doppler laser meters, Optical Engineering, Vol. 42, no. 7, pp. 2025-2028.

[13] Myers, L.E. & Bahaj, A.S., (2010). Experimental Experimental analysis of the flowfield around horizontal axis tidal turbines by use of scale mesh disk rotor simulators, Ocean Engineering, Vol. 37, pp. 218-227.

[14] Cea, L., Puertas, J. & Pena, L. (2006) Velocity measurements on a highly turbulent free surface flow using ADV. In Experimental Fluids, vo. 42, pp. 333-348.

Experimental and numerical results of rotor power and thrust of a tidal turbine operating at yaw and in waves

Pascal W. Galloway[1,*], Luke E. Myers[1], AbuBakr S. Bahaj[1]

[1] *Sustainable Energy Research Group, School of Civil Engineering and the Environment,*
University of Southampton, Southampton, SO17 1BJ, UK.
**Corresponding Author Tel +44(0)23 80595458, E-mail: P.W.Galloway@soton.ac.uk*

Abstract: Little has been done to investigate the behaviour of Marine Current Energy Converters (MCECs) in unsteady flow caused by wave motion and yaw. The additional loading applied to the rotor through the action of waves and whilst operating at yaw could dictate the structural design of blades as well as the proximity to the water surface. The strongly bi-directional nature of the flow encountered at many tidal energy sites may lead to devices employing zero rotor yaw control. Subsequent reductions in device capital cost may outweigh reduced power production and increased dynamic loading for a rotor operating at yaw. The experiments presented in this paper were conducted using a 1/20th scale 3-bladed horizontal axis MCEC at a large towing tank facility. The turbine had the capability to measure thrust and torque via a custom waterproof dynamometer. A BEM (Blade Element Momentum) code developed within the university was modified to include wave and yaw, with a view to further understanding the primary loading upon the rotor and individual blades.

Keywords: *marine current energy converter, wave-current interaction, strain gauge, loading*

1. Introduction

One of the enduring topics of interest in the field of coastal and offshore engineering is that of wave-current interactions and their effect on static and dynamic structures. The co-existence of waves and currents is a common feature in the marine environment [1]. Waves are strained and refracted by currents, causing exchanges of mass, momentum and energy to occur between the waves and mean flow [2]. The main energy in the coastal region can be attributed to tides, surges and wind waves. Interactions occur between these different 'waves' because the tides and surges change the mean water depth and current field experienced by the waves [3]. The usual approach to the interaction problem has been to ignore the interaction between waves and currents and simply add the two together (using their particle velocity vectors) so as to calculate the forces on a body [4].

Marine Current Energy Converter (MCEC) technology is currently at the prototype stage where unique devices are being deployed at specific sites or marine energy testing centers. There is little detailed knowledge of the flow field properties at highly energetic tidal energy sites [5]. Generally peak flow speeds are measured but the effect of wave and bed generated turbulence is neglected. The effect this will have on MCECs is unclear, which may lead to prototype devices being installed at sheltered locations where these effects are minimised [5]. If this becomes a trend with developers it may result in reduced energy capture as blade diameters are constrained and potentially higher energy flows are not utilised. MCECs of a given rated power typically experience four times the thrust of a wind turbine of the same rated power, even though the MCEC will be significantly smaller in diameter. Thus it is expected that rotor loading and general structural integrity could be significant for MCEC devices. Therefore the need to quantitatively assess the blade/rotor loading caused by wave-current interaction is clear. At present, few experimental wave-current studies have been conducted in the presence of MCECs. One particular study combined Blade Element Momentum (BEM) theory for wind turbines and linear wave theory to predict rotor torque and thrust and to assess the influence of waves on the dynamic properties of bending moments at the root of rotor blades [6]. The outcomes were limited, particularly those for the blade loading. In the field, research carried out at the European Marine Energy Centre showed that in a water depth of 45m, wave effects penetrated as far down as 15m whilst turbulence from the bottom boundary layer penetrated up as much as 17m. This resulted in approximately a third of the water column remaining relatively tranquil [7]. If blade loading in the more turbulent regions could be quantified then this may allow for greater energy capture from larger diameter rotors.

2. Methodology

2.1. Towing Tank Experiment

The experiments presented in this paper were conducted in a wave/towing tank (60m long x 3.7m wide x 1.8m deep). A 1/20th - scale tidal turbine model (see Fig.1) was equipped with the capability to measure rotor thrust and torque (utilising a waterproof dynamometer) and rate of rotation (via optical sensors). The parameters varied included: TSR (tip-speed-ratio), turbine yaw and turbine submergence depth. The blades utilised a NACA 48XX profile with varying thickness and twist along the chord length. The waves used had a height of 0.1m and a 1.34s intrinsic period; current speed was $0.9ms^{-1}$.

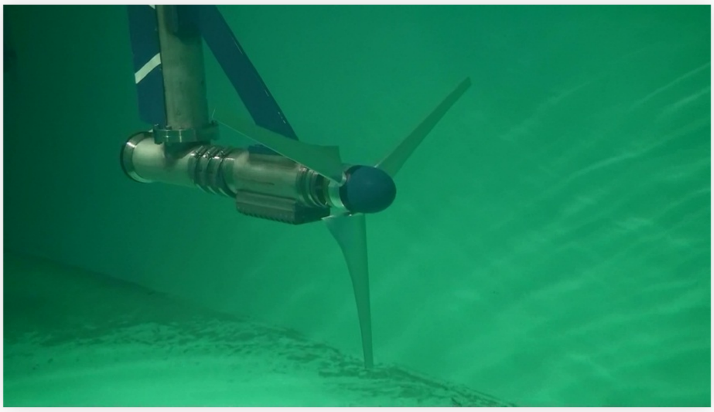

Fig. 1. Underwater photo of 1/20th scale tidal turbine model

The design of the thrust-torque dynamometer utilised for this work is discussed previously [8] and was based on the extensive work carried out by Molland and Turnock [9] for their research on ship propellers. A wireless telemetry system located inside the turbine nacelle collected filtered and amplified signals from the strain gauges before data was conveyed above the waterline via a sealed umbilical cable. The model turbine is a Froude scaled representation of a 16m diameter MCEC. The maximum scaled current speed would be 4m/s, which is significant for a suitable MCEC location; however it is significantly lower than the maximum current speed of 8.55m/s used in the experiments conducted by Barltrop [6]. High velocities tend to be used in turbine experiments because a low Reynolds number can degrade the dynamical properties of the airfoil and can be a source of irregularity between the experimental data and simulation data [6]. Laboratory experiments are useful for approximating these wave-current phenomena since little detailed knowledge exists for tidal energy sites since there has never before been the need for such data [5]. The problem is that the use of a towing tank results in no actual Doppler shift in the waves because there is no real current present (see section 2.2). More complex facilities such as a circulating water channel with wave-making facilities would be more representative; however depths would need to be at least 2m with the ability to generate waves from a range of directions relative to the current.

2.2. Numerical Model

Numerical modelling has shown that the influence of waves complicates the flow with its influence being more than just adding turbulence. The dynamic part of the waves causes significant oscillations in the power and thrust, which in-turn influence the 'quality' of the electrical power production. High frequency oscillations (known as flicker) occur. It is thought that this flicker is caused by variations of the angle of attack under the influence of wave motion [10]. The nature of wave-current interaction is complex: If a current encounters a wave in the same flow direction, the wave height decreases with an increase in wavelength, whilst the current speed increases. The opposite is true if the current encounters a wave in the opposite flow direction [3].

A Doppler shift is observed when surface waves and current velocities interact. The primary effect of a current is to change the frequency of the waves due to a Doppler shift. The observed angular frequency, ω, of the waves in a frame of reference moving with the current, σ, the intrinsic angular frequency and the wave number, k, is given by:

$$\omega = \sigma + kU \tag{1}$$

This relationship describes how the observed wave frequency reduces or increases based on current velocity. A Doppler shift is valid in the case of a constant current, but a more complex effect is noted in the case of sheared currents. Use of linear wave theory superimposed on a uniform current does not give a strictly accurate representation of wave-current interaction effects. It is however a straightforward approach and may yield adequate results for a MCEC. Linear wave theory has been found to be a fairly accurate representation of wave-current interaction in depths of water greater than 12.5m and with significant wave heights lower than 5m for the purposes of dispersion [3].

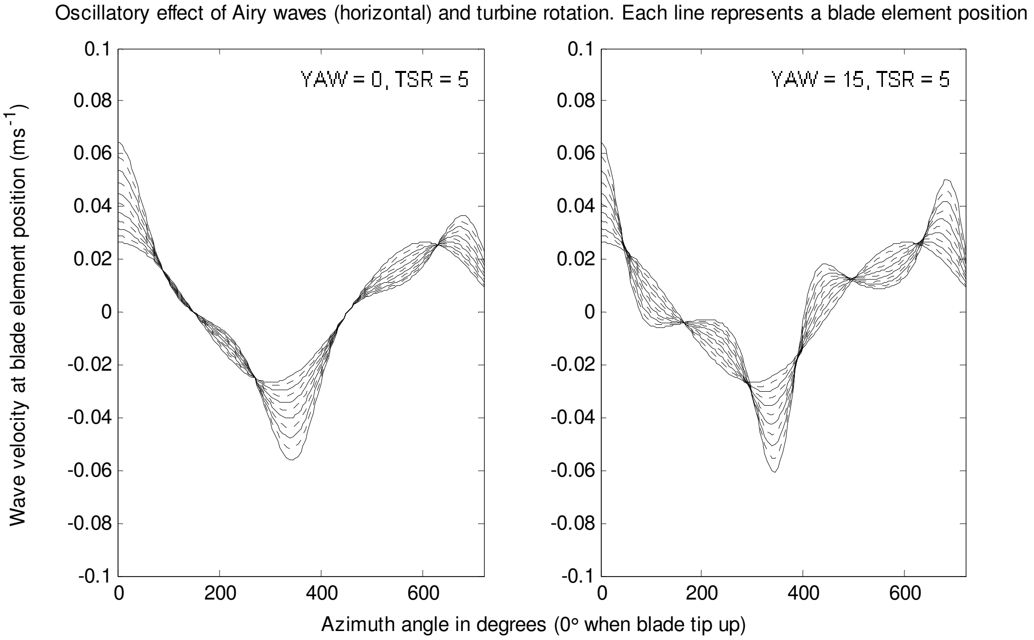

Fig. 2. 1st order wave-current interaction velocities as seen at individual blade elements over two revolutions. The left figure is for zero yaw, the right figure is for 15° yaw. The largest oscillations can be observed at the outer element i.e. at X=1, the tip of the blade (X = elemental radius/blade radius)

It is well known that BEM theory is commonly used by wind turbine designers for predicting loads and power outputs for wind turbines. Although this theory is readily applicable to MCECs there are some differences. Wind for example does not have a characteristic property that resembles wave-current interaction; therefore this must be taken into account when designing prototype MCECs. A BEM code has been modified to include the effect of monochromatic waves on a uniform current with the inclusion of yawed flow if desired. The model assumes that there is no distortion to the incoming flow field or lateral velocity variation and that rotor speed is constant. An example of the wave velocities observed at a single blade can be seen in Fig.2. These velocities are calculated using linear wave theory with a Doppler shift. Based on BEM geometry, these velocities are then calculated instantaneously at each blade element for a given TSR and yaw angle. This output then feeds directly into the BEM code (see Fig.3 for an outline of the numerical model).

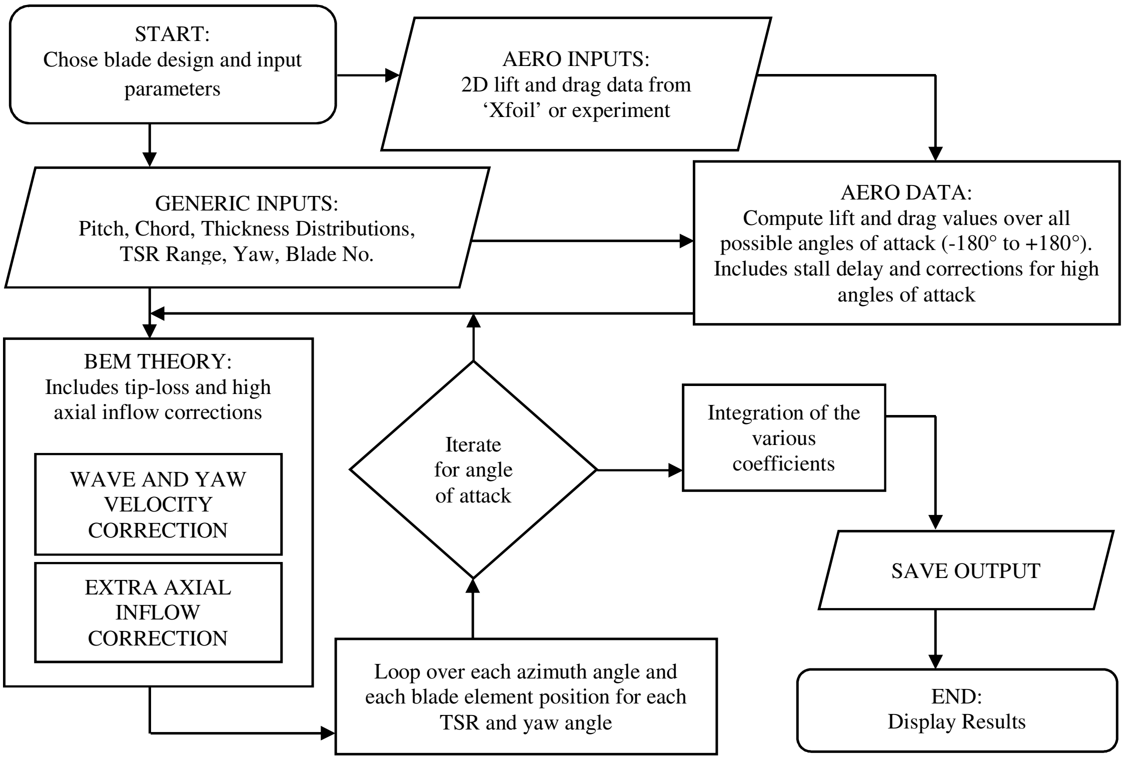

Fig. 3. Flow diagram for BEM numerical model showing the processes involved

3. Results and Discussion

The model MCEC (Fig.1) was used to acquire measurements of thrust, torque and rotor speed for both yawed and wave environments. Fig.4 shows the comparison between experimental data and numerical model for a yawed and un-yawed case. Blockage corrections by Barnsley and Wellicome [11] have been applied to the data. This is a requirement since measurements tend to be over predicted in relatively narrow channels (blockage is ~7%). Figures 5-8 are for a NACA 63-8XX blade, used for comparison with Bahaj et al. [12]. Results show good agreement, which when viewed alongside Fig.4, gives some confidence that the numerical model is valid. No figure is included to show the effect of waves on mean C_P and C_T because the resulting mean wave velocity at the rotor is approximately zero.

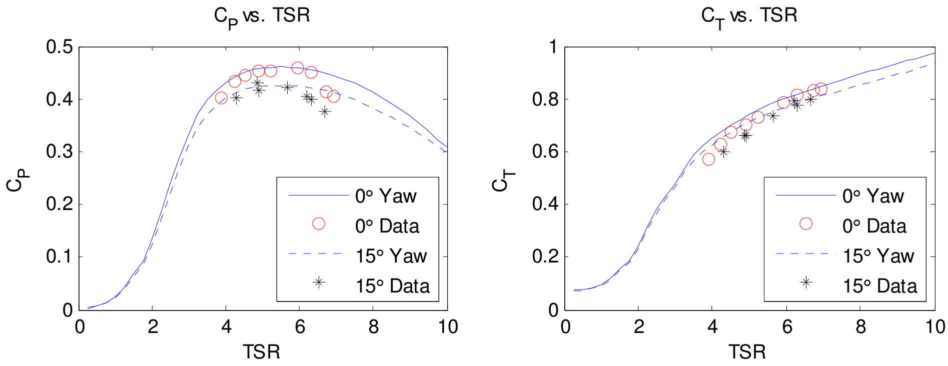

Fig. 4. Left: Power coefficient (C_P) vs. TSR for 0° yaw and 15° yaw with experimental data included for comparison. Right: Thrust coefficient (C_T) vs. TSR for respective yaw angles

The effect of waves is pronounced when investigating the azimuthal variation of C_P and C_T however, and has serious implications for the fatigue loading of blades as shown in Figures 5 and 6. A few of the parameters used in BEM are shown in these figures and the range over which they vary is represented by the plot line thickness. In Fig.5, the gradient of C_P is calculated using several of the other variables shown in the figure, amongst others. At zero gradient, C_{P_MAX} occurs at 85% blade radius, which is also the region of maximum power variation. This model assumes constant rotor speed which is unlikely to occur in reality. The variations seen in the angle of attack are likely to cause acceleration and deceleration of the rotor which may lead to a greater range of C_P.

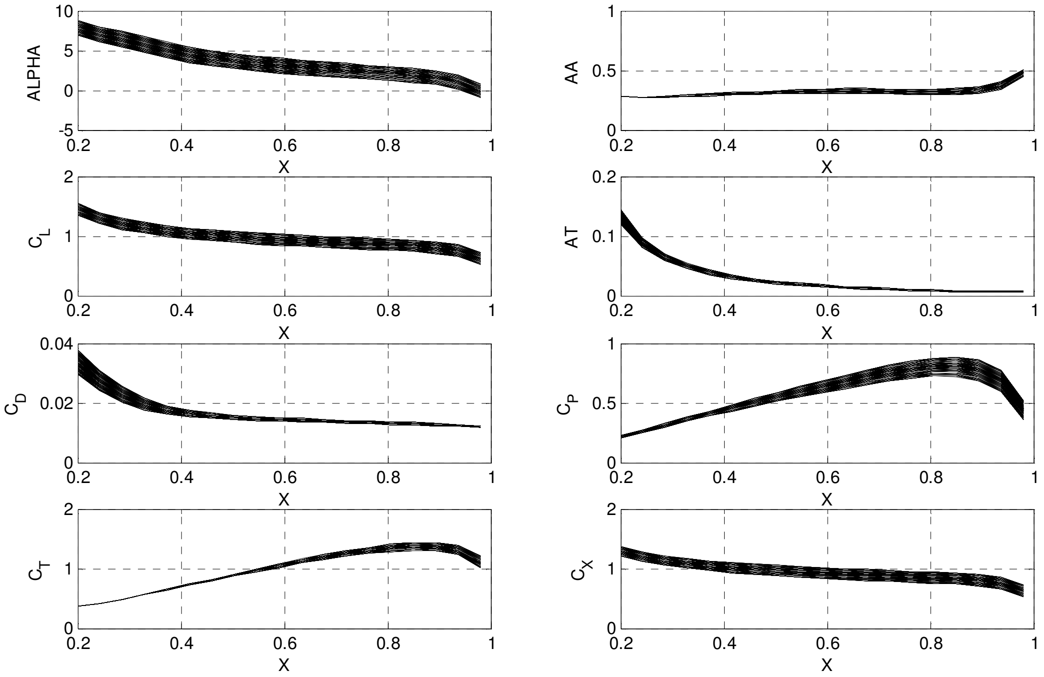

Fig. 5. Plots showing change in Alpha (angle of attack), C_L (lift coeff'), C_D (drag coeff'), AA (axial inflow factor), AT (tangential inflow factor), C_P (power coeff'), C_T (thrust coeff'), C_X (axial force coeff') across the blade span. Line thickness in each plot shows the effect of azimuthal variation. Only small waves are shown here. TSR = 6, Yaw = 0°

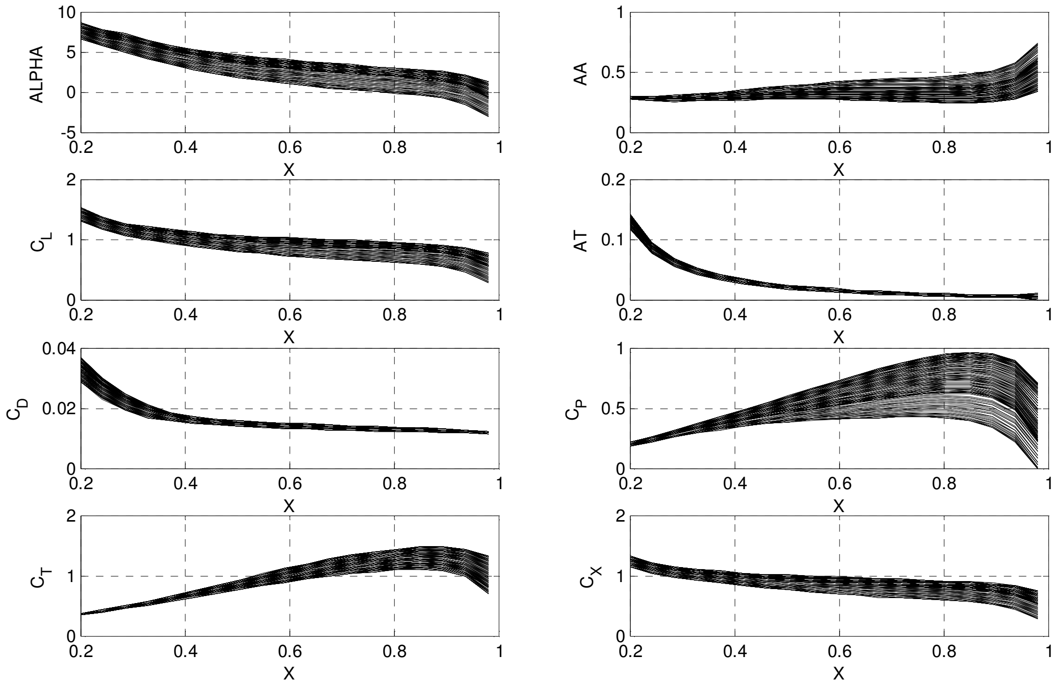

Fig. 6. See Fig.5 for description. Small waves and 15° yaw are shown here. TSR = 6, Yaw = 15°

This vindicates the concerns of flicker due to varying angle of attack (see section 2.2); since high frequency oscillations in voltage, caused by rapid changes in rotor speed, can lead to flicker in the power.

When a turbine is yawed to the flow, both power and thrust are reduced (see Fig.4). This is only apparent above 7.5° yaw with an approximate 20% power reduction at 22.5° yaw [8]. This is a noticeable difference and is likely to be higher than the 20% suggested because the rotor experiences a reduced effective velocity in yawed flow, hence reduced TSR.

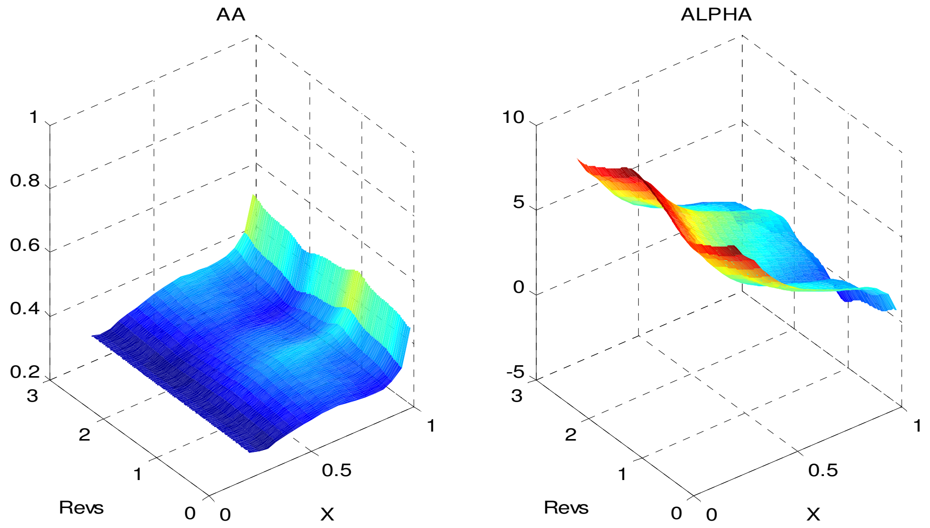

Fig. 7. Surface plots showing axial inflow factor and angle of attack from Fig.5 varying with blade radius and azimuth (3 revolutions)

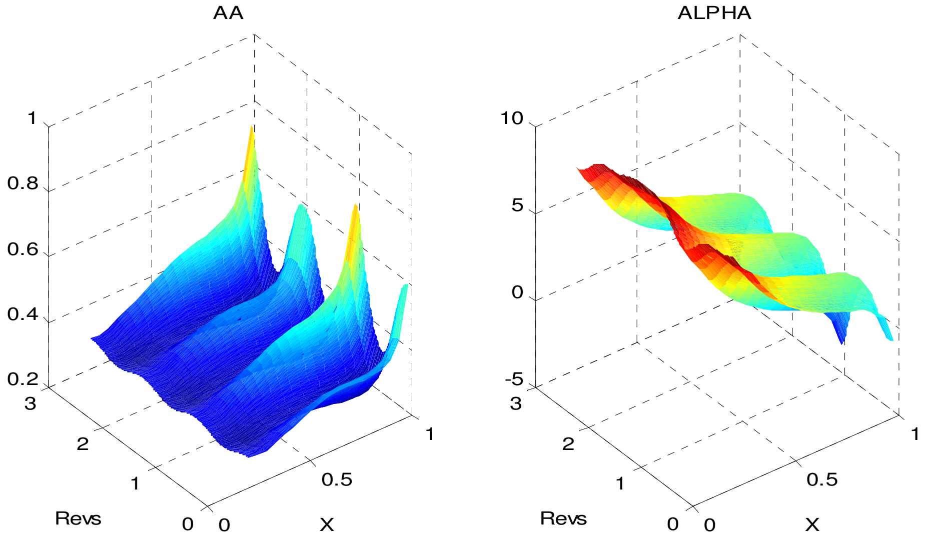

Fig. 8. Surface plots showing axial inflow factor and angle of attack from Fig.6 varying with blade radius and azimuth (3 revolutions)

The inclusion of yaw dramatically increases the range over which some of the parameters vary (see Fig.6). C_P in particular varies ~3 times more at 85% blade radius for 15° of yaw. Surface plots in Figures 7 and 8 have been included to show how the axial inflow factor and the angle of attack vary over 3 blade revolutions, with and without yaw (15°). It should be noted that in Fig.8, the waves have less influence than yaw in the power producing region of the blade. This is an important point because the yaw effect can easily be avoided with the use of a yaw drive.

4. Further Work

This research is ongoing and further work will include more detailed experiments including additional testing at yaw into waves and measurement of individual blade loading. When the effects of linear theory have been properly evaluated, the next phase of testing will be to verify findings using waves on a non-uniform current. Barltrop [6] showed that the bending moments at roots of MCEC blades were found to fluctuate significantly; 50% of the mean value for out-of-plane bending moments and 100% of the mean value for in-plane bending moments. This justifies the need for individual blade loading experiments. In addition, steeper waves were found to impose lower bending moments in both directions about the roots of the rotor blade. It should also be noted that the in-plane bending moment is affected by the gravity bending moment component, so a neutrally buoyant blade would be desirable, if not impractical for a small model.

The BEM code will be expanded to describe the loading effects on a turbine blade in more detail. Further work will include modelling of blade acceleration, gravity effects and added mass, with a view to providing a model for fatigue analysis. This model could then be used for the design of optimised MCEC blades for tidal environments.

5. Conclusions

It has been demonstrated that waves are likely to have a detrimental impact on MCECs. This is not a significant problem in terms of power output, other than to further complicate the power electronics required for smoothing the power/flicker. The main issue with wave-current interaction around a MCEC is the cyclic loading, which will likely result in accelerated fatigue to the rotor and blades. This is particularly evident in the axial flow direction. Another important consideration is whether a rotor yaw drive is required at any specific tidal site. Large amounts of directional swing will occur around headlands and can cause a significant reduction in power and increase in dynamic loading if a yaw drive is omitted. The continuing work presented in this paper will eventually assist in the structural design of MCEC rotor blades, quantify the loading effects caused by waves and maximise rotor diameter to achieve a robust, high energy yield device.

References

[1] Swan, C. & James, R. L. (2000) A simple analytical model for surface water waves on a depth-varying current. In Applied Ocean Research, Vol. 22, 2001, pp331-347.

[2] Smith, J. A. (2005) Wave-Current Interaction in Finite Depth. In Journal of Physical Oceanography, Vol. 36, 2006, pp1403-1419.

[3] Wolf, J. and Prandle, D. (1999) Some observations of wave-current interaction. IN: Coastal Engineering, Vol. 37, (1999), pp471-485.

[4] Srokosz, M. A. (1987) Models of Wave-Current Interaction. In Advances in Underwater Technology, Ocean Engineering, Volume 12: Modelling the Offshore Environment, Society for Underwater Technology, Graham & Trotman, pp313-325.

[5] Myers, L. E. & Bahaj, A. S. (2008) Scale reproduction of the flow field for tidal energy converters. In Proc. 10th World Renewable Energy Congress, Glasgow, UK, 2008.

[6] Barltrop, N. et al. (2005) Wave-current interactions in marine current turbines. In Proc. 6th European Wave and Tidal Conference, Glasgow, UK, 2005. pp33-38.

[7] Norris, J. V. & Droniou, E. (2007) Update on EMEC activities, resource description, and characterisation of wave-induced velocities in a tidal flow. In Proc. 7th European Wave and Tidal Energy Conference, Porto, Portugal, 2007.

[8] Galloway, P. W., Myers, L. E., & Bahaj, A. S. (2010). Studies of a scale tidal turbine in close proximity to waves. In Proc. 3rd International Conference on Ocean Energy, Bilbao, Spain, 2010.

[9] Molland, A. F. (1976) The design, construction and calibration of a five-component strain gauge wind tunnel dynamometer. University of Southampton, Ship Science Report, 1/77, ISSN 0140-3818.

[10] Abonnel, C. et al. (2005) Some aspects of EDF modelling and testing activities, within its marine current energy research and development project. In Proc. 6th European Wave and Tidal Conference, Glasgow, UK, 2005. pp1-10.

[11] Barnsley and Wellicome, Final report on the 2nd phase of development and testing of a horizontal axis wind turbine test rig for the investigation of stall regulation aerodynamics, carried out under ETSU agreement E.5A/CON5103/1746, April 1990

[12] Bahaj, A. et al., (2005) Experimental Investigation into the Hydrodynamic Performance of Marine Current Turbines. *Sustainable Energy Series, Report 3*, 2005.

Studies of a scale tidal turbine in close proximity to waves

P. W. Galloway[1*], L. E. Myers[1], A. S. Bahaj[1]

[1]Sustainable Energy Research Group, School of Civil Engineering and the Environment,
University of Southampton, Southampton SO17 1BJ, UK
*e-mail: p.w.galloway@soton.ac.uk

Abstract

The understanding of wave-current interaction is of increasing interest in the field of coastal and offshore engineering. An area where wave-current interaction is likely to be an important factor is in the development of Marine Current Energy Converters (MCECs). Little has been done to investigate the behaviour of MCECs in unsteady flow caused by wave motion and close proximity of the device to the structure. The additional forces applied to the blades through the action of the waves could very well dictate the structural design of blades as well as the proximity to the water surface. The forces applied to the blades from waves will not be perpendicular to the blades as with marine currents. The forces will be composed of a more complex circular motion. This repeating oscillation will place additional strain on blades, but if the magnitude of this can be quantified it may permit optimised MCEC devices to be placed nearer to the sea surface allowing manufactures to use larger blade diameters to maximise energy extraction.

Keywords: Blade Loading, Marine Current Energy Converter, Strain Gauge, Wave-Current Interaction

1. Introduction

One of the enduring topics of interest in the field of coastal and offshore engineering is that of wave-current interactions and their effect on structures. The co-existence of waves and currents is a common feature of most marine environments [1]. Waves are strained and refracted by currents, causing exchanges of mass, momentum and energy to occur between the waves and mean flow [2]. The main energy in the coastal region can be attributed to tides, surges and wind waves. Interactions occur between these different 'waves' because the tides and surges change the mean water depth and current field experienced by the waves [3]. The usual approach to the interaction problem has been to ignore the interaction between waves and currents and simply add the two together (using their particle velocity vectors) so as to calculate the forces on the structure. There are problems with this approach, namely that it is unclear whether this process will under-estimate or over-estimate the loading on the structure [4].

Marine current energy converter (MCEC) technology is currently at the prototype stage where unique devices are being deployed at isolated testing sites. There is little detailed knowledge of the flow field properties at highly energetic tidal energy sites [5]. Generally peak flow speeds are measured but the effect of wave and bed generated turbulence is neglected. The effect this will have on MCECs is unclear, which may lead to prototype devices being installed at sheltered locations where these effects are minimised [5]. If this becomes a trend with developers it may result in reduced energy capture as blade diameters are constrained and potentially higher energy flows are not utilised. MCECs of a given rated power typically experience three times the thrust of a wind turbine of the same rated power, even though the MCEC will be significantly smaller in diameter. Thus it is expected that rotor loading and general structural integrity could be significant for MCEC devices [6]. Therefore the need to quantitatively assess the blade/rotor loading caused by wave-current interaction is clear.

At present, few wave-current studies have been carried out relative to MCECs. In the laboratory, blade element momentum (BEM) theory for wind turbines has been combined with linear wave theory [7]. This was used to predict torque and thrust and to assess the influence of waves on the dynamic properties of bending moments at the root of rotor blades. The outcomes were limited, particularly those for the blade loading. In the field, research carried out at the European Marine Energy Centre showed that in a water depth of 45m, wave effects penetrated as far down as 15m whilst turbulence from the bottom boundary layer penetrated up as much as 17m. This resulted in approximately a third of the water column remaining relatively tranquil [8]. If the blade loadings in the turbulent regions could be quantified then this may allow for greater energy capture from larger diameter rotors. Several numerical models have been developed with regard to wave-current interaction but not many have been experimentally verified. Two of these models have been compared with model turbine data gathered from a towing tank and cavitation tunnel. One of these models, *GH-Tidal Bladed*, has been designed to combine wave and current loading; however no waves were used in the towing tank experiments so the model cannot be validated for wave-current interaction [9,10].

2. Wave-Current Interaction

When waves and currents interact, both affect the other in many complex ways. If a current flows in the same direction as a wave, the wave height decreases with an increase in wavelength, whilst the current speed increases [3,11,12] (see Fig.1). If a current is introduced from the opposite direction to a wave, the wave height increases with a decrease in wavelength, whilst the current speed reduces [3,11,12] (see Fig.1).

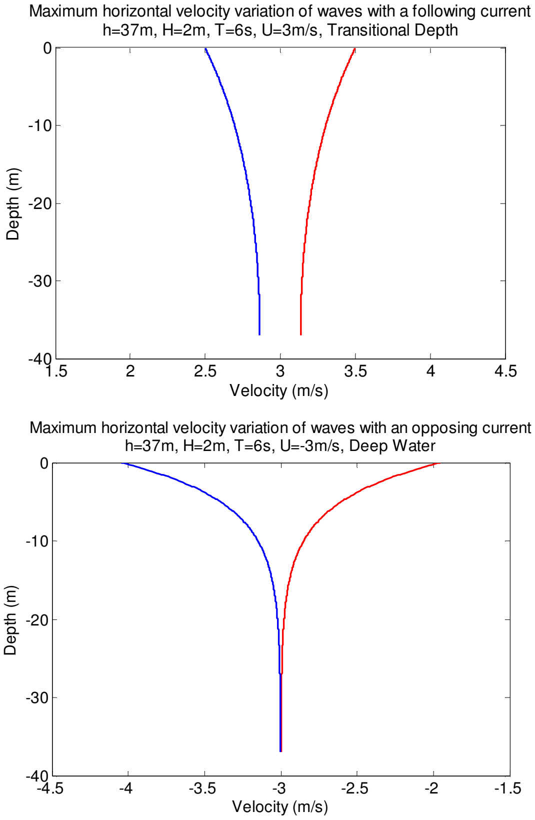

Figure 1: Maximum velocity profile variation. Wave and current superposition (Airy Theory)

Currents can also have the effect whereby they essentially force waves to turn towards the current direction. No turning occurs for waves with a following current, but when the current is opposing the waves they start to turn towards the current direction. [1,3]. In a non-breaking flow field, if the height of an approaching wave and the magnitude of an opposing current are sufficiently large, the wave height of the combined wave-current interaction could take a huge size (known as a rogue wave) [11]. Rogue waves could create great damage to the MCEC arrays they propagate over. Research has shown that wave motion in the upper part of the water column induces large variations in velocity at a particular spatial location i.e. the MCEC [9, 13]. The total unsteadiness in the flow experienced by the MCEC rotor and support structure will be the sum of wave effects and the background turbulence [14].

Much offshore design is modelled by a regular two-dimensional wave motion, superimposed on a one-dimensional current flow aligned along the direction of wave propagation, with a prescribed vertical profile [15]. The traditional design approach is as follows:

1. Calculate the wave velocity profile using suitably chosen nonlinear wave theory (for now the presence of a current is neglected)
2. Establish the current profile up to the still water level using any available engineering or oceanographic insights
3. Extrapolate the current profile up to the wave crest using any hydrodynamic insights.
4. Superimpose the wave and current flows by addition of the velocity and acceleration vector fields (neglecting interaction effects)

A Doppler effect is observed when surface waves and current velocities interact. The primary effect of a current is to change the frequency of the waves due to a Doppler shift. The observed angular frequency, ω, of the waves in a frame of reference moving with the current, σ, the intrinsic angular frequency and the wave number, k, is given by:

$$\omega = \sigma + kU \qquad (1)$$

If the current speed, U, is positive (waves and current travel in the same direction) then the frequency of the waves is increased above that of the still water case. If U is negative (waves and current in opposite directions) then the frequency is reduced [4]. For sufficiently high opposing currents, the waves will be unable to propagate against the current. In these opposing current cases, the wave steepness becomes larger (the crest becomes higher and sharper while the trough becomes shallower and flatter) as the current speed increases. This is due to wave action conservation [3]. A Doppler shift is valid in the case of a constant current, but a more complex effect is noted in the case of sheared currents [16].

Use of linear wave theory superimposed on a uniform current does not give an accurate representation of wave-current interaction effects. It is however a straightforward approach and may yield adequate results for a MCEC. For example, linear superposition can give a good approximation should the method of stretching the current profile be used, without conserving mass flux [15]. Linear wave theory has been found to be a fairly accurate representation of wave-current interaction in depths of water greater than 12.5m and with significant wave heights lower than 5m for the purposes of dispersion [3]. These parameters fit perfectly within the case of a MCEC, however the absolute frequency is unlikely to be constant if the current is not steady, similarly if the current is inhomogeneous, the intrinsic frequency will not be constant [3]. For laboratory testing these parameters will be assumed since the conditions are carefully controlled.

3. Experimental Testing

Laboratory experiments are useful for approximating these wave-current phenomena since little detailed knowledge exists for tidal energy sites since there has never before been the need for such data [5]. The problem is that the use of a towing tank results in no actual Doppler shift in the waves because there is no real current present. More complex facilities such as a circulating water channel with wave-making facilities would be more representative; however depths would need to be at least 2m with the ability to generate waves from a range of directions relative to the current.

The experiments presented in this paper were carried out at Solent University's wave/towing tank (60m long x 3.7m wide x 1.8m deep). A scale tidal turbine model (see Fig.2) was equipped with the capability to measure rotor thrust and torque (utilising a dynamometer) and rate of rotation (via optical sensors). The parameters varied included: TSR (tip-speed-ratio), turbine yaw and turbine submergence depth.

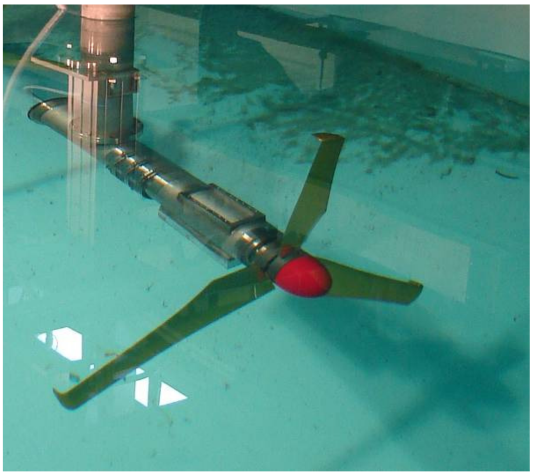

Figure 2: 1m diameter tidal turbine installed in Solent University's wave-towing tank. Photos reproduced with the permission of Atlantis Resources Corporation.

3.1. Load Measurement

The current alone imposes loading on objects in the water but an important loading effect is the combination of wave and currents. This is because the orbital velocities in waves impose a greater range of structural loading, possibly leading to increased fatigue if not immediate structural damage. In addition the drag force on an object in the water has a non-linear dependence on the fluid velocity. Numerical modelling has shown that the influence of waves complicates the flow with its influence being more than just adding turbulence. The dynamic part of the waves causes significant oscillations in the power and thrust, which in-turn influence the 'quality' of the electrical power production. High frequency oscillations (known as flicker) occur. It is thought that this flicker is caused by variations of the angle of attack under the influence of wave motion [17].

Loading on the model turbine rotor was measured using a specially designed dynamometer (see Fig.3). The design of a thrust-torque dynamometer for use on a scale MCEC was based on the extensive work carried out by Molland and Turnock [19] for their research on ship propellers. A robust design has been produced that can be attached to an existing scale MCEC. The measurement of thrust and torque is achieved using strain gauged flexures bending in contraflexure. The dynamometer is attached directly to the end of the turbine shaft, downstream of the rotor but upstream of all bearings and seals. The design differs from those used for ship propellers in that it will be subject to more extreme cyclic loading and will need to be fully waterproof. The torque component utilised an increased number of flexures in order to reduce any vibration caused by wave loading (torque flexures are visible in Fig.3). A wireless telemetry system located inside the turbine nacelle collected, filtered and amplified the signals from the strain gauges before data was conveyed above the waterline via a sealed umbilical cable.

Figure 3: Thrust-Torque dynamometer and rear section of rotor hub

The following operational parameters were used for the design of the dynamometer:

- Thrust coefficient $C_T = 0.9$,
- Mean flow speed, U = 1.5m/s (representative scale flow speed for potential MCEC site [8])
- Power coefficient, $C_P = 0.45$
- Minimum rotation per minute = 80rpm (rpm of model is between 80-200rpm).
- Swept rotor area: $A_d = \pi \times 0.4^2 = 0.5m^2$

Thus:

Power $= 0.5\rho U^3 A_d C_P$

$= 0.5 \times 1000 \times 1.5^3 \times 0.5 \times 0.45 = 382W$

Max torque: $Q = \frac{382}{8.38} = 23Nm$

Max thrust: $F = 0.5\rho U^2 A_d C_T$

$= 0.5 \times 1000 \times 1.5^2 \times 0.5 \times 0.9 = 509N$

The dynamometer was machined from solid aluminium bronze CA104. The maximum allowable strain at the flexure ends was assumed to be 1000με, based on the broad review by Molland [19]. The resulting stress is considered to provide a satisfactory margin with respect of hysteresis and load fluctuations.

3.2. Scaling

The model turbine is a Froude scaled representation of a 16m diameter MCEC. The maximum scaled current speed would be 4m/s, which is significant for a suitable MCEC location; however it is significantly lower than the maximum current speed of 8.55m/s used in the experiments conducted by Barltrop [7]. High velocities tend to be used in turbine experiments because a low Reynolds number can degrade the dynamical properties of the airfoil and can be a source of irregularity between the experimental data and simulation data [7]. There is nothing that can be done to increase this value since the velocity and depth are constrained by the Froude scaling, however it is improbable that this will be important since calculations show that the water in the tank will be fully turbulent. Fraenkel believes there is little use in testing models since the performance of axial flow rotors is well understood and relatively predictable [6]. Whilst this may be true for wind turbines, it does not translate directly to MCECs because the fluids behave differently. Wind for example does not have a characteristic property that resembles wave-current interaction; therefore this must be taken into account when designing prototype MCECs with the use of laboratory testing.

4. Results and Discussion

The model turbine (Fig.2) was used to acquire measurements of thrust, torque and rotor RPM for both yawed and wave environments. An example of the amplified signal response from the turbine's telemetry system can be seen in Fig.4. This clearly shows the carriage acceleration at 20s and deceleration at 55s, providing approximately 15s of steady data once the noise at 32s and 47s has been removed and the data concatenated. The noise is thought to be a mixture of electrical interference and some minor carriage rail imperfections leading to vibrations.

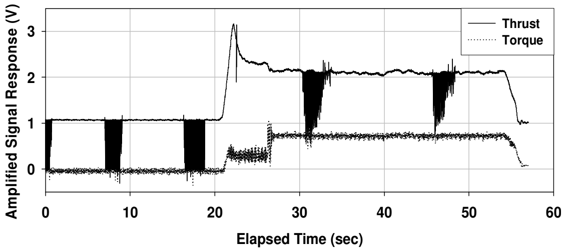

Figure 4: Thrust-torque dynamometer signal response

Thrust and torque traces for the turbine in a wave environment are shown in Fig.5 with a theoretical horizontal particle velocity trace for comparison. The torque signal is relatively noisy. This is possibly due to the rotor acting like spring-mass system and could possibly be solved by combining Wheatstone bridges across all six flexures rather than just a pair of flexures.

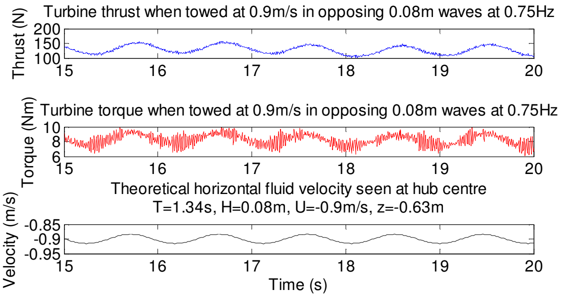

Figure 5: Thrust and torque measurements with horizontal particle velocity trace for comparison

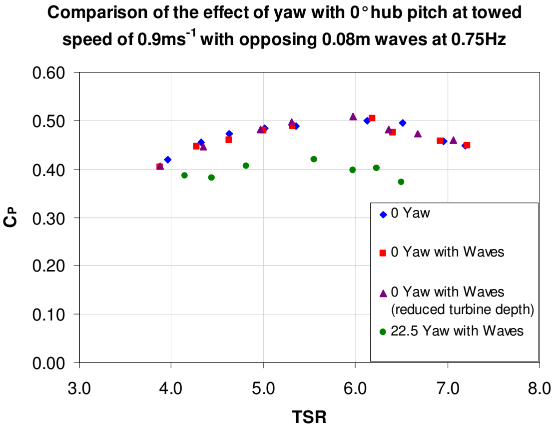

Figure 6: Coefficient of power vs. TSR with varying yaw in a wave environment (no blockage correction)

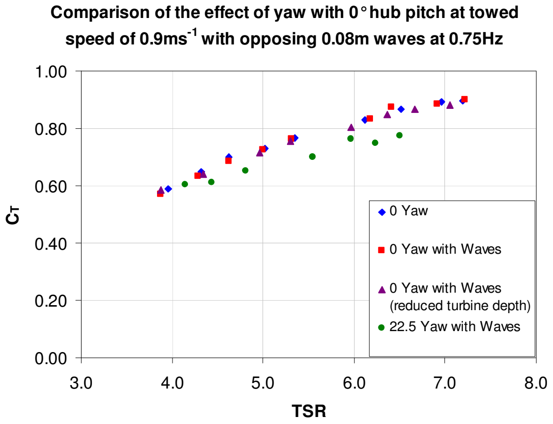

Figure 7: Coefficient of thrust vs. TSR with varying yaw in a wave environment (no blockage correction)

The signals were filtered and averaged to produce C_P (coefficient of power) and C_T (coefficient of thrust) curves, some of which are shown in Fig.6 & Fig.7. Blockage corrections have not yet been applied to the data. This is a requirement since measurements tend to be over predicted in relatively narrow channels (blockage is ~7%). Fig.6 shows the optimum TSR is 6 for the blades used (note – not the same blades as shown in Fig.2). Fig.7 has not quite reached the peak thrust coefficient but it can be seen that the curve is beginning to level out with an expected peak TSR between 7-9.

It can be seen from Fig.6 and Fig.7 that the wave climate used has no effect on the turbine performance. This is because the combined mean velocity observed at the rotor is the same as the current speed (see Fig.1). The reason waves are a concern however, is because of the range of cyclic loading that is applied. Fig.5 shows a range of thrust in the order of 37% of the mean and the torque is around 35% for the turbine at one third depth. This is quite considerable; waves used in the experiments are fairly small (~1.6m full scale in 37m water depth). This cyclic loading is likely to dramatically accelerate the fatigue of turbine blades.

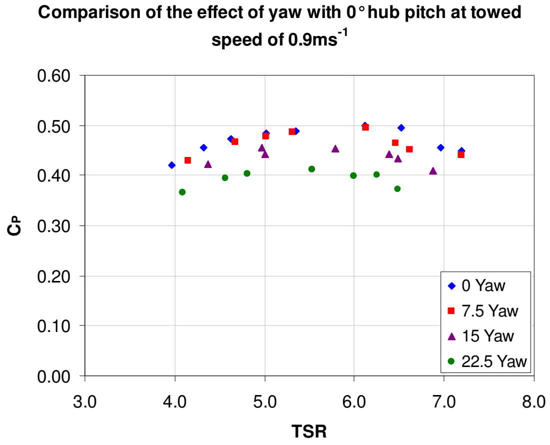

Figure 8: Coefficient of power vs. TSR with varying yaw (no blockage correction)

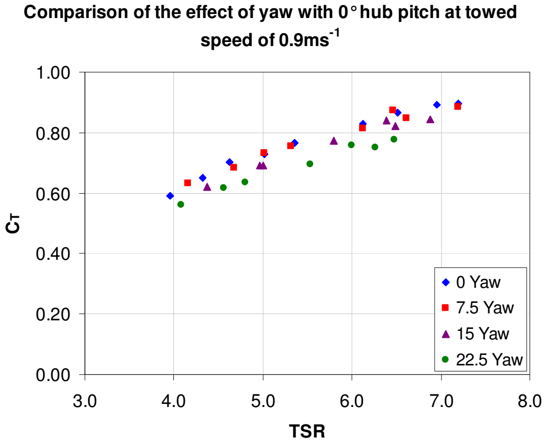

Figure 9: Coefficient of thrust vs. TSR with varying yaw (no blockage correction)

Yawed flow (in this situation the turbine is yawed) reduces power output as well as thrust (see Fig.8 and Fig.9). This is only apparent above 7.5° yaw with an approximate 20% power reduction at 22.5° yaw. This is a noticeable difference and is likely to be higher than Fig.8 suggests because the rotor experiences a reduced effective velocity in yawed flow. This means that the TSR will be reduced for a given current speed and this was observed during testing. These results show good agreement with the extensive testing carried out by Bahaj et al. [20].

5. Further Work

This research is ongoing and further work will include more detailed experiments including further yawed effects, structure effects and individual blade loading. When the effects of linear theory have been properly evaluated, the next phase of testing will be to verify findings using waves on a non-uniform current.

BEM theory will be used to describe the effects of the wave-current interaction on the turbine rotor. The possible problems with the use of BEM theory here is caused by the change of flow velocity around the rotor as well as the pressure field. A numerical model is being developed to simulate the wave effects using this theory. Barltrop [7] showed that the bending moments at roots of MCEC blades were found to fluctuate significantly; 50% of mean value for out-of-plane bending moments and 100% of mean value for in-plane bending moments. This explains the need for individual blade loading experiments. In addition, steeper waves were found to impose less bending moments in both directions about the roots of the rotor blade. It should also be noted that the in-plane bending moment is affected by the gravity bending moment component, so a neutrally buoyant blade would be desirable.

6. Conclusions

It has been demonstrated that waves are likely to have a detrimental impact on MCECs. This is not a significant problem in terms of power output, other than to further complicate the power electronics required for smoothing the power. The main issue with wave-current interaction around a MCEC is the cyclic loading, which will likely result in accelerated fatigue to the rotor and blades. Thrust and torque fluctuations can be greater than 35% of the mean rotor load and must be accounted for in the design process by firmly establishing the environment in which the turbine will operate. This should include extreme wave events.

It is also important to consider whether a rotor yaw drive is required at any specific tidal site. Large amounts of directional swing will occur around headlands and can cause a significant reduction in power and increase in dynamic loading if a yaw drive is omitted

The continuing work presented in this paper will eventually assist in the structural design of MCEC rotor blades, quantify the loading effects caused by waves and maximise rotor diameter to achieve a robust, high energy yield device. Any calculations involving combinations of waves and currents are prone to be in greater error as a result of both limitations in wave-current data and the theoretical understanding of wave-current interaction. Once detailed field data is collected from tidal energy sites, efforts can be made to optimise the flow field reproduction at smaller scales.

Acknowledgements

Blades were supplied by Atlantis Resources Corporation Ltd. for certain elements of the testing.

References

[1] Swan, C. & James, R. L. (2000) A simple analytical model for surface water waves on a depth-varying current. In *Applied Ocean Research*, Vol. 22, 2001, pp331-347.

[2] Smith, J. A. (2005) Wave-Current Interaction in Finite Depth. In *Journal of Physical Oceanography,* Vol. 36, 2006, pp1403-1419.

[3] Wolf, J. and Prandle, D. (1999) Some observations of wave-current interaction. IN: *Coastal Engineering*, Vol. 37, (1999), pp471-485.

[4] Srokosz, M. A. (1987) Models of Wave-Current Interaction. In *Advances in Underwater Technology, Ocean Engineering, Volume 12: Modelling the Offshore Environment,* Society for Underwater Technology, Graham & Trotman, pp313-325.

[5] Myers, L. E. & Bahaj, A. S. (2008) Scale reproduction of the flow field for tidal energy converters. In *Proc. 10th World Renewable Energy Congress*, Glasgow, UK, 2008.

[6] Fraenkel, P. L. (2005) Progress with Marine Current Turbines. In *Proc. 6th European Wave and Tidal Energy Conference*, Glasgow, UK, 2005.

[7] Barltrop, N. et al. (2005) Wave-current interactions in marine current turbines. In *Proc. 6th European Wave and Tidal Conference*, Glasgow, UK, 2005. pp33-38.

[8] Norris, J. V. & Droniou, E. (2007) Update on EMEC activities, resource description, and characterisation of wave-induced velocities in a tidal flow. In *Proc. 7th European Wave and Tidal Energy Conference*, Porto, Portugal, 2007.

[9] Bahaj A.S., Batten W.M.J. & McCann G. (2007) Experimental verifications of numerical predictions for the hydrodynamic performance of horizontal axis marine current turbines. In *Renewable Energy*, Volume 32, Issue 15, 2007, pp2479-2490.

[10] Bossanyi, E. A. (2007) GH Tidal Bladed Theory Manual. GH & Partners Ltd.

[11] Zaman, M. H. (2008) Suppression of Ocean Waves by Uniform Forced Currents. In *Proc. ASME 27th International Conference on Offshore Mechanics and Arctic Engineering*, Estoril, Portugal, 2008. OMAE2008-57370.

[12] Zheng, J. et al. (2008) Experimental study on mean velocity profiles under wave-current interactions. In *Proc. ASME 27th International Conference on Offshore Mechanics and Arctic Engineering*, Estoril, Portugal, 2008. OMAE2008-57007.

[13] Hedges, T. S. (1998) Wave Kinematics and Surface Parameters of Steep Waves Travelling on Sheared Currents. In *Journal of Waterway, Port, Coastal and Ocean Engineering*, Vol. 124, 1999, pp217-218.

[14] Garrad Hassan and Partners Ltd. (2008) Development of a design tool for axial flow tidal stream devices. *Department for Business Enterprise and Regulatory Reform*, Contract Number: T/06/00231/00/00, URN Number: 08/852.

[15] Eastwood, J. W., Townend, I. H. & Watson, C. J. H. (1987) The Modelling of Wave-Current Velocity Profiles in the Offshore Design Process. In *Advances in Underwater Technology, Ocean Engineering, Volume 12: Modelling the Offshore Environment,* Society for Underwater Technology, Graham & Trotman, pp327-341.

[16] Jenkins, A. D. (1987) A Dynamically Consistent Model for Simulating Near-surface Ocean Currents in the Presence of Waves. In *Advances in Underwater Technology, Ocean Engineering, Volume 12: Modelling the Offshore Environment,* Society for Underwater Technology, Graham & Trotman, pp342-352.

[17] Abonnel, C. et al. (2005) Some aspects of EDF modelling and testing activities, within its marine current energy research and development project. In *Proc. 6th European Wave and Tidal Conference*, Glasgow, UK, 2005. pp1-10.

[18] Molland, A. F. and Turnock, S. R. (2002) A Propeller Thrust and Torque Dynamometer for Wind Tunnel Models. *Strain,* 38: 3-10.

[19] Molland, A. F. (1976) The design, construction and calibration of a five-component strain gauge wind tunnel dynamometer. *University of Southampton, Ship Science Report,* 1/77, ISSN 0140-3818.

[20] Bahaj, A. et al., 2005. Experimental Investigation into the Hydrodynamic Performance of Marine Current Turbines. *Sustainable Energy Series, Report 3*, 2005.